

## Supernova studies in the SDSS-II/SNe Survey:

Spectroscopy of the peculiar SN 2007qd, and photometric properties of Type-Ia supernovae as a function of the distance to the host galaxy

LLUÍS GALBANY I GONZÀLEZ



Tesi del programa de Doctorat en Física de la Universitat Autònoma de Barcelona, sota la direcció del Dr. Ramon Miquel i Pascual.

Bellaterra, Octubre del 2011

Copyright © 2011 by Lluís Galbany i Gonzàlez  
All rights reserved

*Eppur si espande (accelerando)*

*A l'atzar agraeixo tres dons: haver nascut fosca,  
indetectable i de pressió negativa.  
I el tèrbol atzur de ser tres voltes rebel.*

Adaptació de Divisa, Maria Mercè Marçal

*Nena, el llamàntol vol tomàquet.*

Josep Pla



# Abstract MadLibs!!

This paper presents a \_\_\_\_\_ method for \_\_\_\_\_  
(synonym for new) (sciencey verb)  
the \_\_\_\_\_. Using \_\_\_\_\_, the  
(noun few people have heard of) (something you didn't invent)  
\_\_\_\_\_ was measured to be \_\_\_\_\_ +/- \_\_\_\_\_  
(property) (number) (number)  
\_\_\_\_\_. Results show \_\_\_\_\_ agreement with  
(units) (sexy adjective)  
theoretical predictions and significant improvement over  
previous efforts by \_\_\_\_\_, et al. The work presented  
(Loser)  
here has profound implications for future studies of  
\_\_\_\_\_ and may one day help solve the problem of  
(buzzword)  
\_\_\_\_\_.  
(supreme sociological concern)

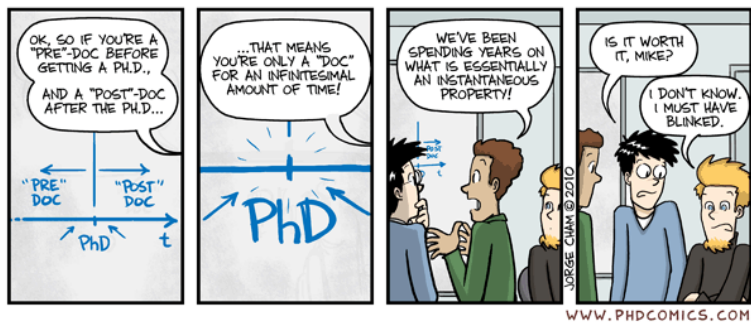
Keywords: \_\_\_\_\_, \_\_\_\_\_, \_\_\_\_\_  
(buzzword) (buzzword) (buzzword)

JORGE CHAM © 2009

WWW.PHDCOMICS.COM



WWW.PHDCOMICS.COM



WWW.PHDCOMICS.COM



---

## Acknowledgements

---

First of all, I would like to thank my supervisor Ramon Miquel for always being generous with his advice and guidance, for his patience and his invaluable support over the years. I should also thank Enrique Fernández for offering me the opportunity to start the PhD at the Institut de Física d'Altes Energies.

I also want to thank many people who helped me during these years in the institute, starting with Marino Maiorino, Julia Campa, Manel Martínez, Santi Serrano and Laia Cardiel, who worked with me during the first years working in the CCD testing. Linda Östman, who always found time to help me, and for the many scientific and nonscientific discussions over the last years. I was very lucky to have had the opportunity to work with Mercedes Mollá in the acquisition of the SNe spectra at TNG and Francisco Javier Castander in the reduction of these spectra. I would like to thank all the SDSS-II Supernova Survey collaborators for their advice and patience during all the interesting and instructive phonecon discussions, and in the meetings at Detroit, Philadelphia and Argonne. I also want to thank the people I met at the Modern Cosmology workshop in Benasque, Carlos Cunha, Diego Blas, Guillem Pérez-Nadal, Aurelio Carnero, Daniel G. Figueroa, Miguel Zumalacárregui, David Alonso and Pablo Arnalte-Mur, for both the interesting discussions we had there, and the time we enjoyed together at the Pyrenees.

I should thank IFAE's students and postdocs for offering me such a fruitful and pleasant atmosphere and making my time working at IFAE both rewarding and enjoyable, Martí Cuquet, Simone Paganelli, Marc Ramon, Diogo Boito, Pere Masjuan, Oriol Domènech, Oriol Romero-Isart, Joan Antoni Cabrer, Volker Vorwerk and so many others that came and left, especially my office mates Ester Aliu and Pol Martí.

Special thanks go to Jordi Nadal, Javi Serra and Mariona Aspachs, who accompanied me during these last five years and, I hope, during many more. I am very grateful to my family and friends who supported and encouraged me over the entire time, and especially to my parents because this is the touchable result/fruit of all their attention. Last but not least, to Laura, Bel, my spring flowers and the forthcoming, because all of this of course would not be possible without their presence in my life.



---

# Contents

---

<b>Acknowledgements</b>	i
<b>1 Introduction</b>	1
<b>2 Cosmology</b>	3
2.1 The Standard Model of Cosmology . . . . .	4
2.1.1 General Relativity and the Cosmological Principle . . . . .	4
2.1.2 Hubble law . . . . .	5
2.1.3 Spectral redshift and expansion . . . . .	7
2.1.4 Friedmann equations . . . . .	8
2.1.5 Cosmological parameters . . . . .	9
2.1.6 Content . . . . .	9
2.1.7 Distances . . . . .	13
2.1.8 Brightness and magnitudes . . . . .	17
2.2 History of the universe since Big Bang . . . . .	19
2.2.1 Early universe . . . . .	20
2.2.2 Nucleosynthesis . . . . .	21
2.2.3 CMB . . . . .	22
2.2.4 Large Scale Structure . . . . .	25
2.3 Summary . . . . .	26
<b>3 Supernovae</b>	27

## CONTENTS

---

3.1	Physics of SNe . . . . .	29
3.2	Spectral classification . . . . .	32
3.3	Spectra of Type Ia SNe . . . . .	34
3.4	Light-curves of Type Ia SNe . . . . .	36
3.4.1	Light-curve parametrization and models . . . . .	41
3.5	Type Ia SN host galaxies . . . . .	44
3.6	Type Ia SN rate of explosion . . . . .	45
3.7	Hubble diagram . . . . .	46
3.8	Surveys . . . . .	46
<b>4</b>	<b>The Sloan Digital Sky Survey-II/SNe</b>	<b>49</b>
4.1	Scientific Goals . . . . .	50
4.2	Technical summary. Instruments . . . . .	50
4.3	Observing strategy . . . . .	52
4.4	Data processing and target selection . . . . .	53
4.5	Spectroscopic and photometric follow-up observations . . . . .	55
4.6	Final Photometry . . . . .	57
4.7	Results . . . . .	58
<b>5</b>	<b>Supernova spectroscopy at the TNG</b>	<b>61</b>
5.1	Telescopio Nazionale Galileo . . . . .	62
5.1.1	The Device Optimized for LOw RESolution (DOLORES) . . . . .	65
5.2	Observations . . . . .	66
5.2.1	Data . . . . .	67
5.3	Reduction of the data . . . . .	69
5.3.1	Debiasing . . . . .	70
5.3.2	Flat Fielding . . . . .	71
5.3.3	Arc fitting . . . . .	72
5.3.4	SN spectra extraction . . . . .	73
5.3.5	Standard stars extraction . . . . .	76
5.3.6	Minor corrections . . . . .	78
5.3.7	Flux calibration of the SNe spectra . . . . .	79
5.4	Supernova Identification (SNID) . . . . .	79
<b>6</b>	<b>The Peculiar Supernova 2007qd</b>	<b>89</b>
6.1	Observations . . . . .	91
6.1.1	Photometry . . . . .	91
6.1.2	Spectroscopy . . . . .	93

---

6.2	Analysis . . . . .	95
6.2.1	Light-curves . . . . .	95
6.2.2	Spectroscopy . . . . .	98
6.3	Discussion and conclusions . . . . .	109
<b>7</b>	<b>Supernova properties as a function of the distance to the host galaxy center</b>	<b>113</b>
7.1	Data Sample . . . . .	114
7.1.1	SDSS-II Supernova Sample . . . . .	114
7.1.2	Host Galaxy Identification . . . . .	115
7.2	Measurements . . . . .	116
7.2.1	Light-curve Parameters . . . . .	116
7.2.2	Host Galaxy Typing . . . . .	119
7.2.3	Galactocentric Distances (GCD) . . . . .	121
7.2.4	Metallicity . . . . .	128
7.3	Results . . . . .	128
7.3.1	Correlations between projected distance and SN color ( $A_V, c$ ) . . . . .	130
7.3.2	Correlations between projected distance and LC shape ( $\Delta, x_1$ ) . . . . .	132
7.3.3	Correlations between projected distance and Hubble residuals . . . . .	134
7.3.4	Correlations between projected distance and local metallicity . . . . .	135
7.4	Discussion . . . . .	136
<b>8</b>	<b>Summary and Conclusions</b>	<b>143</b>
<b>A</b>	<b>TNG images</b>	<b>145</b>
<b>B</b>	<b>Maths</b>	<b>153</b>
B.1	Chebyshev polynomials . . . . .	153
B.2	Binning error calculation . . . . .	154
<b>C</b>	<b>Computation of distances</b>	<b>157</b>
C.1	Spherical trigonometry . . . . .	157
C.2	Projected galactocentric distances (PGCD) . . . . .	159
C.2.1	Angular separation . . . . .	159
C.2.2	Projected galactocentric distance . . . . .	159
C.3	Normalized Galactocentric Distances (NGCD) . . . . .	160
C.3.1	Petrosian normalization . . . . .	160
C.3.2	Sérsic normalization . . . . .	160
C.3.3	Isophotal normalization . . . . .	162

## **CONTENTS**

---

<b>D SNe distance measurements</b>	<b>163</b>
<b>List of Figures</b>	<b>166</b>
<b>List of Tables</b>	<b>171</b>
<b>Bibliography</b>	<b>172</b>

# CHAPTER 1

---

## Introduction

---

This thesis comprises the work I have been doing during the last four years at Institut de Física d'Altes Energies (IFAE) as a PhD student, and has to be understood within the context of the Sloan Digital Sky Survey II Supernova (SDSS-II/SNe) survey.

The content of this thesis is ordered as follows. In the next Chapter (§2) I introduce the main concepts of the Standard Model of Cosmology, presenting the origins, the properties of its contents, and the distance and the brightness measurements. I also reconstruct the history of universe since the Big Bang and summarize some of the most exciting discoveries that have confirmed the Standard Model predictions.

In §3, a detailed explanation of supernovae (SNe) is given, including the physical mechanism that accounts for their explosions, the differences among the several types of SNe, and their spectral classification. We also describe the spectroscopic and photometric properties of Type-Ia SNe. After that, we review the SNe rate of the explosion measurements, the properties of their host galaxies, and their use in Cosmology through the Hubble diagram.

After that, in §4, I describe the SDSS-II/SNe survey, a three-year (2005-2007) extension of SDSS of which I am an external collaborator, which has detected and measured light-curves for several hundred supernovae through repeat scans of the sky.

As a part of the spectroscopic follow-up of the SDSS-II/SNe candidates, we contributed to the project taking spectra of 23 SNe during four nights in October and November (5-6 Oct. and 4-5 Nov.) of 2007 using the Telescopio Nazionale Galileo (TNG) located at the Observatorio del Roque de Los Muchachos (ORM) in La Palma. In §5, the whole reduction procedure, from the acquisition of the raw data by the telescope camera to the final flux-calibrated spectra, is described.

Following the spectra reduction, in §6, I describe one of the most subluminous

## Introduction

---

type-Ia events known, the peculiar 2007qd supernova, for which we took the first spectrum. The observed properties of 2007qd place it in the 2002cx subclass of supernovae, specifically as a member intermediate to 2002cx and 2008ha, linking these objects. We present the photometric and spectroscopic observations of 2007qd and compare its unique properties with a range of other SNe. This work was compiled and published in [McClelland et al. \(2010\)](#).

Then, in §7, the three-year sample of Type Ia supernovae (SNe Ia) discovered by the SDSS-II/SNe Survey is used to look for dependencies between photometric SN Ia properties and the projected distance to the host galaxy center, using the distance as a proxy for local galaxy properties (local star-formation rate, local metallicity, etc.). We find that the excess color of the SN, parametrized by  $A_V$  in MLCS2k2 and by  $c$  in SALT2 decreases with the projected distance, in particular for spiral galaxies. At a lower significance we find that the light-curve width, as obtained from MLCS2k2, is correlated with the SN-galaxy separation for elliptical hosts, so that SNe Ia with narrower light-curves, hence dimmer, are more commonly observed at large distances from the host galaxy core. This analysis was presented in the *Supernovae and their Host Galaxies* conference which was held at Sydney, Australia in June 2011, and will be published in [Galbany et al. \(2011\)](#).

Finally, in §8 we give a summary and the conclusions of this thesis.

## CHAPTER 2

---

### Cosmology

---

**C**OSMOLOGY is the field that studies the origin and evolution of the universe as a whole. Its modern view was developed in the first half of the twentieth century, moving from philosophy to science, and trying to look for physical answers to questions such as what is the universe, what is it made of, or when and how it was formed, for which we have not found concrete answers yet. However, these studies have developed a broad knowledge about it. The Standard Cosmological model forms a coherent framework from which we can interpret the observations and parametrize them in some numbers, the cosmological parameters. We know now that the universe is not only expanding but accelerating its expansion, basically due to one of its components which we do not know much about, called Dark Energy (DE).

In the following chapters, we will focus on Type Ia Supernovae (SNe Ia), a kind of thermonuclear star explosions which have been used as distance indicators. It is since the discovery that the expansion of the universe is currently accelerating ([Riess et al., 1998](#), [Perlmutter et al., 1999](#)) that SNe Ia have acquired a very important role in Cosmology, because they provided the first proof of this acceleration.

In this chapter we will introduce in §2.1 the Standard Model of Cosmology, presenting the origins and its main concepts, equations and measurements. The properties of its contents will also be summarized, especially Dark Energy responsible of the accelerated expansion, and the distance and the brightness measurements. We then reconstruct the history of universe since the Big Bang (§2.2), and summarize some of the most exciting discoveries that have confirmed the Standard Model predictions, as the measurement of the element abundances in the Nucleosynthesis epoch (§2.2.2), the observation of the Cosmic Microwave Background (§2.2.3), and the measurements of

the Baryon Acoustic Oscillations, a natural standard ruler coming from the primordial anisotropies.

For further reading about Cosmology and Astrophysics there are many excellent textbooks, but some of those that the author of this thesis has been using during his graduate student period and helped him to learn are: [Ryden \(2003\)](#), [Roos \(2003\)](#), [Dodelson \(2003\)](#), [Liddle \(2003\)](#), [Carroll et al. \(2006\)](#), [Karttunen et al. \(2007\)](#) and [Weinberg \(2008\)](#), among many other books and review articles.

## 2.1 The Standard Model of Cosmology

### 2.1.1 General Relativity and the Cosmological Principle

The theoretical framework of the current cosmological model comes from the theory of General Relativity (GR) ([Einstein, 1916](#)) and the *Cosmological Principle*, which assumes that the universe is both isotropic and homogeneous on sufficiently large scales, appearing the same at all locations and in all directions, i.e., there is no preferred places nor observers in the universe. It may seem strange to affirm that the universe is homogeneous, because at local scales we see nothing but voids among stars and galaxies. But as we consider larger scales ( $\sim 100$  Mpc)<sup>1</sup>, it can be treated as a homogeneous perfect fluid<sup>2</sup>. This Cosmological Principle has been verified through several observations. The measurement of the Cosmic Microwave Background (CMB)<sup>3</sup> revealing that the temperature of the relic radiation coming from the early universe is mostly isotropic, differing only in one part in  $10^5$  ([Smoot et al., 1991](#), [Komatsu et al., 2011](#)), as well as the quasi-homogeneous matter distribution in structures on large scales ([Eisenstein et al., 2005](#)) are examples of well-studied observational confirmations.

In GR, gravitation is not understood as an attracting force among masses, but as an intrinsic deformation of the space-time depending on the configuration of energy-matter that occupies that place. The metric of space-time in GR comes from the *Minkowski metric* used in the Special Relativity,

$$ds^2 = g_{\mu\nu} dx^\mu dx^\nu = c^2 dt^2 - dl^2, \quad (2.1)$$

adding some assumptions. If space-time is expanding, the spatial component of the metric should evolve with time. Then we can introduce the *scale factor*  $R(t)$  which has all the time dependence of the spatial component,

$$ds^2 = c^2 dt^2 - R(t)^2 dl^2. \quad (2.2)$$

Supposing that the space-time distance between two events in the universe can be measured as in the surface of a 4D hypersphere, we obtain the *Robertson-Walker metric*

---

<sup>1</sup>1 parsec (pc) is defined as the distance at which 1 Astronomical Unit (AU), i.e., the distance from the Earth to the Sun (1 AU = 149597870.7 km), subtends an angle of 1 arcsec. 1 pc =  $3.085677 \cdot 10^{16}$  m = 3.26 light-years.

<sup>2</sup>A fluid with no viscosity or heat conduction.

<sup>3</sup>Detailed explanation in §[2.2.3](#).

(RW), the more general metric that describes an isotropic and homogeneous space,

$$ds^2 = c^2 dt^2 - R(t)^2 \left[ \frac{dr^2}{1 - \kappa r^2} + r^2 (d\theta^2 + \sin\theta d\phi^2) \right], \quad (2.3)$$

where  $t$  is the proper time,  $r, \phi, \theta$  are the comoving spatial polar coordinates, and  $\kappa$  is defined as the curvature of the universe governed by the amount of energy and matter inside it, and, as it does not change with the expansion, can take three different values depending on the geometry,

- $\kappa = +1$  for a closed and finite universe with spherical geometry.
- $\kappa = -1$  for an open and infinite universe with hyperbolic geometry.
- $\kappa = 0$  for a flat and also infinite universe.

One usually defines the scale factor as a dimensionless ratio between the value of  $R(t)$  at time  $t$  and its present value  $\left[a(t) = \frac{R(t)}{R_0}\right]$ . In this form, the present value of  $a(t_0) = a_0$  is 1, and decreases going back in time. As  $a(t)$  is a measurement of the scale of the universe, it can be used to measure the expansion rate of the universe, known as the *Hubble parameter*, named after Edwin Hubble who first measured it:

$$H(t) = \frac{\dot{a}}{a} \quad \text{where} \quad \dot{a} \equiv \frac{da}{dt}. \quad (2.4)$$

### 2.1.2 Hubble law

In 1929, Hubble studied the relationship between the apparent recession velocities of some spiral galaxies (which he called nebulae) and the distance to those galaxies. The velocities were determined through the redshift<sup>4</sup> associated spectroscopically to each galaxy ( $v = cz$ , at low redshift), and the distances through the apparent luminosities of the brightest stars in such galaxies. From his results, he established that the velocity was proportional to the distance from the Earth (Fig. 2.1). Then,

$$v = H_0 d \quad \text{or} \quad z = \frac{H_0}{c} d, \quad (2.5)$$

where  $H_0$  is the proportionality constant known as the *Hubble constant*. Although measuring a galaxy's redshift was relatively easy, measuring distances was more complicated. Hubble found a value for  $H_0$  of  $500 \text{ km s}^{-1} \text{Mpc}^{-1}$ , which is much higher than the currently accepted value<sup>5</sup> due to errors in the calibration used for distances, which made him underestimate the distances to the galaxies. This was a direct measurement of the present value of the expansion rate, pointing out that galaxies are

<sup>4</sup>See §2.1.3

<sup>5</sup>The latest measurement from the Wilkinson Microwave Anisotropy Probe (WMAP) 7-Year results is  $H_0 = 70.4 \pm 1.4 \text{ km s}^{-1} \text{ Mpc}^{-1}$ , assuming a  $\Lambda\text{CDM+SZ+LENS}$  cosmological model and considering other data such as Baryon Acoustic Oscillations (BAO) and Type Ia Supernovae (SNeIa) (Jarosik et al., 2011).

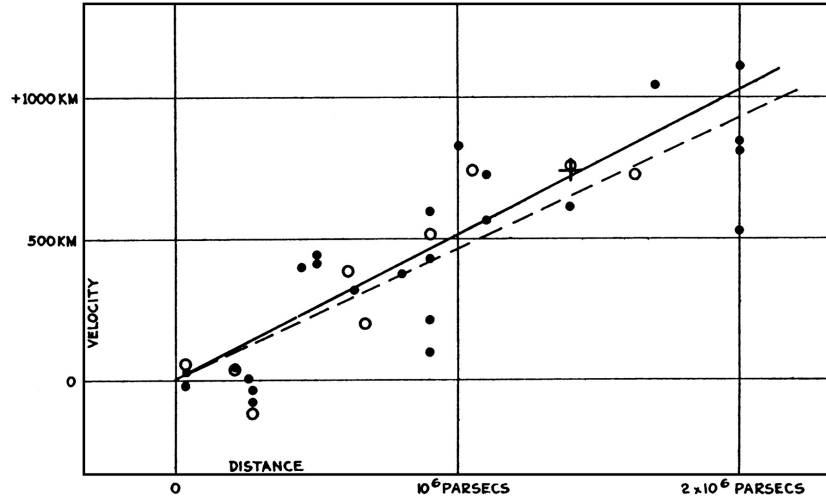


**Figure 2.1:** Original figure from Hubble's paper (Hubble, 1929) relating the recession velocity with distance from the Earth. The solid and dashed lines are linear fits using different corrections for the solar system movement. Note the wrong units in the y axis (km instead of km/s).

receding from us regardless of the direction in the sky, i.e., the greater the distance between any two galaxies, the greater their relative speed of separation. Hubble established that these recession velocities could not be due to peculiar velocities, but to a general expansion of space. That was consistent with the solutions of Einstein's equations of general relativity for a homogeneous, isotropic expanding space, and it was the first observational support for the Big Bang theory proposed by Georges Lemaître in 1927, over other Steady State models, which rejected the expansion.

If galaxies are moving away from each other at a certain rate, it could be possible to determine at which time there were together if that expansion has been constant during this time. As the Hubble constant has units of inverse of time, we can estimate the time that has elapsed since they were in contact. From the current value of  $H_0$ , we obtain

$$H_0^{-1} = t_H = 14.2 \pm 0.3 \text{ Gyr}, \quad (2.6)$$

giving an idea of the age of the universe, and comparable to the ages computed for the oldest known stars (Frebel et al., 2007). We can also make the estimation of the maximum distance that a photon could have travelled since the Big Bang, giving an idea of the size of our universe:

$$c H_0^{-1} = R_H = 4.3 \pm 0.1 \text{ Gpc}. \quad (2.7)$$

However these values do not have to be exactly the age and the size of the universe, because the Hubble constant has not been constant. For instance, if gravity was the only force at work on large scales, it could have slowed down the expansion at the beginning, in the same way that Dark Energy is fastening it up now. So that these are only approximations to the true age and size of the universe, and at small distances,

the Hubble law can be approximated as

$$v = H_0 r + \frac{1}{2}(1 + q_0)(H_0 r)^3 \quad (2.8)$$

$$\text{where } q_0 = -\frac{a(t_0)\ddot{a}(t_0)}{\dot{a}(t_0)^2}, \quad (2.9)$$

is the *deceleration parameter*, a dimensionless measure of the cosmic acceleration of the expansion of space, which appears in the second order term in a power series expansion in terms of the distance. As the expansion is actually accelerating, this parameter is negative ( $q_0 < 0$ ).

### 2.1.3 Spectral redshift and expansion

Most of the information we can obtain from the universe comes from the light we see from stars and galaxies. Using spectroscopy we can measure the absorption lines created in the relatively cool atmospheres of the stars. With this technique we can know which elements are in those atmospheres, since every element has its own characteristic lines. The redshift used by Hubble for measuring the radial velocities is simply a measure of the Doppler effect in those spectral lines. An element with an emission at  $\lambda_{em}$  which is observed at  $\lambda_{obs}$  has a redshift determined by

$$z = \frac{\lambda_{obs} - \lambda_{em}}{\lambda_{em}}. \quad (2.10)$$

It is called redshift because the vast majority of galaxies has  $z > 0$ , meaning that the observed wavelength is longer (i.e. redder) than the emitted wavelength, so that the object is moving away from us. There are objects with negative redshifts (blueshifts) but all are close and their shift is due to a peculiar motions instead of a global contraction.

Redshift can be related to the scale factor considering the path along a null geodesic ( $c^2 dt^2 = R(t)^2 dl^2$ ) of a photon traveling from a distant object to us. If we integrate the time between the emission and the observation of two consecutive wave crests, emitted at  $t_e$  and  $t_e + \delta t_e$  and observed at  $t_0$  and  $t_0 + \delta t_0$  respectively,

$$\int_l^0 dl = \int_{t_e}^{t_0} \frac{c \, dt}{R(t)} = \int_{t_e + \delta t_e}^{t_0 + \delta t_0} \frac{c \, dt}{R(t)}, \quad (2.11)$$

we can reorder the terms as

$$\int_{t_e}^{t_e + \delta t_e} \frac{c \, dt}{R(t)} = \int_{t_0}^{t_0 + \delta t_0} \frac{c \, dt}{R(t)}. \quad (2.12)$$

The result of the integration would be

$$\frac{\delta t_e}{R(t_e)} = \frac{\delta t_0}{R(t_0)}, \quad (2.13)$$

where, considering that the wavelength is proportional to the time between crests, we can obtain

$$\frac{R(t_0)}{R(t_e)} = \frac{\delta t_0}{\delta t_e} \propto \frac{\lambda_0}{\lambda_e} \equiv 1 + z. \quad (2.14)$$

Substituting the definition of the dimensionless scale factor we arrive to

$$a(t_e) = \frac{1}{1+z}. \quad (2.15)$$

For instance, if we detect a galaxy at redshift  $z = 3$ , we are observing it as it was when the universe had a scale factor of  $a(t_e) = \frac{1}{4}$ . Strictly speaking, the redshift is a measure of the expansion factor between the emission and observation of a photon.

#### 2.1.4 Friedmann equations

In 1924, Friedmann combined the Cosmological Principle with the field equation of General Relativity to relate the dynamic evolution of the universe with its matter and energy content (Friedmann, 1924). The equation he found is

$$H(t)^2 = \left(\frac{\dot{a}}{a}\right)^2 = \frac{8\pi G}{3}\rho(t) - \frac{\kappa}{a(t)^2}, \quad (2.16)$$

where  $\rho$  is the energy density of the universe, and  $G$  Newton's Gravitational constant. This equation, together with the *fluid equation*, which describes how the density of a perfect fluid expands constrained to energy conservation,

$$\dot{\rho} + 3H(\rho + P) = 0, \quad (2.17)$$

where  $P$  is the pressure of a perfect fluid, can be combined in order to obtain the *acceleration equation*,

$$\frac{\ddot{a}}{a} = -\frac{4\pi G}{3}(\rho + 3P), \quad (2.18)$$

which describes how the expansion speeds up or slows down with time. However, only two of these three equations are independent, and there are three unknown functions of time: the scale factor  $a(t)$ , the energy density  $\rho(t)$ , and the pressure  $P(t)$ . To solve this system we need the *equation of state*, a relation between  $\rho$  and  $P$ ,

$$P(\rho) = w\rho, \quad (2.19)$$

where  $w$  is the *state parameter*, a dimensionless number which, if it is constant<sup>6</sup>, leads to a solution for the fluid equation of the kind

$$\rho(t) = \rho_0 a^{-3(1+w)}, \quad (2.20)$$

---

<sup>6</sup>in §2.1.6 we analyze a non-constant behavior of  $w$ .

completely describing the dynamics of the universe. The expressions (2.16), (2.17) (2.18) and (2.19) are the key equations that describe how the universe expands.

### 2.1.5 Cosmological parameters

It is common to define the *critical density* ( $\rho_c$ ) as the density that a perfect fluid should have in a spatially flat universe ( $\kappa = 0$ ), from the Friedmann equation,

$$\rho_c(t) = \frac{3H(t)^2}{8\pi G}. \quad (2.21)$$

If the density of the content of the universe is greater than that value, the universe would be positively curved ( $\kappa = +1$ ) and finite, while if it is lower it would be negatively curved ( $\kappa = -1$ ) and infinite. It is also taken as a natural scale when measuring the densities of the different components of the universe. Then, we can define the dimensionless *density parameter*, as the ratio of the density respect to the critical density,

$$\Omega(t) = \frac{\rho(t)}{\rho_c(t)} = \frac{8\pi G\rho(t)}{3H(t)^2}, \quad (2.22)$$

from which the Friedmann equation can be written as

$$\Omega - 1 = \frac{\kappa}{a^2 H^2}, \quad (2.23)$$

where we can recover that if  $\Omega = 1$  (i.e.  $\rho = \rho_c$ ), the universe is flat ( $\kappa = 0$ ).

Current observations measure  $\rho_c(0) = (9.2 \pm 1.8) \cdot 10^{-27} \text{ kg m}^{-3}$ , equivalent to a density of six hydrogen atoms per cubic meter, and  $\Omega_0 = 1.0023 \pm 0.0056$  from WMAP, based on the first peak of the CMB angular power spectrum, consistent with zero curvature (Komatsu et al., 2011).

### 2.1.6 Content

By now, we have talked about the universe as a perfect fluid, but we know that there are several kinds of particles which act in different ways under the influence of fundamental forces. Then, the components can be generally divided in three different groups: matter, radiation and dark energy. In order to find solutions to the cosmological equations we can parametrize them through their different state parameter  $w$ .

#### Cold Matter

This group includes all the non-relativistic particles, both baryons ( $b$ ) and Dark Matter<sup>7</sup> ( $DM$ ). Although it is supposed that today  $DM$  dominates in content over  $b$ , we will generally refer to the whole group as *matter* ( $m$ ), which is characterized by a value of the state parameter  $w = 0$ , given the

---

<sup>7</sup>Called Dark because it does not interact electromagnetically and has to be detected from its gravitational effects with baryonic matter. (Rubin et al., 1980, Zwicky, 1933)

fact that performs a null pressure. This gives an expression for the matter energy density from equation (2.20)

$$\rho_m = \rho_{m,0} a^{-3}, \quad (2.24)$$

so the evolution of its density is proportional to the physical volume of the universe. In a matter-dominated universe we can see from the Friedmann equation (2.16), that the scale parameter evolves with time as

$$a_m(t) \propto t^{2/3}. \quad (2.25)$$

The latest results of the matter density parameters from the WMAP 7-years are:

$$\Omega_{b,0} = 0.0456 \pm 0.0016 \quad \Omega_{DM,0} = 0.227 \pm 0.014 \quad (2.26)$$

$$\Omega_{m,0} = \Omega_{b,0} + \Omega_{DM,0} = 0.272 \pm 0.016 \quad (2.27)$$

### Hot Matter (Radiation)

This group contains all relativistic particles, called generally *radiation* ( $r$ ). They have a state parameter of  $w = 1/3$ , which leads to an expression for the radiation energy density of

$$\rho_r = \rho_{r,0} a^{-4}. \quad (2.28)$$

In an expanding universe, the radiation energy density decreases faster than the volume expansion. The extra factor of  $1/a$  is due to the cosmological redshift, since the energy of the radiation decreases as  $E \propto \nu \propto \lambda^{-1}$ . Just as we did with matter, we can extract from the Friedmann equation (2.16) that, for a radiation-only universe, the scale factor follows a relation with time of

$$a_r(t) \propto t^{1/2}. \quad (2.29)$$

Current measurements (Komatsu et al., 2011) point that, compared to the matter content, the radiation contribution ( $\Omega_{r,0}$ ) to the total energy density is now insignificant.

### Dark Energy

Current observations indicate that the universe is experiencing an epoch of accelerated expansion. Introducing the equation of state (2.19) into the acceleration equation (2.18), we can notice that any component with  $w < -\frac{1}{3}$  would provide a positive acceleration. This exotic component is generally referred to as *Dark Energy*. The theoretical explanations of its nature cover a wide range of possibilities, from the chance that General Relativity breaks down on cosmological scales, through a parametrization using a

scalar dynamic field called *Quintaessence*, to a Cosmological Constant ( $\Lambda$ ) associated with the vacuum energy density<sup>8</sup>.

The introduction of the  $\Lambda$  term into the field equations of GR by Albert Einstein was motivated by its desire to allow a static cosmological model. But, after the demonstration by Lemâitre that these solutions were in fact unstable, together with the discovery of the expansion of the universe by Edwin Hubble in 1929,  $\Lambda$  was dropped. It was after the discovery in 1998 of the accelerated expansion of the universe, when this constant was reinterpreted as a new component of the universe associated to the energy vacuum, which drives the acceleration of the expansion. It has a value of the state parameter near  $w \sim -1$  (Fig. 2.2), which means that its density remains constant with the expansion (from Eq. 2.20,  $\rho_\Lambda(t) = \rho_{\Lambda,0}$ ). This gives a relation between the pressure it performs and its energy density of

$$P_\Lambda = -\rho_\Lambda. \quad (2.30)$$

Again, using the Friedmann equation (2.16), for a universe containing only vacuum energy, we can obtain

$$a_\Lambda(t) \propto e^{H_0 t}. \quad (2.31)$$

That is an exponentially accelerated expansion. From the latest measurements from the WMAP 7-years results, the vacuum energy density is determined to have the value,

$$\Omega_{\Lambda,0} = 0.734 \pm 0.029. \quad (2.32)$$

We supposed the state parameter  $w$  constant, but there exist other general DE parameterizations that would allow a different value from  $-1$ . For example, it could be given by two factors

$$\Omega_\Lambda(z) = \frac{\Omega_{\Lambda,0}}{a^{3(1+w_0)}}, \quad (2.33)$$

or we could allow  $w$  to evolve with time. One popular parametrization (Chevallier et al., 2001, Linder, 2003) is:

$$w(z) = w_0 + w_a \frac{z}{1+z}. \quad (2.34)$$

The model that best describes the current observations is known as  $\Lambda$ CDM (an abbreviation for Lambda-Cold Dark Matter), which is a spatially flat universe which contains matter, radiation and vacuum energy. Mixing all these components we can

---

<sup>8</sup>For a review on Dark Energy see Frieman et al. (2008a)

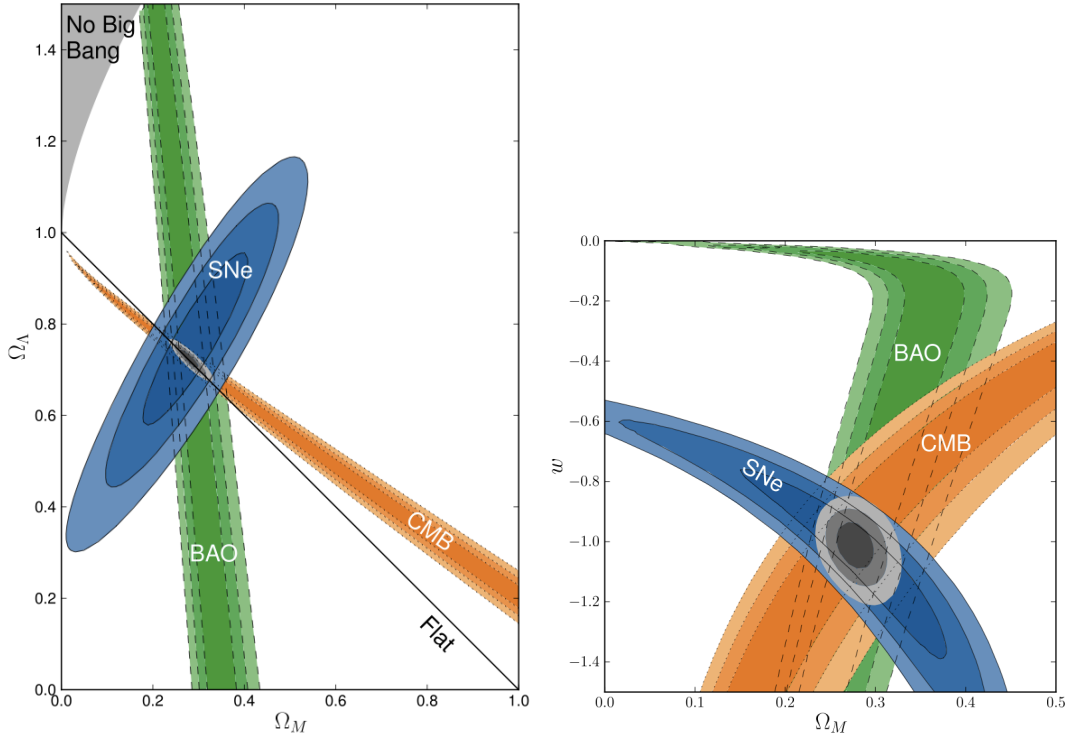


**Figure 2.2:** Left: measurements of the density parameters of Dark Energy ( $\Omega_\Lambda$ ) and matter ( $\Omega_m$ ), from the 68.3%, 95.4%, and 99.7% confidence regions obtained combining SNe Ia, BAO and CMB constrains, and assuming constant DE state parameter ( $w = -1$ ). The resulting region is compatible with a flat and accelerating universe. Right: the same confident regions for the ( $\Omega_m$ ,  $w$ ) plane. Zero curvature and constant  $w$  have been assumed. Figures taken from [Amanullah et al. \(2010\)](#).

write the total energy density as

$$\rho_T = \sum \rho_i = \rho_m + \rho_r + \rho_\Lambda, \quad (2.35)$$

and analogously the total pressure as

$$P_T = \sum P_i = P_r + P_\Lambda. \quad (2.36)$$

where  $P_m$  is zero. The Friedman and acceleration equations can be rewritten as

$$H^2 = \left( \frac{\dot{a}}{a} \right)^2 = \frac{8\pi G}{3} (\rho_m + \rho_r) - \frac{\kappa}{a^2} + \frac{\Lambda}{3}, \quad (2.37)$$

$$\frac{\ddot{a}}{a} = -\frac{4\pi G}{3} (\rho_m + \rho_r + 3P_r) + \frac{\Lambda}{3}, \quad (2.38)$$

which, for historical reasons, are expressed using  $\Lambda = 8\pi G\rho_\Lambda$ . Taking the density parameter of each of the components previously discussed, we can also rewrite the

Friedmann equation (2.23) as

$$\Omega_T \equiv \Omega_m + \Omega_r + \Omega_\Lambda = 1 - \Omega\kappa, \quad (2.39)$$

where  $\Omega_X = \rho_X/\rho_c$ , except for curvature for which the associated definition of the density parameter is  $\Omega_\kappa = -\kappa/a^2H^2$ . Using this formalism, it is also interesting to obtain an expression of the Hubble parameter as a function of the redshift. First, we can reorder Eq. (2.23) to obtain

$$H^2(1 - \Omega_T) a(t)^2 = -\kappa, \quad (2.40)$$

which at  $t = t_0$  takes the form,

$$H_0^2(1 - \Omega_{T,0}) = -\kappa. \quad (2.41)$$

Then, from the definition of the density parameter (2.22) we can get the following relation comparing its definition to its present value:

$$\frac{\Omega_T}{\Omega_{T,0}} = \frac{\rho}{\rho_0} \frac{H_0^2}{H^2}. \quad (2.42)$$

Combining the three equations (2.40), (2.41) and (2.42), we arrive to

$$\begin{aligned} H(z) &= H_0(1+z) \left[ \frac{\rho}{\rho_0} \frac{\Omega_{T,0}}{(1+z)^2} + 1 - \Omega_{T,0} \right]^{1/2} = \\ &= H_0 \left[ \Omega_{m,0}(1+z)^3 + \Omega_{r,0}(1+z)^4 + \Omega_{\Lambda,0} + (1 - \Omega_{T,0})(1+z)^2 \right]^{1/2}, \end{aligned} \quad (2.43)$$

which is the expression of the Hubble parameter as a function of the redshift, and will be useful for the distance measurements.

### 2.1.7 Distances

Measuring distances in the universe is not only something difficult to do, but also difficult to define. Due to its expansion, the distance to a certain object varies with the propagation time of the emitted light. Several methods for measuring cosmic distances exist and will be discussed in turn.

#### Comoving distance

The distance between two objects in a coordinate system which expands with the universe, i.e., this distance remains constant with time if these objects are moving with the Hubble flow<sup>9</sup> (do not have peculiar velocities). The *comoving distance* from an observer to a distant object (e.g. galaxy) can be found by measuring the time that a photon, which travels along null

---

<sup>9</sup>Objects with no peculiar velocities recede due to the expansion of the universe. This movement is called Hubble flow.

geodesics ( $ds^2 = 0$ ), has spent to reach us. Putting this into the RW metric (2.3) we can obtain

$$c^2 dt^2 = R(t)^2 \frac{dr^2}{\sqrt{1 - \kappa r^2}} \equiv R(t)^2 d\chi^2, \quad (2.44)$$

where we have used the *comoving coordinate*  $\chi$ . Reordering the terms, we arrive at the expression,

$$\chi = c \int_{t_e}^{t_o} \frac{dt'}{R(t')}, \quad (2.45)$$

where  $t_e$  is the time of the emission, and  $t_o$  is the time of observation.

### Proper distance

While the comoving distance remains fixed as the universe expands, the *proper distance* grows simply because of the expansion, as it is the physical distance we would measure with a ruler (if it were possible). Therefore, if comoving and proper distances are numerically equal at the current age of the universe, they will differ in the past and in the future. Then, we can obtain the proper distance from the expression of the comoving distance at time  $t_0$  (when the scale factor is  $R_0$ ),

$$d_P(t) = R_0 \chi = c \int_{t_e}^{t_o} \frac{dt'}{a(t')}. \quad (2.46)$$

It is useful to parametrize the proper distance using redshift instead of time, given the fact that we can easily measure  $z$  (because it is an observable). Differentiating the relation between scale factor and redshift (2.15) with respect to time, we can obtain

$$\frac{dz}{dt} = -\frac{\dot{a}(t)}{a(t)^2} \quad \frac{dt}{a(t)} = -\frac{dz}{H(z)}, \quad (2.47)$$

which substituted in Eq. (2.46), changing the integration limits ( $t_e \rightarrow z$  and  $t_0 \rightarrow z_0 = 0$ ), and using the expression of the Hubble parameter with respect to time (2.43), we arrive at

$$\begin{aligned} d_P(z) &= c \int_0^z \frac{dz'}{H(t')} = \\ &= \frac{c}{H_0} \int_0^z \frac{dz'}{\sqrt{\Omega_{m,0}(1+z)^3 + \Omega_{r,0}(1+z)^4 + \Omega_{\Lambda,0} + (1-\Omega_{T,0})(1+z)^2}}. \end{aligned} \quad (2.48)$$

Unfortunately, the proper distance cannot be really directly measured. For this reason, we should find other distances that we can measure and relate to the proper distance.

### Angular diameter distance

We can measure the distance to an object when its physical extent is known ( $l$ ), by measuring its apparent angular size ( $\theta$ ). The *angular diameter distance* is defined as

$$d_A = \frac{l}{\theta}. \quad (2.49)$$

The light we observe from an extended object was emitted at  $t_e$ , when the universe had the scale factor  $R(t_e)$ . Then, the angular size we observe is

$$\theta = \frac{l}{R(t_e)\chi}. \quad (2.50)$$

Reordering, we can obtain the relation between proper and angular distances:

$$d_A = R(t_e)\chi = R_0(1+z)^{-1}\chi = \frac{d_P(z)}{1+z} \quad (2.51)$$

### Luminosity distance

Another indirect measurement of the distance is the observed energy flux ( $F$ ) by an object with known luminosity ( $L$ ), the amount of electromagnetic energy that radiates per unit of time<sup>10</sup>. In a flat and static universe, the flux decreases as the inverse of the squared distance ( $F = L/(4\pi r^2)$ ). Reordering, we can express the *luminosity distance* ( $d_L$ ) as

$$d_L = \sqrt{\frac{L}{4\pi F}}. \quad (2.52)$$

Photons emitted at time  $t_e$  have spread out to a sphere of area  $A(t_0) = 4\pi R_0^2\chi^2$ , at the present time  $t_0$ . We also have to take into account that the flux in an expanding universe decreases by a factor  $(1+z)^{-2}$ . This is due to, on one hand, the increase of the wavelength of the emitted photons by Doppler effect ( $\lambda_0 = (1+z)\lambda_e$ ), and on the other hand, the greater interval between two photon detections ( $\delta t_0 = (1+z)\delta t_e$ ). Then, the relation between the observed flux and the luminosity of a distant object is

$$F = \frac{L}{4\pi R_0^2\chi^2} \frac{1}{(1+z)^2}, \quad (2.53)$$

from where we can extract the expression for the luminosity distance, and the relation with the other distance definitions:

$$d_L = R_0(1+z)\chi = (1+z)d_P(z) = (1+z)^2 d_A. \quad (2.54)$$

---

<sup>10</sup>These objects are known as *Standard Candles*. Type Ia Supernovae, discussed in §3, can be turned into one of such objects

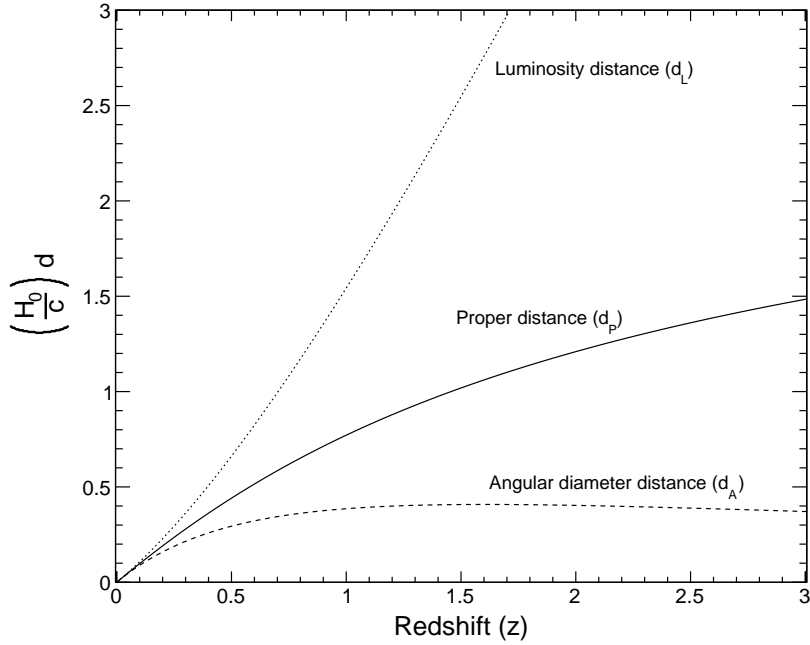


**Figure 2.3:** Redshift dependence of the different definitions of distance. It can be seen that for low redshifts the three definitions give the same quantity. But for higher redshifts, the luminosity distance ( $d_L$ ) is clearly greater, while the angular diameter distance ( $d_A$ ) is smaller than the proper distance. Note that the angular distance has a maximum near  $z \sim 1.6$ , so that, the angular size of an object of fixed length increases at higher redshifts.

In Fig. 2.3 we show the dependence with redshift of the previous definitions of distance. It can be seen that for low redshifts ( $z \lesssim 0.2$ ) the three definitions converge, while for higher redshifts, the luminosity distance ( $d_L$ ) is larger than the proper distance, and the angular diameter distance ( $d_A$ ) is smaller than  $d_p$ .

We can explore the relation between these distances at low redshift. We start with a Taylor expansion of  $a(t)$  about  $t = t_0$ :

$$a(t) \sim 1 + H_0(t - t_0) - \frac{1}{2}q_0H_0^2(t - t_0)^2 + O[(t - t_0)^3]. \quad (2.55)$$

Inverting and keeping up to the second order we obtain

$$\frac{1}{a(t)} \sim 1 - H_0(t - t_0) + \frac{1+q_0}{2}H_0^2(t - t_0)^2, \quad (2.56)$$

which introduced in Eq. (2.46) and integrating gives

$$d_P(t_0) \sim c(t_0 - t_e) + \frac{cH_0}{2}(t_0 - t_e)^2, \quad (2.57)$$

where the first term is the proper distance in a static universe, and the second term is the distance correction due to the expansion during the time the light was traveling. In order to change the dependence of this expression to a measurable quantity, we can take the relation between the redshift and the scale factor (2.15), and expand again in Taylor series around  $z = 0$ . We obtain

$$z \sim H_0(t_0 - t_e) + \frac{1+q_0}{2} H_0^2(t_0 - t_e)^2, \quad (2.58)$$

where isolating  $t_0 - t_e$

$$t_0 - t_e \sim \frac{1}{H_0} \left[ z - \frac{1+q_0}{2} z^2 \right], \quad (2.59)$$

and substituting in (2.57)

$$d_P(z) \sim \frac{c}{H_0} z \left[ 1 - \frac{1+q_0}{2} z \right], \quad (2.60)$$

we arrive to the same approximation of the proper distance but relative to redshift. Thus it holds true in the limit  $z \ll 2/(1+q_0)$ .

In the same way, we can obtain similar expressions for  $d_L$  and  $d_A$

$$d_A(z) \sim \frac{c}{H_0} z \left[ 1 - \frac{3+q_0}{2} z \right] \quad (2.61)$$

$$d_L(z) \sim \frac{c}{H_0} z \left[ 1 + \frac{1-q_0}{2} z \right]. \quad (2.62)$$

As mentioned before, those are good approximations only for redshifts close to zero. To first order, all these distances agree:  $d_P(z) \sim d_A(z) \sim d_L(z) \sim \frac{cz}{H_0}$ .

### 2.1.8 Brightness and magnitudes

Most of the knowledge we have about our universe is the result of the detailed analysis of the light we receive from distant stars and galaxies. Since Hipparchus' brightness scale which he made observing by naked eye, our modern understanding of astrophysics and cosmology has been improved spectacularly through new technology, methods and analysis tools. But the idea remains the same. An object has its own luminosity, but we are only able to measure the brightness through the radiant flux we receive from it.

Historically, Hipparchus assigned an *apparent magnitude* ( $m$ ) to the objects in the sky,  $m = 1$  to the brightest star and  $m = 6$  to the dimmest. Due to the logarithmic response of the eye to a difference of brightness, the modern definition of apparent magnitude is such that a difference of 5 magnitudes corresponds to a factor of 100 in brightness, so that a difference of 1 magnitude corresponds to a ratio of 2.512 in brightness. Then, in general

$$\frac{F_2}{F_1} = 100^{(m_1 - m_2)/5}, \quad (2.63)$$

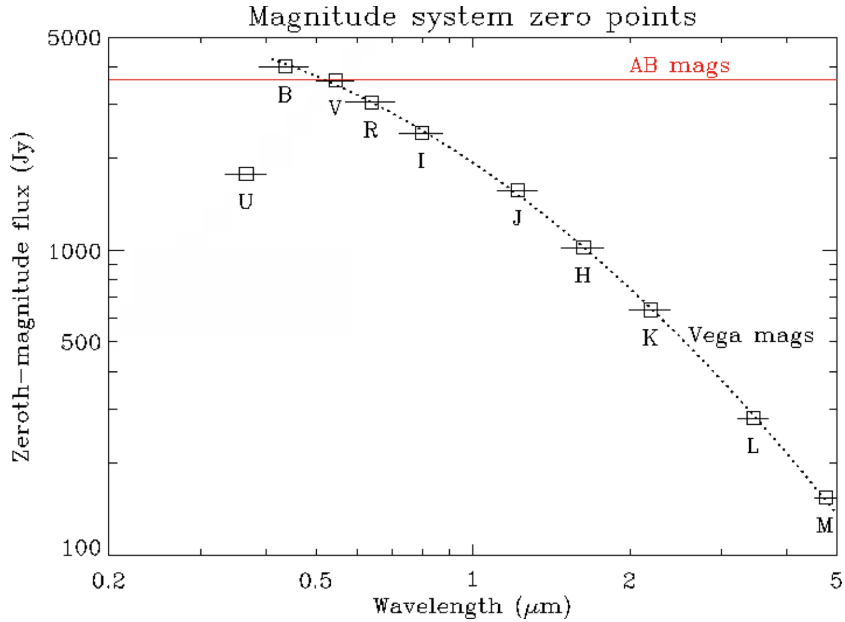


**Figure 2.4:** Zero points for AB and Vega magnitude system definitions. The squares are the flux values in  $\text{Jy}$  corresponding to  $m_{\text{Vega}}^X = 0$  in the  $X$  filter. The black solid horizontal lines show the approximate wavelength range for each band; the dotted line is a fit to the  $B$  to  $M$  fluxes; the red solid line shows the AB magnitude zero point. (Adapted from Ivan K. Baldry: <http://www.astro.ljmu.ac.uk/~ikb/convert-units/convert-units.html>)

or alternatively,

$$m_1 - m_2 = -2.5 \log_{10} \left( \frac{F_2}{F_1} \right), \quad (2.64)$$

where we are taking here bolometric magnitudes, i.e., measured over all wavelengths of light. However, it is common to have the magnitude measurements in a certain region of the electromagnetic spectrum, using filters (sometimes called *bands*). The definition is the same but only in this particular band.

The magnitude scale extends in both directions from -26.83 for the Sun to  $m = 30$ , the faintest object detected. Historically, the bright star Vega ( $\alpha$  Lyrae) has been used as a reference ( $m = 0$  in all bands) because it was found to have a fairly constant energy flux in the optical part of the spectrum. But in modern astronomy, several methods for calculating magnitudes are available. Another commonly used method is the AB magnitude system, calculated using the formula

$$m_{AB} = -2.5 \log_{10} F - 48.60, \quad (2.65)$$

where the flux density  $F$  is measured in  $\text{erg s}^{-1}\text{cm}^{-2}\text{Hz}^{-1}$  (Oke et al., 1983), and the value of 48.60 is selected such that a source of  $F_v = 3631 \text{ Jy}$  has zero apparent magnitude<sup>11</sup>. The conversion between these two systems (Fig. 2.4) is simply given by

<sup>11</sup>1 Jansky (Jy) is a non-SI unit of the spectral flux density, and is equivalent to  $10^{-26} \text{ Wm}^{-2}\text{Hz}^{-1}$ .

the AB magnitude of Vega:

$$m_{AB}(Vega) = -2.5 \log_{10} F_{Vega} - 48.6. \quad (2.66)$$

It is also useful, in order to compare the characteristics of different objects, to know the *absolute magnitude* ( $M$ ), the apparent magnitude that an object would have if it were located at a distance of 10 pc from the observer. Taking Eq. (2.63),

$$100^{(m-M)/5} = \frac{F_{10}}{F} = \left( \frac{d_L}{10 \text{ pc}} \right)^2. \quad (2.67)$$

The difference between apparent and absolute magnitudes is called *distance modulus* ( $\mu \equiv m - M$ ). The relation between distance modulus and luminosity distance is given by,

$$\mu(z) = m(z) - M = 5 \log_{10} \frac{d_L(z)}{10 \text{ pc}} = 25 + 5 \log_{10} d_L(z) \quad (2.68)$$

where  $d_L$  is measured in Mpc.

## 2.2 History of the universe since Big Bang

A first approximation to the history of the universe can be done from the expressions of the energy density of its contents, and its relation with the scale factor. In particular, we can find the value of the scale factor at the epoch when the energy density of two contents were equal ( $\Omega_1 = \Omega_2$ ). Using the three components considered we can find

$$a_{rm} = \frac{\Omega_{r,0}}{\Omega_{m,0}} \sim 2.8 \cdot 10^{-4} \quad a_{r\Lambda} = \left( \frac{\Omega_{r,0}}{\Omega_{\Lambda,0}} \right)^{1/4} \sim 0.10 \quad a_{m\Lambda} = \left( \frac{\Omega_{m,0}}{\Omega_{\Lambda,0}} \right)^{1/3} \sim 0.75, \quad (2.69)$$

which correspond to the redshifts

$$z_{rm} \sim 3500 \quad z_{r\Lambda} \sim 8.6 \quad z_{m\Lambda} \sim 0.33. \quad (2.70)$$

From these numbers, we can reconstruct the expansion of the universe since the Big Bang, distinguishing three different epochs. First, from the Big Bang singularity until the *radiation-matter equality* ( $a_{rm}$ ), radiation dominated the composition of the universe ruling its behavior, and making the scale factor grow as  $a(t) \propto t^{1/2}$ . After  $a_{rm}$ , matter started to dominate and the scale factor increased its growth with time to  $a(t) \propto t^{2/3}$ . Radiation was losing importance, while vacuum energy density was equilibrating with the other two. At some point ( $z \sim 8.6$ ) during the matter domination epoch, the *radiation-dark energy equality* ( $a_{r\Lambda}$ ) occurred. But it is not until the *matter-dark energy equality* ( $a_{m\Lambda}$ ) when the vacuum energy started having a key role in the future of the universe, accelerating its expansion till now. In Fig. 2.5 the density parameters of the components as a function of redshift, are shown.

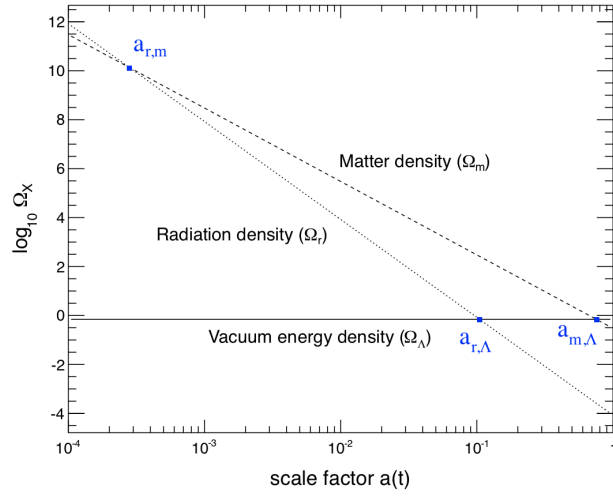


**Figure 2.5:** Density parameter ( $\Omega_X$ ) as a function of the scale factor ( $a(t)$ ) for the three components we discussed in section §2.1.6: matter ( $m$ ), radiation ( $r$ ) and vacuum energy ( $\Lambda$ ). In blue, we mark the values of the scale factor at which the domination in the universe changes from one component to another.

### 2.2.1 Early universe

According to what we have seen about the Standard Model of Cosmology, we can extract that if the universe is experiencing an expansion, as we get back in time, it should have been smaller, denser and, as a consequence, hotter. But there are some problems when one tries to apply the laws of physics at very early times. Before what it is known as the *Planck time*,

$$t_P = \left( \frac{G\hbar}{c^5} \right)^{1/3} \sim 5.4 \cdot 10^{-44} \text{ s}, \quad (2.71)$$

it is supposed that the four fundamental forces (gravitation, electromagnetism, weak interaction and strong interaction) had the same strength, thus allowing for a combined description in terms of a single unified force. This seems to require a quantum theory of gravity which is not well established yet.

As the expansion was taking place, the universe turned colder and less dense. As a consequence fundamental forces started to decouple from each other. Gravitation was the first to separate, then the strong interaction, and finally the electro-weak force splitted in electromagnetism and weak nuclear forces. The primordial plasma of particles and anti-particles began an imperfect annihilation process, leaving a residual amount of matter, and no anti-matter left. Firstly, hadrons annihilated leaving leptons to dominate in number, which, as the temperature decreased, also started to annihilate leaving photons to dominate. At that point ( $t \sim 10$  s,  $T \sim 10^{10}$  K), the universe was a dense broth of particles: the relative number of photons over baryons ( $\eta = n_\gamma/n_b$ ) was  $10^{10}$ , and the ratio between protons and neutrons ( $n_p/n_n$ ) was 6. The imbalance

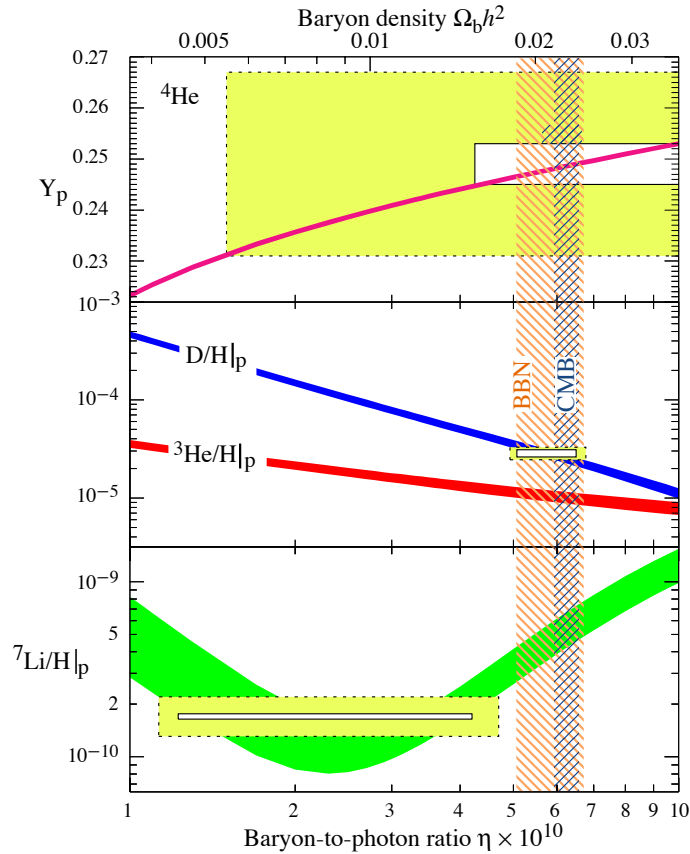
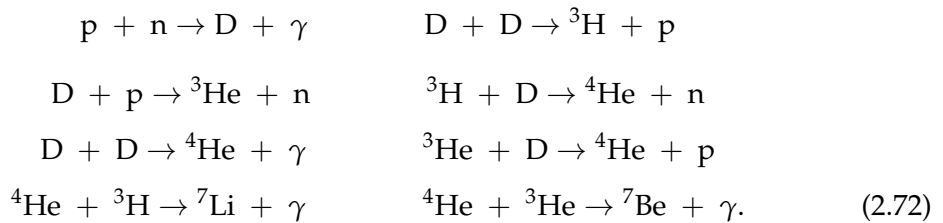


**Figure 2.6:** Observational constraints on the relative abundances of the lightest nuclei. Note that at the present moment  $\eta \sim 6 \cdot 10^{-10}$  and, assuming a value for  $h = 0.71$  equivalent to  $H_0 = 71$ , we have  $\Omega_b = 0.04$ , the value we discussed in §2.1.6. The white bands are the statistic uncertainties ( $\pm 2\sigma$ ), and in yellow the systematic uncertainties are added. Figure from Nakamura et al. (2010).

started due to the instability of the neutron, which, via the  $\beta$  disintegration, was liberating neutrinos in what is known as the *neutrino decoupling*.

### 2.2.2 Nucleosynthesis

This broth was expanding and getting colder, but it was not until protons and neutrons were cold enough to form bound systems ( $t \sim 3\text{min}$ ,  $T \sim 10^9 \text{ K}$ ), when they began to combine into the lightest atomic nuclei (Deuterium, Helium, Lithium and Beryllium), through the following reactions:



This process is known as *Big Bang Nucleosynthesis* (BBN). The abundances of the nuclei produced depend on the ratio of protons and neutrons, which increased to 7 during BBN. However, it only lasted for about ten minutes, after which the temperature and density of the universe had fallen to the point where nuclear fusion could not continue, and the nuclei abundances got fixed. It remained three times more hydrogen ( $\sim 75\%$  of the total mass) than helium ( $\sim 25\%$ ), and only small traces of Lithium and Beryllium (Fig. 2.6). No elements heavier than  $^7\text{Be}$  were created, due to the lack of sufficient time during the BBN to produce heavier elements, and because the absence of stable nucleus with 5 or 8 nucleons which caused a bottleneck.

Historically, it was assumed that the stars were formed by Hydrogen and the heavier elements were synthesized through nuclear fusion reactions (Stellar Nucleosynthesis<sup>12</sup>). But, there was evidence<sup>13</sup> that younger stars began their lives with heavier elements than Hydrogen, and their observed abundances seemed to agree with the primordial gas after the Nucleosynthesis. This finding gave one of the first evidences supporting the theory of the Big Bang.

The ratio between baryons and photons ( $\eta$ ) is determined through the measurement of the relative abundance of the lightest elements, and constraints the baryon energy density parameter ( $\Omega_b$ ), in the same way that the measurement of the temperature of the microwave background emission (§2.2.3) can constrain the photon energy density parameter ( $\Omega_\gamma$ ). The constrained value of  $\Omega_b$  calculated by BBN was much less than the observed mass of the universe based on calculations of the expansion rate, and suggested the existence of a non-baryonic matter that was called *Dark Matter*.

### 2.2.3 CMB

Once the lightest nuclei had been formed, the universe, full of photons and electrons, kept on expanding, decreasing its temperature and getting less dense. Radiation lost importance in favor of matter, up to the epoch of the radiation-matter equality ( $z_{rm} \sim 3500$ ,  $t \sim 70000$  yr). At some point, the temperature was cool enough to allow the nuclei of hydrogen and helium to capture electrons, forming electrically neutral atoms. Then, the mean free path of photons increased due to the smaller number of  $e^-$  available for Thomson scattering. This period is known as Recombination ( $z_{rec} \sim 1300$ ,  $t \sim 380000$  yr), and lasted until the mean free path of the photons was greater than the size of the universe, the photons were totally decoupled from matter and the universe became transparent.

The last scattering surface of this photon decoupling has been propagating freely through the universe, and can be detected today. Gamow, Alpher and Herman (Gamow, 1948a,b, Alpher et al., 1949) predicted that there should exist a relic radiation of this decoupling. But it was not until 1964, when Penzias and Wilson measured haphazardly an “excess of antenna temperature” at a wavelength of 7.3 cm in a radiometer that they intended to use for radio astronomy and satellite communication (Penzias et al., 1965, Wilson et al., 1967). This finding was another evidence supporting the

---

<sup>12</sup>Massive stars can produce elements up to *Fe*. Hans Bethe first published those reactions in Bethe (1939). Heavier elements are only formed in Novae and Supernovae explosions.

<sup>13</sup>see Hoyle et al. (1964).

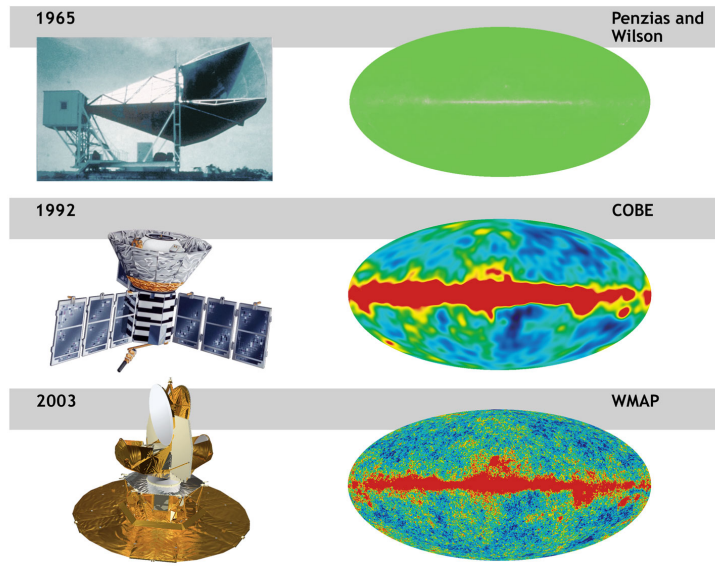


**Figure 2.7:** The Cosmic Microwave Background (CMB) signal measured by Penzias and Wilson in 1965, by the Cosmic Background Explorer (COBE) satellite in 1992, and by the Wilkinson Microwave Anisotropy Probe (WMAP) mission in 2003. Image from NASA/WMAP Science Team.

theory of the Big Bang. This signal is now known as the *Cosmic Microwave Background* (CMB). From the CMB we can learn how the universe was at the epoch at the end of recombination<sup>14</sup> (see Fig. 2.7).

In 1992 the *Cosmic Background Explorer* (COBE) satellite confirmed the CMB black-body radiation at a temperature of approximately 3 K, with the data obtained through its *Far-Infrared Absolute Spectrophotometer* (FIRAS) (Mather et al., 1994). The measured value of the signal is that of a blackbody radiation with temperature

$$T_{\text{CMB}} = 2.725 \pm 0.001 \text{ K.} \quad (2.73)$$

Moreover, another instrument onboard the COBE satellite, the *Differential Microwave Radiometers* (DMR), determined that although the microwave signal was essentially isotropic, it has some anisotropies in temperature (Smoot et al., 1992). There was a great anisotropy at the  $10^{-3}$  level because of the Doppler effect due to the proper motion of the Solar System with respect to the CMB emission (known as Dipole anisotropy). Once the effect of this signal is corrected, there is another smaller anisotropy ( $\Delta T / T \sim 10^{-5}$ ,  $20 \mu\text{K}$ ) related to the matter fluctuations at the recombination era.

These anisotropies are due to several effects such as the Sachs-Wolfe effect (SW), which is produced by the metric perturbations at the surface of last scattering, which caused photons to change frequency (Sachs et al., 1967). Other effects involved are the Integrated Sachs-Wolfe effect (ISW), caused by the evolution in time of the gravita-

---

<sup>14</sup>In the same way that the CMB is the relic of the last scattering surface of photons, there should exist a Cosmic Neutrino Background as a result of the neutrino decoupling, which would have today a temperature of  $\sim 1.9$  K.

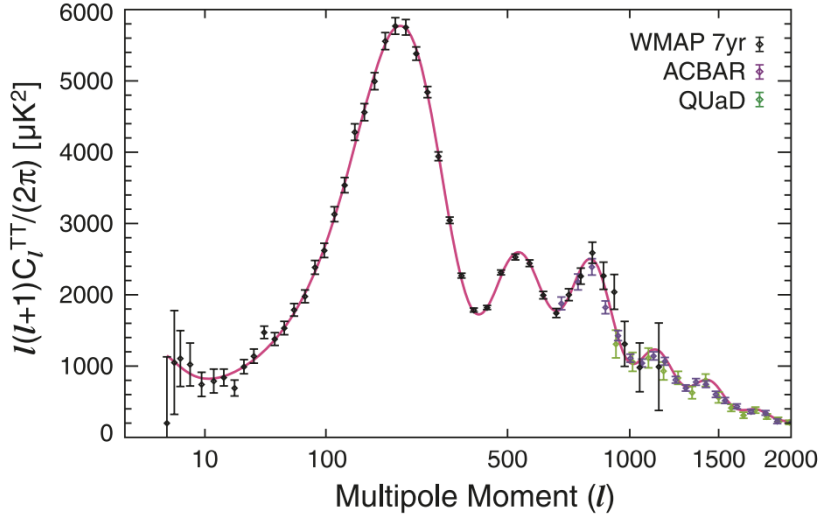


**Figure 2.8:** The WMAP 7-year temperature power spectrum (Larson et al., 2011), along with the ACBAR (Reichardt et al., 2009) and QUaD (Brown et al., 2009) experiments. The first peak  $l \sim 200$  gives information about the curvature of the universe ( $\kappa$ ) and the matter density parameter ( $\Omega_m$ ), while the secondary peaks tell us about the baryon density parameter ( $\Omega_b$ ). The solid line shows the best-fitting 6-parameter flat  $\Lambda$ CDM model to the WMAP data alone. Figure from Komatsu et al. (2011).

tional potential (between the surface of last scattering and the Earth), and the Sunyaev-Zel'dovich effect (SZ), which is produced when the radiation suffers Compton scattering ( $\gamma e \rightarrow \gamma' e'$ ) by clouds of hot electrons, transferring some of their energy to the CMB photons (Sunyaev et al., 1980). A review of this processes and the physical interpretation of the anisotropies can be found, among others, at Nakamura et al. (2010). In order to estimate the contribution of all these phenomena to the anisotropy temperature distribution of the CMB, it is common to decompose the anisotropy map in spherical harmonics:

$$\frac{\Delta T(\theta, \phi)}{T_0} = \sum_{l=0}^{\infty} \sum_{m=-l}^l a_{l,m} Y_{l,m}(\theta, \phi). \quad (2.74)$$

Assuming  $a_{l,m}$  independent, they are completely characterized by the angular power spectrum

$$C_l = \frac{1}{2l+1} \sum_{m=-l}^l |a_{l,m}|^2, \quad (2.75)$$

where  $l$ , the multipole moment, corresponds to an angular scale  $l \sim \pi/\theta$ . In Fig. 2.8, the first peak at  $l \sim 200$  can be seen, which corresponds to an angle  $\theta \sim 1^\circ$ . The scale and amplitude of this first peak in relation to the secondary peaks, provide a measure of the geometry of the universe (curvature), as well as the matter and baryon densities. The last measurements of these quantities come from the WMAP 7-year results (Komatsu et al., 2011), while updated results are expected from Planck (Ade et al., 2011) soon.

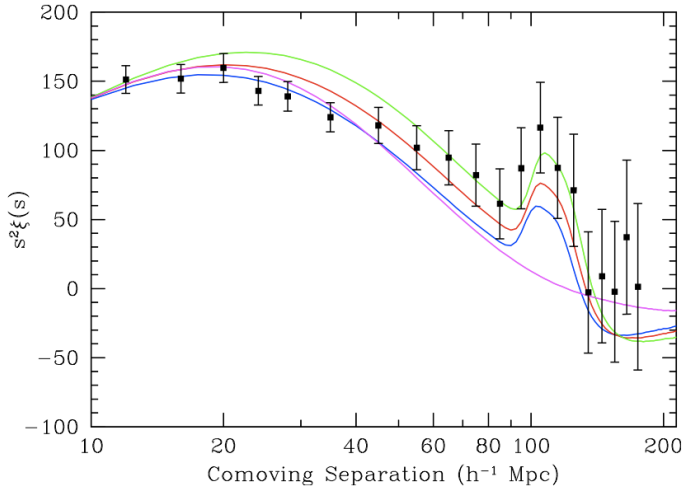


**Figure 2.9:** The large-scale redshift-space correlation function of the SDSS LRG (Large Luminous Galaxies) sample. The peak can be seen at  $100 \cdot h^{-1} \text{ Mpc} \sim 150 \text{ Mpc}$ . The color lines correspond to different cosmological models:  $\Omega_m h^2 = 0.12$  (in green), 0.13 (red), and 0.14 (blue), all with  $\Omega_b h^2 = 0.024$ , and the magenta line shows a pure CDM model without baryons ( $\Omega_m h^2 = 0.105$ ), which lacks the acoustic peak. Figure from [Eisenstein et al. \(2005\)](#).

### 2.2.4 Large Scale Structure

The CMB anisotropies at medium scales ( $0.1^\circ < \theta < 2^\circ$ ), were caused by oscillations of the baryon and photon plasma during recombination, called Baryon Acoustic Oscillations (BAO). After the matter-radiation equality ( $t_{rm}$ ), the denser regions started to attract more matter, while the radiation was repelling them. As a result of these two opposite forces, baryons oscillated between contractions and dilutions until the decoupling time ( $t_{dec}$ ), when baryons were accumulated at a fixed distance, leaving a footprint equal to the sound horizon length at this time. This BAO scale is accurately determined by CMB observations  $r_{BAO} = 146.6 \pm 1.6 \text{ Mpc}$  for a flat  $\Lambda\text{CDM}$  universe ([Jarosik et al., 2011](#)), constitutes a “standard ruler” of known physical length, and can be measured at different redshifts (see Fig. 2.9). The footprint of these oscillations can be detected as a peak in the correlation function of the distribution of mass at large scales, the image of the first peak of the CMB in the Large Scale Structure.

Galaxy surveys such as the 2-degree Field Galaxy Redshift Survey (2dFGRS), Sloan digital Sky Survey (SDSS), or the future Dark Energy Survey (DES) or Physics of the Accelerated universe (PAU), which are 3-dimensional catalogs of objects in the sky, allow the measurement of the angular size of the BAO scale projected in the sky ( $\delta\theta_{BAO}$ ), and along the line of sight ( $\delta z_{BAO}$ ), giving complementary information

$$r_{BAO}(z) = d_A(z)\delta\theta_{BAO}(z)(1+z) = (c/H(z))\delta z_{BAO}(z). \quad (2.76)$$

The existence of this natural standard ruler, measurable at different redshifts, makes it possible to probe the expansion history of the universe.

### 2.3 Summary

The success of the Standard Cosmological Model, commonly known as Big Bang Cosmology, rests on three observational pillars which have been reviewed in this chapter: the Hubble diagram exhibiting expansion, the light element abundances in line with Big Bang Nucleosynthesis, and the detection of the blackbody radiation (CMB). There are yet some other developments (the existence of Dark Matter and Dark Energy, the evolution of perturbations around zero order (smooth universe), and inflation as a generator of perturbations) that are now being investigated, and which will be the hot topics in the present and future of Cosmology.

By now, this is the best model that describes the observations. From the application of its equations we conclude that the universe is composed by 73% of Dark Energy, 23% of non-baryonic matter (Dark Matter), and only 4% of baryons, the substance that we are made of (see Fig. 2.10).

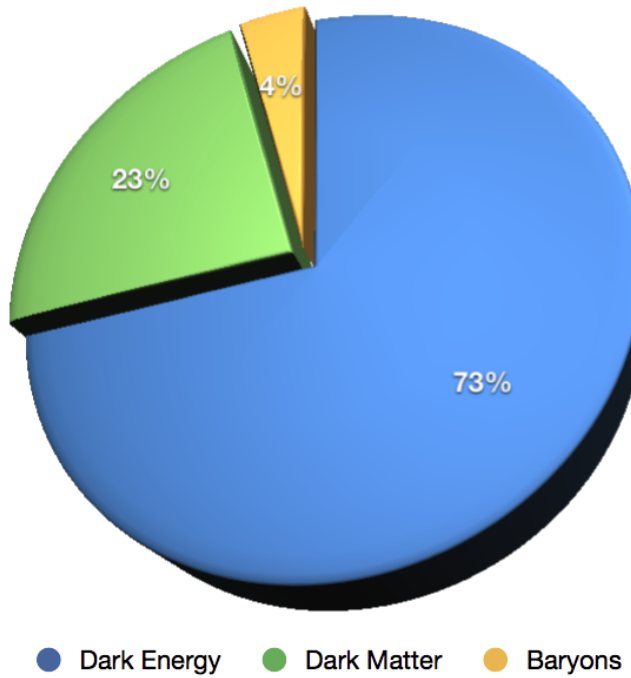


**Figure 2.10:** Composition of the universe according to the  $\Lambda$ CDM model.

## CHAPTER 3

---

### Supernovae

---

SUPERNAOVAE (SNe) are basically stars that have reached the end of their lives in a huge explosion. This occurs when its nuclear fuel is exhausted and the star is no longer supported by the release of nuclear energy. SN explosions are extremely luminous and cause a burst of radiation that lasts for several weeks or months. Their name comes from the need to distinguish them from other stellar process called Novae, which are produced when white dwarfs start to accrete hydrogen from larger companions. The captured gas is compacted on the white dwarf's surface and, as it is being compressed, it ignites and starts nuclear fusion. Although the brightness of the white dwarf increases, they are simply surface explosions. In contrast, the prefix "super" was added to scenarios where the whole star explodes<sup>1</sup>, and in which we are interested.

The first SN to be detected of which there exists written documentation occurred in the year 185 between the constellations of Circinus and Centaurus. After that, some other SNe have been seen in the sky with the naked eye, and reported in many writings by several civilizations. The brightest event was in April 1006 in the constellation of Lupus, and reached  $m \approx -7.5$ . In 1054, another explosion was detected in Taurus. Its remnant is known as the Crab Nebula, and it is one of the most studied objects outside the Solar System. Other famous events are SN1572 in Cassiopeia, and SN1604 in Ophiuchus, discovered respectively by Tycho Brahe and Johannes Kepler, and with which they battled about the immutability of the universe. Those were the latest to be observed by the naked eye, and that exploded in the Milky Way. However, in 1987 another SN occurred in the Large Magellanic Cloud, a satellite galaxy of the Milky

---

<sup>1</sup>See Baade et al. (1934).

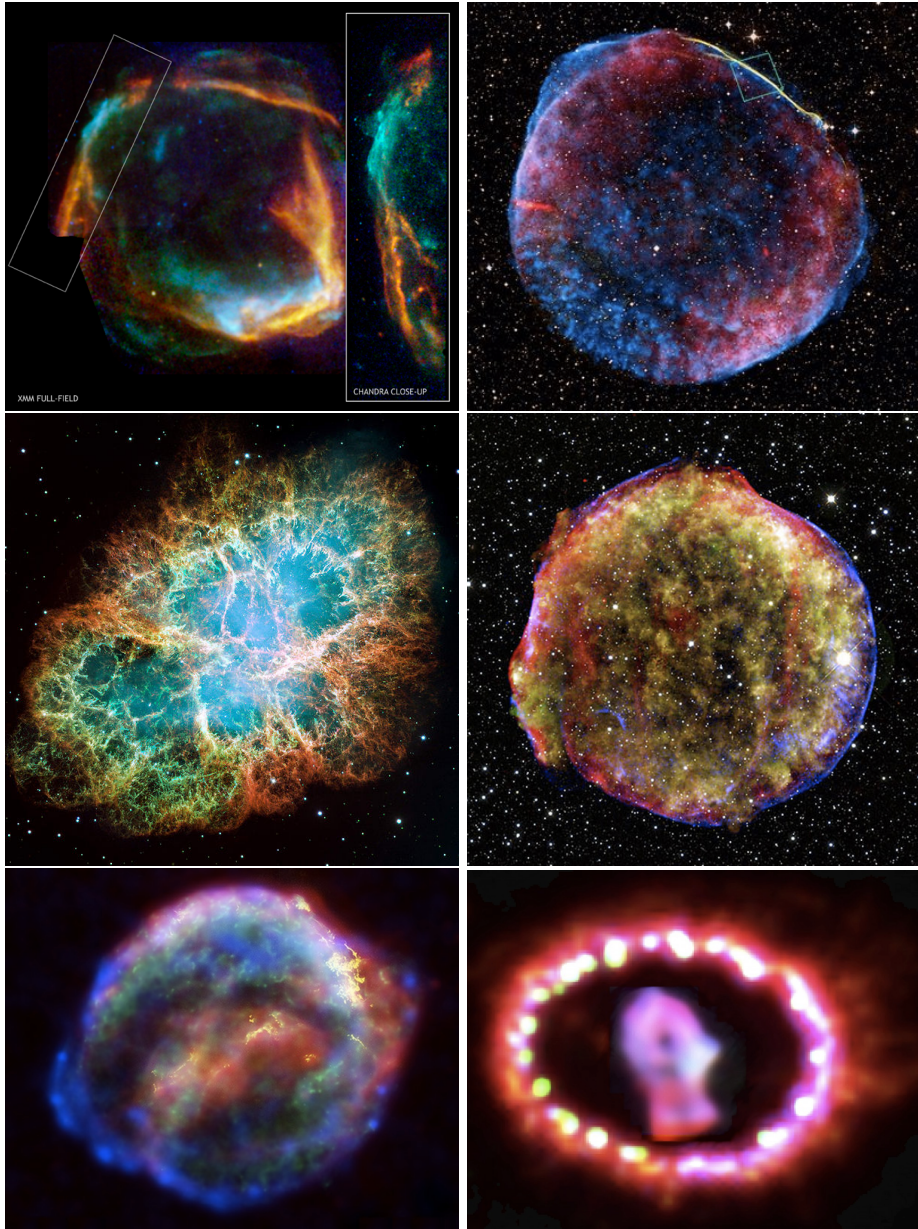


**Figure 3.1:** Remnants of the historical supernovae. From left to right, and top to bottom: SN185, SN1006, SN1054, SN1572, SN1604, and SN1987A. Images from NASA/Chandra X-Ray observatory.

Way, which can be observed by the naked eye. Images of the remnants of these SNe, which appear as expanding clouds of gas, are shown in Fig. 3.1.

When a SN is discovered, it is reported to the International Astronomical Union (IAU), which publishes a circular confirming the explosion. The name assigned to the supernova is the acronym *SN* followed by the year of discovery, and by one or two letters. The first 26 SNe of the year are designated with a capital letter from A to Z, and the following with pairs of lower-case letters: aa, ab, and so on. This

notation is used since 1885, and previously they were known simply by the year they occurred. Until 1987, two-letter designations were rarely needed, although since 1988, two-letters have been needed every year. The reason is not that they are getting more common, but the better telescopes used for their discovery.

Historically, SNe were classified in several types depending on their spectral features. Nowadays, although we still maintain the names of those classes, we also distinguish between the processes responsible for the explosion, and the differences among light-curves. But, from all those classes, there is a set of features that make a SN type named Ia acquire a key role in cosmology. Type Ia SNe are used to measure distances since they seem to have very similar absolute magnitudes, with only small dispersion. As we discussed in §2.1.8, if we are able to find objects whose intrinsic luminosities are known, it is possible to constrain the cosmological parameters by comparing the distance estimates of the distance modulus ( $\mu$ ) and the redshift (recall Eq. 2.68). These objects are known as *standard candles*, and type Ia SNe are (almost) one of those objects. The intrinsic dispersion of the absolute magnitude at the epoch of maximum brightness has been found to correlate with their decline rate in brightness. This was reported as far back as Pskovskii (1977), but was quantified statistically, and popularized as a useful observational tool, by Phillips (1993). Therefore, this correlation is commonly referred to as the *Phillips relation* and has since been parameterized in different ways and exploited by various methods (Riess et al., 1996, Perlmutter et al., 1997a, Goldhaber et al., 2001, Guy et al., 2005, 2007, Jha et al., 2007) to provide accurate relative distance measurements to type Ia SNe, with a precision of  $\sim 7\%$ . Once standardized, their distance-redshift relation points to an acceleration of the expansion of the universe, and gives clues about the nature of Dark Energy.

In this chapter, we want to summarize the knowledge about SNe. We will describe in §3.1 the physical mechanism that accounts for their explosions. Then, in §3.2, we will list the differences among the several types of SNe, and their spectral classification. In §3.3, we will focus on Type Ia SNe, describing the properties of their spectra. In §3.4, the light-curves will be reviewed, emphasizing the photometry and the models that fit the data obtained. After that, in §3.6, we discuss how common these explosions are, followed by a short description of the properties of their host galaxies (§3.5), and their use in Cosmology through the Hubble diagram (§3.7). Finally we will summarize past, current and future SN surveys in §3.8.

### 3.1 Physics of SNe

As discussed in §2.2.2, during the Big Bang Nucleosynthesis, only nuclei of the lightest elements up to Beryllium were created. Hans Bethe proposed that the heavier elements had to be processed in stars through some nuclear fusion reactions, which he presented in Bethe (1939). But until stars were formed, the universe consisted, basically, of large quantities of Hydrogen and Helium gas clouds. The process through which these clouds collapsed forming stars, can be shortly reviewed taking into account that, as the mass of these clouds increases, they collapse as a result of their own gravity. The compression of this gas makes the temperature of the cloud core

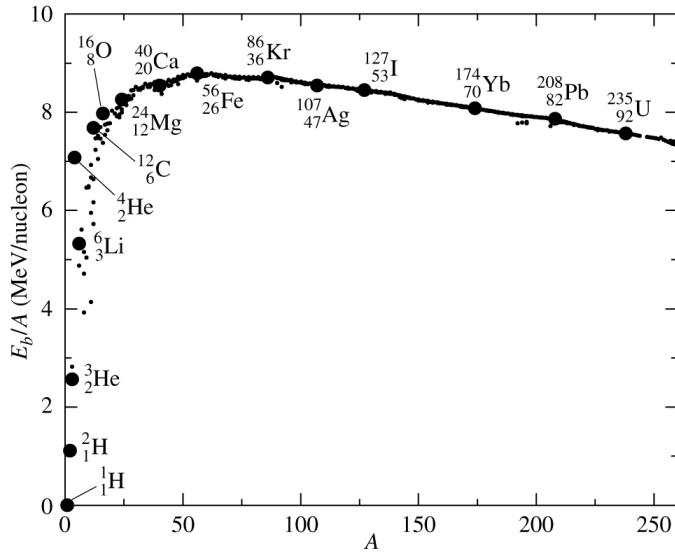


**Figure 3.2:** The binding energy per nucleon ( $E_b/A$ ) as a function of mass number ( $A$ ). At the peak of the curve there is  $^{56}\text{Fe}$ , the most stable of all nuclei, having the greatest binding energy per nucleon. Figure from [Carroll et al. \(2006\)](#).

increase, allowing the nuclear fusion of Hydrogen producing Helium ( $T \sim 5 \cdot 10^6$  K). The temperature of the nuclei keeps growing as the reactions multiply, balancing the gravitational collapse and arriving to a *hydrostatic equilibrium*. At this point, the energy released by the nuclear reactions is able to compensate the weight of the star.

After that, a battle for the stability of the star begins. A subtle decline in the rate of nuclear reaction allows a small compression of the star under its own weight, which results in an increment of the nuclei temperature, enough to bring the reactions up to a new equilibrium in a self-organized system. But, this is a finite mechanism. When the fuel, i.e., Hydrogen, is totally burned, the reactions stop, the star begins to compress, and its temperature rapidly increases. When the temperature arrives at  $10^8$  K, the Helium created by the Hydrogen reactions can start their own fusion reaction forming Carbon. The equilibrium is reached again until the star runs out of Helium, and Carbon starts another fusion reaction that produces Oxygen. However, this chain of successive nuclear reactions arrives to an end: either the mass of the star is not enough to compress the core to reach the temperature necessary to start the fusion of an intermediate element, or the reactions stop when the core ends up being essentially composed of Iron, as it is the first nucleus to have endothermic reactions (See Fig. 3.2). In either case, the gravitational compression is no more balanced, and the star collapses.

The evolution of the star is simply conditioned by the initial mass. If it is less than 0.08 solar masses ( $M_\odot$ ), the gravitational compression is not enough to reach the temperature needed for the Hydrogen burning, and the compressed gas remains as a *brown dwarf*<sup>2</sup>. For greater masses up to  $0.26 M_\odot$ , only the Hydrogen can be

<sup>2</sup>Sub-stars that occupy the mass range between large gas giant planets and the lowest-mass stars.

burned and the star remains as a *white dwarf*, composed mostly of Helium. For greater masses, Helium can be burned too. These low mass stars avoid the collapse due to the *electron degenerate pressure* (EDP), which is originated by a quantum effect related to the Pauli exclusion principle, which forbids fermions to occupy identical quantum states, and the uncertainty principle. Due to the compression of matter, each electron is confined in a restricted space and has a great uncertainty in the velocity, resulting in a strong agitation that gives rise to a pressure force (Fermi pressure), which prevents the collapse of the star.

This mechanism has an upper limit on the mass ( $M_{Ch} \sim 1.4 M_{\odot}$ ) known as the *Chandrasekhar limit* (Chandrasekhar, 1931, Branch et al., 1995), beyond which EDP cannot contrarest the gravitational collapse. Stars with lower masses, eject progressively the surface layers of burned elements into planetary nebulae, as the contraction occurs, also ending up as white dwarfs. But, for stars with masses greater than  $M_{Ch}$ , the EDP no longer supports their weight, and they collapse very fast as a result of their gravitational potential, exploding in what is known as *core-collapse supernovae* (CCSNe). The outer parts are violently ejected at high velocities producing planetary nebulae around the core, and the energy released ( $\sim 10^{46}$ J) is such that the brightness of the explosion is similar to that of a whole galaxy. There exists another threshold on the mass of the remnant in these explosions ( $M_{TOV} \sim 3.3 M_{\odot}$ ) called *Tolman-Oppenheimer-Volkoff limit* (Oppenheimer et al., 1939, Bombaci, 1996), that determines if the core further evolves contracting into a neutron star<sup>3</sup> in case the mass is lower than  $M_{TOV}$ , or into a black hole if it is higher. The heaviest stars ( $M \gtrsim 15 M_{\odot}$ ), which are the only that reach high enough temperature in the core to produce Iron, follow CCSNe explosions and end up as a black hole. A review of different models of CCSNe explosions can be found in Mochkovitch (1994) and Woosley et al. (2005).

### Thermonuclear explosions

This core-collapse process is not the only mechanism available for SN explosions. There is another process by which a low mass star that has evolved into a white dwarf can end its life as a SN. It is known as a *thermonuclear supernova*, and it occurs when the star is not alone, but in a system of two or more stars, which can have different masses, or be in different stages of evolution.

The mass of the white dwarf can increase by accretion of a significant portion of the material of its companion. This is possible when the surface of the companion arrives to a point where the gravitational attraction of the two stars is equal (Roche lobe, Paczyński, 1971). When this happens, Hydrogen and Helium, which are in the outer regions of the companion, are transferred to the surface of the white dwarf, where they are burned very fast forming carbon. The mass of the white dwarf grows gradually, and just before reaching  $M_{Ch}$ , it can light the fusion of carbon into oxygen. Then, the star experiences a runaway thermonuclear explosion that destroys the star in a few seconds. The light emitted is such that it can be brighter than the whole host galaxy, and is higher than that of a gravitational supernova.

---

<sup>3</sup>A star which is more compact than a white dwarf, balanced by the degeneracy pressure of neutrons.

There is active debate about how exactly these explosions occur. Models distinguish among the stage of evolution of the companion star, if the companion is a regular non-degenerate star (single degenerate, SD), or if this mechanism occurs between two white dwarfs (double degenerate, DD), although other scenarios are also considered. There are also differences if the thermonuclear flame that engulfs the star from inside out is subsonic, a deflagration, or if it is supersonic, a detonation. Other parameters considered are the location and the conditions of the ignition process, the rotation of the white dwarf, and the velocity of the burning front. Detailed reviews of different models are available in [Nomoto et al. \(1997\)](#), [Hillebrandt et al. \(2000\)](#), [Woosley et al. \(2007\)](#), [Bravo et al. \(2008\)](#) and [Röpke et al. \(2010\)](#).

### 3.2 Spectral classification

SNe were basically classified according to the absorption lines of different elements appearing in their spectra. It could be done as soon as the use of spectrographs began and the features could be measured in detail. As we discussed in §[2.2.2](#), Hydrogen is the most prominent element in the universe, so it was reasonable to expect that SNe had it in their spectra. But in 1941, it was discovered that there existed some SNe with and some without H absorption lines in the spectrum ([Popper, 1937](#), [Minkowski, 1941](#)). This allowed for a first division depending on the appearance (Type II) or not (Type I) of H lines. Nowadays, this historical division has been improved taking into account photometric characteristics, different progenitor explosion scenarios, and also emission lines other than H.

#### Type I

This group has no H in the spectrum, but depending on the presence of other features, they can in turn be divided into three different subclasses. If they present absorption around 6150 Å in the rest-frame spectrum, caused by the presence of Silicon<sup>4</sup>, they are assigned as Type Ia. If they do not, and depending on the presence of Helium 5876 Å lines or not, they are assigned as Type Ib (with He) or Type Ic (without) ([Wheeler et al., 1990](#), [Harkness et al., 1990](#)).

These spectral differences can be explained by different explosion mechanisms. Type Ib and Ic SNe are supposed to be the result of the collapse of massive stars ( $> 15 M_{\odot}$ ) that have lost their H and He (in Ic) envelopes through a strong wind ([Swartz et al., 1993](#), [Woosley et al., 1993](#)) or for the benefit of a companion ([Nomoto et al., 1994](#), [Woosley et al., 1995](#)). Moreover, these objects show a wide diversity in their spectral features and light-curves. On the other hand, a Type Ia SN is supposed to come from a carbon-oxygen white dwarf thermonuclear explosions, where the progenitor had been accreting mass from a companion up to the Chandrasekhar limit. As the mass at this point is known and fixed, the explosions are expected to have similar magnitude, providing mostly homogenous light-curves and spectra.

---

<sup>4</sup>Absorption lines of Si II at 6347 Å and 6371 Å, collectively called 6355 Å, that are blueshifted due to the photospheric velocity of the ejecta in the direction of the observer.

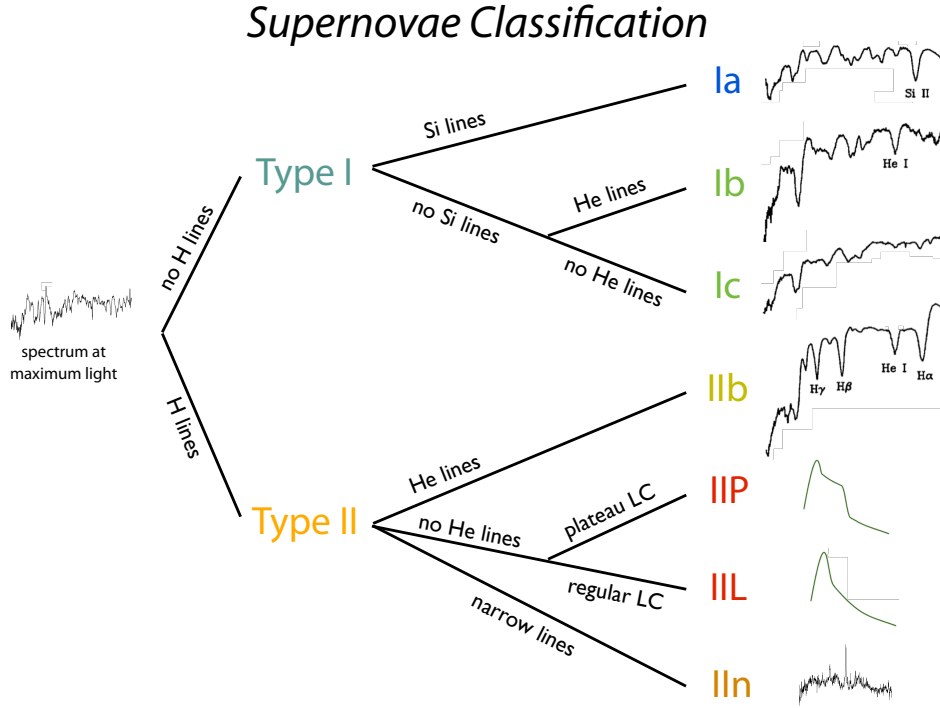


**Figure 3.3:** Scheme of the SN classification depending on the absorption features in their spectra and light-curve characteristics.

### Type II

This group has H in the spectrum. The progenitor of a Type II SN is supposed to be a red giant, an old and massive star with a mass greater than  $8 M_{\odot}$ , that ends its life in a core-collapse explosion. Their mechanism of explosion is very similar to that for Ib/c. Type II SNe can also be divided in subclasses, but in this case also considering the evolution of their light-curve (Barbon et al., 1979). Those whose brightness decreases linearly are called IIL, where L stands for *linear*. Some of them, when decreasing in brightness, stop the declining and remain with the same brightness for some days, before they continue to decrease. They are classified as IIP, where the P comes from *plateau*. Moreover, some Type II SNe show relatively narrow features compared to the common broad lines of most Type II SNe, which indicate large expansion velocities. Those are classified as IIIn, where n stands for *narrow*. Finally, some show H lines at early times, but over time, become dominated by Helium lines. Those are called IIb, due to their evolution similar to a Type Ib SNe. Other Type II SNe that do not fit into the normal classifications are designated II-pec for peculiar.

In Fig. 3.3 a scheme of the classification discussed above is shown, while in Fig. 3.4 four spectra of Type Ia, Ib, Ic, and II SNe are plotted together, and the most relevant line absorptions are labeled in order to compare their spectral features. Detailed reviews of this classification can be found in Filippenko et al. (1992b), Filippenko (1997), and Matheson et al. (2008), among others.

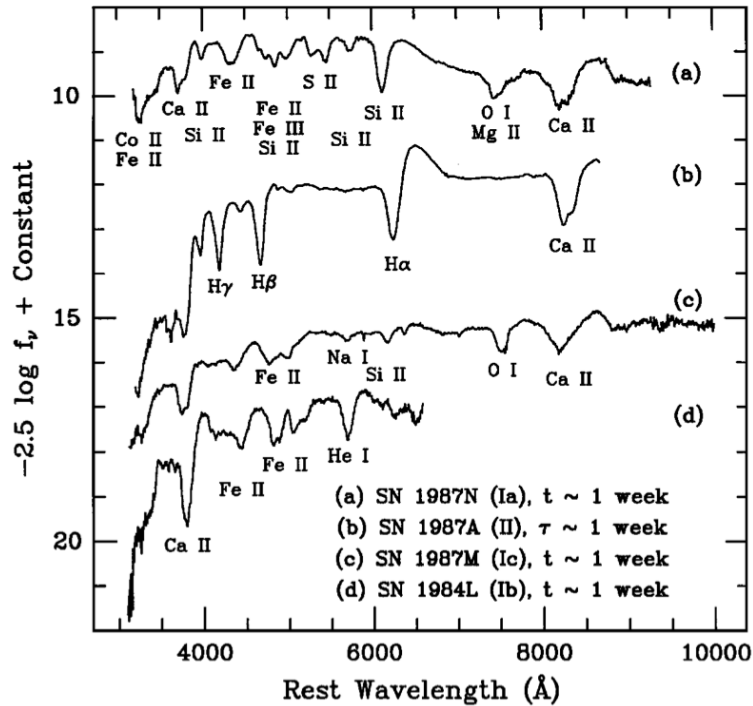


**Figure 3.4:** Spectra of four different SNe types (From top: Ia, II, Ic and Ib). They are taken approximately one week after the maximum brightness in B band. From [Filippenko \(1997\)](#).

### 3.3 Spectra of Type Ia SNe

The spectra of Type Ia SNe reveal details about their chemical composition, and about their evolution with time. From all the Type Ia SNe discovered by now, we can see that approximately 85% have spectra that resemble a common spectrum and have similar light-curves. These are commonly known as *Branch-normal* type Ia SNe ([Branch et al., 2006](#)). Their early time spectra (less than a week after the maximum brightness) have broad absorptions due to the high velocities of the ejecta. There are mostly lines of intermediate-mass elements (O, Mg, Si, S, Ca), with some contribution of iron-peak elements (Fe, Co). The strongest features are the blueshifted line of Si II around 6150 Å and the H and K lines of Ca II (3934 Å and 3968 Å, respectively). As the explosion evolves, the relative contribution of iron-group elements (Fe, Co) increases. At two weeks after the observed *B*-band maximum the spectrum is already dominated by lines of Fe II, pointing to a progenitor with an iron-rich core ([Harkness, 1991](#)), although other lines of intermediate-mass elements are still present (e.g. Si II, Ca II). Thereafter the spectral changes are more gradual ([Filippenko, 1997](#)).

However, there exist differences amongst type Ia SNe events. The absorption lines do not have the same width at a given phase, meaning that the ejecta do not always have the same velocity ([Branch et al., 1988](#)), with the smallest velocities found in elliptical galaxies ([Branch et al., 1993](#)). Differences were also found between SNe exploding in young stellar populations, which are more luminous ([Hamuy et al., 1995](#)). Spectro-

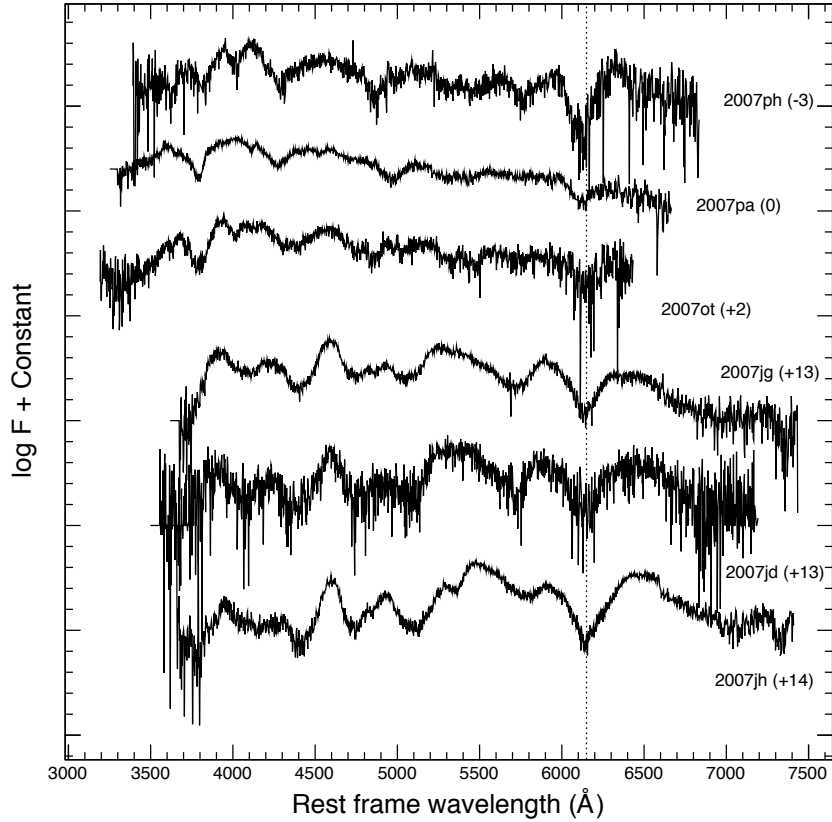


**Figure 3.5:** Spectra of several type Ia SNe at different epochs (in brackets). The Si II feature at  $6150\text{ \AA}$  is marked with a dotted line. One can see the common features of these two groups, in particular, the Ca II doublet at  $3900\text{ \AA}$ , the S II lines near  $5500\text{ \AA}$ , and the Fe II lines near  $4000$ ,  $4400$  and  $5000\text{ \AA}$ .

scopic differences between SNe Ia in spiral and elliptical galaxies clearly indicate that there should be physical differences among those SNe Ia.

Some Type Ia SNe show weak absorption of Si, Ca and S only at early epochs, and have brighter peak magnitudes than Branch-normal events. SNe that belong to this group are called 1991T-like events (Filippenko et al., 1992a, Phillips et al., 1992, Ruiz-Lapuente, 2007). On the opposite side, there are other events that have fainter magnitudes at peak (subluminous by  $\sim 1.6$  mag in  $V$  and  $\sim 2.5$  mag in  $B$ , compared with normal SNe Ia), exhibit a Si line at  $5700\text{ \AA}$  and a Ti window between  $4100$  and  $4400\text{ \AA}$ . These underluminous type Ia events are categorized as 1991bg-like events (Filippenko et al., 1992b, Leibundgut et al., 1993, Turatto et al., 1996, Garnavich et al., 2004). In addition, several other peculiar Type Ia SNe have been observed<sup>5</sup>, which do not exhibit any of the characteristics of the other subclasses. They are labeled as *Ia-pec*. In Fig. 3.5 there are six spectra of Branch-normal Type Ia SNe, where the homogeneity among them can be noted.

<sup>5</sup>For references, see Li et al. (2001) for 2000cx, Li et al. (2003) for 2002cx, Deng et al. (2004) for 2002ic, Howell et al. (2006) for 2003fg, Phillips et al. (2007) for 2005hk, McClelland et al. (2010) for 2007qd, and Valenti et al. (2009) for 2008ha.

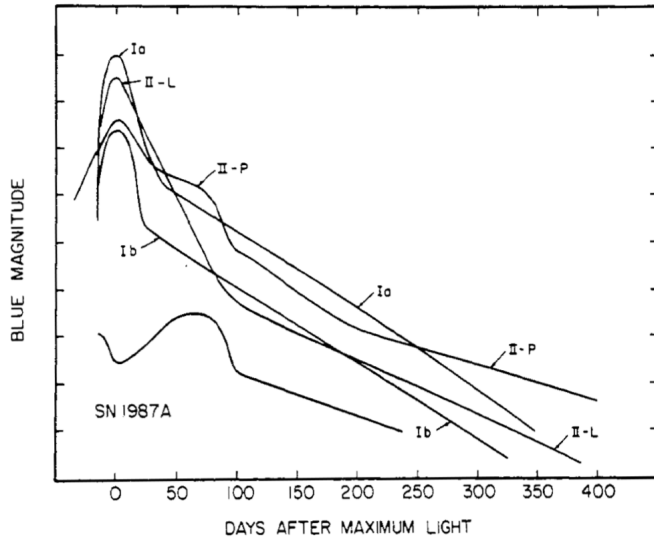


**Figure 3.6:** Schematic representation of light-curves of five different SNe types (Ia, Ib, Ic, IIP, IIL), and SN1987A. Note that Type Ia SNe light-curves have, on average, the brightest peak magnitude. From Wheeler et al. (1990).

### 3.4 Light-curves of Type Ia SNe

The light-curve (LC) is the representation of the evolution of the star brightness with time. The brightness of the SN increases very fast during the first two weeks after the explosion, until it achieves its maximum brightness, for then to decrease with time. The LCs differ for each type of SN, as can be seen in Fig. 3.6, where schematic representations of the *B*-band (defined later in this section) LCs for Type Ia, Ib, Ic, IIL, and IIP, are shown together with the LC of SN1987A.

In particular, in the LCs of Type Ia SNe, we can distinguish between two different decreases. During the first month after the maximum, the LC decreases sharply powered by the radioactive decay of  $^{56}\text{Ni}$ <sup>6</sup>. In the late-time tail of the LCs, the brightness decreases more slowly than previously, and it is due to the decay of  $^{56}\text{Co}$ <sup>7</sup> (Colgate et al., 1969).

Since Type Ia SNe are the fruit of explosions of the same kind of stars, with similar masses and evolutionary state, they are expected to have similar peak luminosities and homogeneous LCs. Measurements of the absolute magnitude of Type Ia SNe at their peak determined on average a value of  $-19.46 \pm 0.05$  (Richardson et al., 2002), exceeding the brightness of other types of gravitational SNe (with a magnitude range between -17 and -19). Their extreme luminosity allows the detection and monitoring at considerable distances, so due to its homogeneity, they could be used as standard candles for cosmology.

But, in fact, SNe Ia are not intrinsically standard candles, as they present a scatter

<sup>6</sup>  $^{56}\text{Ni} \rightarrow ^{56}\text{Co} + e^+ + \nu_e + \gamma$

<sup>7</sup>  $^{56}\text{Co} \rightarrow ^{56}\text{Fe} + e^+ + \nu_e + \gamma$

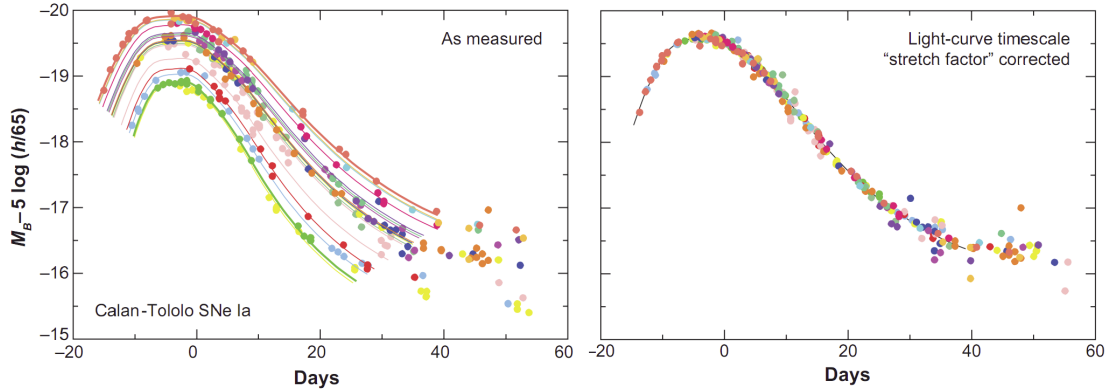


**Figure 3.7:** Seventeen light-curves, in the  $B$  band, of low-redshift Type Ia SNe from the Calan-Tololo survey (Hamuy et al., 1996b). They show an intrinsic scatter of  $\sim 0.3$  magnitudes in peak luminosity. After correcting for the brightness-decline correlation, the dispersion decreases to only  $\sim 0.15$  mag, as shown in the right plot. Figure from Kim et al. (2004).

of  $\sim 0.3$  magnitudes in peak luminosity which would limit their usefulness (see left plot in Fig. 3.7). As the peak luminosity is correlated to the amount of  $^{56}\text{Ni}$  produced in the explosion (Contardo et al., 2000), different masses of  $^{56}\text{Ni}$  in the progenitor can be the cause of the differences in the maximum brightness.

However, a strong correlation between the value of the maximum brightness and the rate at which the luminosity declines with time after peak is observed (Pskovskii, 1977). This correlation indicates that brighter Type Ia SNe, have a slow rate of decline, and fainter SNe decline faster. After correcting for this correlation, SNe Ia can be turned into standard candles, as can be seen in the right plot in Fig. 3.7. We will discuss this in detail in §3.4.1.

### Photometry

The magnitudes used to construct the light-curves of SNe, are commonly measured using broadband photometry, i.e., the measurement of the flux integrated on a certain wavelength range. The range, or *band*, is determined by the transmission of a standard filter. There exist several photometric systems, a selected set of spectral bands that cover the visible and near-infrared electromagnetic spectrum. The usefulness of these standard sets rests on the ability to compare the brightness values in certain fixed regions, by different observers using different equipments. One of the most used systems is the Johnson-Cousins (Bessell, 1990, Cousins, 1974, Johnson et al., 1953). It consists of five bands,  $UBVRI$ , located between the near-ultraviolet and near-infrared<sup>8</sup>. Another commonly used set is the SDSS photometric system  $ugriz$  (Fukugita et al., 1996). The wavelength ranges of the bands of these two photometric systems are shown in Fig. 3.8.

Using these photometric systems, we are able to measure the magnitudes of the

<sup>8</sup>The letters of the bands come from the range at which the filters work. U: ultraviolet, B: blue, V: visible, R: red, and I: infrared.

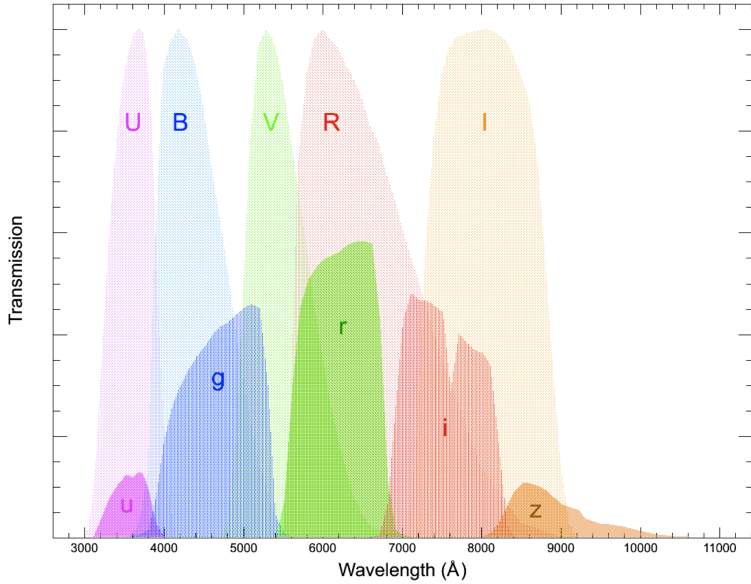


**Figure 3.8:** Johnson and SDSS photometric systems. SDSS filter transmissions include the CCD efficiency. The relative transmission of the two systems has been increased in order to make easier the comparison of the wavelength range for all bands.

SNe in certain regions of the spectrum. Depending on the band in question, the measured magnitudes and their evolution can be very different. For instance, the date of maximum light varies a few days depending on the band, appearing first at longer wavelengths and then in B and V bands (Contardo et al., 2000). Magnitudes are also used to determine the *colors* of the SNe, the differences in magnitudes between two bands, which are also used for the SN standardization, as we will see in §3.4.1. The measurement of the magnitude of a SN in the band  $X$ , as discussed in §2.1.8, is

$$X \equiv m_X = -2.5 \log_{10} \left[ \frac{\int F(\lambda) S_X(\lambda) \lambda d\lambda}{\int F_{ref}(\lambda) S_X(\lambda) \lambda d\lambda} \right], \quad (3.1)$$

where  $F(\lambda)$  is the flux received per wavelength,  $S_X(\lambda)$  is the  $X$  band filter transmission, and  $F_{ref}(\lambda)$  is the reference flux in the  $X$  band<sup>9</sup>.

### The K-correction

Until now, we have not taken into account the redshift. But, as we discussed in §2.1.3, the wavelength of the emitted light by a distant object is redshifted due to its recession velocity from us. If we measure the spectrum of a SN, we are going to see the expected features at longer wavelengths, depending on the redshift of the SN. For the same reason, if we want to measure its magnitude in a certain band, as we would integrate the flux in a fixed range of wavelengths (in the observer-frame), we would

<sup>9</sup>This reference value depends on the magnitude system used. For the Vega system,  $F_{ref}(\lambda)$  is the flux of Vega, while for the AB system it is the flux of the reference object described in §2.1.8.

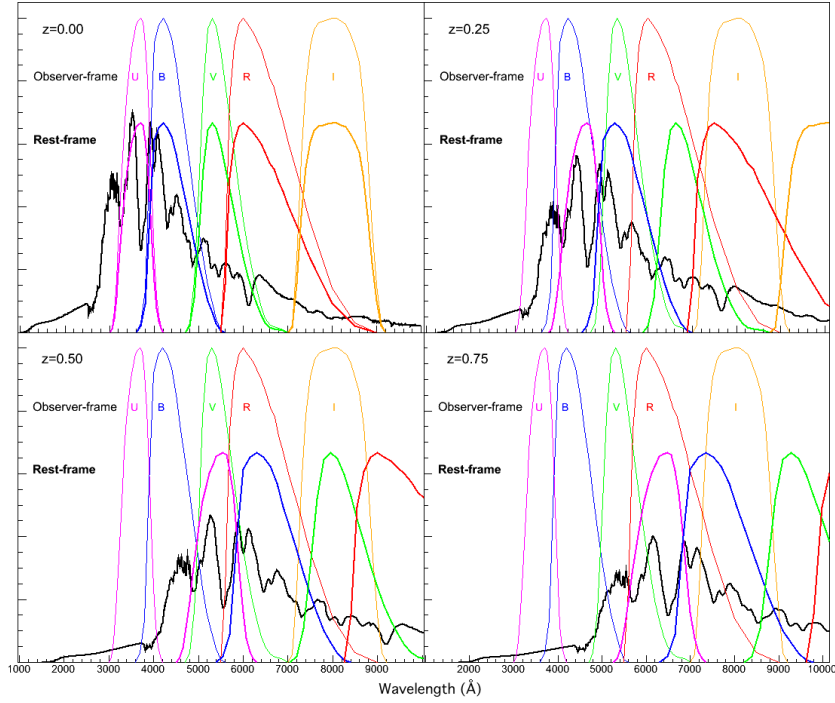


**Figure 3.9:** Johnson bands (UBVRI) are shown in the rest frame and in the observer frame for four different redshifts, together with the spectrum of the same object redshifted accordingly. Note that the spectral features are in the same bands in the rest-frame, but in different bands in the observer-frame, for different redshifts. In particular, at  $z = 0.5$  we see that the  $B$  and  $V$  bands in the SN rest-frame lay in the same wavelength range that  $R$  and  $I$  bands, respectively, in the observer frame. In general, if we do not consider the K-correction, we are making a large error in the magnitude measurement, and in the distance modulus calculation.

be considering different regions of the spectrum in the rest-frame of the SN. Then, we would be making a mistake if we took the measured value of the magnitude directly (see Fig. 3.9).

This effect complicates the comparison of magnitudes among objects which have different redshifts. But it can be solved by adding a term in the magnitude measurement, called *K-correction*, which takes into account the difference between the measured flux in a band (observer-frame), and the intrinsic flux in the rest-frame of the SN, even in another band. This correction is composed of two terms: the first accounts for the fact that the flux at a certain wavelength in the rest-frame of the SN,  $F(\lambda_e)$ , will be the flux at the transformed wavelength in the observer frame  $F(\lambda_o/(1+z))$ . The second is because with the effective band width at the observer-frame we will measure a narrower part of the spectra due to its expansion by a factor  $(1+z)$ . The first term of the correction were zero if the spectrum would be flat, but the second has to be always taken into account (Oke et al., 1968).

The K-correction from the measured magnitude in X band to the rest-frame mag-

nitude in  $Y$  band is written as  $m_Y = m_X + K_{XY}$ , with

$$K_{XY} = -2.5 \log_{10} \left[ \frac{\int F_{ref}(\lambda) S_X(\lambda) \lambda d\lambda}{\int F_{ref}(\lambda) S_Y(\lambda) \lambda d\lambda} \right] + 2.5 \log_{10}(1+z) \\ + 2.5 \log_{10} \left[ \frac{\int F(\lambda) S_X(\lambda) \lambda d\lambda}{\int F[\lambda/(1+z)] S_Y(\lambda) \lambda d\lambda} \right], \quad (3.2)$$

where  $F(\lambda)$ ,  $S_X(\lambda)$ ,  $S_Y(\lambda)$ , and  $F_{ref}(\lambda)$  are defined in the previous section. If  $X$  and  $Y$  are the same band, the K-correction is independent of the reference flux. Note that, the implementation of the K-corrections implies knowledge of the spectrum and the redshift of the SN, as well as the profiles of the bands (Nugent et al., 2002).

### Dust extinction

There is another source of error to take into account, the presence of dust in the interstellar and intergalactic medium. The first evidence for its existence was published in (Trumpler, 1930). Before that, it had been thought that the space was completely transparent. Now we know that this dust both absorbs some of the light emitted by the stars, usually reemitting them at longer wavelengths<sup>10</sup>, and scatters another amount away from the line of sight. All these radiation losses are called *extinction*. This effect is more accused at short wavelengths, since the extinction follows a law proportional to the inverse of wavelength ( $1/\lambda$ ).

Let us consider an object which is emitting a flux  $F_e(\lambda)$ , and is located in a position where between it and us, the light has to go through a column of dust of thickness  $L$ . The observed flux will be

$$F_o(\lambda) = F_e(\lambda) e^{-\tau_\lambda} \quad \text{with} \quad \tau_\lambda \equiv \sigma_\lambda \int_0^L dl = \sigma_\lambda L, \quad (3.3)$$

where  $\tau_\lambda$  is the optical thickness integrated along the dust column, and  $\sigma_\lambda$  is the opacity, a factor that tells how effectively the medium can obscure the radiation<sup>11</sup>. We can then define the absorption in a given band  $X$  as

$$m_{o,X} = m_{e,X} + A_X \quad \text{with} \quad A_X = 2.5 \tau_X \log_{10}(e), \quad (3.4)$$

where we substituted the observed flux obtained previously into the definition of the apparent magnitude (2.64). The difference of the extinction between two bands (i.e.  $X$  and  $Y$ ), known sometimes as *color excess* ( $E_{X-Y} = A_X - A_Y$ ), gives a measurement of the reddening caused by interstellar medium.

$$(X - Y)_o = \left( M_X + 5 \log_{10} \frac{d}{10 \text{ pc}} + A_X \right) - \left( M_Y + 5 \log_{10} \frac{d}{10 \text{ pc}} + A_Y \right) \\ = M_X - M_Y + A_X - A_Y = (X - Y)_e - E_{X-Y}, \quad (3.5)$$

---

<sup>10</sup>The *Diffuse Infrared Background Experiment* (DIRBE) mounted on the COBE satellite measured a map of dust at  $100 \mu\text{m}$ , which was used to estimate the Milky Way galactic extinction (Schlegel et al., 1998).

<sup>11</sup>Opacity is zero for vacuum, and approaches infinity when the dust becomes really murky.

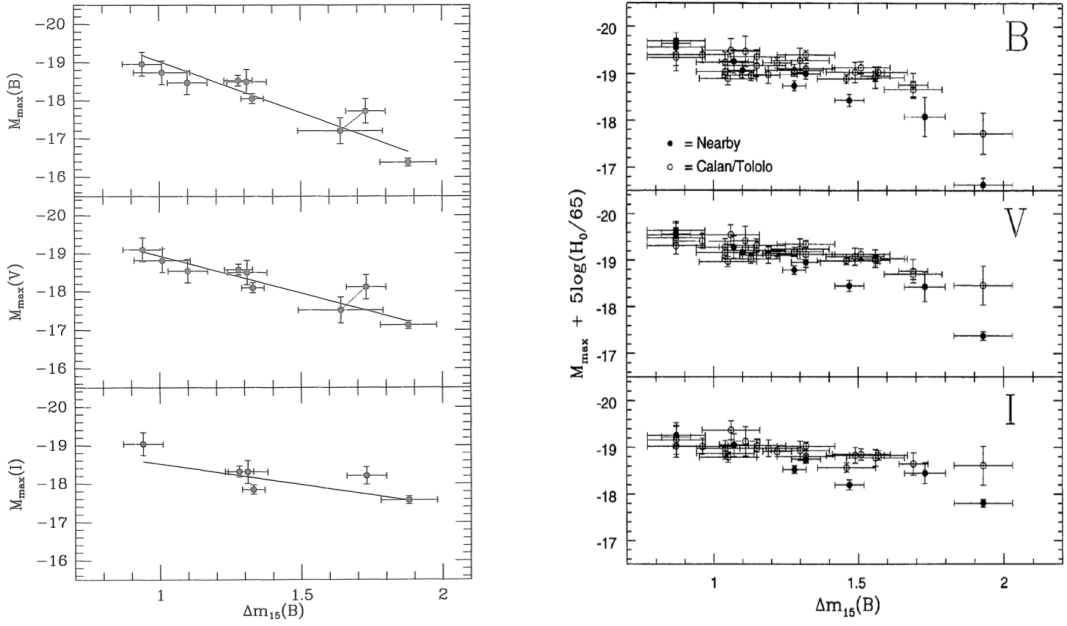


**Figure 3.10:** Brightness-decline relation. On the left, original figure from [Phillips \(1993\)](#) showing this relation for  $B$ ,  $V$ , and  $I$  bands. On the right, the same figure but with measurements made in [Hamuy et al. \(1996a\)](#).

where  $(X - Y)_o$  is the observed color, and  $(X - Y)_e = M_X - M_Y$  is the intrinsic emitted color of the object. The most commonly used is  $E_{B-V}$  because, as mentioned before, the extinction affects more the wavelength range delimited by  $B$ . One can define  $R_V = A_V / (A_B - A_V)$ , to take as a reference in order to measure the color excess in other bands compared with  $V$ , and it will be useful in the following section when we talk about the modelization of the LC. For the Milky Way, its measured value is  $R_V \sim 3.1$  ([Cardelli et al., 1989](#)).

### 3.4.1 Light-curve parametrization and models

There exist many approaches to standardize the light-curves of Type Ia SNe, in order to reduce the scatter in magnitudes at the maximum light of the LC, and to make use of the more precisely measured distances for determining the cosmological parameters.

One of this approaches is the relation between the width of the light-curve and the brightness at maximum light. This relation was seen in [Barbon et al. \(1973\)](#), but it was first parametrized by [Pskovskii \(1977\)](#), relating the slope of the LC just after the maximum with the magnitude at the peak. [Phillips \(1993\)](#) found a linear relationship between the magnitude at the peak in the  $B$  band, and the difference between this and its value 15 days after the maximum brightness,

$$\Delta m_{15} = m_B(t_{\max}) - m_B(t_{\max+15 \text{ days}}), \quad (3.6)$$

currently known as the *Phillips relation* (see Fig. 3.10). Others have also used the

LC measurements before the peak. That is the case of [Perlmutter et al. \(1997b\)](#), who parametrized the LC linearly stretching or compressing the rest-frame timescale of an average LC template ([Leibundgut et al., 1991](#)) by a *stretch factor* ( $s$ ). [Goldhaber et al. \(2001\)](#) also used the same parameter but added a dependence with redshift. These parametrizations have reduced the dispersion in  $M_B$  at the peak by a factor of two, from  $\sigma_{M_B} \sim 0.3$  to  $\sigma_{M_B} \sim 0.15$ .

Another approach is the consideration of the excess color to standardize the LC. Some works that have introduced this parameter are the following: [Tripp \(1998\)](#) used a two-parameter parametrization that correlates the  $B$  band magnitude at maximum with a  $(B - V)$  color term also measured at maximum. [Wang et al. \(2006\)](#) proposed to correlate the shape of the LC to the  $B$  magnitude when the color is  $(B - V) = 0.6$ , instead of at maximum light, because this value would be less sensitive to extinction corrections. [Wang et al. \(2005\)](#) combined the  $\Delta m_{15}$  parameterization with a measurement of the  $(B - V)$  color 12 days after maximum in  $B$  band ( $\Delta C_{12}$ ).

Some attempts to consider spectral features have been tried, such as in [Bailey et al. \(2009\)](#) who tried to correlate the  $B$  band maximum with spectral ratios of certain lines, but none have substantially decreased the scatter at maximum.

Considering all the corrections we discussed in this section (K-correction, dust extinction, brightness-decline relation, and color relation), Type Ia SNe are almost standardizable candles, but still not perfect. Once corrected, their use in cosmology is in the precise measurement of distances. There are some models (SiFTO [Conley et al. \(2008\)](#), Parab-18 [Goldhaber et al. \(2001\)](#), CMAGIC [Wang et al. \(2002\)](#), among others) that take into account all these corrections, but probably, the most commonly used, and those which we will use in the following chapters, are the *Multicolor Light Curve Shape* (MLCS) and The *Spectral Adaptative Light-curve Template* (SALT2), which we will now describe.

## MLCS2k2

The current model ([Jha et al., 2007](#)), is an improved version of the MLCS method ([Riess et al. \(1996\)](#), updated in [Riess et al. \(1998\)](#) to include a quadratic term), which was used by the *High-z Supernova Search Team* ([Schmidt et al., 1998](#)) in the co-discovery of cosmic acceleration.

According to the description of [Kessler et al. \(2009a\)](#), the LC model is written as,

$$m_{MLCS2k2}^{t,f} = M^{t,f'} + p^{t,f'} \Delta + q^{t,f'} \Delta^2 + X_{host}^{t,f'} + X_{MW}^{t,f} + K_{ff'}^t + \mu, \quad (3.7)$$

where  $t$  is the epoch index that runs over the observations,  $f$  is the filter in which the SN was measured,  $f' (= UBVR)$  are the filters in the rest-frame of the SN for which the model is defined,  $\Delta$  is the parameter that takes into account the correlation between the brightness and shape of the light-curve,  $X_{host}$  is the extinction of the host galaxy,  $X_{MW}$  is the Milky Way extinction,  $K_{ff'}$  is the K-correction between the rest-frame and observer-frame filters, and finally,  $\mu$  is the distance modulus of the supernova, which satisfies  $\mu = 5 \log_{10}(d_L/10 \text{ pc})$ , where  $d_L$  is the luminosity distance.

$M^{t,f'}$ ,  $p^{t,f'}$  and  $q^{t,f'}$  are model vectors that describe the pattern of the SN LC.  $M^{t,f'}$  is

the absolute magnitude for a SN with  $\Delta = 0$ , and  $p^{t,f'}$  and  $q^{t,f'}$  are linear and quadratic time-dependent corrections in  $\Delta$ , which translate the value of  $\Delta$  into a change in the SN absolute magnitude. These three functions are common to all SNe and are determined using a well-observed low-redshift SN training set. This training set consists of Type Ia SNe measured in the *UBVRI* bands, compiled from large homogenous sets, such as [Hamuy et al. \(1996b\)](#), [Riess et al. \(1999\)](#) and [Jha et al. \(2006b\)](#), and creates a continuum of template light-curves.

The estimations of the K-corrections are independent of the LC adjustment, and are computed following the prescription of [Nugent et al. \(2002\)](#), which requires a SN spectrum at each epoch, the spectrum of a reference star, and the reference star magnitude in each passband.

In the MLCS2k2 model, observed supernova color variations are assumed to be due to the extinction by dust of the host galaxy. This is assumed to behave in a fashion similar to dust in the Milky Way, with some color smearing (Cardelli law, [Cardelli et al. \(1989\)](#)).  $A_V$ , the extinction in magnitudes in the  $V$  band, is estimated by comparing the expected color (that of the template) and the observed color, while the relative extinction in other passbands is determined by the parameter  $R_V$ , which can be fixed at 3.1 ([Jha et al., 2007](#)) or left as a free parameter to be adjusted ([Kessler et al., 2009a](#)).

As a result, the fit of the light-curve uses a likelihood  $L$  of the observed magnitudes or fluxes as a function of four model parameters for each SN: the epoch of peak luminosity in rest-frame  $B$  band ( $t_{max}$ ), the shape-luminosity parameter ( $\Delta$ ), the host-galaxy extinction at the central wavelength of rest-frame  $V$  band ( $A_V$ ), and the distance modulus ( $\mu$ ).

## SALT2

The current light-curve model SALT2 ([Guy et al., 2007](#)), is an improved version of SALT ([Guy et al., 2005](#)), which was developed by the Supernova Legacy Survey (SNLS) Collaboration ([Guy et al., 2010](#)). This model describes the temporal evolution of the rest-frame spectral energy distribution (SED) for Type Ia SNe, made through the combination of hundreds of spectra, with a time resolution of 1 day, and wavelength resolution of  $\sim 10$  Å. The range in wavelengths spans from 2000 Å to 9200 Å in the rest-frame, and from -20 to +50 days relative to maximum light in rest-frame times. As this model has a continuum evolution of the spectra, the K-corrections can be measured consistently for each redshift and the errors can be correctly propagated throughout the model.

The rest-frame flux of the SALT2 model at wavelength  $\lambda$  and time  $t$  (such that  $t = 0$  at  $B$ -band maximum), is given by the formula,

$$F(t, \lambda) = x_0 [M_0(t, \lambda) + x_1 M_1(t, \lambda)] \exp [c CL(\lambda)], \quad (3.8)$$

where  $M_0(t, \lambda)$  is the average spectral time sequence,  $M_1(t, \lambda)$  describes the observed variability about this average, and  $CL(\lambda)$  is a time-independent color correction term (in opposition to the time dependent extinctions in MLCS2k2), which can be well

approximated by the Cardelli law, over most of the optical spectrum. These factors are determined from the training process described in Guy et al. (2007).

Thus, the free parameters that are determined from the fitting process are:  $x_0$ , the normalization of the flux,  $x_1$ , the stretch parameter (the analog of the MLCS2k2- $\Delta$  parameter), and  $c$ , a color offset relative to the average value at the time of maximum brightness in the  $B$ -band ( $c = (B - V)_{MAX} - \langle B - V \rangle_{MAX}$ ).

Unlike in the MLCS2k2 model, the extraction of the distance to a SN is part of a global fit that includes cosmological parameters. The SALT2 output can be used to produce a corrected distance, using the expression,

$$\mu_i = m_{B,i} - M + \alpha x_{1,i} - \beta c_i, \quad (3.9)$$

where the index  $i$  denotes the SN, and  $M$ ,  $\alpha$  and  $\beta$  are global parameters that describe the global stretch and color laws of SNe Ia and are determined through minimizing the scatter of the Hubble diagram around a cosmological model, using all available SNe.

### 3.5 Type Ia SN host galaxies

Another different approach to the standardization of the Type Ia SN light-curves, could come from the study of the environment of the SN event. Over the years, several analyses have tried to find correlations between SN properties and host galaxy parameters, in order to take those into account for a better standardization, reducing the scatter in the LC.

It is known that Type Ia SNe occur primarily in late-type galaxies (Oemler et al., 1979). Moreover, some studies showed a correlation between the brightness of Type Ia SNe and the morphological type of their host galaxy (Hamuy et al., 1995, 1996a, 2000, Jha et al., 2007), indicating that they not only are more common in late-type (spiral) galaxies, but also more luminous than those that explode in early-type (elliptical) galaxies. This fact cannot simply be an effect of extinction, since spiral galaxies are younger and have more dust than ellipticals, and suggests that the detailed study of the host galaxy can be extended to other characteristics such as star-formation rate (SFR) (Sullivan et al., 2006b), mass (Kelly et al., 2010), age (Neill et al., 2009), or metallicity (Gallagher et al., 2008), and used to reduce the systematic uncertainties of the intrinsic luminosity of Type Ia SNe.

In particular, a recent analysis by Sullivan et al. (2010) shows that, once standardized, Type Ia SNe exploding in more massive and less active hosts are, on average,  $\sim 0.08$  mag brighter (at  $4\sigma$  of significance) than those in less massive and more active galaxies. They also found that Type Ia SNe in less active galaxies have smaller dependence on color, and smaller scatter in SN Ia Hubble diagrams, than those in active hosts. Lampeitl et al. (2010a) confirmed that fainter, quickly declining SNe Ia favor passive host galaxies, while brighter, slowly declining Ia's favor star-forming galaxies, although those in passive host galaxies become brighter ( $\sim 0.1$  mags) than those in active after the standardization of the light-curves, for both MLCS2k2 and

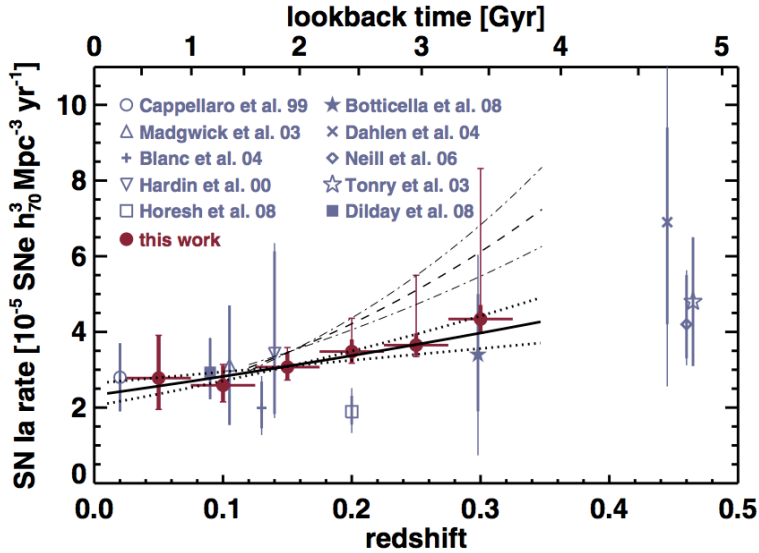


**Figure 3.11:** SN Ia rate as a function of redshift for a selection of measurements from the literature. “this work” refers to [Dilday et al. \(2010b\)](#), where the measurement is done in bins of size  $\Delta z = 0.05$ , and assuming that the rate is constant in each bin. The thick error bars denote the statistical uncertainty, while the thin error bars denote the systematic uncertainty. The solid line shows the best-fit power-law rate model, and the dotted lines the  $1\sigma$  uncertainty of the best-fit model. The dashed line shows the best-fit power-law rate model, assuming a larger mean value of dust extinction, and the dash-dotted line shows the corresponding  $1\sigma$  uncertainty of the rate model.

SALT2 fitters. [Gupta et al. \(2011\)](#) showed that older and more massive galaxies host brighter SNe than average after LC standardizations. The metallicity of the environment significantly influences the mass of  $^{56}\text{Ni}$  produced; however, it is not easy to perform a direct measurements of the metallicity of the hosts, and indirect measurements are commonly used. [D’Andrea \(2011\)](#) found that LC-corrected Type Ia SNe are  $\sim 0.1$  magnitudes brighter in high-metallicity hosts than in low-metallicity hosts, using photometric estimates of the host mass as a proxy for global metallicity.

These results point to the need to incorporate, in future cosmological analyses, information about host galaxy parameters in order to reduce the scatter in brightness.

### 3.6 Type Ia SN rate of explosion

The precise knowledge of the rate of type-Ia explosions can give information on the enrichment of the interstellar medium and the galaxy star formation rate, which help to constrain the possible progenitor models. It could also serve to find correlations that reduce the dispersion in the Hubble diagram, thus improving the constraints on cosmological parameter estimation, and the systematic uncertainty on their measurements. However, SNe are not very common events, and the measurement of their rate of explosion is full of uncertainties, since it requires a statistically significant sample and excellent control of the detection efficiency.

The rate seems to vary as a function of redshift, so with the age of the universe,

because the stellar populations themselves are changing due to metallicity (Cooper et al., 2009), or through changes in the galaxy star formation rate (Greggio et al., 2009). The values of the rate of thermonuclear and gravitational SNe are of the same order of magnitude (Bazin et al., 2009, Dilday et al., 2010b, Neill et al., 2006), but the latter is slightly higher since their progenitor stars are more frequent. The rates are measured in terms of events per unit of volume and time ( $\text{Mpc}^{-3} \text{ h}^3 \text{ year}^{-1}$ ). The measured value for Type Ia SNe rate from Dilday et al. (2010b) is shown in Fig. 3.11.

### 3.7 Hubble diagram

The Hubble diagram relates the distance to a set of objects, or an equivalent observable as  $\mu$ , to their redshifts. The distance estimations come from the light-curve fitters. MLCS2k2 gives as an output the distance modulus  $\mu$ , while for SALT2 we can calculate  $\mu$  from the apparent magnitude  $m_B$ , the stretch parameter  $x_1$  and the color parameter  $c$  (see Eq. 3.9). Then the parameters obtained from the modeled LCs are subtracted from an assumed cosmology.

Figure 3.12 shows two Hubble diagrams and their residuals to a cosmological model with only matter ( $\Omega_M, \Omega_\Lambda = (0.3, 0.0)$ ). Three different cosmologies are fitted to the data. The distance modulus estimations are measured using both MLCS2k2 (with 497 Type Ia SNe) and SALT2 (with 412 Type Ia SNe). The two models generate small differences in the distance estimation, but the adjusted cosmology is coherent between them. These differences are due to the different assumptions made by the models. A detailed analysis comparing the two fitters can be found in Kessler et al. (2009a).

### 3.8 Surveys

As discussed in the previous section, once standardized, Type Ia SNe are able to determine the expansion rate of the universe accurately. As the number of events measured increases, the determination of the cosmological parameters is more precise. Many projects have surveyed the sky with the ambition of not only determining the cosmological parameters, but also to understand the diversity of the type Ia population. Examples of dedicated SN searches at low ( $z < 0.1$ ), intermediate ( $0.1 < z < 0.5$ ) or large redshifts ( $z > 0.5$ ) include: Calán/Tololo Survey ( $\sim 50$  nearby SNe, Hamuy et al., 1993), Carnegie Supernova Project (CSP,  $\sim 100$  SNe at  $z \lesssim 0.05$ , Freedman et al., 2009), Harvard-Smithsonian Center for Astrophysics Supernova Search (CfA, 185 SNe at  $z \lesssim 0.08$ , Hicken et al., 2009), the High-z SN Search Team (HzSST, Schmidt et al., 1998, Riess et al., 1998), the Supernova Cosmology Project (SCP, Perlmutter et al., 1999, Knop et al., 2003), the Supernova Legacy Survey (SNLS, 242 SNe at  $0.07 \lesssim z \lesssim 1.06$ , Guy et al., 2010), the Nearby Supernova Factory ( $\sim 200$  SNe at  $0.02 \lesssim z \lesssim 0.08$ , Aldering et al., 2002), Lick Observatory Supernova Search (LOSS, 274 SNe at  $z \lesssim 0.05$ , Li et al., 2011), the Equation of State Supernova Trace Cosmic Expansion (ESSENCE, 102 SNe at  $0.15 \lesssim z \lesssim 0.75$ , Miknaitis et al., 2007), Probing Acceleration Now with Supernovae (PANS/HST,  $\sim 60$  SNe Ia at  $0.2 \lesssim z \lesssim 1.8$ , Strolger et al., 2005) project, and the Sloan Digital Sky Survey-II Supernova Survey (SDSS-II/SNe,  $\sim 500$  SNe at  $0.01 \lesssim z \lesssim 0.45$ , Frieman et al., 2008b).

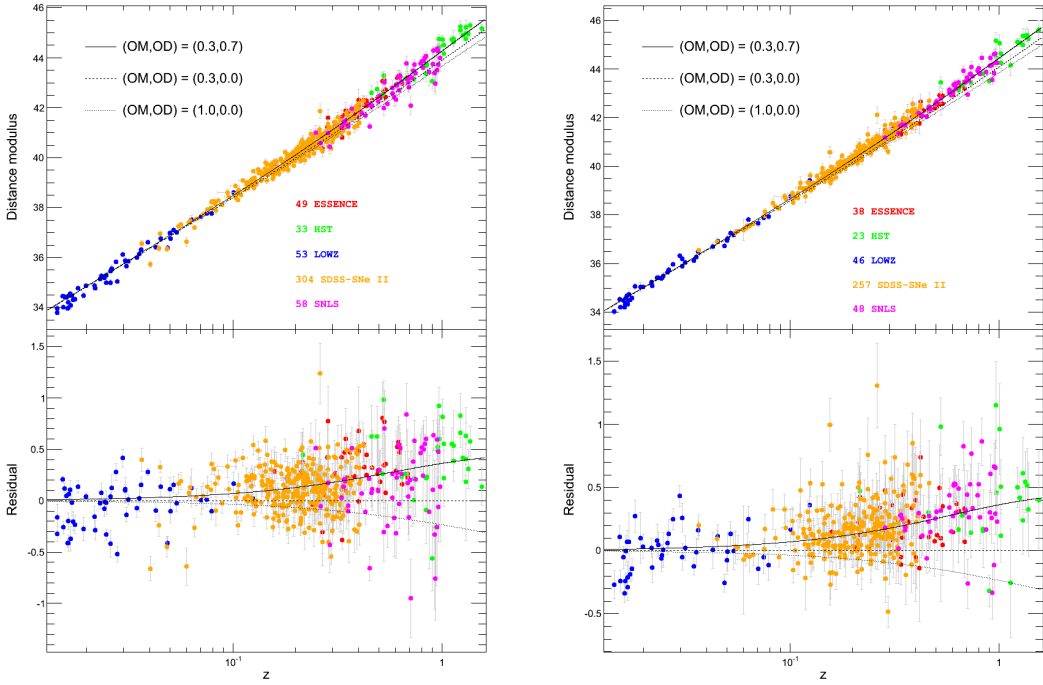


**Figure 3.12:** On the left, 497 SNe were used to measure the distance modulus using the MLCS2k2 light-curve fitter. On the right, the same plot for SALT2 fitter, using 412 SNe. Below the Hubble diagrams, the residuals to the  $(\Omega_M, \Omega_\Lambda) = (0.3, 0.0)$  cosmological model. Other two models are overplotted, in particular the best fit discussed in §2,  $(\Omega_M, \Omega_\Lambda) = (0.3, 0.7)$ .

Programs for observation and study of type Ia SNe continue to be of high priority for the astronomy community, and large SN samples are expected in the near future from new SN search projects. Future surveys will increase dramatically the number of SN discovered, making impossible their spectroscopic follow-up. The SNe redshift estimations have to be based either on the spectroscopy of the host galaxy, or using their photometric light-curves. Then, an effort in the minimization of systematic uncertainties has to be made, such as a better control of photometric measurements, or with satellite missions.

Some future projects that will search SNe from the ground are: the Palomar Transient Factory (PTF,  $z \lesssim 0.14$ , [Rau et al., 2009](#)), the LaSilla/QUEST Variability Survey ( $z \lesssim 0.1$ , [Hadjiyska et al., 2011](#)), the Dark Energy Survey (DES,  $z \lesssim 1$ , [Abbott et al., 2005](#)), and Panoramic Survey Telescope and Rapid Response System (Pan-STARRS,  $z \lesssim 0.5$ , [Kaiser et al., 2002](#)), the SkyMapper Southern Sky Survey ( $z \lesssim 0.1$ , [Keller et al., 2007](#)), the Large Synoptic Survey Telescope (LSS,  $0.45 \lesssim z \lesssim 1.4$  [Tyson et al., 2003](#)).

The particularity of the SDSS-II/SNe project is that it covers the *desert* range at intermediate redshift. With its data, SDSS has the ability to bridge this gap in the Hubble diagram and better constrain the cosmic expansion history of the universe in this redshift range along with the properties of Dark Energy.



## CHAPTER 4

---

### The Sloan Digital Sky Survey-II/SNe

---

THE Sloan Digital Sky Survey-II Supernovae Survey (SDSS-II/SNe) is one of the three components of the SDSS-II project (along with the *Legacy* and *SEGUE* surveys), a three-year (2005-2007) extension of SDSS ([York et al., 2000](#))<sup>1</sup>, with the motivation to detect and measure light-curves for several hundred supernovae through repeat scans of the sky. The main work of this thesis has to be framed within this collaboration.

In this Chapter the search program of the project will be described. An extensive overview of the SDSS-II Supernova Survey is given in [Frieman et al. \(2008b\)](#). Technical details of the operations are given in [Sako et al. \(2008\)](#). Descriptions of spectroscopic and photometric data reductions are given in [Zheng et al. \(2008\)](#) and [Holtzman et al. \(2008\)](#), respectively. [Kessler et al. \(2009a\)](#), [Sollerman et al. \(2009\)](#) and [Lampeitl et al. \(2010b\)](#) have used the first year (2005) sample for detailed cosmological analyses, while [Dilday et al. \(2008, 2010a,b\)](#) measured the SN Ia volumetric rate. Extensive studies of the peculiar SNe 2005hk, 2005gj and 2007qd are given in [Phillips et al. \(2007\)](#), [Prieto et al. \(2006\)](#), and [McClelland et al. \(2010\)](#) respectively. SN2007qd will be extensively discussed in §6. The full three-year sample was used by [Lampeitl et al. \(2010a\)](#) to analyze the effect of global host-galaxy properties on light-curve parameters, [Smith et al. \(2011\)](#) studied the SN Ia rate as a function of host-galaxy properties, [D'Andrea \(2011\)](#) correlated the Hubble residuals of type Ia SNe to the global star-formation rate in their host galaxies, and [Gupta et al. \(2011\)](#) related the ages and masses of the SN Ia host galaxies to SN properties. [Nordin et al. \(2011a,b\)](#) and [Konishi et al. \(2011\)](#) studied relationships of spectral line widths with light-curve and host-galaxy properties.

---

<sup>1</sup> Additionally, a half-scale engineering run of the SDSS-II/SNe Survey was carried out in the Fall of 2004 ([Sako et al., 2005](#)).

## 4.1 Scientific Goals

The SDSS-II/SNe Survey was designed with the following goals:

- Identify and measure multicolor light-curves for several hundred intermediate-redshift ( $0.05 < z < 0.45$ ) Type Ia SNe, where there is a lack of events, thus building a bridge in the Hubble diagram, and leading to more robust constraints on the properties of the dark energy, and the expansion history.
- Understand better the SN systematic uncertainties, due to the essential role of these errors for future SN cosmology studies, which will have larger datasets and low statistical errors. SDSS has made an effort to minimize the systematics from the photometric calibration (Ivezić et al., 2007, Smith et al., 2002).
- Anchor the Hubble Diagram with a large high-quality low-redshift sample ( $z \lesssim 0.15$ ), and re-train light-curve fitters with this homogeneous sample, instead of the heterogeneous low-redshift samples employed up to now.
- Provide rest-frame UV light-curve templates for high-redshift SN surveys ( $z \gtrsim 1$ ). The future high-z surveys will only be able to measure SN LCs as far as the near UV range (in the SN rest-frame), which, at the redshift range studied by SDSS, lays on the u and g bands. SDSS will substantially improve the rest-frame UV template data available (Ellis et al., 2008, Jha et al., 2006b).
- Provide an excellent testing ground for development of the photometric identification of the SN type and determination of the SN redshift (Poznanski et al., 2002, Sako et al., 2011, Sullivan et al., 2006a). Future SN surveys (Abbott et al., 2005, Kaiser et al., 2002, Tyson et al., 2003) will discover a large number of SNe, for which it will be impossible to obtain the spectrum, being necessary to better understand and develop photometric methods.
- Study other SN properties such as the explosion rates, the progenitor stars, the host galaxy properties, and the peculiarities of rare SNe.

## 4.2 Technical summary. Instruments.

To achieve these goals, SDSS-II/SNe has used the dedicated SDSS 2.5m telescope at Apache Point Observatory (Gunn et al., 2006), and its 2.5 deg wide-field CCD camera (Gunn et al., 1998) to survey a  $300 \text{ deg}^2$  area of the southern sky at moderately high cadence during the Fall seasons (September to November) from 2005 to 2007, producing multicolor light-curves of a large number of transient objects at intermediate redshifts ( $0.05 \lesssim z \lesssim 0.4$ ). The characteristics of the telescope and the region scanned distinguish SDSS-II/SNe from other existing surveys, which either select a large fraction of the sky with a smaller telescope to probe local objects, or use a larger instrument to image several smaller sized fields to discover high-redshift objects.

The SDSS telescope is a modified two-corrector Ritchey-Chrétien design with a 2.5 m primary mirror with  $f/2.25$ , a 1.08 m secondary mirror, a Gascoigne astigmatism

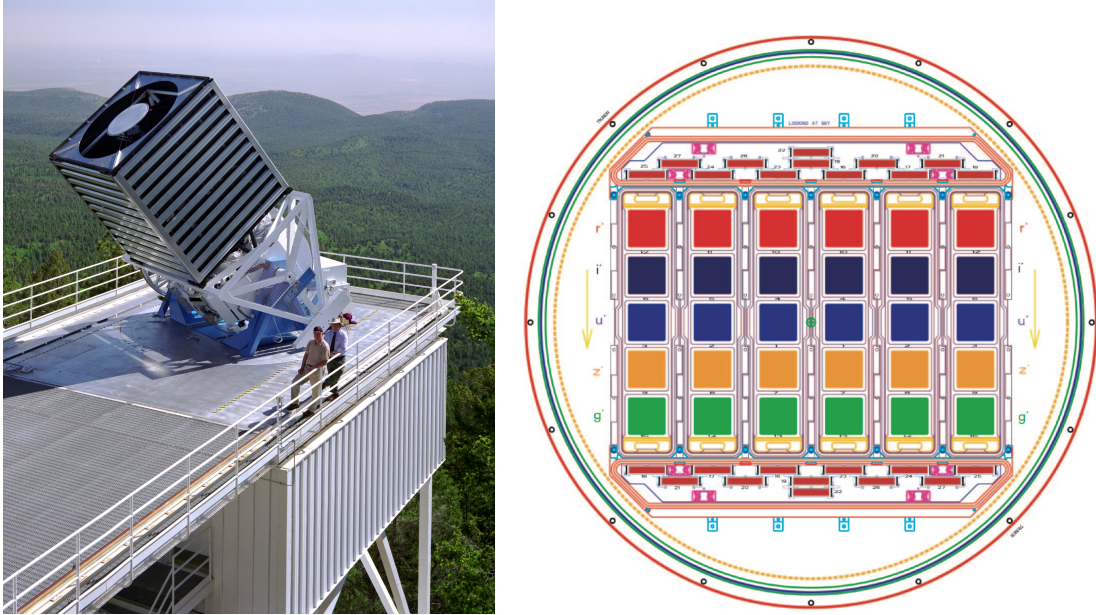


**Figure 4.1:** On the left, SDSS telescope at Apache Point, New Mexico. On the right, the SDSS CCD camera with its thirty  $2048 \times 2048$  and twenty-four  $400 \times 2048$  pixel sensors.

corrector, and two interchangeable highly aspheric correctors near the focal plane (one for imaging and the other for spectroscopy). The final focal ratio is  $f/5$ . Apart from the SDSS camera, the telescope is instrumented with two fiber-fed double spectrographs ([Uomoto et al., 1999](#)). It has a  $3^\circ$  diameter (0.65 m) focal plane that has excellent image quality and small geometric distortions over a wide wavelength range (3000–10600 Å) in the imaging mode, and good image quality combined with very small lateral and longitudinal color errors in the spectroscopic mode (see left image in Fig. 4.1).

The SDSS camera consists of two arrays, a photometric array that uses 30  $2048 \times 2048$  SITe/Tektronix CCDs ( $24 \mu\text{m}$  pixels) with an effective imaging area of  $720 \text{ cm}^2$  and an astrometric array that uses 24  $400 \times 2048$  CCDs with the same pixel size (see the right image in Fig. 4.1). The instrument carries out photometry essentially simultaneously in five color bands spanning the range accessible to silicon detectors ( $ugriz$ ; [Fukugita et al., 1996](#)) on the ground in the time-delay-and-integrate (TDI) scanning mode, which provides efficient sky coverage. The photometric detectors are arranged in the focal plane in six columns of five chips each, such that two scans cover a stripe  $2.5^\circ$  wide.

The SDSS-II/SNe Survey performed 55-s integrated exposures in each passband, thus the instrument covered the sky at a rate of approximately  $20 \text{ deg}^2 \text{ h}^{-1}$  and achieved 50% detection completeness for stellar sources at  $u = 22.5$ ,  $g = 23.2$ ,  $r = 22.6$ ,  $i = 21.9$ , and  $z = 20.8$  ([Abazajian et al., 2003](#))<sup>2</sup>. For comparison, the typical peak magnitude for a SN Ia with no extinction is  $r \sim 19.3$ , 20.8, and 21.6 mag at  $z = 0.1$ , 0.2, and 0.3.

<sup>2</sup>All magnitudes are expressed in the *AB* system.

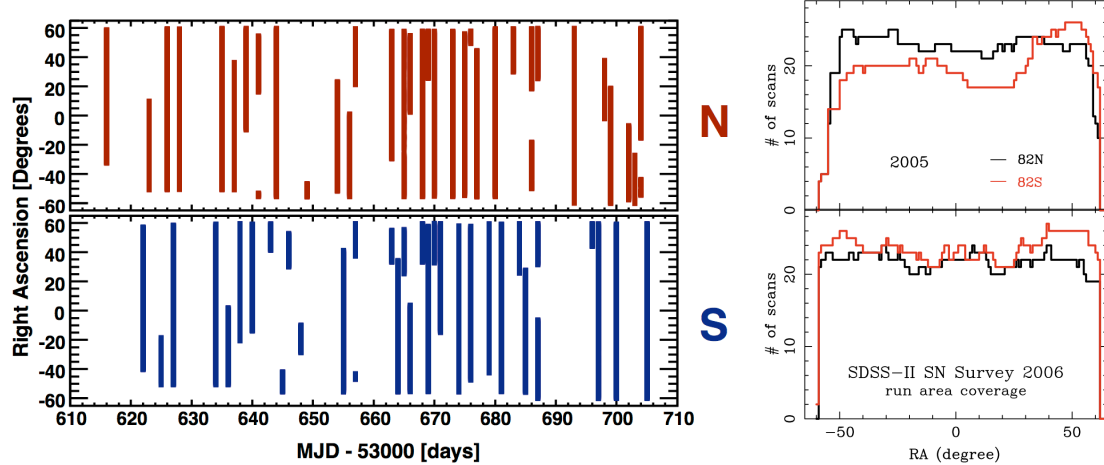


**Figure 4.2:** Left: R.A. range covered by SDSS-II/SNe for the 2005 season vs. epoch. In red the North and in blue the South strip of stripe 82. Adapted from [Dilday et al. \(2008\)](#). Right: Number of imaging scans of the Northern (in black) and Sourthern (in red) strips for the 2005 (top) and 2006 (bottom) seasons as a function of R.A.. Note that the 2006 scans are more evenly distributed in R.A. From [Sako et al. \(2008\)](#).

### 4.3 Observing strategy

The SDSS-II/SNe Survey covered a region (designated as stripe 82) centered on the celestial equator in the southern galactic hemisphere ([Stoughton et al., 2002](#)) that is  $2.5^\circ$  wide ( $-1.258^\circ < \delta_{J2000} < 1.258^\circ$ ) and runs between right ascensions of 20h and 4h ( $-60^\circ < \alpha_{J2000} < 60^\circ$ ).

Stripe 82 has been imaged multiple times in photometric conditions by the SDSS-I survey (2000-2005) and the resulting co-added images ([Annis et al., 2006](#)) provided high-quality deep template images and veto catalogs of variable objects for carrying out image subtraction to discover supernovae. It has low Milky Way extinction except near its ends ([Schlegel et al., 1998](#)), can be observed from Apache Point at low airmass from September through November, and is accessible from almost all ground-based telescopes in both the northern and southern hemispheres, for subsequent spectroscopic follow-up in order to confirm supernova type and redshift.

Due to the gaps between the six CCD columns in the focal plane, this area is typically covered by alternating between the northern (N) and southern (S) declination strips of the stripe, on successive nights of observation. Each strip encompasses  $\sim 162 \text{ deg}^2$  of sky, with a small overlap between them, so that the survey covered  $\sim 300 \text{ deg}^2$ . Each part of the survey region was observed, on average, once every four nights during an observing season, including the five brightest nights around full moon, which are used for telescope engineering, and occasional nights used by the SDSS-II SEGUE project. The lists of all SDSS-II/SNe runs and their corresponding R.A. ranges taken during the first two seasons are available in [Sako et al. \(2008\)](#). In Fig. 4.2 the observed regions scanned during the first season are shown as an example, together with the number of imaging scans for the first two seasons as a function of right ascension.

## 4.4 Data processing and target selection

The survey images are processed locally on a dedicated computer cluster that runs at APO, which reduces a full night’s worth of data within  $\sim 20$  hours. All the procedures to take the raw images to the point where they are transferred to the central SN database server at Fermilab can be divided in five main parts: the photometric reduction of the image in SDSS *ugriz* bands, the frame subtraction, the automated object detection, the visual inspection, and the light-curve fitting for spectroscopic target selection.

*Photometric reduction.* The raw data are first processed through a modified version of the Photo pipeline ([Lupton et al., 2001, 2002, Stoughton et al., 2002](#)), which produces the corrected frames and generates bad-pixel maps, position-dependent point-spread functions (PSFs), and astrometric solutions ([Pier et al., 2003](#)) that are used in subsequent processing stages.

*Image subtraction.* To identify new transients in the search data, the images are run through a modified version of Photpipe, a differential imaging pipeline used in previous transient searches ([Smith et al., 2002](#)), renamed Framesub. The deeper co-added reference images are first convolved to match the point-spread functions (PSF) of the search measured frames. In order to save processing time, this matching is limited to the *gri* bands, which are the bands most useful for SN detection in the redshift range of interest. Finally, all the data on the object is differenced, including the *u* and *z* bands. The subtracted images are then processed through an automated object detection algorithm ([Schechter et al., 1993](#)), which also produces initial photometric measurements. The signal-to-noise threshold for object detection is  $g \sim 23.2$ ,  $r \sim 22.8$  and  $i \sim 22.5$  for typical conditions.

*Object selection.* The individual peaks found by Framesub were automatically filtered through a software called doObjects to remove statistical fluctuations and identify true astronomical sources prior to handscanning. Sources detected in at least two of the three *gri* filters within  $0.8''$ , were entered into a MySQL database and were flagged as *objects*. This process removed cosmic rays, single-band spurious noise fluctuations, a large fraction of asteroids, and other rapidly moving objects detected by the survey. The list of objects was then compared against the veto catalog of Stripe 82, to remove cataloged variable stars, active galactic nuclei (AGN), and other persistently varying sources. In addition to SNe, the *objects* database included a variety of physical transients (non-rejected slow-moving asteroids, not cataloged AGN and variable stars, and high proper-motion stars) and non-physical sources of contamination, as improperly masked diffraction spikes from bright stars and artifacts of imperfect image subtraction (dipoles).

*Visual inspection.* Many of these background objects that are clearly not supernovae can, however, be quickly rejected by visual inspection. To make the handscanning

process convenient, a webpage interface was developed that displayed images of the object (in all three processed bands) along with information on the current detection, and on any previous detections at the same coordinates. For each scanned object, a list of choices for classification of the object was available:

None - Objects that do not appear to be a real astrophysical transients, often indistinguishable from noise.

Artifact - Objects that extend across two frames and have been improperly masked out.

Moving - Objects with an apparent offset in the *g* and *r* filters, the most separated in the camera.

Saturated star - A bright star which did not subtract cleanly.

Dipole - Object with adjacent regions of positive and negative subtraction residuals, where the PSF matching has not worked perfectly.

Variable - Object that appears to be near the core of a star-like source, and may have detections in a large period of time.

Transient - A single-observation object, that is not obviously moving, but does not have a host galaxy.

Cosmic ray - A sharply defined transient unresolved detection. In practice the requirement of a matching detection in at least two filters removes cosmic rays, and this category is almost never used.

Further to these non-supernova classifications there are four categories of SN candidates. In all cases a SN classification implies that the object has the appearance of a SN (i.e. a point source), and does not fall into any of the categories of background listed above.

SN Gold - Object associated with, and is well separated from, a galaxy-like object.

SN Silver - Object with no host galaxy, but is not a moving object. In most cases a SN Silver is an object that was classified as a transient on its first epoch.

SN Bronze - Object associated with, and is near the center of, a galaxy-like object. Detections of AGN are generally classified as SN Bronze.

SN Other - Object that has features inconsistent with a normal SN, but is nevertheless an interesting astrophysical transient. Including this category allows keeping a record of objects that may prove to be of interest, but that are not necessarily of high priority for immediate spectroscopic follow-up.

An average of about 4000 objects were inspected per full night of imaging during the first season. Based on this experience a new software filter called the *autoscanner* (described in [Sako et al., 2008](#)) was implemented, which identifies all objects detected in

more than one epoch, as well as bright ( $g$  or  $r < 21$  mag) objects detected for the first time, and uses statistical classification techniques to identify and filter out first-epoch background non-SN objects. This reduced the number of objects manually scanned by more than an order of magnitude, with no reduction in the quality or quantity of confirmed SNe. While scanning a single camera column in 2005 typically took 2-3 hours per person for a full night of data, in 2006 a scanner could cover two columns in only 10-20 min. Objects visually classified into one of the four SN categories are denoted as *candidates*. These candidates are given a unique supernova identification (SN ID) number. Subsequent object detections in difference images at the same position are automatically associated with the same candidate and are not manually scanned again.

*Spectroscopic target selection.* In the last stage, the *gri* light-curves of all SN candidates are compared against a template library of Type-Ia ([Nugent et al., 2002](#)), Type-Ib/c and Type-II SNe ([Richardson et al., 2001](#)) LC, in order to quickly estimate the type and the redshift, as well as other quantities that are useful for prioritizing follow-up spectroscopy. The LC of the candidates are predicted on a grid of four parameters: the redshift, the  $A_V$  extinction parameter, the time of *B*-band maximum light, and either the  $\Delta m_{15}(B)$  parameter for Branch-normal Ia models, or the peculiar SN template for 91bg and 91T-like Ia and core-collapse models. The best-fit  $\chi^2$  is recorded for each of the three supernova types (Ia, Ib/c, II), and the nearest galaxy within  $10''$  from the candidate position is then searched in the SDSS galaxy catalog, and its spectroscopic (or photometric) redshift is used as a prior for refitting and retying the LC ([Adelman-McCarthy et al., 2007](#), [Oyaizu et al., 2008](#)). For some candidates, difference imaging in the *u* and *z* bands is carried out, in order to better distinguish Type II and Type Ia SNe that tend to have a significantly different  $u - g$  color at early epochs. After this photometric typing process, other quantities are computed that help prioritize the target list for spectroscopic observations, such as the estimate of the candidate epoch (preferably before peak brightness), the galaxy light contamination (preferably farther from the galaxy center), and the dust extinction (preferably less extinguished). All SN Ia candidates found before peak and with estimated current *r*-band magnitude  $\lesssim 20$  are placed on the target list. They are generally accessible with 3-4 m class telescopes, so the follow-up observations are nearly complete out to that magnitude.

### 4.5 Spectroscopic and photometric follow-up observations

The classification of SNe is defined by their spectroscopic features. In addition, spectroscopy provides a precise redshift determination and, in a number of cases, host galaxy spectroscopic-type information. Spectroscopic follow-up of the SDSS-II/SNe candidates was undertaken by a number of telescopes. The spectra were analyzed at the observatories to provide quick reductions confirming SN type and provisional redshift information(see Fig. 4.3). The primary telescopes used in the survey were the Astrophysical Research Consortium (ARC) 3.5m at Apache Point Observatory, the New Technology Telescope (NTT) 3.6m at La Silla Observatory, the William-Herschel

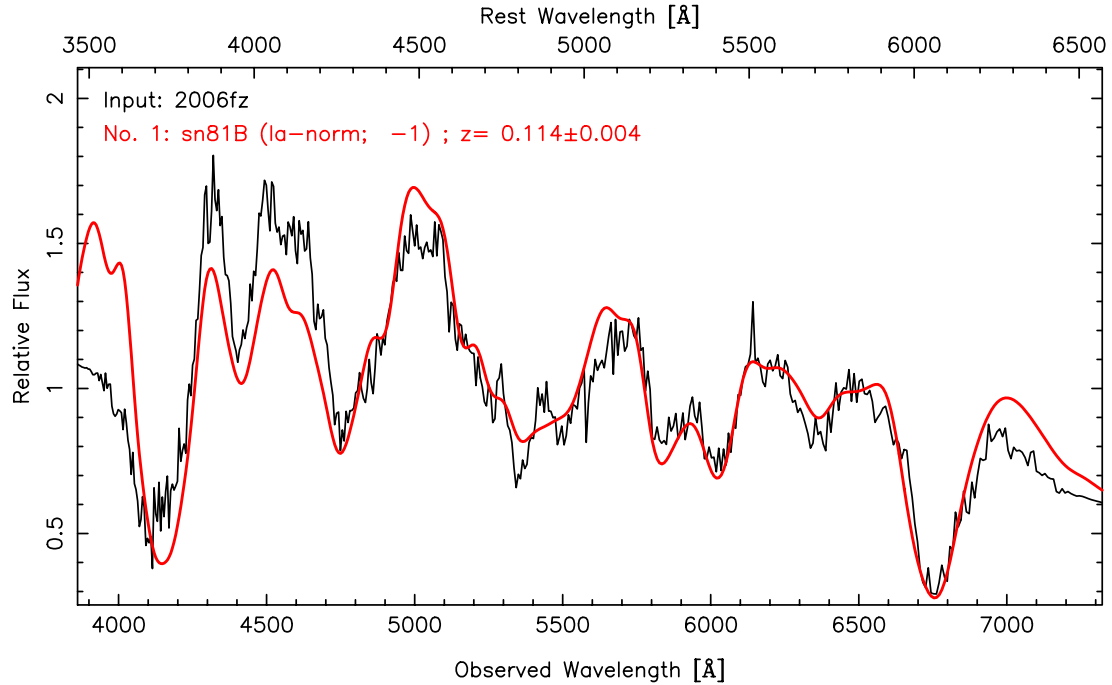


**Figure 4.3:** Example of a quickly reduced spectrum of the SN2006fz measured at the Hiltner Telescope. Galaxy light has not been subtracted from the spectrum. The red curve is a template spectrum of SN1981B, which best fits the observed, showing that the object is a Branch-normal Type Ia SN at  $z = 0.114 \pm 0.004$  and is observed one day before peak brightness.

Telescope (WHT) 4.2m, the Hiltner 2.4m at the MDM Observatory, the Nordic Optical Telescope (NOT) 2.5m and the Telescopio Nazionale Galileo (TNG) 3.58m at Roque de los Muchachos Observatory, and Kitt Peak National Observatory (KPNO) 3.5m at National Optical Astronomy Observatory, for low redshift objects, whilst the Hobby-Eberly Telescope (HET) 9.2m at McDonald Observatory, Subaru 8.2m and KECK 10m on Mauna Kea Observatory, and SALT 11m at the South African Astronomical Observatory, were used for high redshift objects.

In addition, several observatories were used to image SDSS SNe to provide additional photometric data points on the light-curves, and extend them between the survey seasons. Telescopes used for this purpose include the University of Hawaii 2.2m, the Hiltner 2.4m at MDM Observatory, the New Mexico State University 1m at APO, the ARC 3.5m, the 1.8m Vatican Advanced Technology Telescope at Mt. Graham, the 3.5m WIYN telescope at Kitt Peak, the 1.5m optical telescope at Maidanak Observatory in Uzbekistan, and the 2.5m Isaac Newton Telescope at La Palma. In addition, the Carnegie Supernova Project (CSP, [Hamuy et al., 2006](#)) obtained optical and near-infrared (NIR) imaging for many of the SDSS SNe, and the SNFactory ([Aldering et al., 2002](#)) obtained optical spectroscopy. Figure 4.4 shows the distribution of the number of SDSS photometry epochs for the spectroscopically confirmed SNe from the first two seasons for all types (in black) and for SNe Ia (in red).

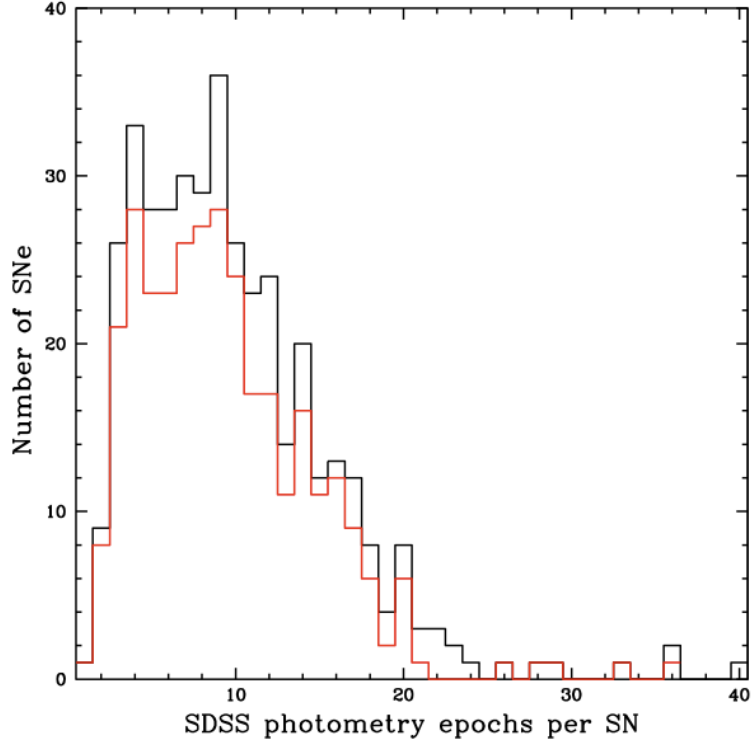


**Figure 4.4:** Distribution of number of SDSS photometry epochs for confirmed SNe of all types (in black) and for SNe Ia (in red) for the 2005 and 2006 seasons, based on the on-mountain photometric reductions. From [Frieman et al. \(2008b\)](#).

The fully reduced spectra are then analyzed (see Fig. 4.5, [Zheng et al. \(2008\)](#)) to determine supernova type, redshift and host galaxy information, where available, such that the whole SDSS-II supernova sample is analyzed in the same fashion. The redshift determination is based on galaxy features when they are present, otherwise SN features are used. In some cases, particularly at low redshift, a high-quality spectrum of the SN host galaxy is available from the SDSS-I spectroscopic survey. Comparison with those spectra indicate that the follow-up spectroscopic redshifts are determined to an accuracy of  $\Delta z \sim 0.0005$  when galaxy features are used, and  $\Delta z \sim 0.005$  when SN features are used. The SN type is determined applying the cross-correlation technique of [Tonry et al. \(1979\)](#) to the spectrum and the template library. The SDSS-II/SNe defines two categories of SNe Ia: those that are considered to be identified securely as SNe Ia (*Ia*), and those that are considered probable SNe Ia based on the analysis of their spectra (*Ia?*). These classifications are somewhat subjective, but are guided by the statistics of the cross-correlation analysis.

## 4.6 Final Photometry

To obtain more precise photometry than the on-mountain difference imaging pipeline, the imaging data in all five *ugriz* SDSS filters for all confirmed SNe, and other inter-

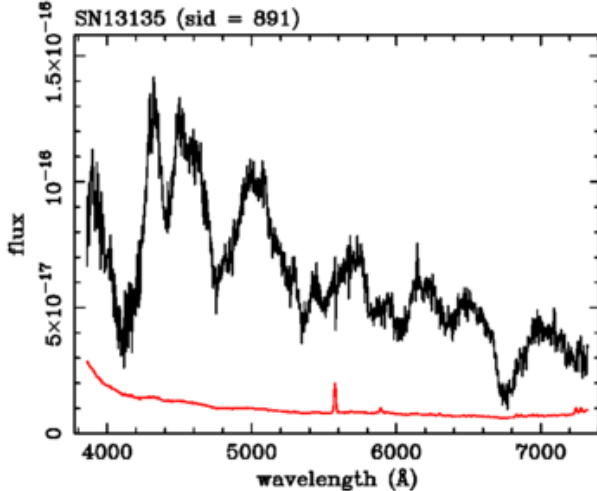


**Figure 4.5:** Final version of the SN2006fz spectrum, the same shown in Fig. 4.3, but now flux calibrated. In red, the subtracted galaxy flux contribution.

esting supernova candidates, was re-processed through a final photometry pipeline (see Fig. 4.6, Holtzman et al. 2008). In this *scene-modelling photometry* (SMP) pipeline the supernova and host galaxy (the scene) are modeled respectively as a time-varying point-source and a background that is constant in time, both convolved with a time-varying PSF. This model is constrained by jointly fitting all available images at the SN position, including images well before and after the SN explosion. Since there is no spatial resampling or convolution of the images that would correlate neighboring pixels, the error on the flux can be robustly determined. The SMP pipeline often provides photometric measurements at additional epochs compared to the survey operations pipeline.

## 4.7 Results

After the early run (2004) and the three years of operation, the SDSS-II/SNe survey discovered and confirmed spectroscopically 564 type Ia SNe, of which 518 were confirmed by the SDSS-II/SNe collaboration, 37 are likely confirmed and 9 were confirmed by other groups. Besides those spectroscopically confirmed, SDSS-II/SNe has 808 SNe photometrically classified as type Ia by their light-curves, with spectroscopic redshifts of the host galaxy measured either previously by SDSS or newly by the SDSS-III Baryon Oscillation Spectroscopic Survey (BOSS, Eisenstein et al. 2011). The number of photometrically identified SNe has been largely increased after the BOSS contribution. The whole SDSS-II/SNe sample combining the spectroscopic and photometric samples consists of 1372 Type Ia SNe. Table 4.1 contains a detailed summary of the number of SN candidates that were classified during the whole SDSS-II/SNe survey, while Fig. 4.7 shows the images of all Type Ia SNe spectroscopically confirmed from the 2005-2007 seasons.

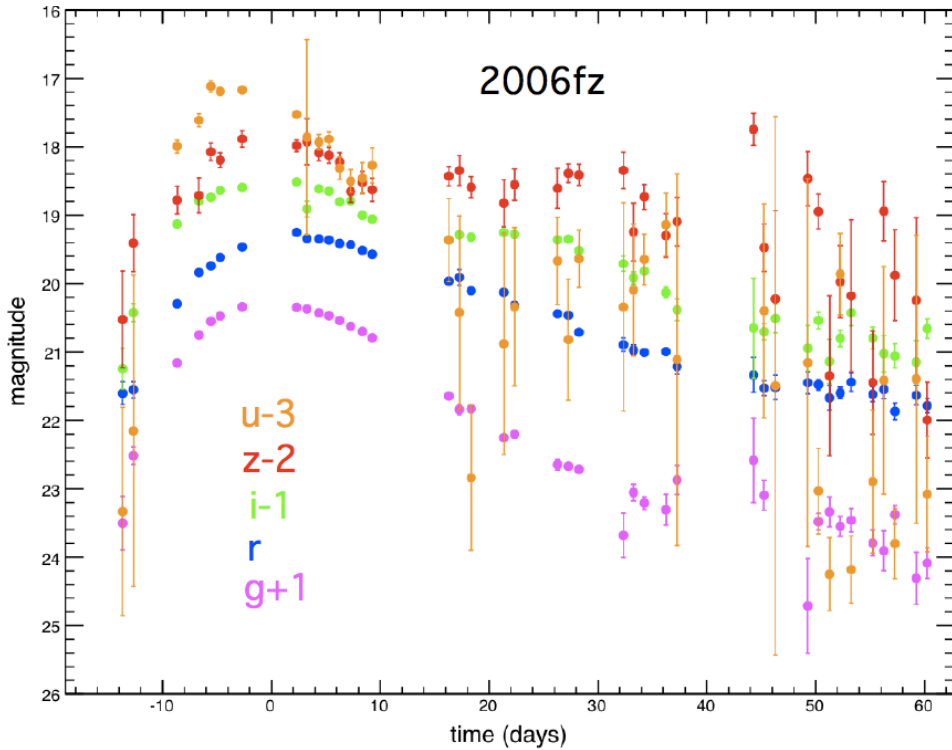
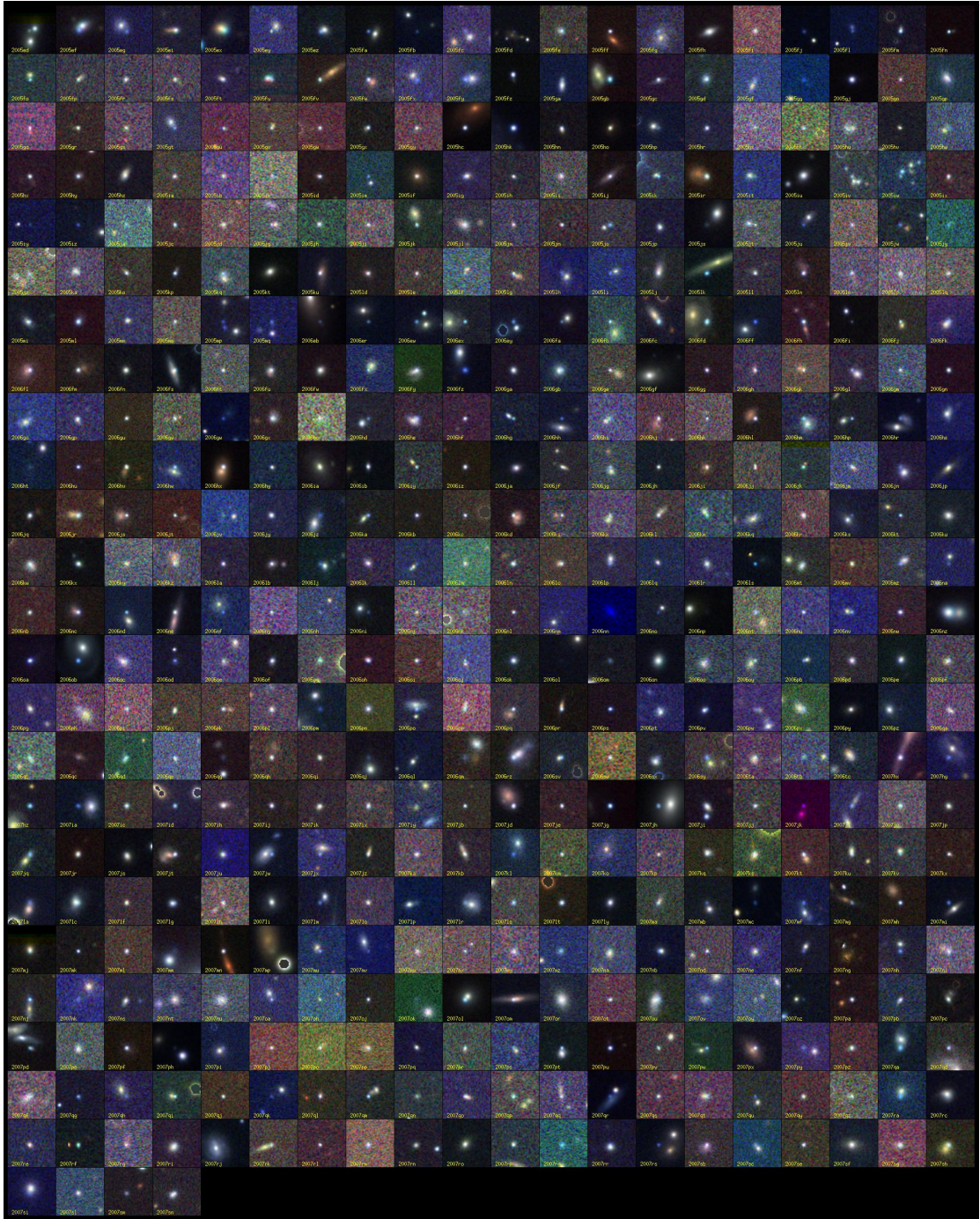


**Figure 4.6:**  $ugriz$  light-curves for SN2006fz, a confirmed SN Ia at  $z = 0.10351$ .

**Table 4.1:** All SDSS-II/SNe candidates classified in groups. SNe with BOSS host-galaxy redshifts are included in class [105].

SNe classes	2004	2005	2006	2007	all
[104] photo-Ia no spec-z	-	228	277	239	744
[105] photo-Ia + host spec-z	-	304	286	218	808
[106] photo-non-Ia + host spec-z	-	105	91	89	285
[111] SDSS-confirmed Ib	1	3	3	1	8
[112] SDSS-confirmed Ic	-	4	4	3	11
[113] SDSS-confirmed II	4	10	19	37	70
[115] externally-confirmed Ib	-	-	-	1	1
[117] externally-confirmed II	-	1	-	-	1
[118] externally-confirmed Ia	-	1	5	3	9
[119] likely confirmed Ia	-	16	12	9	37
[120] SDSS-confirmed Ia	16	129	197	176	518
Total	21	801	894	776	2492
Type Ia SNe					
[105]+[118]+[119]+[120] Ia	16	450	500	406	1372

**Figure 4.7:** Spectroscopically confirmed Type Ia SNe from the 2005-2007 SDSS-II/SNe campaigns.



## CHAPTER 5

---

### Supernova spectroscopy at the TNG

---

As part of the spectroscopic follow-up of the SDSS-II/SNe candidates, we contributed to the project taking spectra of 23 SNe during four nights in October and November (5-6 Oct. and 4-5 Nov.) of 2007, the last observing season of the project. In situ, we performed a quick analysis of these spectra confirming their type and measuring provisional redshifts, in order to, if it was the case of an interesting object, allow other telescopes to measure high-resolution spectra, or spectra in other wavelength ranges or epochs. Among all the objects for which we obtained spectra, 13 were Type Ia SNe, 7 were Type II SNe, and 3 were too faint to determine the type.

A detailed reduction of all spectra, removing the host galaxy flux contribution and calibrating in flux and wavelength, was then performed. The finished product was finally sent to be added to the whole SDSS-II/SNe sample, which was available for further analysis by any member of the collaboration. The three-year spectroscopy and photometry data is going to be published in the next months ([Sako et al., 2011](#)), and our spectra will be included in that paper.

In this chapter, the whole reduction procedure, from the acquisition of the raw data by the telescope camera to the final flux-calibrated spectra, will be described. In §5.1 the telescope and the instrument used to obtain the SN spectra is summarized, and then in §5.2, we will explain the observations obtained, together with the format of the data. The whole reduction process is detailed in §5.3, and the software used for the calibration and determination of the SN parameters is described in §5.4, together with the result of the analysis.

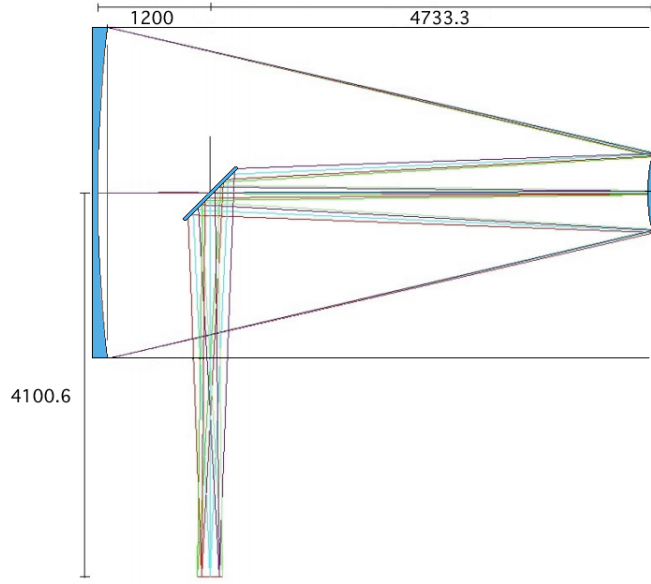


**Figure 5.1:** Schematic drawing of the TNG parts. Light comes from the right, shining on the 3.58 m concave hyperbolic primary mirror, which reflects it to the 0.875 m convex hyperbolic secondary mirror, already reflecting the light to the flat and elliptical tertiary, with a major axis of 0.84 m and a minor of 0.6 m, that redirects the light towards one of the two Nasmyth foci. The final focal ratio is  $f/11$  and the diameter of the usable Field of View (FoV) is 30 arcmin.

## 5.1 Telescopio Nazionale Galileo

The *Telescopio Nazionale Galileo* (TNG) is an alt-azimuthal reflecting telescope with a Ritchey-Chrétien<sup>1</sup> optical configuration, composed of a 3.58 m concave hyperbolic primary mirror, a 0.875 m convex hyperbolic secondary, and a flat and elliptical ( $a = 840$  cm,  $b = 600$  cm) tertiary mirror, all made by Schott in Zerodur ceramic and polished by Zeiss, feeding two opposite Nasmyth foci. The final focal ratio is  $f/11$  and the diameter of the usable Field of View (FoV) is 30 arcmin. It has a design derived from the New Technology Telescope (NTT), an ESO 4 m class telescope located in La Silla (Chile). Therefore, the optical quality of the telescope is ensured by an active optics system (AO) which performs real-time corrections of the optical components and compensates the deformations of the thin primary mirror, and the positions of the secondary and tertiary mirrors. The interface between the telescope fork and the instruments at both Nasmyth foci is provided by two rotator/adapters, that compensate for the field rotation by a mechanical counter rotation. One of the best qualities of the TNG is that all the available instruments are permanently mounted at the telescope. This guarantees flexibility during an observing session, since it is possible to change instrument during the night with a loss of time limited to a few minutes. A schematic drawing of the light path in TNG is shown in Fig. 5.1.

The TNG building is held by a structure of 24 m in height composed by a rotating

---

<sup>1</sup>An improved Cassegrain configuration, which gives a field of view free of coma and spherical aberrations.



**Figure 5.2:** Images of the Telescopio Nazionale Galileo (TNG) at the Roque de los Muchachos Observatory (ORM).

octagonal dome, a lower rounded building enclosing the central pillar, and an annex service building. The control room is located next to the dome, and rotates with it when the telescope moves. The thermal stability is achieved by an air conditioning system, five tiltable flaps set in the rear wall of the dome, and by a movable screen in the front wall. It is one of the largest telescopes hosted by the Roque de los Muchachos Observatory (ORM), a very important observing site in the northern hemisphere, protected most of the year by a high-pressure system which prevents access to storms. The typical wind flow does not create problems to observations because it carries homogeneous oceanic air. The best period is around May, with almost 90% of photometric nights. It is located on the island of San Miguel de La Palma in the Canary archipelago at a latitude of  $28^{\circ}45'28.3''$  N,  $17^{\circ}53'37.9''$  W, and 2358 meters above sea level. Images of the TNG building and its surroundings are shown in Fig. 5.2.

The telescope saw its first light in 1998, and was originally operated by the *Centro Galileo Galilei* (CGG), which was created in 1997 by the *Consorzio Nazionale per l'Astronomia e l'Astrofisica* (CNAA). Since 2002 it is operated by the *Fundación Galileo Galilei-Fundación Canaria* (FGG), a non-profit institution which manages the telescope on behalf of the *Italian National Institute of Astrophysics* (INAF). Observations can be proposed through the Italian Time Allocation Committee (TAC) which assigns, based solely on the scientific merit of the proposals, 75% of the available time. The rest of the time is at disposal of the Spanish (20%) and international (5%) astronomical communities. Calls for proposals are issued twice a year, typically in March-April and September-October.

The science based on observational data from the TNG is varied. Proposed observing programs go from the study of the planets and minor bodies of the solar system up to research of cosmological interest (e.g. large-scale structure of the universe and systems of galaxies).



**Figure 5.3:** DOLORES instrument mounted on the Nasmyth B focus of the TNG.

The TNG is equipped with three instruments that are permanently operating on both Nasmyth foci and offer a large variety of observing modes covering the optical and near infrared wavelength ranges and spanning from broad band imaging to high resolution spectroscopy:

- *Spettrografo ad Alta Risoluzione del Galileo* (SARG), high-resolution spectrometer covering the visible wavelength range (4000-9000 Å) and especially designed for high accuracy radial velocity measurements. It also includes a polarimetric module.
- *Near Infrared Camera and Spectrometer* (NICS), CCD camera and spectrograph with a field of view of  $4.3 \times 4.3$  arcmin for observations in the near-infrared (900-2500 nm, Y and K bands). Imaging-polarimetry and spectro-polarimetry modes are also available.
- *Device Optimized for LOw RESolution* (DOLORES), CCD camera and low-resolution spectrograph with a field of view of  $8.6 \times 8.6$  arcmin for observations in the visible. It also includes a multi-slit mode using masks produced with a punching machine.

In the next section we are going to briefly describe the latter, since it was the instrument used for taking the spectra of the SDSS-II/SNe candidates.

### 5.1.1 The Device Optimized for LOw RESolution (DOLORES)

The *Device Optimized for LOw RESolution* (DOLORES), LRS in short, is a low resolution spectrograph permanently installed in the B Nasmyth focus of the TNG. An image of the LRS mounted on the telescope is shown in Fig. 5.3. The main parts of the instrument are (from the de-rotator outward):

- The entrance slider, which allows the insertion in the optical path of a mirror for wavelength calibration with Thorium and Argon lamps, an off-board set of lamps (Helium, Neon and Halogen) for wavelength and Flat Field calibrations, or a flat mirror which feeds the light to the high resolution spectrograph SARG.
- The tram located at the telescope focal plane, which can carry 5 fixed width Long Slit Units (0.7'', 1.0'', 1.5'', 2.0'' and 5.0'') or up to 5 Multi Object Spectroscopy (MOS) plates. Each plate consists of a mask with some vertical slits of the same width (either 1.1'' or 1.6'') and different lengths, which can be positioned anywhere within the mask, in order to take spectra of several objects at the same time.
- The optical collimator.
- The filter wheel. Normally, eleven imaging filters are mounted on the wheel (Johnson-Cousins *UBVRI*, Sloan *ugriz*, and a  $\sim 560$  nm cut-on filter), but up to 17 special and narrow-band filters are available, which are normally not mounted, but can be introduced on demand.
- The grisms wheel, which carries 9 dispersing optical elements (grisms) and the focusing-pyramid device. At present, 7 of the 9 installed grisms are *Volume Phase Holographic* grisms, which provide a dispersion in a narrow band (500-2000 Å) with high-precision ( $\sim 0.5$  Å/px), while the other two (LR-B and LR-R) have less resolution but the spectra obtained ranges from 3000 to 8430 Å and 4470 to 10073 Å, respectively, with a precision of  $\sim 2.5$  Å/px.
- The shutter, which allows exposure times as low as 0.02 s with uniform illumination of the field.
- The CCD camera equipped with a  $2048 \times 2048$  E2V 4240 thinned back-illuminated, deep-depleted, astro-broadband coated CCD with a pixel size of  $13.5\ \mu\text{m}$ . The scale is 0.252 arcsec/px which yields a field of view of about  $8.6 \times 8.6$  arcmin. Its quantum efficiency (QE), shown in Fig. 5.4, peaks at 85.8% around 450 nm and is 47.7% at 900 nm. The CCD conversion factor is  $0.97\ e^-/\text{ADU}$  and the typical readout noise is slightly below  $9\ e^-$  r.m.s. The linearity is better than 1% over the whole dynamical range. Dark current is unappreciable even for long exposures and saturation occurs at  $\sim 65500$  ADU. The full-frame readout time is 25 s, although smaller windows can be easily set to reduce the CCD read-out time. This camera is mounted since January 2008.

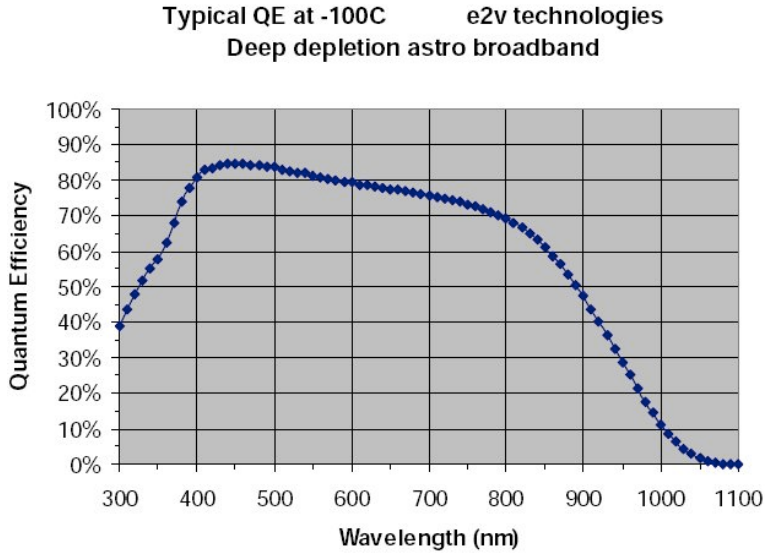


**Figure 5.4:** Quantum efficiency of the E2V CCD mounted on the LRS camera.

When all the elements are taken away, LRS can be used for imaging, and thanks to its design, switching to spectroscopy takes about 2 min in the worst case. All the optical elements (filters, slits and grisms) can be inserted by motors into the optical path soon after the collimator.

## 5.2 Observations

We<sup>2</sup> observed during two nights in October (5th and 6th) and two more in November (3rd and 4th) of 2007. We used TNG and the low resolution spectrograph LRS through its user interface and obtained in total 305 images. We generally took, at first, several flat images (at least 5) for each of the slits used, with an Halogen lamp, and some with the shutter closed to use as a bias of the CCD camera. After that, we also took for each of the slits some images with the lamps (Helium, Argon and Neon) which would be used to calibrate the wavelengths, since the emission lines of the lamps are known. Finally, and before taking SN spectra, we took some spectra of known stars well suited for calibration in flux.

Once all the calibration images were obtained, we started taking the spectra of SNe. For this, we always used the LR-B grism (3000-8430 Å), one of the available slits (0.7'', 1.0'', 1.5'', 2.0'' and 5.0'') depending on the brightness of the object and the seeing, and no filters. The procedure followed to obtain the SN spectra was, at first, take an image of the open field, in order to precisely correct the position of the telescope putting the SN in the center. Then, a second image with the slit, in order to check if the SN was exactly placed in the center of the slit. And finally, the spectrum image. When the conditions were favorable, two spectral images of 20 or 30 minutes each

<sup>2</sup>Francisco Javier Castander (ICE, Barcelona) and Ramon Miquel (IFAE, Barcelona) in October, and Mercedes Mollá (CIEMAT, Madrid), Ramon Miquel and Lluís Galbany (IFAE, Barcelona) in November.

were usually taken, and then averaged, in order to correct for turbulences and cosmic rays. Sometimes this was not possible and only one spectrum was taken, usually early in the morning before sunrise.

A quick determination of the type was performed in real time using the SN Identification (SNID, described in §5.4) software. An image of the output of SNID, where a measurement of the type, the redshift, and the epoch of the SN are shown, was sent to the collaboration from the mountain, in order to, if it was the case of an interesting object, allow other telescopes to measure high-resolution spectra, or spectra in other wavelength ranges or epochs.

### 5.2.1 Data

Of the 305 images saved, 46 were spectra of 23 different SNe. The other images contain flat fields, lamps spectra, calibration stars, bias of the camera and measurements of the slit position. A summary of all the images saved from those four days can be found in Appendix A. The discovery of these SNe and the confirming spectroscopy taken by us and others was reported in Central Bureau Electronic Telegrams (CBET) 1098 ([Bassett et al., 2007b](#)) and 1128 ([Bassett et al., 2007c](#)). And the discovery of the peculiar SN2007qd and the spectroscopy taken by us at TNG and others was reported in CBET 1137 ([Bassett et al., 2007a](#)).

#### FITS

All the images obtained through LRS are in a format called FITS, which stands for *Flexible Image Transport System* and is the standard data format used by the scientific world in astronomy and endorsed by the International Astronomical Union (IAU). It was originally developed in the late 1970's, and it is primarily designed to store scientific data sets consisting of multi-dimensional arrays (1-D spectra, 2-D images or 3-D data cubes) and 2-dimensional tables containing rows and columns of data. This allows one, for instance, to have the same image in different filters saved in only one file.

A FITS file consists of one or more Header and Data Units (HDUs), where the first HDU is called the *Primary HDU*, and contains an N-dimensional array of pixels. The following HDUs are called FITS *extensions*, and can be one of these types:

- *Image Extension*, a N-dimensional array of pixels, like in a primary array
- *ASCII Table Extension*, rows and columns of data in ASCII character format
- *Binary Table Extension*, rows and columns of data in binary representation

Every HDU consists of an ASCII formatted *Header Unit* followed by an optional *Data Unit*. Each Header Unit consists of any number of 80-character keyword records which have the general form:

*KEYNAME* = value/comment string.

## Supernova spectroscopy at the TNG

---

```

SIMPLE = T / file does conform to FITS standard
BITPIX = 16 / number of bits per data pixel
NAXIS = 2 / number of data axes
NAXIS1 = 2100 / length of data axis 1
NAXIS2 = 2100 / length of data axis 2
EXTEND = T / FITS dataset may contain extensions
COMMENT FITS (Flexible Image Transport System) format is defined in 'Astronomy
COMMENT and Astrophysics', volume 376, page 359; bibcode: 2001A&A...376..359H
EXPTIME = 600.000 / Exposure time
TELESCOP= 'TNG' / data have been taken at the TNG
INSTRUME= 'LRS' / instrument name
EXP_ID = 'JKVA0186' / exposure identifier
FILENAME= 'JKVA0186.fits' / FITS filename ([EXP_ID].fits)
DATE = '2007-10-06' / date file was written
TIME = '05:42:40' / time file was written
ORIGIN = 'CGG' / file written at CGG
RA-RAD = 0.9427546262741089 / right ascension (radians as float)
DEC-RAD = 0.019313950091600418 / declination (radians as float)
RA-DEG = 3.601057529449463 / right asc. (hours as float)
DEC-DEG = 1.1066077947616577 / declination (degrees as float)
ROT-OFF = 0.604058444999695 / Rotator Offset Angle rad (-pi +pi)
EQX-OBS = 2000.0 / equinox = 2000
EQUINOX = 2000.0 / equinox of Catalogue Coordinate
AIRMASS = 1.247084617614746 / air mass
AZ = 0.8035422563552856 / starting azimuth radians
EL = 0.9304187893867493 / starting elevation radians
ROT-POS = 2.132646322250366 / starting Derotator angle radians
PARANG = 0.6826338768005371 / starting Parallactic angle radians
CRVAL1 = 0.0 / reference X value is 0
CRVAL2 = 0.0 / reference Y value is 0
CTYPE1 = 'PIXEL' / units are pixel
CTYPE2 = 'PIXEL' / units are pixel
OBJCAT = 'SN17886' / Object name catalog
RA = 3.600399971008301 / RA of catalog, float hours
DEC = 1.1033999919891357 / DEC of catalog, float degrees
LST = 5.3119001388549805 / Local Sideral Time
PIXSIZE = 13.5 / size of pixel on detector (microns)
NCHIPS = 1.0 / chips number
CRPIX1 = 1.0 / reference X pixel
CRPIX2 = 1.0 / reference Y pixel
CRDELT1 = 1.0 / binning (X axis)
CRDELT2 = 1.0 / binning (Y axis)
DETOFF1 = 0.0 / X offset on detector
DETOFF2 = 0.0 / Y offset on detector
DETSIZ1 = 2100.0 / detector size (X axis)
DETSIZ2 = 2100.0 / detector size (Y axis)
DETRDMOD= 0.0 / detector read mode 0 left, 1 right, 2 both
EXPSTART= '05:32:17' / exposure start time (UT)
DATE-OBS= '2007-10-06' / date of observation
GAIN-LEFT = 1.0 / Gain left factor electron ADU
GAIN-RIG= 1.0 / Gain right factor electron ADU
DET_ID = 'E2V4240' / Detector ID
OBS-TYPE= 'OBJECT' / observation type
PROGRAM = 'A16CAT_78' / program name
FLT_ID = 'Open' / Filter type
GRM_ID = 'LR-B' / Grism type
SLT_ID = '1.0_arcsec' / Slit type
LMP_ID = 'Parking' / Lamp type
FLT_ENC = 1724523.0 / Encoder Filter
GRM_ENC = 23797.0 / Encoder Grism
SLT_ENC = 491998.0 / Encoder Slit
LMP_ENC = 4250.0 / Encoder Lamp
FOC_ENC = 401.0 / Encoder Focus
BIAS_1 = 27.194782257080078 / ODLR
BIAS_2 = 15.11650276184082 / RDL
BIAS_3 = 15.095788955688477 / RDR
BIAS_4 = 22.15741539001465 / DD
BIAS_5 = 7.0034708976745605 / SS
BIAS_9 = 0.9949259757995605 / OG1
BIAS_10 = 1.996901035308838 / OG2
E_GAIN = 2.0 / Electronic Gain
E_FILTER= 2.0 / Electronic Filter
TENS = 13.300000190734863 / Temperature Ens Plate
TBAR4 = 13.300000190734863 / Temperature bar 4
TBAR8 = 13.600000381469727 / Temperature bar 8
TGRM = 12.600000381469727 / Temperature grm plate
TCAMERA = 12.300000190734863 / Temperature camera
TSHUTTER= 11.399999618530273 / Temperature shutter
BSCALE = 1.0 / BSCALE
BZERO = 32768 / BZERO
END

```

**Figure 5.5:** Header Unit of a FITS file of one of our images obtained at TNG.

The keyword names may be up to 8 characters long and can only contain uppercase letters, the digits 0-9, the hyphen, and the underscore character. After that, there is usually an equal sign and a space character (= ) in columns 9 and 10, followed by the value of the keyword. At the end of the Header there should always be the *END* keyword. Each header unit begins with a series of required keywords that specify the size and format of the following data unit. The required keywords may be followed by other optional keywords to describe various aspects of the data, such as the date and time of the observation. Other COMMENT or HISTORY keywords are also frequently added to further document the contents of the data file. One of the great advantages of this format is that the user can examine the headers to study an unknown file. An example of the FITS Header Unit of one image from TNG, is shown in Fig. 5.5. There one can find the required keywords mentioned and other comments that point to the telescope used, the instrument, the coordinates of the object selected, the airmass, the exposure time, the slit and grism used, among others.

The data unit, if present, immediately follows the header unit. Note that it is possible that some HDUs do not have a data unit and only consist of the header unit.

### 5.3 Reduction of the data

The resulting image of a observation using a telescope equipped with a spectrograph is a 2-D image, the horizontal direction corresponding to the different wavelengths and the vertical to different locations along the slit. The supernova is placed in the center of the slit, while the host galaxy, gas regions, other stars or just empty sky, could be in the other regions along the slit.

Unfortunately, the extraction of the SN spectrum is not as straightforward as simply extracting the central region of the image. The image should be first corrected due to the errors of the CCD camera, the spectrograph behavior, and the atmosphere contribution. All of these effects have to be corrected to obtain the pure supernova spectrum.

#### IRAF

In order to process all the images obtained by the CCD telescope camera, and to reduce the spectra of the SNe, we used several scripts within IRAF<sup>3</sup> (Image Reduction and Analysis Facility), a large collection of software written in the 80's by astronomers and programmers at the National Optical Astronomy Observatory (NOAO) in Arizona. IRAF is focused on the processing of astronomical images in FITS format, although it is compatible with other formats. Its architecture allows external packages to be added easily. Through IRAF one can do things like add, subtract, multiply or divide images, average them, cut regions, plot, change their format, and more. All of this in order to extract the relevant information from them. IRAF is accessed through an operating system called *Command Language* (CL), in which the commands to perform any task are similar to those of the UNIX system. It also allows you to program your own scripts in CL language, to perform a set of tasks repeatedly.

---

<sup>3</sup><http://iraf.noao.edu/>

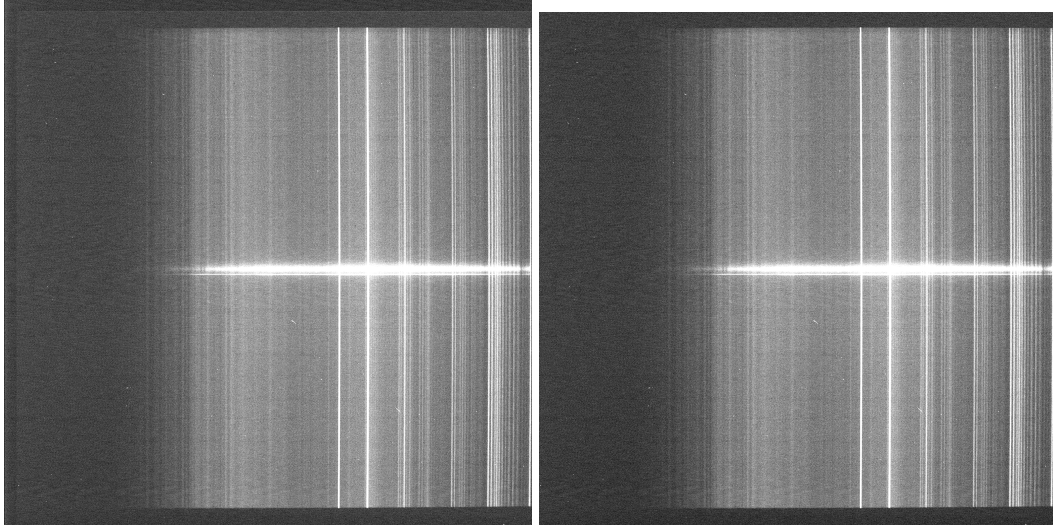


**Figure 5.6:** FITS file JKVA0185 containing the SN2007jh spectrum before and after *debias*. The slit was placed in the center and vertically; in this way, the SN spectrum is the brighter horizontal line in the center. In this image there is also the spectrum of the galaxy, which is the bright horizontal cloud just above the SN spectrum. The brighter vertically lines correspond to the interstellar medium that occupies all the field of view. On the right, the median value (3252.35) of ADUs in the pixels is subtracted from all pixels, and the overscan region (the first 52 columns and rows) is cut out.

## Procedure

The images obtained by the TNG CCD camera have  $2100 \times 2100$  pixels. Since the CCD only has one readout channel, it can only produce one vertical and one horizontal overscan region. Starting from the top-left of the images, the first 52 columns and rows are the overscan region. The rest ( $2048 \times 2048$ ) contains the reading of the pixels of the CCD which have been exposed to the light. In order to prepare the images to obtain the SNe spectra, we first have to do preliminary calibration steps. In the following we detail all the processes to which the images are subjected, until the final SN spectra are extracted.

### 5.3.1 Debiasing

The first thing to do is to subtract the bias level, the offset charge added during the readout of the pixels by the CCD camera. This bias does not correspond to the real photon counts from the exposures, and can be measured reading out a bias strip created when the preamplifier keeps reading out after all of the exposed columns have already been read (overscan region).

This procedure, the debiasing, is done to every image separately as the bias level could be slightly different. A script called *debias*, measures the median value of counts (the pedestal) in a region of the overscan (all the pixels from the column 11 to 45), and generates a new image file with this average subtracted from all the pixels, and the overscan region cut out. In Fig. 5.6 one original image from the camera, and the output once *debias* is run on the image, are shown.

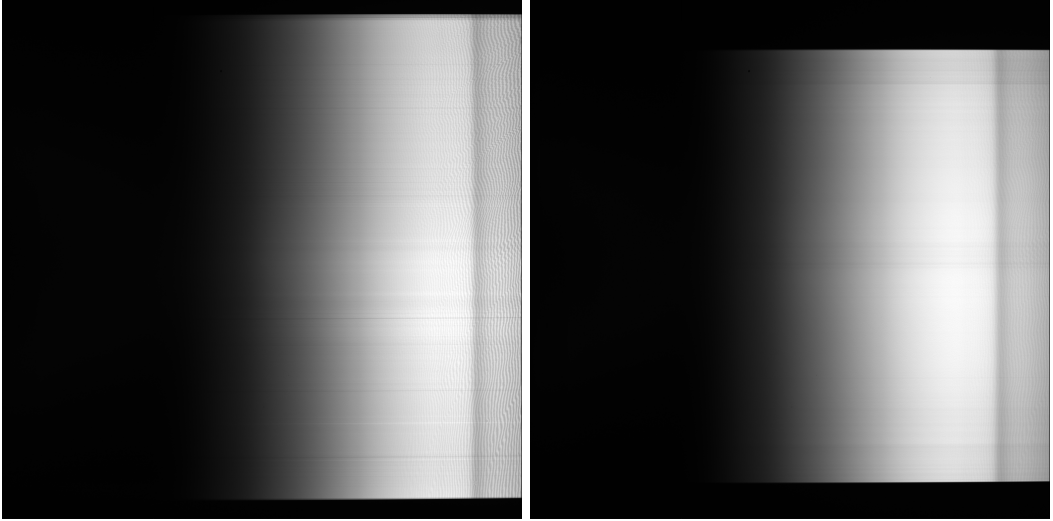


**Figure 5.7:** Averaged flat fields using slits of 1.0 and 5.0 arcsec. Note that the 5.0 arcsec slit is shorter.

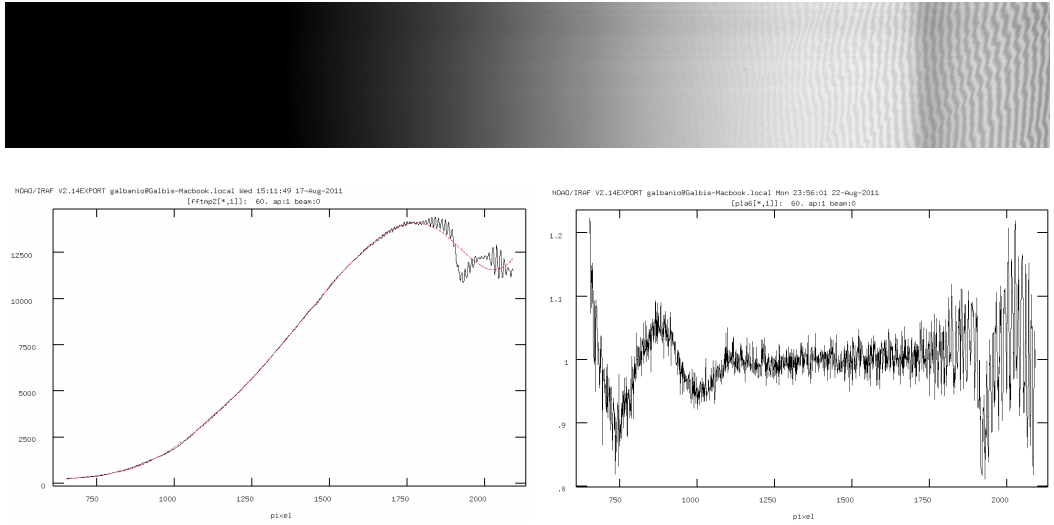


**Figure 5.8:** On top, the region extracted from the flat field image using the 1.0 arcsec slit in Fig. 5.7. On the left, the column average of the region of the flat image in black, and the fit of a cubic spline of 6 pieces in red. On the right, the ratio between the black and the red lines.

### 5.3.2 Flat Fielding

There are two errors which are intrinsic to CCD cameras. First, there is a slight pixel to pixel variation in the sensitivity. Second, there is a wavelength-dependent interference phenomenon at the thin silicon layers of the CCD, whose thickness is comparable to the detected wavelengths. There is constructive and destructive interference between the rays reflected at the boundaries of the layers. Moreover, the silicon layers are not perfectly even, and this leads to a complex pattern known as fringing which typically

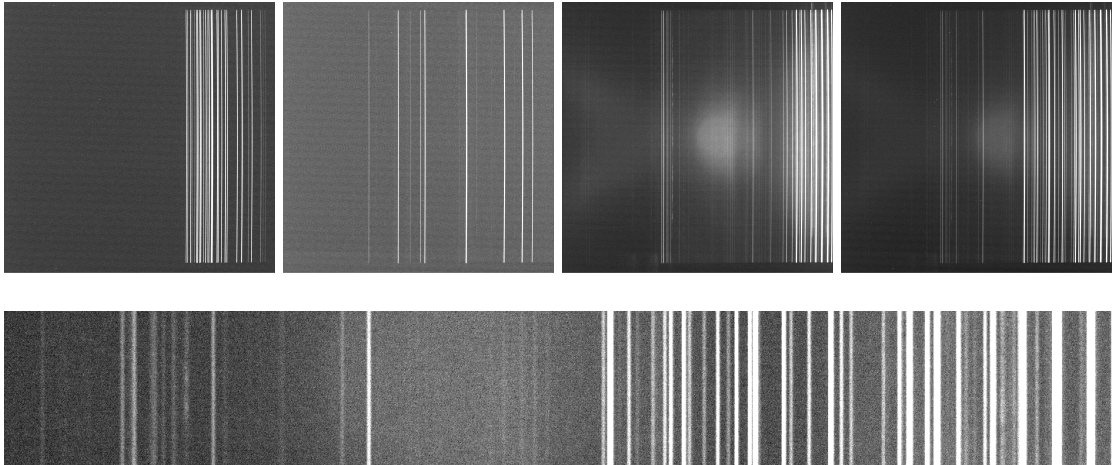


**Figure 5.9:** Top: spectra of the Neon (JKVA0015), Helium (JKVA0016), Argon (JKVA0018) lamps, and the sum of the three used for wavelength calibration. All done with the 1.0 arcsec slit. Below: the region from the summed image that will be used for the calibration in wavelength.

occurs most strongly in the region where the longer wavelengths are dispersed.

Both effects remain fixed while using the same grism, because the spectral resolution of the light in the CCD is the same. Then, we can correct these effects with flat field images, exposing the camera to a comparison lamp. This is known as *flat fielding*.

A tungsten halogen lamp is placed in the light path before the grism, obtaining its continuous spectrum. This procedure has to be done separately for different slits. All the flat field images for each slit, after having been debiased, are averaged into a total flat field. In Fig. 5.7 the averaged flat fields obtained for the slits of 1.0 and 5.0 arcsec are shown.

From these final flat field images, a region of  $1440 \times 200$  pixels is selected (columns 601-2040, rows 901-1100). This region is not totally flat, since there is a variation in the horizontal direction (spectral direction) due to the fact that the lamp spectrum is continuous but not totally flat. The average spectrum of the halogen lamp can be measured compressing the 2-D region into a 1-D row, adding up all the pixels of the same column and dividing by the number of pixels in each column. After that, the spectrum is fitted to a cubic spline of 6 pieces, and then divided by the fit result, to obtain the final flat field. The fitted 1-D row, and the resulting ratio are shown in Fig. 5.8.

This final flat field will be used to divide the spectra of the SNe and the standard stars, eliminating the errors due to the pixel to pixel variation in the CCD camera sensitivity and due to fringing. Note that the flat-fielding correction factor goes from 0.8 to 1.2.

### 5.3.3 Arc fitting

The correspondence between pixels and wavelengths is not strictly linear, it depends on the grism used. The images with the lamps are used to calibrate in wavelength,

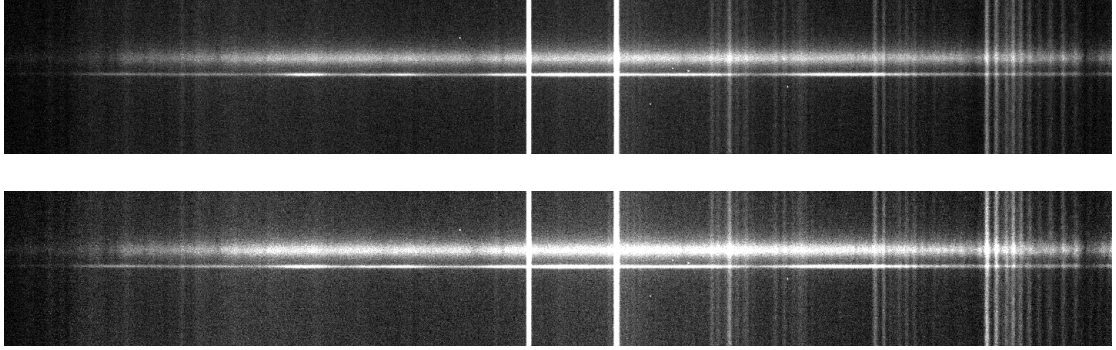


**Figure 5.10:** Region used from image JKVA0186 for the SN2007jh spectrum reduction, before (above) and after (below) the flat field correction. The bright horizontal line in the center of the figures is the SN spectrum, while the bright cloud is the spectrum of the host galaxy. Other lines are due to sky contamination.

since we can match the known emission lines to the pixel column where they appear, and then interpolate the rest of the pixels through a sum of Chebyshev polynomials<sup>4</sup> up to order 5, whose coefficients are saved in a text file in case they are needed afterwards. The images obtained with these lamps are called *arcs*.

Usually, low-pressure lamps are used for this purpose. LRS is equipped with Helium, Argon and Neon lamps for calibration. Since the Helium lamp is fainter compared to the other two, the exposure times with this lamp are longer, or several images have to be taken in order to have similar fluxes, as can be seen in the summary Table A.1. The images with the three different lamps are summed in order to have more emission lines to use in the matching between pixel column and wavelength. As in the flat fields, it has to be done separately for each slit. In Fig. 5.9 the spectra of the three lamps using the 1.0 arcsec slit, the sum of the three, as well as the region of  $1440 \times 200$  pixels (columns 601-2040, rows 901-1100) extracted to use for wavelength calibration of the SNe spectra, are shown.

The emission lines of the three lamps used are known, and the wavelengths are shown in Table 5.1. We will use these numbers to manually fix some of the features and interpolate automatically the rest of the spectrum through IRAF routines.

#### 5.3.4 SN spectra extraction

Once the flat field and the arc images are prepared, we can extract preliminary spectra of the SNe calibrated in wavelengths. Before starting, we average the SN images of the SNe for which we have more than one spectrum, in order to correct for fluctuations.

For the spectral extraction, we also cut a region of  $1440 \times 200$  pixels (columns 601-2040, rows 901-1100) from the SN spectrum image, the same region as in the flat field and arc images. An example of the region extracted is shown in the top image in Fig. 5.10. The first thing we do is to divide all the rows of the SN image by the flat field 1-D spectrum. The result is shown in the bottom image in Fig. 5.10.

<sup>4</sup>A description of the Chebyshev polynomials can be found in §B.1.

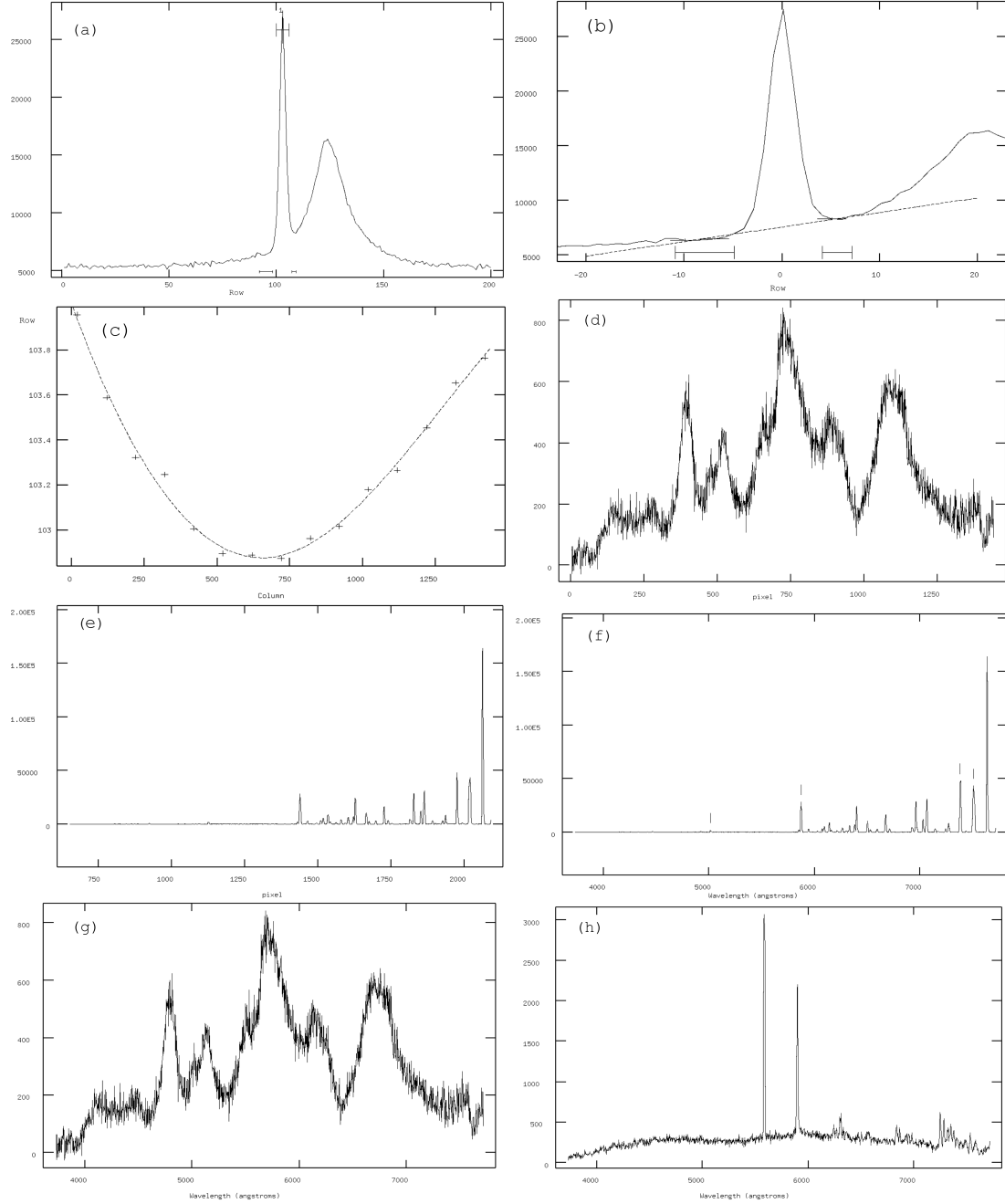


**Figure 5.11:** SN spectrum extraction, step by step. (a) Result of the sum of all columns. The narrow peak is the thin line that can be seen in previous figures corresponding to the rows where the spectrum of the SN is located. The wider peak is the host galaxy. (b) Determination of the background in order to subtract it. (c) Trace of the SN spectrum along the columns. (d) SN spectrum extracted uncalibrated in wavelength. (e) Arc file summed in rows. (f) Arc file calibrated in wavelength, after the manual matching and the interpolation. (g) SN spectrum calibrated in wavelength. (h) Sky spectrum calibrated in wavelength.

Once the SN image is flat-field corrected, we perform a row compression of the image in one column, as shown in Fig. 5.11 (a), which allows us to separate the data corresponding to the SN from the host galaxy light and the sky background. The result of this vertical compression is usually a single peak profile but sometimes, when the host galaxy or other objects are also in this region of the slit, their light is also shown as a wider peak. Since our aim is to extract the SN spectrum, we should determine what is the background in order to subtract it. In Fig. 5.11 (b) the same SN peak is shown, in a zoomed view which emphasizes the background. The two horizontal lines at the bottom define the region where the sky background is being sampled, and the dotted line is the fit to a sum of Chebyshev polynomials of orders one and two, that determines what is signal and what is background. The peak is then cut and treated as if it were alone. Fig. 5.11 (c), shows the position of the SN peak (in row number), along the dispersion (horizontal) direction, known as the trace. IRAF needs to determine its shape to accurately extract the spectrum, in case it were not completely horizontal, which is the case of the example. We can see that the spectrum moves between two rows along the columns. This trace is fitted to a cubic spline of two pieces, which is the function that IRAF will use to extract the spectrum. The information along the pixels in which the peak is located is then spread out in a 1-D file of 1440 columns and only one row. The data obtained is shown in Fig. 5.11 (d), where the vertical axis is not calibrated and is in CCD counts, and the horizontal axis is still the pixel column number.

The next step of the reduction of the SN spectrum is the calibration of the dispersion axis in wavelength. We will use the region of the arc image to perform the correspondence between pixels and wavelength. A similar procedure is performed: all the columns are summed obtaining a 1-D spectrum of the arc, shown in Fig. 5.11 (e). In this spectrum we assign manually a wavelength to some of the peaks, and an interpolation through a sum of Chebyshev polynomials up to order 5 is performed automatically, assigning a wavelength to every column. After this first fit, more wavelengths can be assigned manually, refitting again with the new anchoring points. Two IRAF routines, called *hedit* and *dispcor*, are able to interactively match the peaks to the known wavelengths stored in a text file, and perform the interpolation. Finally, we obtain the correspondence, as shown in Fig. 5.11 (f), and it is used to translate the horizontal axis of the SN spectrum from column number to wavelength. A sky spectrum taken from the border rows of the SN spectrum image is saved as an extension in the same FITS file of the extracted SN spectrum. These two spectra are shown in Figs. 5.11 (g) and (h).

This wavelength calibration only has to be performed once, since the correspondence between columns and wavelength is the same for all images, because we always have used the same grism for all spectra. A text file with the coefficients of the Chebyshev polynomials is created, and then used automatically in the following spectrum reductions.

It is possible to manually check if the wavelength calibration has been done properly. Sometimes, even having made the calibration properly, it may have systematic errors, so that the spectrum could be shifted a few angströms. In order to avoid a shift

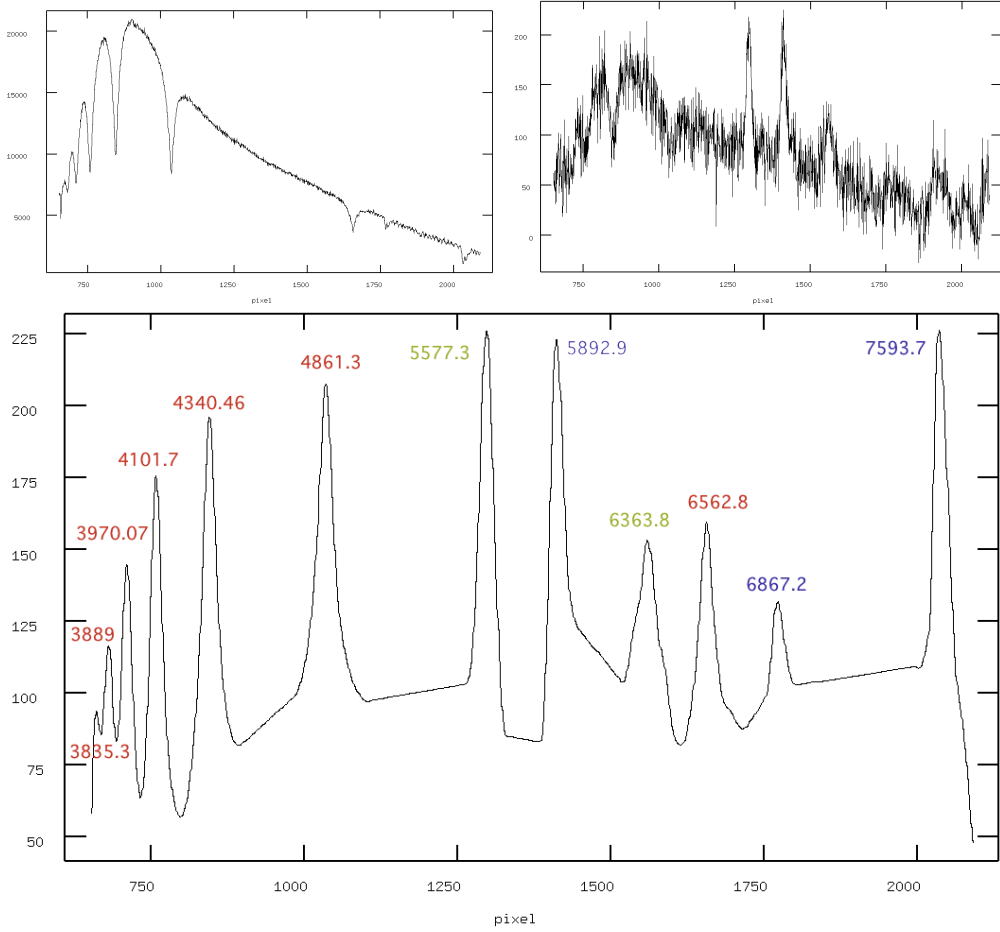


**Figure 5.12:** Top: Reduced spectrum of the standard star G93-48, and the spectrum of the sky obtained from the same image. Below, the spectrum constructed from the two previous images, used for the calibration in wavelength of the standard stars. The wavelength of the peaks (in Å) is given. In blue, the A, B and D Fraunhofer lines ( $O_2$  and Na); in green, telluric lines (O in the atmosphere); and in red, the Hydrogen Balmer lines.

in the calculation, we can edit the sky spectrum, and check the wavelength of the sky emission peaks. If we find a shift in those peaks, we can edit the text file where the Chebyshev coefficients, the range, and the central wavelength are saved, and sum or subtract the shifted angstroms to this last number. As the correspondence between columns and angstroms is the same for all spectra, the shift found is used for all the images.

### 5.3.5 Standard stars extraction

The usefulness of the standard spectra is that they allow the calibration in flux, since these stars are well studied and the density flux as a function of wavelength is well known. A similar procedure as for the SN spectra is done for the reduction of the standard stars spectra. Note that these images are taken with the 5.0" slit since they

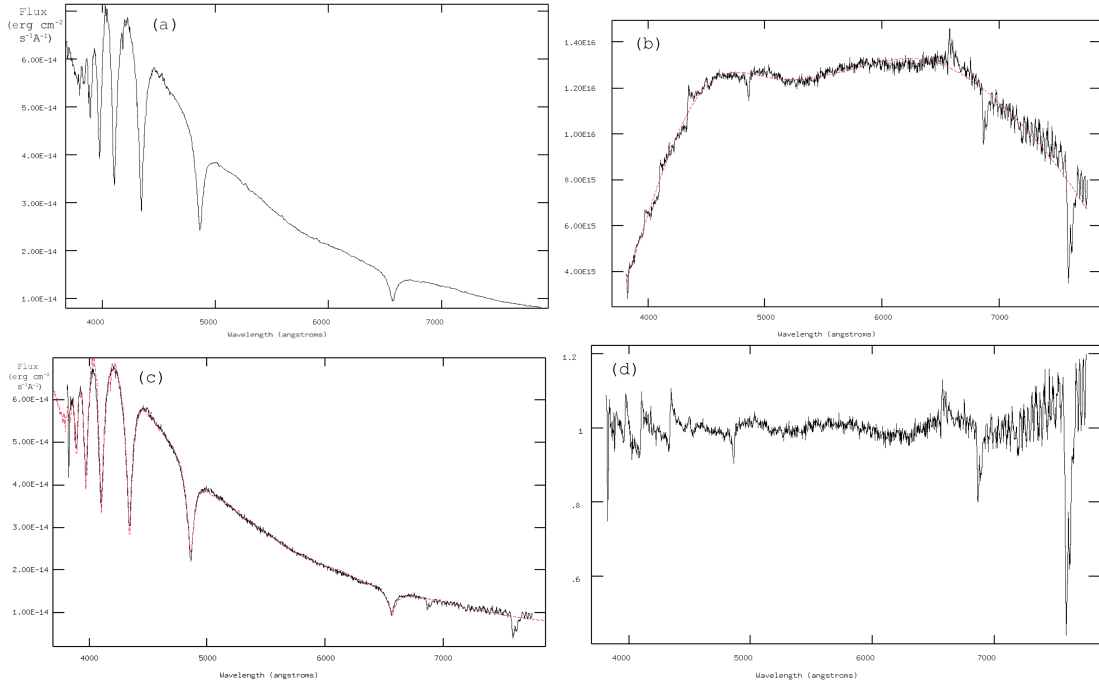


**Figure 5.13:** Obtention of the flux calibration layer. (a) A standard spectrum downloaded from the ESO database. Note the Balmer series absorptions. (b) Ratio between the downloaded and the measured spectra. The fit of a cubic spline of six pieces is shown in red. (c) The downloaded (red) and the measured spectra (black) flux calibrated, are plotted together. The two absorptions at long wavelengths are due to the atmosphere and should be subtracted. (d) The layer with the correction factor that will be used for the telluric lines correction.

are brighter, and the wavelength calibration should be done with the correct arc image. Instead of this, we use an alternative method, which uses the absorptions in the standard spectra and the emission lines of the sky for the calibration in wavelength<sup>5</sup>. Once we have reduced a standard star spectrum in the same way as the SN spectrum, we save a copy of the inverted 1-D spectrum of the standard star and add it to the sky spectrum properly scaled to have the emission peaks of similar size. The result is a curve with known peaks and absorptions, which can be used, as the arc spectra, to transform columns in wavelengths. An image of a reduced spectrum of a standard star, a spectrum of the sky, and the smoothed summed image used for the wavelength calibration of the standard star spectra are shown in Fig. 5.12.

Once calibrated in wavelength, we need the calibration in flux. In the Header Unit of the FITS files for the standards, there is a keyword that gives the name assigned to this star. Once we know what object it is, we can download its flux calibrated spectrum from scientific databases, e.g. the European Southern Observatory (ESO) webpage<sup>6</sup>. We have taken the standard stars images under the same conditions of the SN images, thus with the calibrated standard spectrum we can calculate the factor

<sup>5</sup>Wavelengths of the Hydrogen Balmer series, the Fraunhofer and telluric lines, are listed in Table 5.1.

<sup>6</sup><http://www.eso.org/sci/observing/tools/standards/spectra/stanlis.html>.

**Table 5.1:** Spectral lines of the Hydrogen Balmer series, the sky lines (Fraunhofer and atmospheric), and the three lamps available in LRS, used to calibrate in wavelength the SNe and standard stars spectra. All the wavelengths are in angstroms ( $\text{\AA}$ ).

Balmer	Sky	Neon	Helium	Argon
3835.38	5577.34	6032.1	3888.6	5852.49
3889.05	5892.94	6416.3	4471.5	5944.83
3970.07	6300.30	6752.8	4713.1	6143.06
4101.73	6363.78	6871.3	4921.9	6266.49
4340.46	6867.19	6965.4	5015.7	6334.43
4861.32	7593.70	7147.0	5875.6	6402.25
6562.80		7272.9	6678.2	6506.53
		7384.0	7065.2	6598.95
		7509.3	7281.3	6678.20
		7948.2		6717.04
		8011.5		6929.47
			7032.41	
			7173.94	
			7245.17	
			7438.90	
			7488.87	

between the units of counts in the CCD of our images, and the flux density units of  $\text{erg cm}^{-2}\text{s}^{-1}\text{\AA}^{-1}$ .

An image of one spectrum downloaded from the ESO database is shown in Fig. 5.13 (a). We divide our standard spectrum, calibrated in wavelength, first by the exposure time, and second by the flux calibrated spectrum. The result is fitted to a cubic spline of six pieces (both shown in Fig. 5.13 (b)). The standard spectrum in unit counts is divided by the result of the fit, obtaining the flux calibrated spectrum of the standard star. The comparison between our spectrum and that downloaded from the ESO database is shown in Fig. 5.13 (c). The difference between the two is due to the absorptions in the atmosphere. Dividing the two spectra (Fig. 5.13 (d)), we obtain a layer which will be used afterwards in the telluric correction.

### 5.3.6 Minor corrections

#### Telluric lines correction

All the spectra obtained show absorption lines due to the water, oxygen and carbon dioxide present in the atmosphere. In particular, in the layer factor we obtained comparing the standard star spectrum measured by us to the downloaded from the ESO database, we can see two prominent absorptions at long wavelengths. They have to be removed from the SN and standards spectra, since they do not occur in those objects but in the Earth's atmosphere. What we have to do is divide those SN and standard star spectra by the layer factor. For this, we used an IRAF routine called *telluric* that shifts and scales to best divide out the telluric features from data spectra.

### Heliocentric velocity correction

Another correction to take into account is that due to the motion of the observer in the direction of the observation. We should take into account the proper motion of the Earth, which is rotating on itself (diurnal velocity), with respect to the center of masses Earth-Moon (lunar velocity), around the Sun (annual velocity), and around the galaxy center (solar velocity). All this together causes a Doppler shift in the spectrum.

To apply this correction we need the date and time of the observation, the direction of observation, the location of the observation, and the direction and magnitude of the solar motion relative to some standard of rest. All these parameters can be measured through an IRAF routine called *rvcorrect*, which calculates some of them from keywords available in the Header of the FITS files. Another task called *dopcor*, with the information measured with *rvcorrect*, corrects the shift.

### Vacuum wavelength correction

The spectra of the objects we measured are in air wavelengths, since we observe within the atmosphere. So, we should transform the spectra to vacuum wavelengths, which are slightly longer than those in air. The IRAF task *disptrans* converts the spectrum from air wavelengths to vacuum wavelengths, using the air index of refraction as computed from the formulae in [Allen \(1973\)](#), considering temperature, pressure, and water vapor terms with the standard values being  $T = 15^\circ\text{C}$ ,  $p = 760 \text{ mmHg}$ ,  $f = 4 \text{ mmHg}$ , respectively.

### 5.3.7 Flux calibration of the SNe spectra

The last step in the reduction of the SN spectra is to calibrate them in flux. In order to achieve a proper calibration, we should divide the non-calibrated spectra by their exposure time, thus we obtain the spectra in one-second of exposure. Since the calibration layer measured in §[5.3.5](#) was also for one second exposition, we only have to divide the non-calibrated one second spectra of the object by the calibration layer, to obtain the final spectra in units of density flux. Finally, we extract an ASCII file with two columns, the wavelength in angstroms and the flux in  $\text{erg cm}^{-2}\text{s}^{-1}\text{\AA}^{-1}$ , using the IRAF task *wspectext*. The calibrated spectra of the 23 SNe observed at TNG are shown in Figs. [5.14](#) to [5.19](#).

## 5.4 Supernova Identification (SNID)

The Supernova Identification (SNID) software<sup>7</sup> is able to determine the type, redshift, and age of a SN, using a single spectrum. The algorithm is based on the correlation techniques of [Tonry et al. \(1979\)](#), and relies on the comparison of an input spectrum with a database of high-S/N template spectra. The program was originally written by John Tonry to determine redshifts of Type Ia SNe, and was re-written and expanded by Stephane Blondin to include type and age determination, as well as an interactive plotting package. A description of its operation can be found in [Blondin et al. \(2007\)](#).

---

<sup>7</sup>Publicly available in <http://marwww.in2p3.fr/~blondin/software/snid/index.html>.

**Table 5.2:** Preliminary classification of the spectra given by the SNID software. The epoch is in days respect to the  $B$  maximum brightness.

Day	SDSS SN Id	# spectra	Best-fit template	Temp.	Type	epoch	$z$
Oct 5	SN18408	2	SN93J	IIb		-17	$0.037 \pm 0.011$
Oct 5	SN18321	3	SN04et	IIP		4	$0.102 \pm 0.003$
Oct 5	SN18441	2	SN04et	IIP		1	$0.033 \pm 0.003$
Oct 5	SN17886	2	SN94D	Ia		14	$0.040 \pm 0.003$
Oct 6	SN15892	2	SN86G	Ia-91bg		-3	$0.317 \pm 0.008$
Oct 6	SN14445	2	SN94Q		Ia	12	$0.428 \pm 0.008$
Oct 6	SN18297	2	SN05cs	IIP		5	$0.069 \pm 0.003$
Oct 6	SN17884	2	SN94ae	Ia		9	$0.240 \pm 0.007$
Oct 6	SN18457	2	kcSB3	Galaxy		—	$0.083 \pm 0.003$
Oct 6	SN18109	1	SN04et		IIP	4	$0.066 \pm 0.005$
Oct 6	SN18299	2	SN99em	IIP		6	$0.126 \pm 0.006$
Oct 6	SN17880	1	SN96X	Ia		13	$0.073 \pm 0.005$
Oct 6	SN17784	1	SN96X	Ia		13	$0.038 \pm 0.002$
Nov 3	SN19940	2	SN05hj	Ia		0	$0.154 \pm 0.005$
Nov 3	SN19775	2	SN02bo	Ia		-5	$0.155 \pm 0.005$
Nov 3	SN19953	2	SN99aa	Ia-91T		-1	$0.130 \pm 0.005$
Nov 3	SN20084	1	SN02er		Ia	-8	$0.143 \pm 0.010$
Nov 3	SN19969	1	KcSa	Galaxy		—	$0.000 \pm 0.007$
Nov 4	SN20350	2	SN98bu		Ia	-3	$0.129 \pm 0.005$
Nov 4	SN19992	3	SN04eo	Ia		2	$0.226 \pm 0.007$
Nov 4	SN19658	2	SN96X	Ia		2	$0.204 \pm 0.004$
Nov 4	SN20208	3	SN91T	Ia-91T		11	$0.068 \pm 0.004$
Nov 4	SN19849	2	SN91T		Ia-91T	16	$0.294 \pm 0.019$

We used this code to give a preliminary measurement of these three parameters (type, redshift and age) of the SN spectra reduced. The SNID results are summarized in Table 5.2. Figure 5.20 shows one example of SNID fit and output. The calibrated spectra and the preliminary results were added to the SDSS-II/SNe database, which was available to the whole collaboration for further analyses. The final results after a detailed study of the spectra are given in Table 5.3, resulting in 13 Type Ia SNe, 7 Type II SNe, and 3 untyped.

## 5.4 Supernova Identification (SNID)

---

**Table 5.3:** SN spectra from the TNG in the SDSS-II/SNe database.

SDSS SN Id	Type	IAUC Name	Right Ascension (hh:mm:ss)	Declination (dd:mm:ss)	Redshift	Peak MJD (approx)
SN18408	SNII	2007lj	21:28:41.93	-0:4:2.2	0.05000	54379.0
SN18321	SNII	—	1:55:29.32	+1:9:33.7	0.10410	—
SN18441	SNII	2007lb	3:49:9.53	-0:44:9.2	0.03300	54384.4
SN17886	SNIa	2007jh	3:36:1.54	+1:6:12.1	0.04075	54365.0
SN15892	—	—	—	—	—	—
SN14445	—	—	—	—	—	—
SN18297	SNII	2007ky	1:6:11.53	-0:36:50.9	0.07358	54376.0
SN17884	SNIa	2007kt	1:50:23.96	+1:10:19.5	0.23900	54365.8
SN18457	SNII	2007ll	1:58:40.14	-0:14:56.6	0.08097	54387.0
SN18109	SNII	2007kw	2:10:16.83	-0:15:57.1	0.06805	54376.0
SN18299	SNII	2007kz	3:36:4.58	-0:12:4.3	0.12742	54379.0
SN17880	SNIa	2007jd	2:59:53.37	+1:9:38.5	0.07265	54363.0
SN17784	SNIa	2007jg	3:29:50.81	+0:3:24.6	0.03710	54367.0
SN19940	SNIa	2007pa	21:1:34.45	-0:16:6.6	0.15710	54405.7
SN19775	SNIa	2007pc	21:15:49.46	+0:39:4.6	0.13790	54402.9
SN19953	SNIa	2007pf	22:11:43.32	+0:34:44.7	0.12000	54414.6
SN20084	SNIa	2007pd	23:11:54.07	-0:34:41.1	0.13990	54405.7
SN19969	SNIa	2007pt	2:7:38.51	-0:19:26.4	0.17529	54402.0
SN20350	SNIa	2007ph	20:51:13.40	-0:57:21.0	0.12946	54412.0
SN19992	SNIa	2007pb	23:48:25.00	-1:11:6.0	0.22780	54402.5
SN19658	SNIa	2007ot	0:35:36.77	-0:13:57.7	0.20000	54399.6
SN20208	SNIa	2007qd	2:9:33.56	-1:0:2.2	0.04313	54378.8
SN19849	—	—	—	—	—	—

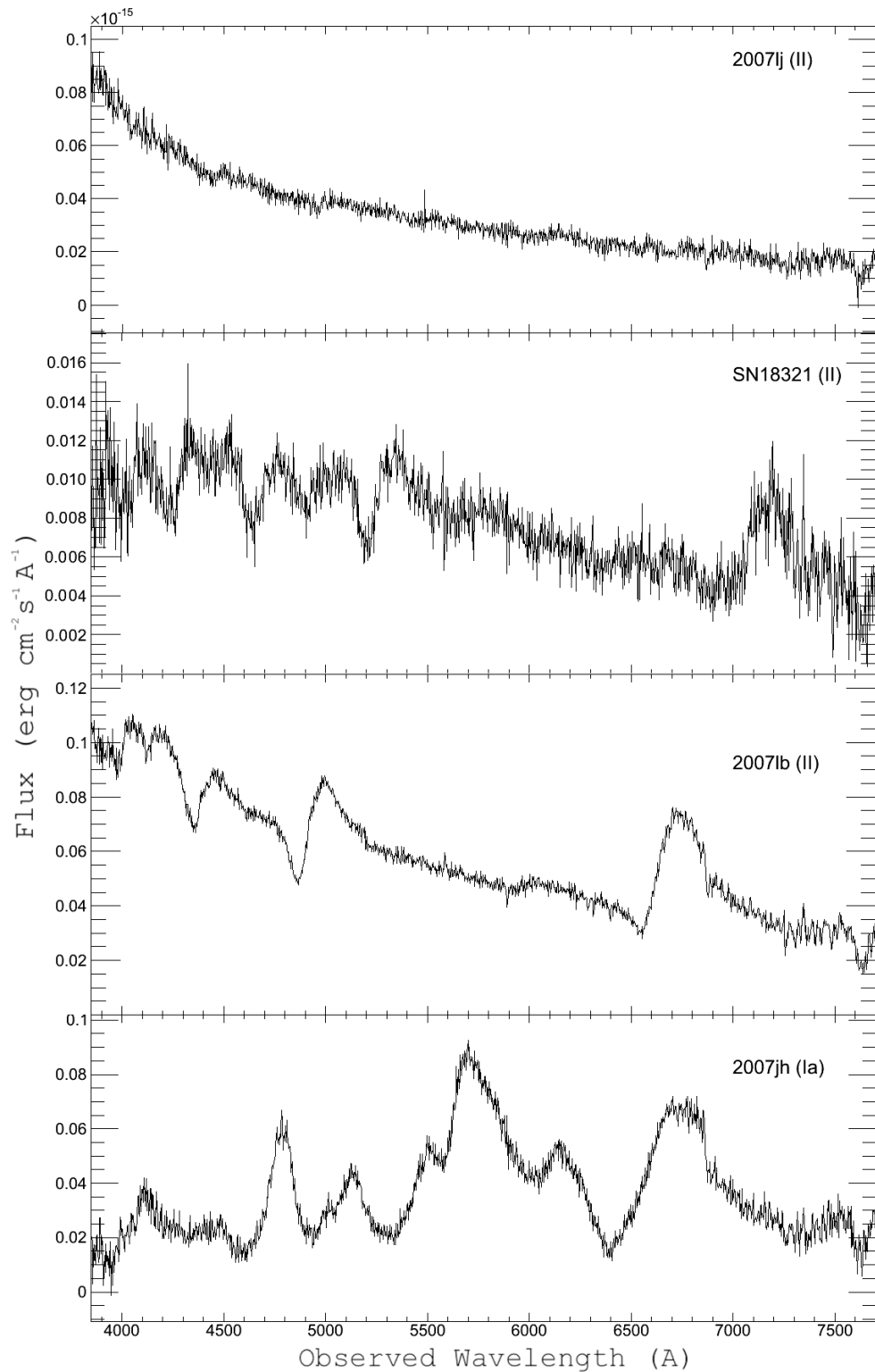


**Figure 5.14:** Calibrated spectra of four SNe observed at TNG. For those SNe which have been named and typed by IAU, a label is shown. If not, the SDSS-name is shown. (1)

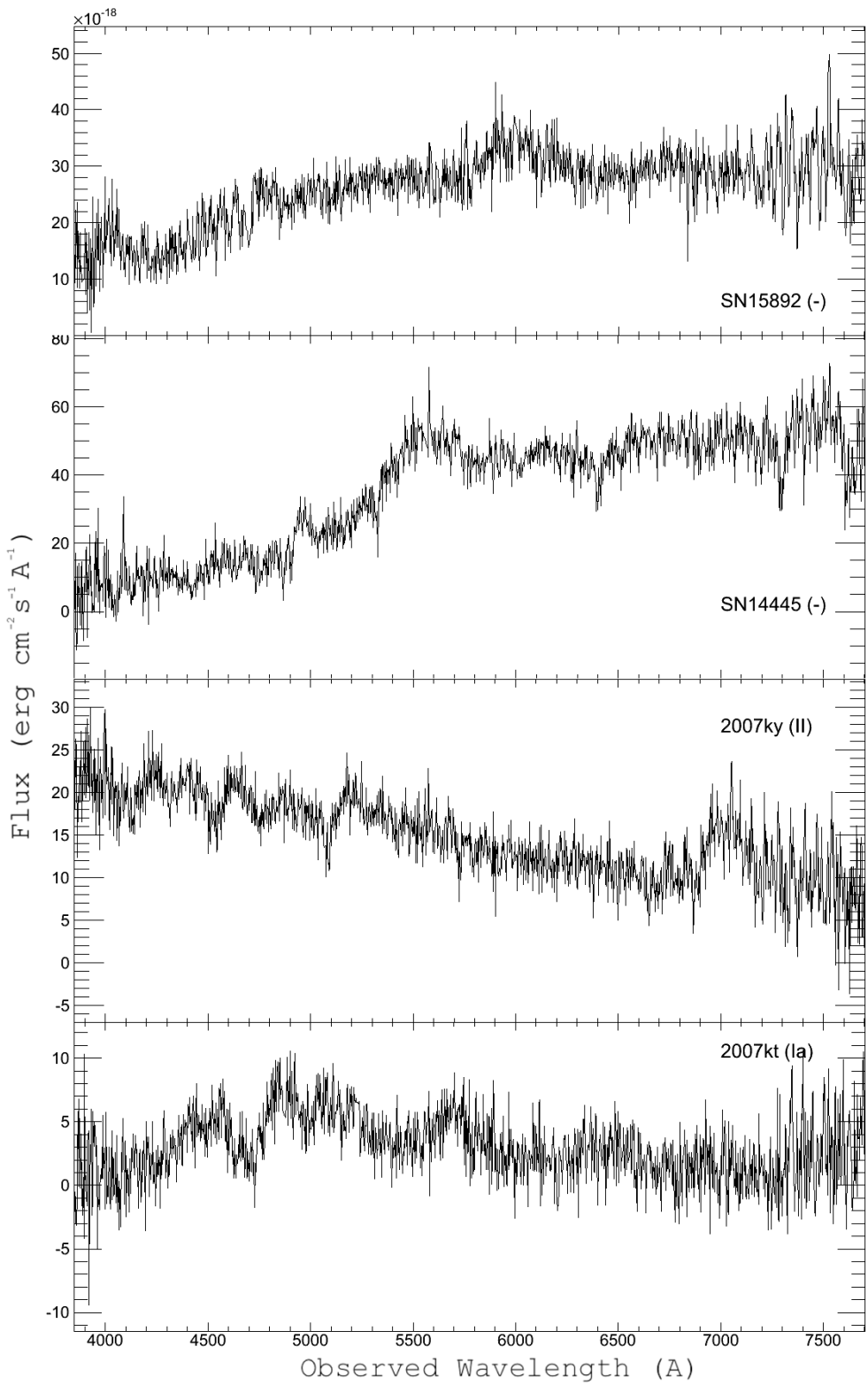


**Figure 5.15:** Calibrated spectra of four SNe observed at TNG. For those SNe which have been named and typed by IAU, a label is shown. If not, the SDSS-name is shown. (2)

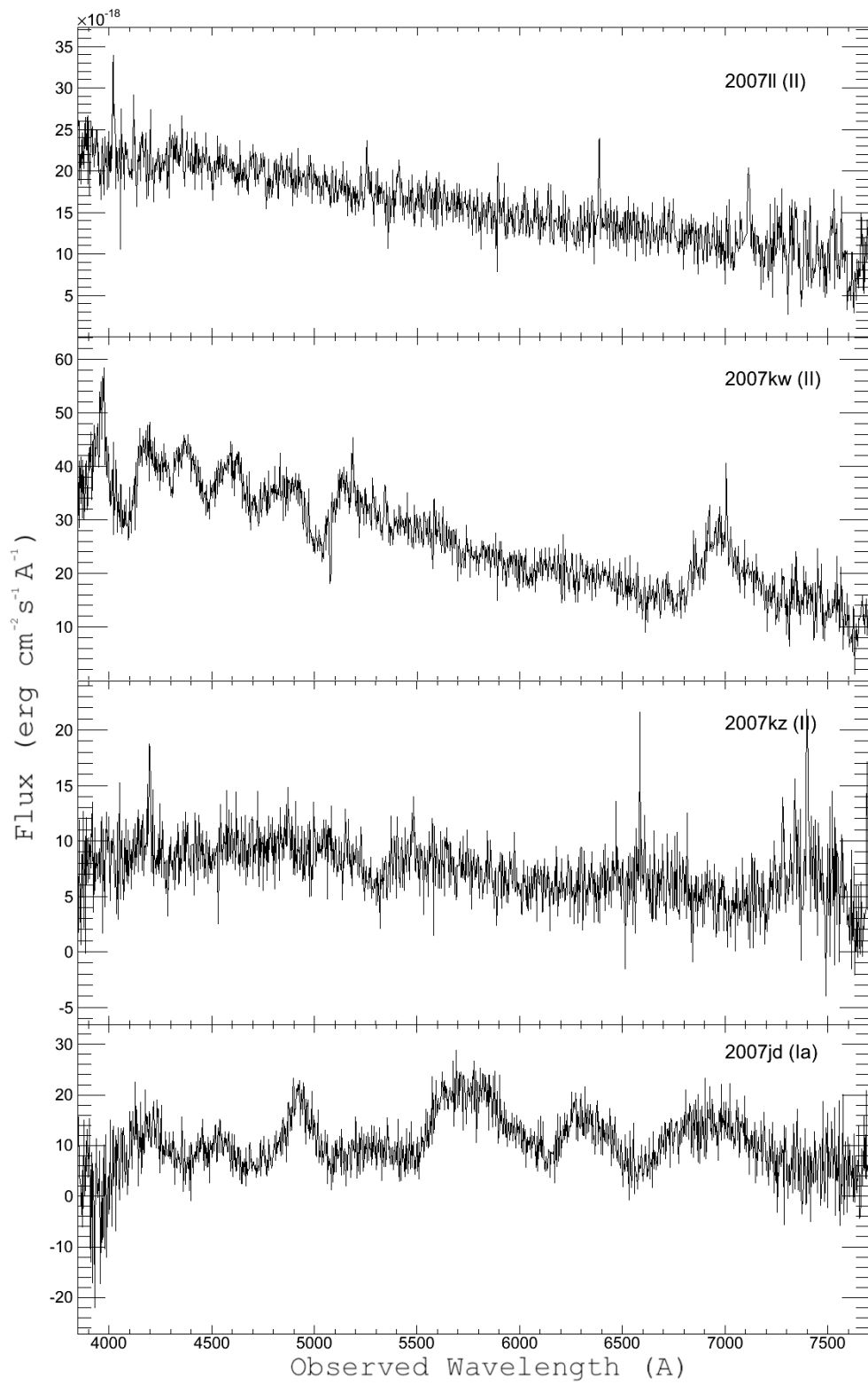


**Figure 5.16:** Calibrated spectra of four SNe observed at TNG. For those SNe which have been named and typed by IAU, a label is shown. If not, the SDSS-name is shown. (3)

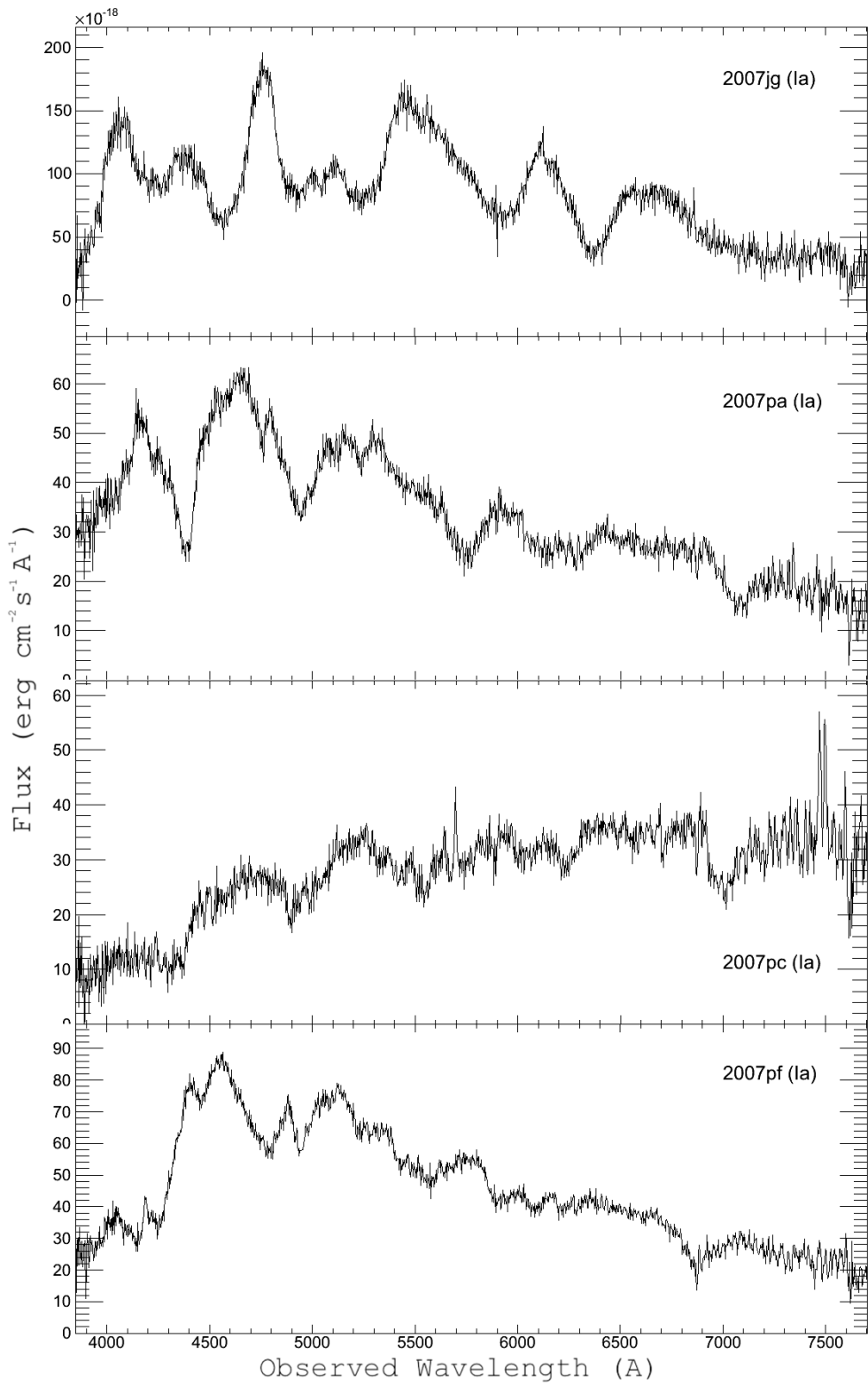


**Figure 5.17:** Calibrated spectra of four SNe observed at TNG. For those SNe which have been named and typed by IAU, a label is shown. If not, the SDSS-name is shown. (4)

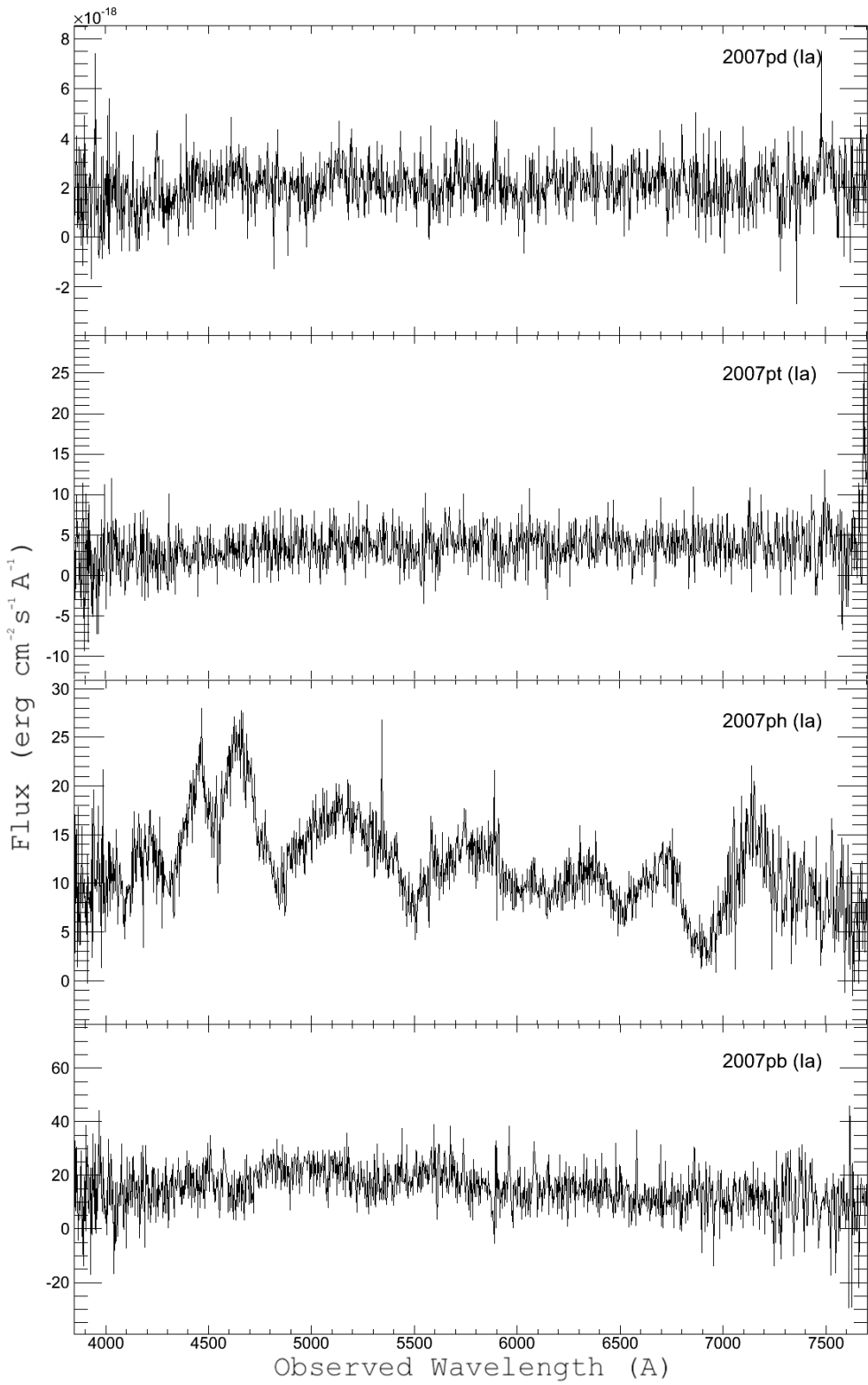


**Figure 5.18:** Calibrated spectra of four SNe observed at TNG. For those SNe which have been named and typed by IAU, a label is shown. If not, the SDSS-name is shown. (5)

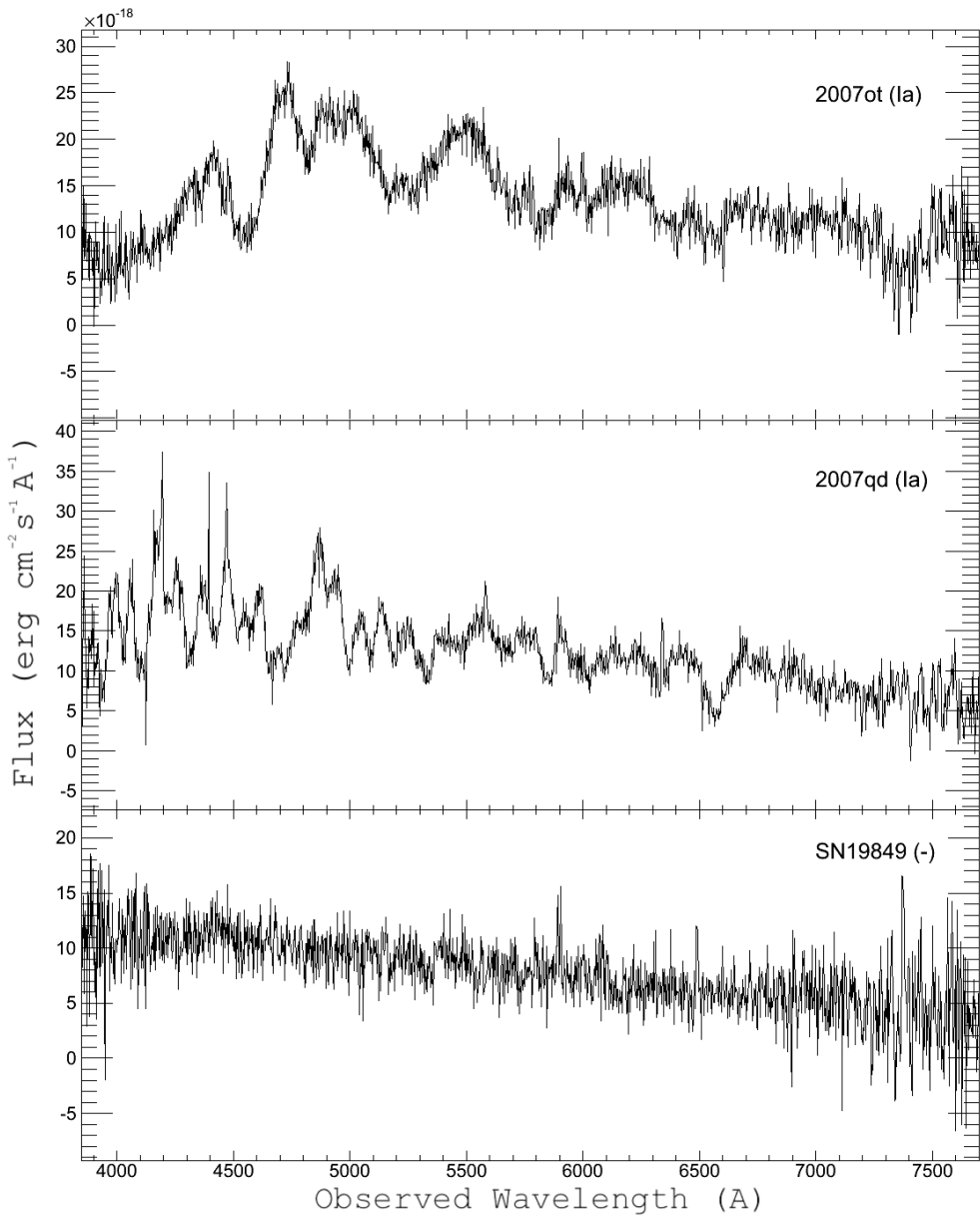


**Figure 5.19:** Calibrated spectra of three SNe observed at TNG. For those SNe which have been named and typed by IAU, a label is shown. If not, the SDSS-name is shown. (6)

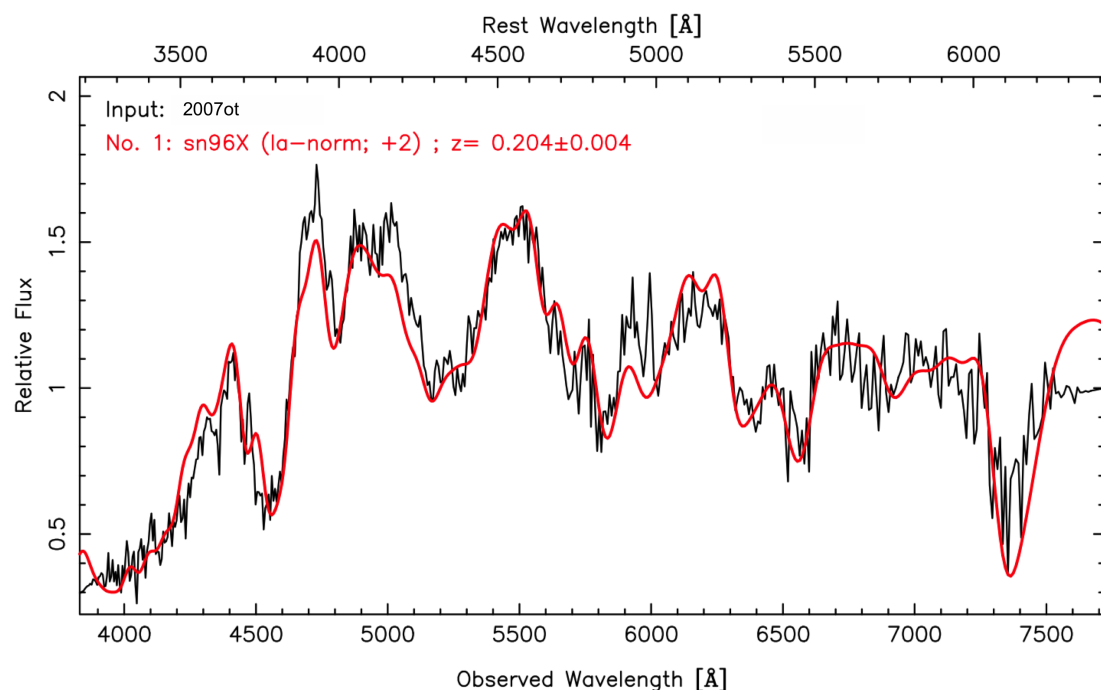


**Figure 5.20:** SNID output of the SN spectra of the SN2007ot obtained on November 4th.

## CHAPTER 6

---

### The Peculiar Supernova 2007qd

---

TYPE IA supernovae (SN Ia) show a range of energies and spectral characteristics, but most of them are quite homogeneous when compared with other supernova types<sup>1</sup>, allowing their use as precise distance indicators. An approach to improve their reliability as distance indicators is to study events that do not conform to the general SN Ia homogeneity in their spectra or luminosity. Subclasses of SN Ia have been determined, such as 1991T-like and SN 1991bg-like<sup>2</sup> events, which were quickly recognized as being peculiar, although much of the spectroscopic diversity is now known to be caused by a range of photospheric temperatures (Nugent et al., 1995). Recently, additional subclasses of SN Ia have been identified. For example, SN 2002ic (Hamuy et al., 2003) and SN 2005gj (Aldering et al., 2006, Prieto et al., 2005) are luminous objects that show hydrogen emission lines in their spectra, unlike normal SN Ia. It is suspected that they may be SN Ia interacting with dense circumstellar material, although a core-collapse scenario has also been proposed (Benetti et al., 2006).

SN 2002cx (hereafter 02cx, Li et al., 2003) was especially peculiar (Filippenko, 2003, Li et al., 2003). It showed a hot (91T-like) spectrum at early times, but it cooled quickly after maximum brightness and its expansion velocities were well below typical for an SN Ia. 02cx deviated significantly from the Phillips (1993) relation between peak luminosity and decline rate. It was subluminous for its light-curve shape by  $\sim 1.8$  mag in the B and V bands. The well-observed SN 2005hk (hereafter 05hk, Phillips et al. (2007)) was spectroscopically very similar to 02cx, both exhibited photospheric velocities of roughly  $7000 \text{ km s}^{-1}$ . Photometrically, 05hk was faint on the Phillips

---

<sup>1</sup>Discussed in §3.3 and §3.4.

<sup>2</sup>See §3.3.

relation by  $0.6 - 1.0$  mag in the optical, but  $\sim 0.5$  mag more luminous than 02cx.

[Jha et al. \(2006a\)](#) have identified several other 02cx-like objects and postulated that their extreme subluminosity suggests that they constitute a class of pure thermonuclear deflagrations: that is, the fusion front moving through the white dwarf fails to make the transition to supersonic burning ([Branch et al., 2004](#)) and is unable to generate the large amounts of radioactive nickel observed in typical SN Ia ([Foley et al., 2009](#)). The thermonuclear burning of carbon and oxygen at moderate densities will create intermediate-mass elements (IMEs) such as silicon, sulfur, and calcium that dominate the spectrum. Though typical SNe Ia experience this phase only briefly, [Jha et al. \(2006a\)](#) reasoned that 02cx-like objects may burn completely via this mechanism. For a list of 02cx-like events, see Table 9 of [Foley et al. \(2009\)](#).

An extremely subluminous transient, SN 2008ha (hereafter 08ha, [Foley et al., 2009](#)), appears to be an additional member of the 02cx class, although [Valenti et al. \(2009\)](#) have proposed that the extreme nature of 08ha (and other 02cx-like objects) is better matched by the core collapse of a massive star where most of the synthesized radioactive elements fall back to a black hole. With the discovery of Si II and S II in the early-time spectra of 08ha ([Foley et al., 2010](#)), that proposition becomes less likely.

SN 2007qd (hereafter 07qd, [Bassett et al., 2007a](#)), labeled by the SDSS-II Supernova Survey (SDSS-II/SNe) as the candidate 20208, of which we have taken the first spectrum at TNG, turned out to be an extremely faint object with physical properties intermediate to those of the peculiar 02cx and the extremely low-luminosity SN 08ha. 07qd was classified as a peculiar Type Ia SN, since the multi-band photometric observations taken at Apache Point Observatory (APO), indicated that it had an extraordinarily fast rise time of  $\gtrsim 10$  days and a peak absolute  $B$  magnitude of  $-15.4 \pm 0.2$  at most, making it one of the most subluminous SN Ia ever observed. After the obtention of its spectrum at TNG, our early notice allowed that other three spectra be obtained in the following days (8, 10 and 15 days after  $B$  maximum light) by other telescopes (HET, KECK and HET, respectively). All of these spectra unambiguously show the presence of IMEs which are likely caused by carbon/oxygen nuclear burning. Near maximum brightness, 07qd had a photospheric velocity of only  $2800 \text{ km s}^{-1}$ , similar to that of 08ha but about 4000 and 7000  $\text{km s}^{-1}$  less than those of 02cx and normal SN Ia, respectively.

A detailed analysis of the 07qd spectra was performed in order to determine its properties. For this, SYNOW ([Fisher et al., 1997](#), [Fisher, 2000](#)), a spectrum synthesis software, was used to reproduce the spectra measured. It was also shown that the peak luminosities of 02cx-like objects are highly correlated with both their light-curve stretch and photospheric velocities. 07qd's strong apparent connection to other 02cx-like events suggests that 07qd is also a pure deflagration of a white dwarf, although other mechanisms cannot be ruled out. It may be a critical link between 08ha and the other members of the 02cx-like class of objects. This work was published in [McClelland et al. \(2010\)](#). This chapter of the thesis draws heavily to that paper.

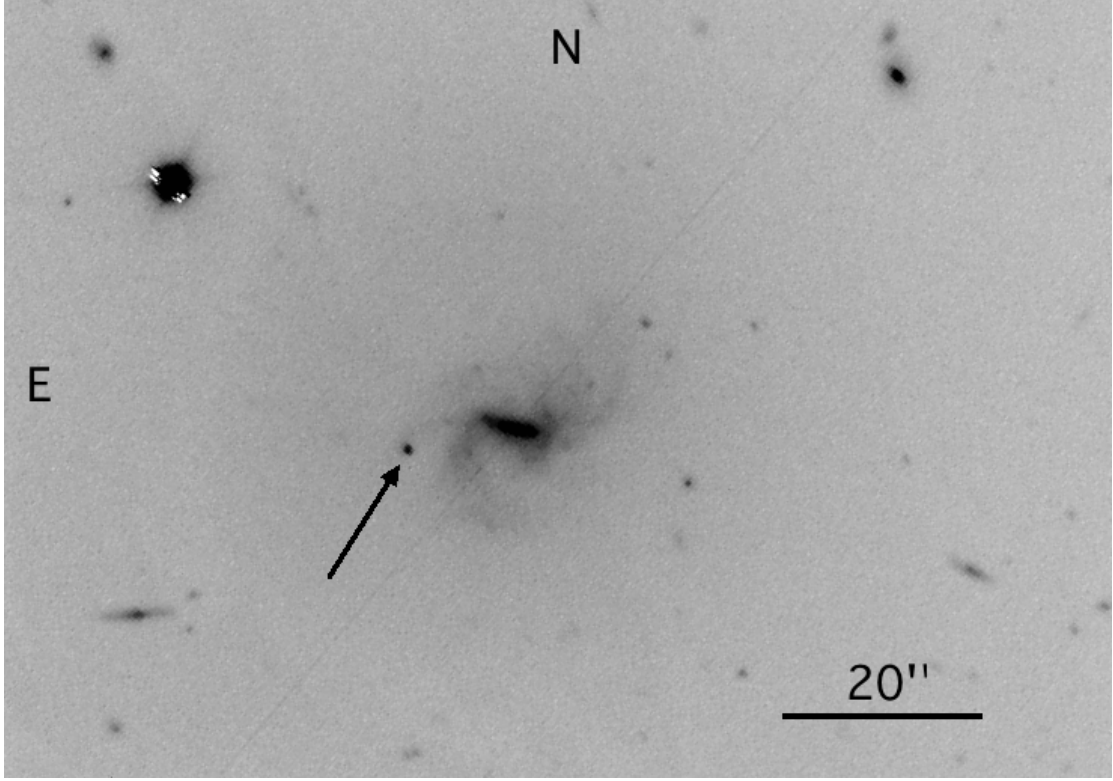


**Figure 6.1:** Image of 07qd (denoted by arrow) relative to its host galaxy in a  $120'' \times 90''$  window. The 90 s unfiltered exposure was taken by us on MJD 54409.08 with the TNG telescope.

## 6.1 Observations

### 6.1.1 Photometry

07qd ([Bassett et al., 2007a](#)) was discovered on October 31st 2007 during the SDSS-II/SNe Survey using the SDSS Camera on the 2.5 m telescope ([Gunn et al., 1998, 2006](#)) at APO. The SN was located amidst a spiral arm at  $\alpha = 02^h 09^m 33^s.56$ ,  $\delta = -01^\circ 00' 02''.2$  (J2000.0), a projected distance of 10.6 kpc from the nucleus of the SBb/SBc host-galaxy SDSS J020932.73-005959.8 centered at  $\alpha = 02^h 09^m 32^s.73$ ,  $\delta = -00^\circ 59' 59''.8$  ([Bassett et al., 2007a](#)). The redshift of the host is  $z = 0.043147 \pm 0.000004$ , as measured from the SDSS galaxy redshift survey ([Adelman-McCarthy et al., 2008](#), [York et al., 2000](#)). Figure 6.1 shows an image of 07qd and its location in its host galaxy, which has a prominent bar and two major spiral arms. The low inclination allows minor spiral arms to be distinguishable, one of which contains the location of 07qd. The classifications of SBb or SBc suggest ongoing star formation, but 02cx-like SNe Ia appear to span a wide variety of galactic morphologies ([Foley et al., 2009](#), [Valenti et al., 2009](#)). The foreground Milky Way extinction in the direction of 07qd is  $E(B - V) = 0.035$  mag as calculated from the dust maps of [Schlegel et al. \(1998\)](#).

The photometry was calibrated in the standard SDSS *ugriz* photometric system ([Fukugita et al., 1996](#), [Smith et al., 2002](#)). The flux from the supernova was estimated

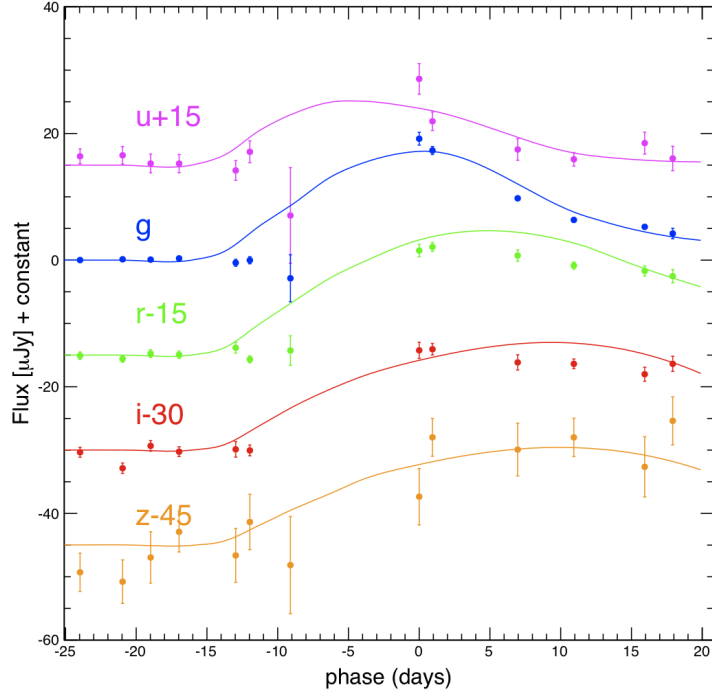


**Figure 6.2:** SDSS apparent light-curves of 07qd given in flux-density units. The lines represent the SDSS light-curve data of 05hk positioned over its maximum brightness epoch. With respect to the early nondetections, 07qd rose faster than other peculiar Type Ia SNe in the  $u$ ,  $g$ ,  $r$ , and  $i$  bands. Neither light-curve has been corrected for host-galaxy extinction.

**Table 6.1:** Observed SDSS photometry for 07qd (SN 20208), converted into fluxes. All measurements are given in  $\mu\text{Jy}$ , and have not been corrected for reddening. Data associated with poor seeing have been omitted from this list.

MJD	$u$ [ $\mu\text{Jy}$ ]	$g$	$r$	$i$	$z$
54346.41	-0.010 ± 2.726	1.620 ± 1.230	0.880 ± 1.235	-0.730 ± 1.281	-1.100 ± 3.851
54348.41	-1.780 ± 1.614	0.610 ± 0.648	1.520 ± 0.698	0.200 ± 1.019	1.600 ± 3.929
54355.42	1.500 ± 2.146	-0.470 ± 0.530	0.410 ± 1.111	-0.370 ± 1.813	5.870 ± 5.868
54358.37	4.310 ± 1.878	0.870 ± 0.530	-0.000 ± 0.707	-1.480 ± 1.159	-1.940 ± 4.186
54365.40	0.000 ± 0.971	-0.180 ± 0.315	0.000 ± 0.496	-1.500 ± 0.719	-1.470 ± 3.225
54381.42	1.400 ± 1.165	0.010 ± 0.362	-0.090 ± 0.590	-0.340 ± 0.790	-4.300 ± 3.010
54384.43	1.550 ± 1.396	0.130 ± 0.393	-0.580 ± 0.557	-2.860 ± 0.817	-5.780 ± 3.438
54386.41	0.260 ± 1.478	0.080 ± 0.489	0.230 ± 0.634	0.670 ± 0.846	-1.960 ± 4.057
54388.42	0.240 ± 1.431	0.270 ± 0.399	0.060 ± 0.587	-0.250 ± 0.779	2.090 ± 3.177
54392.42	-0.840 ± 1.554	-0.420 ± 0.556	1.160 ± 0.837	0.120 ± 1.228	-1.630 ± 4.251
54393.42	2.100 ± 1.731	-0.020 ± 0.564	-0.670 ± 0.546	-0.050 ± 0.850	3.650 ± 4.373
54396.29	-7.950 ± 7.556	-2.870 ± 3.713	0.720 ± 2.329	-	-3.160 ± 7.688
54405.39	13.620 ± 2.416	19.170 ± 1.007	16.510 ± 0.990	15.750 ± 1.281	7.640 ± 4.463
54406.33	6.930 ± 1.466	17.310 ± 0.638	17.080 ± 0.709	15.930 ± 0.912	17.020 ± 2.989
54412.35	2.470 ± 1.702	9.760 ± 0.514	15.720 ± 0.899	13.850 ± 1.204	15.080 ± 4.166
54416.32	0.920 ± 1.072	6.350 ± 0.388	14.140 ± 0.574	13.620 ± 0.769	17.010 ± 3.035
54421.33	3.480 ± 1.736	5.250 ± 0.502	13.290 ± 0.797	11.980 ± 1.110	12.360 ± 4.757
54423.31	1.060 ± 1.924	4.200 ± 0.829	12.460 ± 1.058	13.620 ± 1.197	19.620 ± 3.800
54433.33	-	5.430 ± 1.501	8.780 ± 2.494	9.740 ± 2.832	5.980 ± 6.150

**Table 6.2:** Spectra observation schedule

Telescope	Date	Time [UT]	Days since $B_{max}$	Exposure [s]	Range [\AA]
TNG	5 Nov, 2007	02:06:10	+3	$3 \times 1800$	3673-7401
HET	10 Nov, 2007	04:23:12	+8	1200	4075-9586
Keck	12 Nov, 2007	12:39:01	+10	1500	3073-8800
HET	17 Nov, 2007	03:58:29	+15	1200	4074-9586

by using the scene modeling technique (Holtzman et al., 2008) from individual calibrated images and without spatial resampling. Figure 6.2 shows the 07qd light-curves in the  $ugriz$  bands. The data are listed in Table 6.1. The time of peak bolometric flux for 07qd is not well defined, but probably occurred within a span of 2 days around maximum apparent  $g$ -band magnitude  $20.69 \pm 0.06$  mag on MJD 54405.39. We base this on both the available  $u$ ,  $g$ , and  $r$  data detected on that date, and the fact that the  $u$  and  $g$  fluxes were falling while the  $r$ ,  $i$ , and  $z$  fluxes were still rising.

Bassett et al. (2007a) noted that the spectrum of 07qd was similar to that of 05hk, so comparing their light-curves, we can see that while the maximum  $g$ -band apparent magnitude of 05hk was  $g = 16.32 \pm 0.02$ , it achieved a peak  $B$ -band absolute magnitude of  $M_B = -18.0 \pm 0.3$ . This is rather dim for a typical SN Ia ( $M_B \sim -19$  mag), but  $\sim 2.6$  mag brighter than 07qd (see §6.2.1). Featured in Fig. 6.2 are the 05hk light-curves for the same filters, using SDSS and CSP photometry (Phillips et al., 2007). Ignoring possible differences in dust extinction, 05hk is more luminous than 07qd in all of the SDSS bands, and 05hk both rose and declined more slowly in  $u$ ,  $g$ , and  $r$  than 07qd, whose light-curves are similar to those of 08ha (Foley et al., 2010, 2009). The light-curve widths of the two supernovae are similar at near-infrared wavelengths (SDSS  $i$ ,  $z$ ), though 07qd shows a very slow decline rate at red wavelengths. 05hk also appears to peak later than 07qd as the bandpass becomes progressively redder.

The colors of normal SN Ia are fairly well established (Phillips et al., 1999, Riess et al., 1996) and are used to estimate the reddening caused by dust in the host galaxy. However, the intrinsic colors of peculiar 02cx-like events are uncertain, making the estimation of host-galaxy extinction problematic. Figure 6.3 compares the color evolution of 07qd to that of 05hk, and reveals the former to be bluer near maximum brightness. This suggests that dust extinction is not the major cause of the low luminosity of 07qd compared with 05hk. Additionally, 07qd appears to decline slower in the  $i$  and  $z$  light-curves.

### 6.1.2 Spectroscopy

Apart from the 07qd spectrum obtained at TNG<sup>3</sup> three days after  $B_{max}$ , three more spectra were obtained at different epochs. The Hobby-Eberly Telescope (HET) at the McDonald Observatory in Texas collected 20 minute exposure times spectra utilizing

<sup>3</sup>A detailed description of the instrument and the spectra can be found in §5

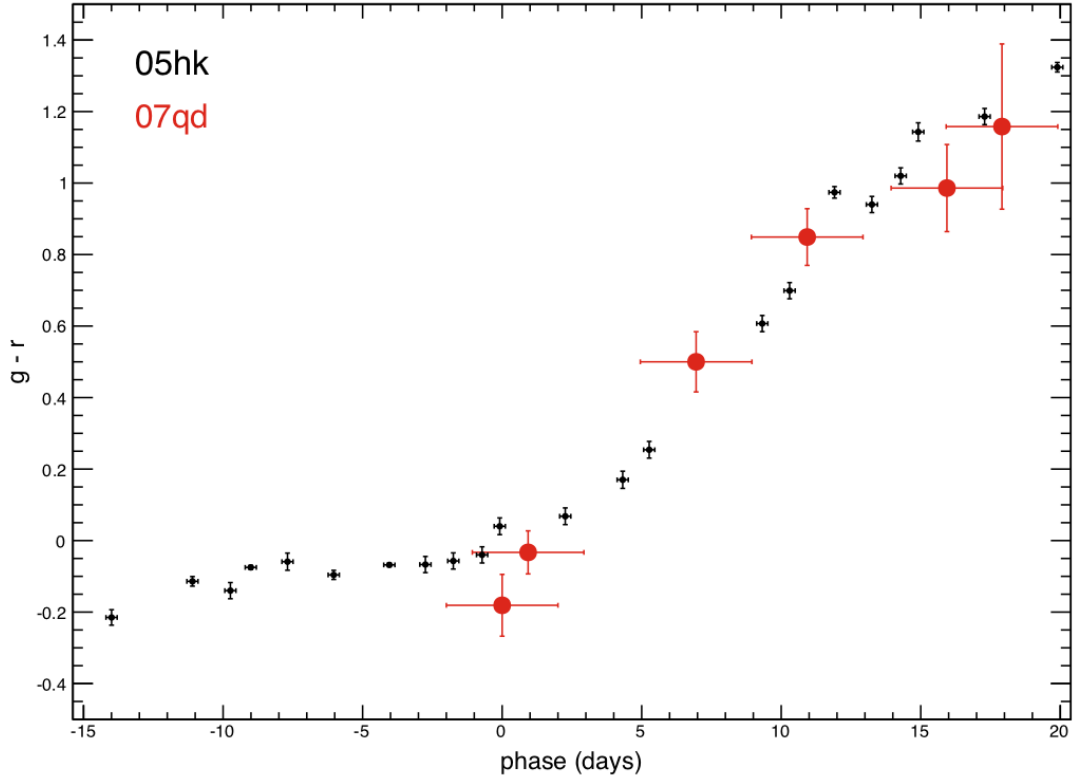


**Figure 6.3:**  $g - r$  color of 05hk and 07qd for the first three weeks past maximum brightness. The large uncertainty in the phase of 07qd stems from the two-day uncertainty in the time of maximum. Neither SN has been corrected for reddening.

the Marcario Low Resolution Spectrograph (LRS; [Duenas et al. \(1998\)](#)) at 8 and 15 days past maximum. At the prime focus, the LRS employed a  $0.^{\prime\prime}235 \text{ pixel}^{-1}$  plate scale with a  $1.^{\prime\prime}$  wide by  $4.^{\prime}$  long slit and covered the  $4075\text{-}9586 \text{ \AA}$  range, though low signal-to-noise ratios severely limit visibility past  $8000 \text{ \AA}$ . A low-resolution spectrum at 10 days past maximum brightness was also obtained with the Low Resolution Imaging Spectrometer (LRIS; [Oke et al. \(1995\)](#)) on the 10 m Keck-I telescope on Mauna Kea, Hawaii. The Keck measurement was able to cover bluer wavelengths than the other observations, spanning the  $3073\text{-}8800 \text{ \AA}$  range. For all spectra, standard CCD processing and spectrum extraction were performed with IRAF<sup>4</sup>. A journal of the spectroscopic observations is given in Table 6.2, and the resulting extracted and reduced spectra are in Fig. 6.4.

<sup>4</sup>See §5.3.

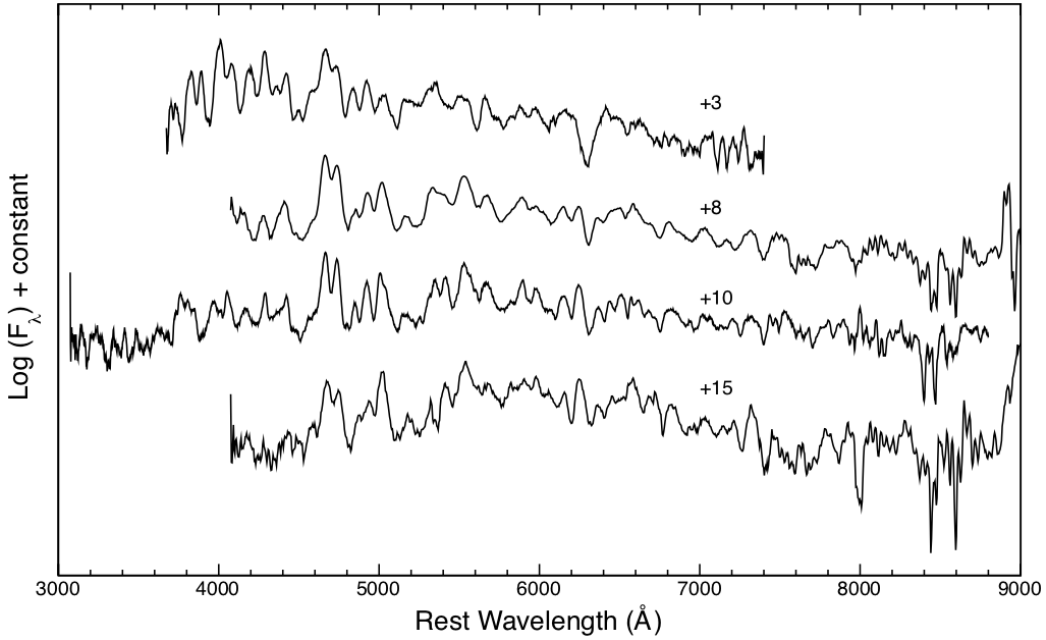


**Figure 6.4:** Temporal evolution of the spectrum of 07qd with a boxcar smoothing of 3 pixels in order to clearly show major features. Times in this figure are given in days past  $B$ -band maximum, telluric absorption has been removed, and wavelengths have been corrected to the SN rest frame. No extinction corrections have been applied.

## 6.2 Analysis

### 6.2.1 Light-curves

We infer a rise time of  $10 \pm 2$  days based on the nondetections in the SDSS-II data, much shorter than that of typical SN Ia (Hayden et al., 2010). We began our analysis by applying the light-curve fitters MLCS2k2 (Jha et al., 2007) and SALT2 (Guy et al., 2007) to the 02cx, 05hk, 07qd and 08ha data using the SNANA platform (Kessler et al., 2009b). The resulting fits, shown in Figs. 6.5 and 6.6 for MLCS2k2, were of very poor quality, with  $\chi^2/\text{dof}=312.8/110$ ,  $203.1/36$ ,  $117.3/67$  and  $103.9/69$  respectively. For 07qd and 08ha, the SNANA results correctly point to underluminous events (large  $\Delta$ ), while for 02cx and 05hk the high  $\chi^2/\text{dof}$  suggests the inability of these algorithms, trained on normal events, to fit the colors and light-curve shapes of 02cx-like peculiar supernovae.

We decided to take a simpler approach and estimate the  $B$ -band light-curve stretch (Goldhaber et al., 2001) versus peak brightness for the peculiar events and some normal SNe Ia. We used SNANA to convert from  $ugriz$  to the standard  $UBVRI$  for all SDSS-II SN Ia with  $z < 0.12$  (see Sako et al. (2008) for a list of these SNe), verifying the accuracy campaign with the conversions of Fukugita et al. (1996). SNANA applies the MLCS2k2 K-correction algorithm, which is based on a color-matched normal SN Ia spectral energy distribution (SED). This may introduce small errors due to differences in the spectral features between 07qd and typical SN Ia.

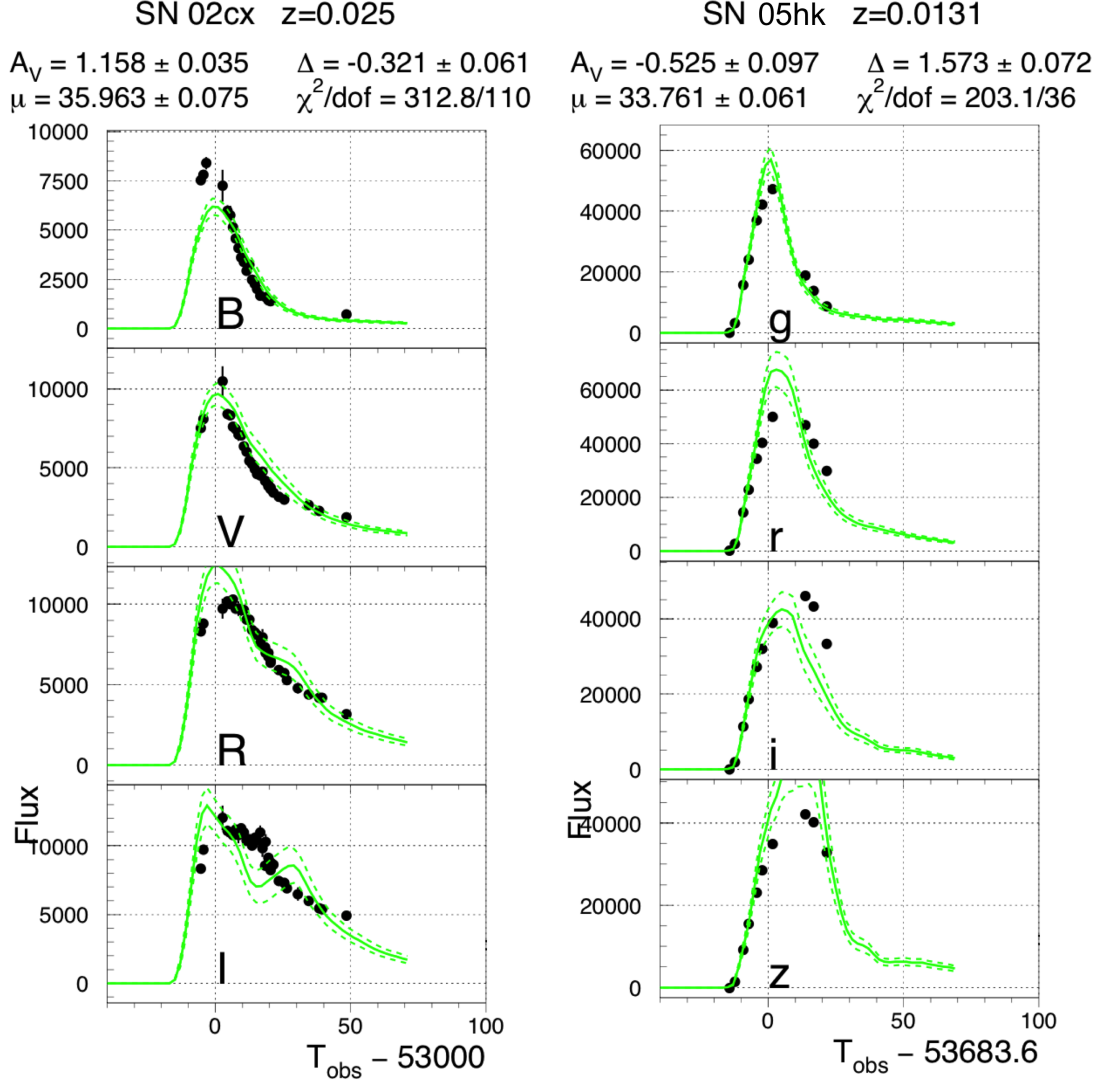


**Figure 6.5:** SNANA fits for the 02cx and 05hk events. The MLCS2k2 fit for 02cx gives a negative (bright)  $\Delta$  with a high extinction. For 05hk, MLCS2k2 gives a positive (faint)  $\Delta$  and negative extinction. The two fits have reduced  $\chi^2$  greater than 2.5.

For 07qd, we find a maximum absolute magnitude (after correcting only for Milky Way extinction) of  $M_B = -15.4 \pm 0.2$  mag. We estimate that the time of peak  $B$  brightness occurred on MJD  $54405 \pm 2$ , though the true value could be smaller due to the lack of data on the rise. The slopes of the blue light-curves of 07qd flatten out rapidly after 10 days. Consequently,  $\Delta m_{15}(B) \sim 1.5$  mag for 07qd, or roughly the same as that of 05hk (Phillips et al., 2007). As seen in Fig. 6.2, 07qd clearly fades more quickly than does 05hk, suggesting that in this case, the measurement of  $\Delta m_{15}(B)$  does not compare well with other SN Ia.

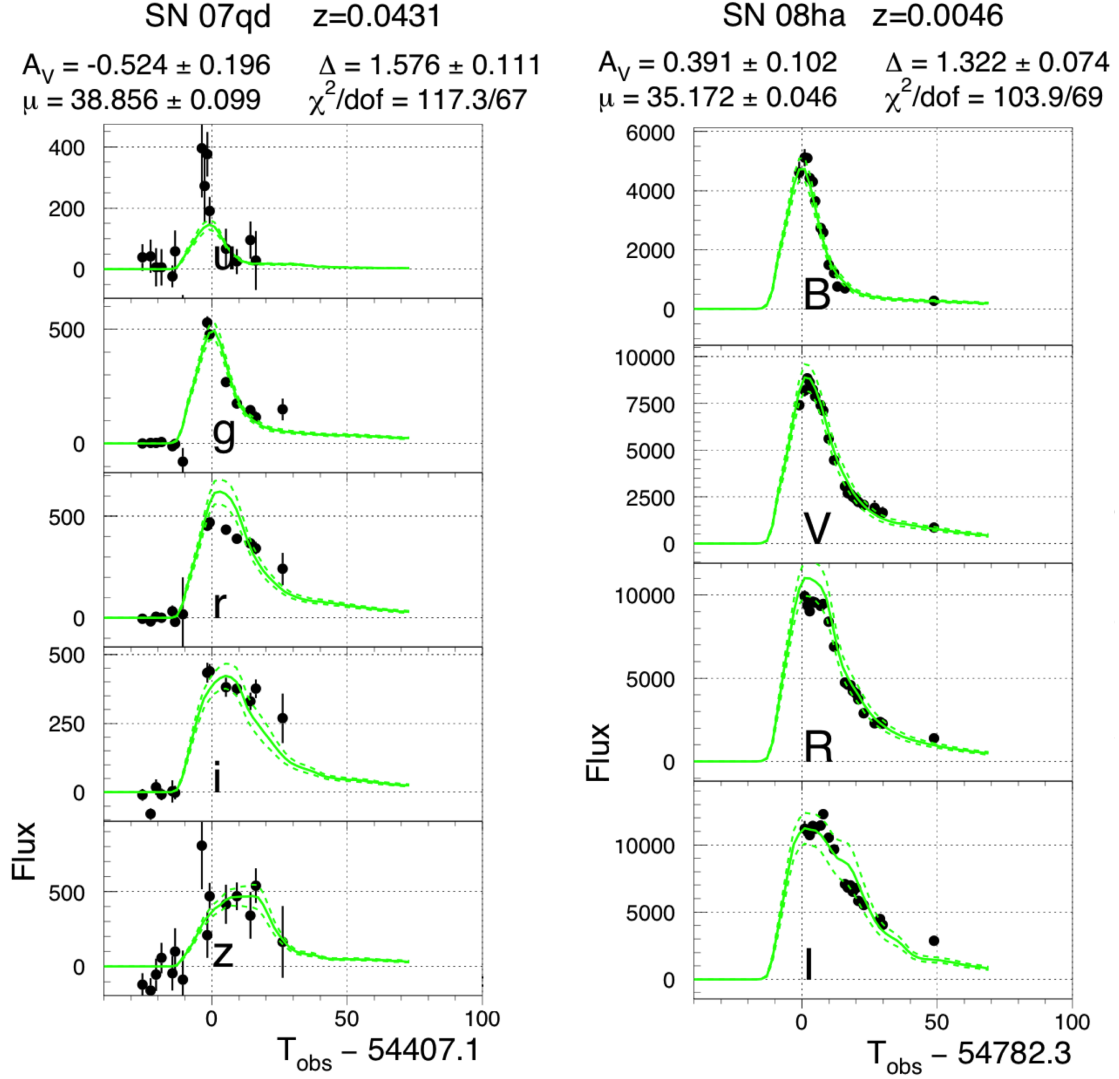


**Figure 6.6:** SNANA fits for 07qd and 08ha events. The MLCS2k2 fits for both SNe give a positive (faint)  $\Delta$ . The two fits have reduced  $\chi^2$  greater than 1.5.

Based on our estimation of the rise time, Fig. 6.7 compares the absolute magnitude of 07qd and its  $B$ -band stretch with those of 02cx, 05hk, 08ha, and the normal SDSS-II SN Ia with  $z < 0.12$ . The low-redshift set of SDSS-II contains a handful of 91bg-like events with stretch parameters  $\sim 0.8$ , but 07qd and 08ha have narrower light-curves and are much fainter. There appears to be a sequence connecting the bright, peculiar events 05hk and 02cx to the extreme 08ha with the intermediate 07qd in Fig. 6.7.

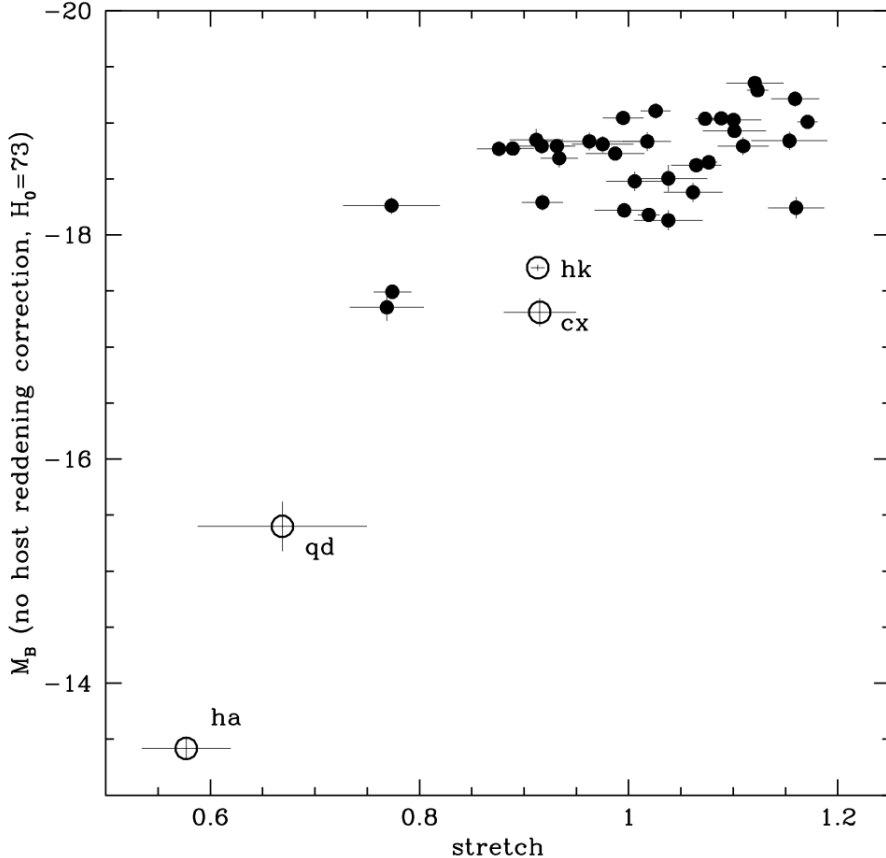


**Figure 6.7:** Light-curve stretch factors are compared to the absolute magnitudes of peculiar SN Ia (open circles) along with SDSS-II SN Ia at  $z < 0.12$  (Frieman et al., 2008b, Sako et al., 2008). Maximum  $B$  for 07qd is based on an estimated 10 day rise time. No correction for host-galaxy extinction has been made. Figure from McClelland et al. (2010).

### 6.2.2 Spectroscopy

We used SYNOW (Fisher et al., 1997, Fisher, 2000), a parameterized supernova spectrum synthesis code, to fit our spectra to profiles of various ions at specific velocities, excitation temperatures, and opacities. These ions are simulated in a spherical expanding photosphere of a chosen blackbody temperature, where the absorptions are formed by resonance scattering (treated in the Sobolev approximation<sup>5</sup>), and the resulting spectra can be compared with data.

The first version of SYNOW is based on code written by D. Branch (Branch et al., 1985, 1983), then updated by A. Fisher in the early 1990's (Fisher et al., 1995). One has to provide some input parameters, such as the expansion velocity of the photosphere ( $v_{\text{phot}}$ ), the blackbody temperature of the continuum emitted from the photosphere ( $T_{\text{bb}}$ ), the wavelength range to be considered, and the precision of the output synthetic

<sup>5</sup>The Sobolev approximation assumes that the rapid expansion of the atmosphere dominates radiative transport. See Jeffery (1990).

**Table 6.3:** SYNOW Parameters for Fig. 6.8 (3 days after  $B$ -max), using a photospheric velocity ( $v_{\text{phot}}$ ) of 2800 km/s and a black-body temperature ( $T_{\text{bb}}$ ) of 10000 K. Velocities ( $v_{\text{min}}$ ,  $v_{\text{max}}$ , and  $v_e$ , described in §6.2.2) are given in units of 1000 km/s and  $T_{\text{exc}}$  values are given in units of 1000 K.

Ion	$\tau$	$v_{\text{min}}$	$v_{\text{max}}$	$v_e$	$T_{\text{exc}}$
C II	0.002	2.8	$\infty$	1	10
C III	0.5	5.0	8.0	2	10
O I	9.5	2.8	6.5	3	10
O III	1.8	2.8	$\infty$	1	10
Na I	0.5	2.8	4.5	1	10
Na I	0.3	4.5	8.0	4	10
Na I	0.1	8.0	10.0	2	10
Mg I	0.5	2.8	$\infty$	2	12
Al I	3.0	2.8	$\infty$	1	10
Si II	3.0	2.0	$\infty$	1	8
Si III	2.0	2.8	$\infty$	1	10
S II	2.7	2.8	3.3	2	10
Ca I	2.0	5.0	$\infty$	1	10
Ca II	10.0	2.8	3.0	2	12
Ti I	1.0	2.8	$\infty$	1	10
Cr I	2.0	2.8	4.0	2	10
Fe III	0.7	2.8	$\infty$	1	10
Fe II	1.0	2.8	$\infty$	1	10
Co II	3.0	2.8	$\infty$	1	10

spectrum. Then, for each ion, one can tune the ionization stage, the optical depth in the strongest optical line of the ion ( $\tau$ ), the velocity range in the envelope where the ion is present ( $v_{\text{min}}-v_{\text{max}}$ ), the e-folding velocity at which the optical depths of the lines are assumed to fall off exponentially a factor  $e$  ( $v_e$ ), and the excitation temperature of the ion ( $T_{\text{exc}}$ ). SYNOW uses an extensive database of 40 million atomic transitions provided by Kurucz ([Kurucz et al., 1995](#)) to simulate the ions in the photosphere. The output from SYNOW provides three columns that determine the synthetic spectrum: wavelength, relative flux, and blackbody flux.

We systematically fit our spectra with ions commonly seen in SN Ia at similar epochs (Fe II, Co II, Si II; see [Hatano et al. \(1999\)](#) and [Maeda et al. \(2010\)](#) for lists of expected ions and isotopic yields), and attempted to simulate hydrogen and helium to rule out the possibility of a Type II or Ib SN. The photospheric velocity was fixed at each epoch by the best fit for the Fe II lines, and subsequent elements were fit either residing in that photosphere or at detached velocities. After confirming the presence or absence of these species, we tried to fit elements uncommon to normal SN Ia in order to fit any remaining line profiles.

#### 6.2.2.1 +3 day spectrum

Figure 6.8 and Table 6.3 present the results of our SYNOW fit to the spectrum three days after maximum brightness, as well as a decomposition of the fit to show the

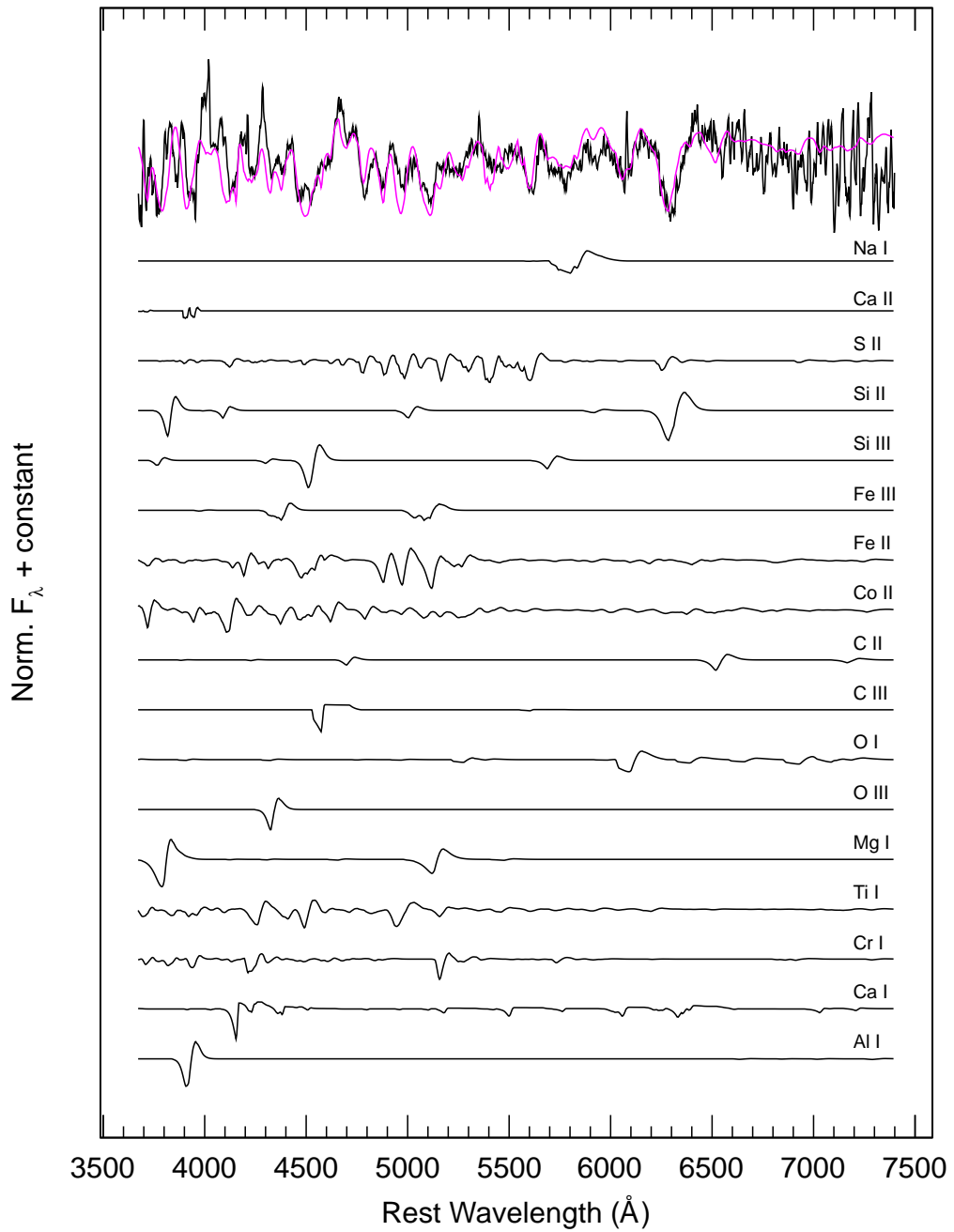


**Figure 6.8:** Spectrum of 07qd at 3 days past maximum (top) and the best SYNOW fit (purple line). The contribution of each individual species is also shown. All spectra have been normalized to the radiation of a black-body at 10000 K, while the data and combined fit have been scaled up by a factor of 2 for clarity. Our more confident identifications are presented near the top while lines at the bottom are less likely.

**Table 6.4:** SYNOW Parameters for Fig. 6.9 (8 days after  $B$ -max), using a photospheric velocity ( $v_{\text{phot}}$ ) of 2800 km/s and a black-body temperature ( $T_{\text{bb}}$ ) of 9000 K. Velocities are given in units of 1000 km/s and  $T_{\text{exc}}$  values are given in units of 1000 K.

Ion	$\tau$	$v_{\text{min}}$	$v_{\text{max}}$	$v_e$	$T_{\text{exc}}$
C III	0.4	2.8	$\infty$	5	9
O II	0.4	2.8	$\infty$	5	9
O III	1.0	2.8	$\infty$	1	9
Na I	0.3	2.8	4.0	2	9
Na I	0.2	4.0	7.0	8	9
Na I	0.2	7.0	10.0	3	9
Si II	2.0	2.8	3.5	2	9
Sc II	1.0	2.8	$\infty$	1	9
Fe II	2.0	2.8	$\infty$	1	9
Co II	5.0	2.8	$\infty$	1	9

influence of each ion. We found from the Fe II lines a photospheric velocity of 2800 km s<sup>-1</sup> (Branch, 1977), which is extraordinarily low since typical SN Ia photospheric velocities at this epoch are often in excess of 10,000 km s<sup>-1</sup> (Branch, 1981, Pskovskii, 1977). The low velocities found for most of the regions make it highly unlikely that the strong feature at 6300 Å is from hydrogen or helium either in the photosphere or detached. The best fit to the 6300 Å absorption was Si II, since the velocity of Fe II was constrained when fitting the ~6100 Å, ~6200 Å, and ~6400 Å features as well as others in the bluer spectral regions. Si II fits the absorption best when at a velocity of 800 km s<sup>-1</sup> lower than that of the iron-group ions. Also prominent in the ~6100 Å region is a broad primary O I line. The secondary signatures of O I are weakly detected at ~5300 Å, but masked at ~6400 Å due to the strong Si II feature nearby.

Si III and C III were implemented in a manner similar to that used by Chornock et al. (2006) to help Co II shape the area around ~4600 Å. C II, also present in the maximum-light spectrum of 08ha (Foley et al., 2010), was necessary for an absorption feature at ~6550 Å. Our SYNOW fits suggest the presence of Mg I, Ti I, Cr I, Ca II, and Al I. Hatano et al. (1999) do not predict these species in a thermonuclear explosion when Si III is strong. It is likely that the features we attribute to these ions are due to other unidentified species or different velocities for existing ones, though we cannot definitively rule out these unusual identifications. It should also be noted that C I, O II, Ni II, and Co III, predicted by Hatano et al. (1999), may be added with little effect on the overall fit. We were unable to fit the absorption between 3800 and 3900 Å at this photospheric velocity with anything other than K II, though its inclusion would introduce other discrepancies to the fit.

### 6.2.2.2 +8 day spectrum

Figure 6.9 and Table 6.4 present the results of our SYNOW fit to the spectrum eight days after maximum brightness, as well as the influence of each ion separately. Most

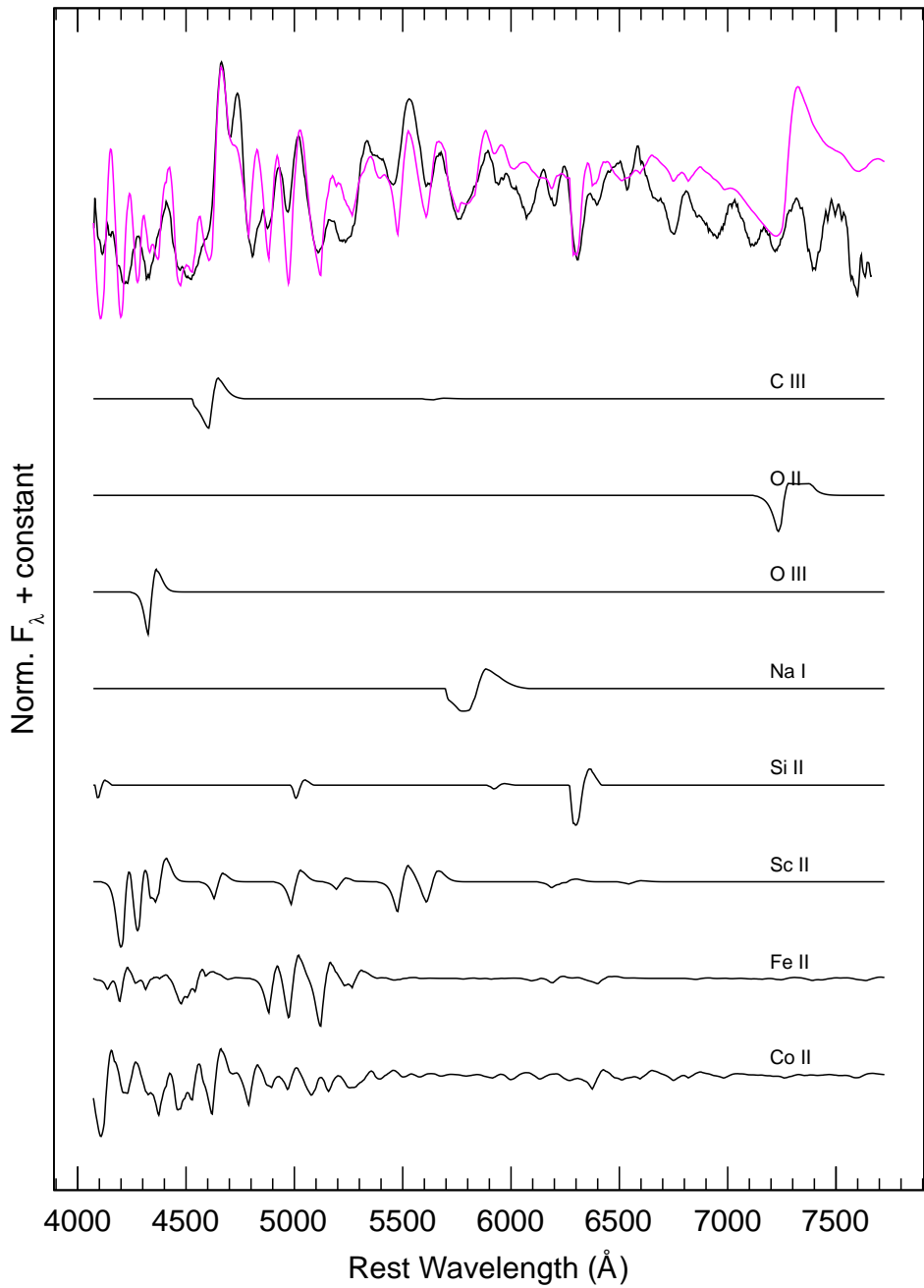


**Figure 6.9:** Normalized 07qd spectrum 8 days after maximum, with SYNOW fit and its constituents. Again, the spectra have been normalized to the radiation of a black-body at 9000 K, and the observed spectrum and the combined fit have been scaled up by a factor of 2 for clarity.

**Table 6.5:** SYNOW Parameters for Fig. 6.10 (10 days after  $B$ -max), using a photospheric velocity ( $v_{\text{phot}}$ ) of 2800 km/s and a black-body temperature ( $T_{\text{bb}}$ ) of 8000 K. Velocities are given in units of 1000 km/s and  $T_{\text{exc}}$  values are given in units of 1000 K.

Ion	$\tau$	$v_{\text{min}}$	$v_{\text{max}}$	$v_e$	$T_{\text{exc}}$
O I	1.0	2.8	$\infty$	1	8
O II	0.2	3.5	$\infty$	1	8
O III	2.0	2.8	$\infty$	1	8
Na I	0.4	2.8	4.8	1	8
Na I	0.3	4.0	7.0	8	8
Na I	0.3	7.0	11.0	3	8
Si II	3.0	2.8	3.8	1	8
Ca II	35.0	2.8	4.8	1	8
Sc II	1.0	2.8	5.8	1	10
Fe II	10.0	2.8	3.8	1	8
Co II	10.0	2.8	3.8	1	8

of the ions fitted in the +3 day spectrum are used. However, the ions in a neutral ionization stage are excluded here (except Na I) because, although they matched some of the +3 day spectrum features, their presence were not clear in the previous spectrum, and they do not fit any of the absorptions in the +8 day spectrum. The temperature of the blackbody radiation chosen for this spectrum is 9000 K, intermediate to those of the +3 day and +10 day spectra.

Practically all the lines are due to Fe II and Co II, though other ions help them to better describe the absorptions, except for the Si II line at  $\sim 6300$  Å, the O II line at  $\sim 7200$  Å, and the Na I wide absorption at  $\sim 5800$  Å which are clearly caused by these ions. This Si II resides within the photosphere and enhances the spectrum at  $\sim 4100$  Å, but less so at  $\sim 3850$  Å and  $\sim 5025$  Å. The existence of some ions measured at 3 days past maximum cannot be ruled out, in part due to the influence of the dominant Fe II lines (Baron et al., 2003). The Cr II in the 02cx fit by Branch et al. (2004) is also not necessary, as there is insufficient data to examine regions below 4000 Å at this and later epochs. We were unable to identify any ionization stage of Ti at this epoch, despite the possibility of observing Ti I at 3 days past maximum. Foley et al. (2009) identified Ti II at the same epoch in 08ha, but its addition here does little to the overall fit. The secondary absorption lines S II are no longer apparent at this epoch, as Sc II is able to effectively represent the 5400-5700 Å region without aid.

### 6.2.2.3 +10 day spectrum

The SYNOW fit in Fig. 6.10 is derived from parameters used to fit 02cx at 12 days past maximum (Branch et al., 2004), except that the velocities and blackbody temperature have been reduced to accommodate the unique nature of 07qd (see Table 6.5 for these parameters). This fit was chosen due to its consistency in representing 08ha, 02cx, and 05hk at similar epochs, as seen in Fig. 6.12. The similarity is especially apparent with 08ha, which shares most absorption features with 07qd. The relative shift between

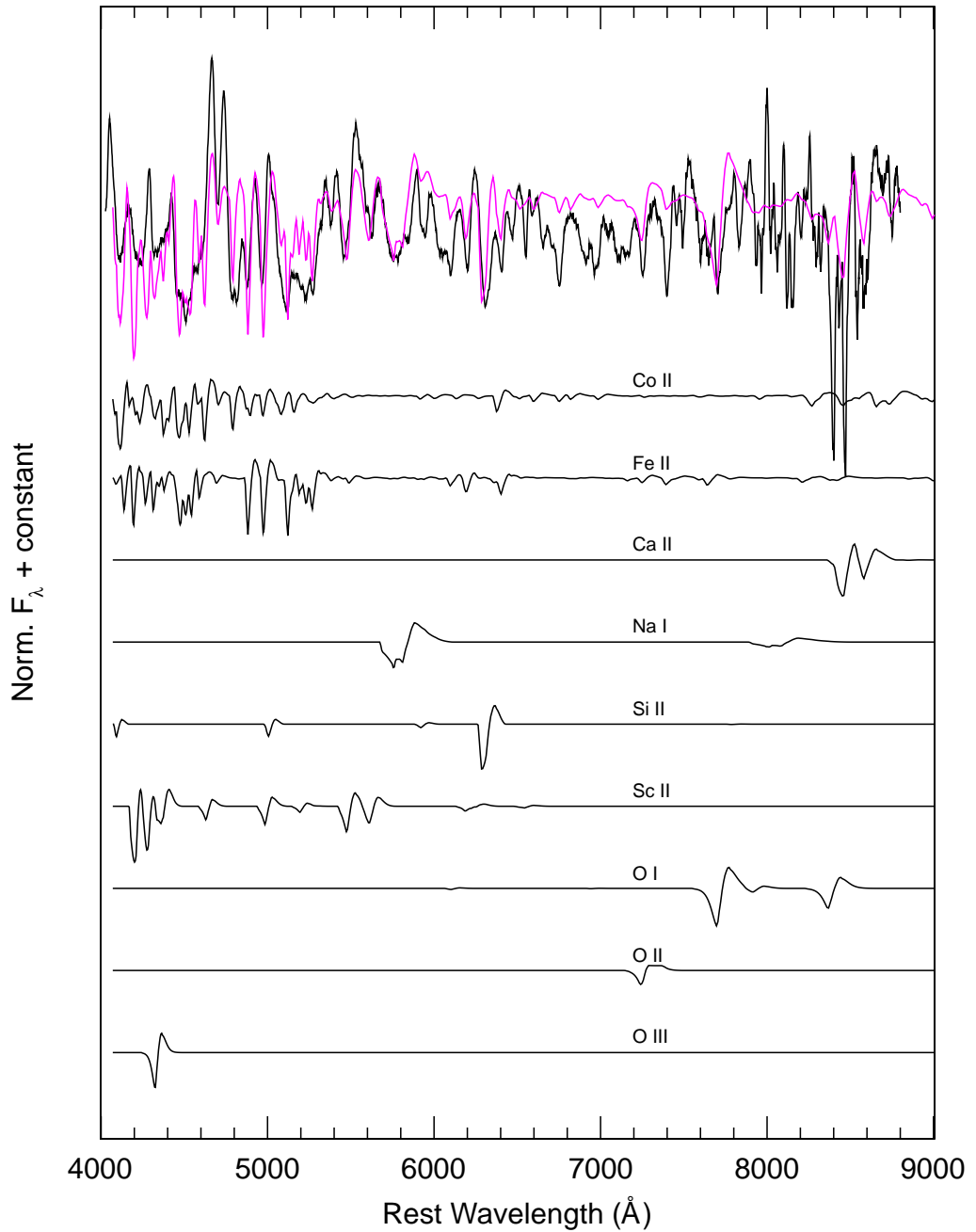


**Figure 6.10:** Normalized 07qd spectrum 10 days after maximum, with SYNOW fit and its constituents. Again, the data and combined fit have been scaled up by a factor of 2 for clarity.

these two spectra was measured to be  $\sim 800 \text{ km s}^{-1}$ ; the photospheric velocity of 08ha at this epoch is  $2000 \text{ km s}^{-1}$ , while the best-fit SYNOW photospheric velocity of 07qd is  $\sim 2800 \text{ km s}^{-1}$  with a blackbody temperature of 8000 K.

Much of the continuum is dominated by narrow Fe II lines, with Co II playing a large role below 5000 Å as well, consistent with most iron-core SNe ([Harkness, 1991](#)). The SYNOW fit also continues to include a prominent Si II feature at 6300 Å necessitated by the inability of Fe II to fit it without losing other features. Ca II was also included for the H and K lines.

The signal-to-noise ratio of the data appears to be lower than it actually is, due to the low-velocity nature of this particular photosphere. Much of the absorption blending in the regions blueward of 4500 Å proved difficult to fit with SYNOW models, especially where P-Cygni profiles are no longer apparent; it is suspected to be a consequence of the narrow absorption features of several iron-group elements.

H $\alpha$  and Helium ions were tested in SYNOW fits, though no match could be found. We expect and observe host-galaxy H $\alpha$  emission at 6563 Å, though just blueward of this feature we see a small absorption that we identify with C II. The nature of the trough at  $\sim 6750 \text{ \AA}$  is unclear at this time; very few ions are capable of modeling it without severely affecting the fit elsewhere. He I was of particular interest in the SYNOW fit to the 08ha spectrum 13 days past maximum conducted by [Valenti et al. \(2009\)](#) and to SN 2007J, another 02cx-like SN ([Foley et al., 2009](#)), but the Na I D line dominates over the predicted He I line. At 10 days past maximum, all other He I features fail to match the spectrum.

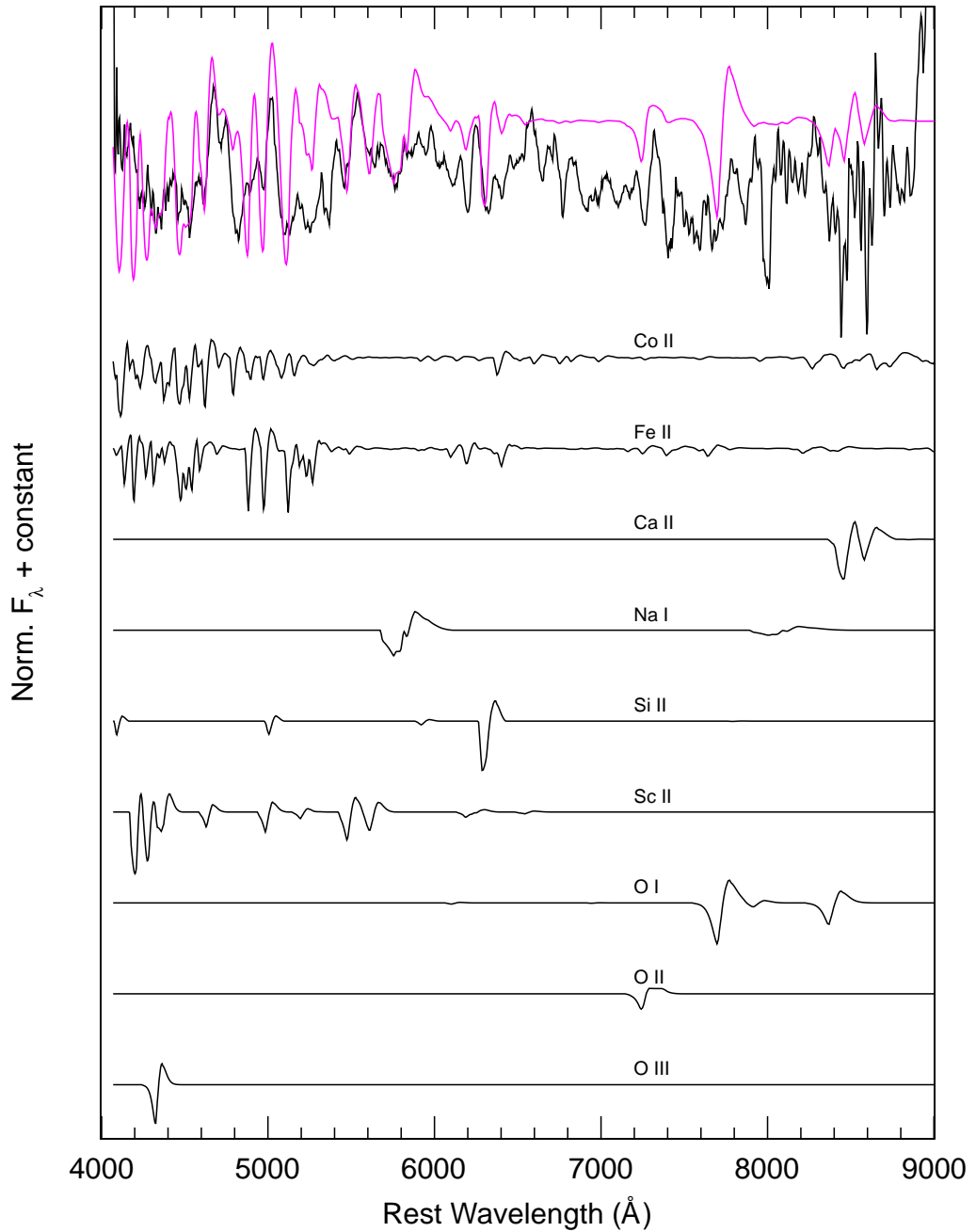
#### 6.2.2.4 +15 day spectrum

As can be seen in Fig. 6.4, the two spectra taken at +10 and +15 day after maximum are very similar. In Fig. 6.11 we present the results of the SYNOW fit to the spectrum 15 days after maximum brightness, as well as a decomposition of the fit to show the influence of each ion. The ions used are the same than for the +10 day spectrum (see Table 6.5), only decreasing the black-body temperature by 2000 K to 6000 K, reducing the optical depth of Fe II from 10 to 7, and of Co II from 10 to 5, and all the excitation temperatures of the ions to 6000 K.

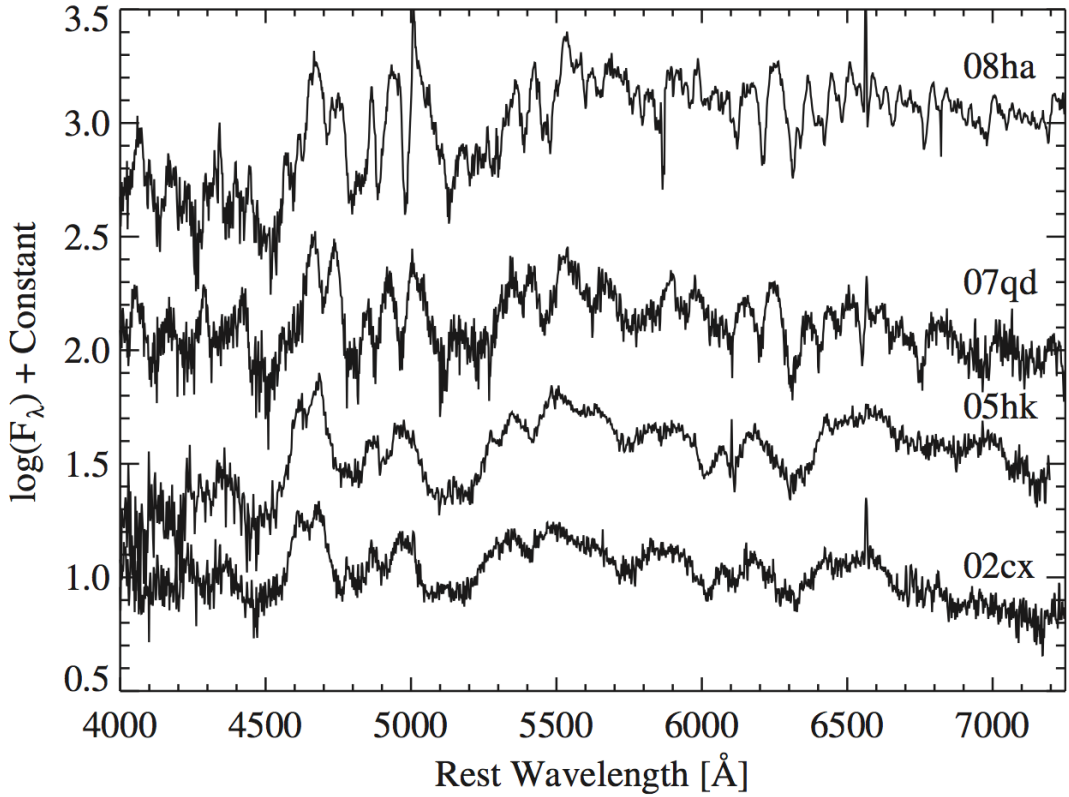
#### 6.2.2.5 Spectral evolution and similarity with other SN Ia

Using these SYNOW fits to the individual epochs, the spectral evolution of 07qd given in Fig. 6.4 provides a detailed picture of a developing photosphere. Examining the contributions near  $\lambda 4550$  and  $\lambda 5200 \text{ \AA}$  present at +3 day but absent at +10 day, Fe III has either greatly fallen in opacity or recombined into Fe II, which has increased in influence. Na I and S II have also decreased in intensity, but remain crucial to the region between 5000 and 6000 Å.

The Si II feature endures through two weeks past maximum, but its strength has lessened, becoming roughly equal to that of Fe II by day 15. Much of the spectrum in the blue region was not measured at subsequent epochs, though extended red wavelengths are given, revealing probable O I and O II signatures. It is apparent,



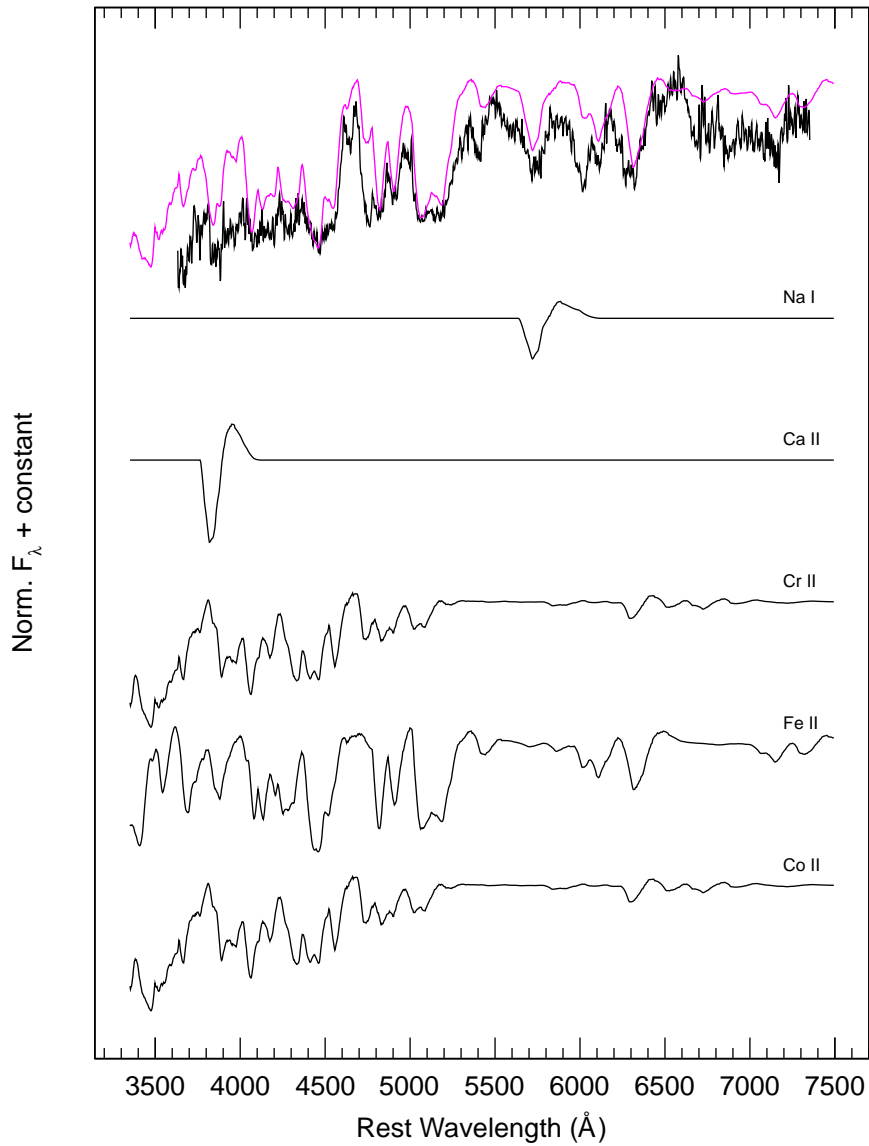
**Figure 6.11:** Normalized 07qd spectrum 15 days after maximum, with SYNOW fit and its constituents. The data and combined fit have been scaled up by a factor of 2 for clarity.



**Figure 6.12:** Comparison of the spectrum of 07qd at 10 days past maximum brightness with that of 08ha (Foley et al., 2009), 05hk (Phillips et al., 2007), and 02cx (Branch et al., 2004) at similar epochs (10 days for 08ha, and 12 days for both 05hk and 02cx). All spectra have been appropriately shifted to their rest frames. Each feature of 07qd is redward of those of 05hk and 02cx, indicating significantly slower photospheric velocities, while only slightly blueward of those of 08ha. Figure from McClelland et al. (2010).

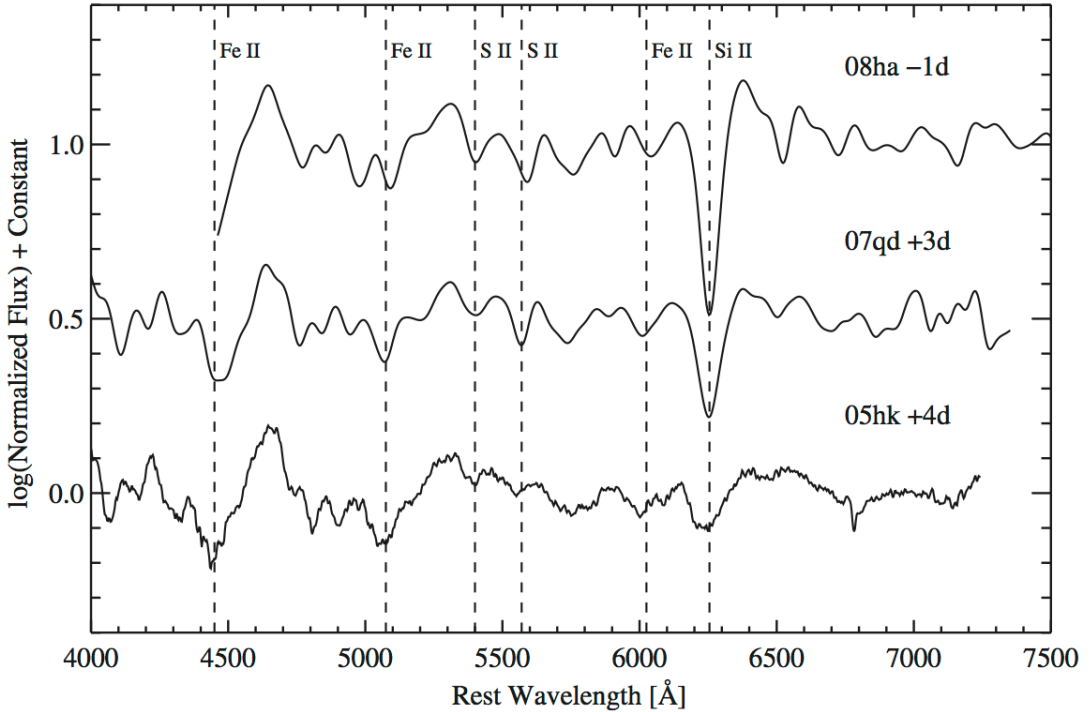
however, that the late-time spectra beyond 8000 Å demonstrate the presence of the Ca II near-IR feature, though the Ca II H and K near-UV lines persist. Blackbody temperatures have fallen to 9000 K at 8 days past maximum and to 7000 K at 15 days, further intensifying the influence of Fe II profiles over the continuum. It remains to be seen whether the other unidentified line profiles can be remedied with more exotic ions.

Figure 6.12 shows the spectra of four 02cx-like SNe Ia compared at similar epochs ( $\sim 10$  days). 07qd clearly bears the strongest resemblance to 08ha; very few features differ. 02cx and 05hk exhibit much faster photospheres than 07qd and 08ha, and are likewise shifted toward the blue. The faster photosphere ( $7000 \text{ km s}^{-1}$ ) and higher excitation temperatures (9000 K) used in the SNOW fit of 02cx (see Fig. 6.13, Branch et al. (2004)) broaden many of the Fe II lines, effectively masking the primary Si II absorption, but other major velocity features remain consistent. It should be noted, however, that SNOW's highly parameterized fitting routine permits many degrees of freedom.



**Figure 6.13:** Normalized 02cx spectrum 12 days after maximum, with SYNOW fit and its constituents. A blackbody temperature of 9000 K and a photosphere velocity of  $7000 \text{ km s}^{-1}$  is used. Reproduced from [Branch et al. \(2004\)](#).

Similarly, we may compare the maximum-light spectra of 07qd, 08ha, and 05hk, as seen in Figure 6.14. The spectra of both 07qd and 08ha, with photospheres blueshifted by  $2000 \text{ km s}^{-1}$  and  $1750 \text{ km s}^{-1}$  (respectively), mirror many of the major features. Although the Si II and S II profiles are noticeably stronger in 07qd and 08ha, their pres-



**Figure 6.14:** Normalized spectra of peculiar SN Ia, observed near maximum brightness. The spectra of 07qd and 08ha have been blueshifted by 2000 and 1750 km s<sup>-1</sup>, respectively, to roughly match the photospheric velocity of 05hk. 07qd and 08ha have also been convolved by 50 Å FWHM Gaussians, while 05hk was smoothed with a 5 Å FWHM Gaussian. Figure from [McClelland et al. \(2010\)](#).

ence in 05hk is clear. The similarity between 07qd and 05hk below 5000 Å is striking (identical structures in this region are indicative of similar iron-group contributions).

The greatly different photospheric velocities apparent in 07qd and 05hk are examined along with 02cx and 08ha in Fig. 6.15, suggesting a relation between the luminosities and expansion velocity in these peculiar cases, and confirming 07qd as a link between 08ha and the other members of the 02cx-like class of objects.

### 6.3 Discussion and conclusions

The striking similarity of the +10 day (relative to B maximum) spectrum of 07qd to that of 08ha suggests that they are indeed similar explosions. Since 07qd is also spectroscopically linked to 05hk and thus to 02cx as well, these four peculiar events range in peak luminosity by 4 mag, but constitute a single spectral class.

[Valenti et al. \(2009\)](#) argued that 08ha and possibly other 02cx-like objects are actually core-collapse SNe; their low luminosity is the result of either the collapse of a  $\gtrsim 30 M_{\odot}$  star directly to a black hole, or electron capture in the core of a 7–8  $M_{\odot}$  star. However, the clear presence of IMEs (notably Si II  $\lambda\lambda 6355$  and S II  $\lambda\lambda 5968, 6359$ ) in 07qd suggests low-density thermonuclear burning and not a core-collapse SN Ib or SN Ic explosion (see §3.2 for a review of SN spectroscopic classification). Except for

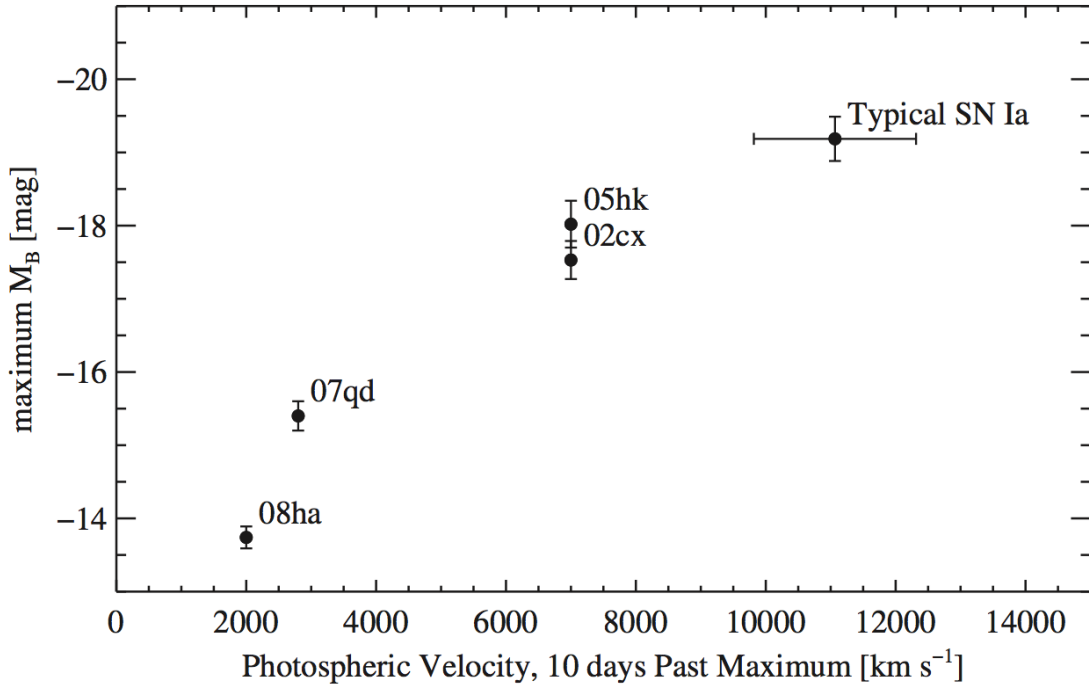


**Figure 6.15:** Estimated photospheric velocities at  $\sim 10$  days past maximum brightness plotted against maximum absolute magnitudes (based on a  $\sim 10$  days rise time for 07qd). The *typical* point in the upper-right corner is the maximum  $B$  magnitude and velocity of a normal SN Ia (Benetti et al., 2005). Figure from McClelland et al. (2010).

the photospheric velocities, the spectra of 07qd are similar to Branch-normal SNe Ia, further strengthening the arguments that it is a thermonuclear runaway.

The presence of these IMEs mirrors the findings of Foley et al. (2010). SN Ibc has been observed with traces of Si II (Valenti et al., 2008) or S II (Brown et al., 2007, Nomoto et al., 2000). However, these lines are quite strong in 07qd, suggesting that it is an SN Ia rather than a core-collapse event. Additionally, the light-curve of 07qd, though displaying a sharp rise that is unusual for a typical SN Ia, does not show the fast decline typical of a low-luminosity SN Ic or the “plateau” of an SN IIP that achieves similar peak luminosity.

When compared with other 02cx-like SN, spectra of 07qd mirror those of 08ha and display striking relationships to others. These comparisons also imply that strong Si II is possible in 02cx and 05hk, though “disguised” by Fe II blending due to their higher photospheric velocities. The fast evolution of 07qd suggests that these IMEs are only detectable for a brief time, and become masked by Fe II or recombine as the photosphere slows and cools. The presence of carbon and oxygen ions in the photosphere echoes the results of deflagration models, including those of Gamezo et al. (2004), suggesting the presence of unburned white dwarf material and supporting that this class stems from such a progenitor.

In conclusion, analyzing the photometry and spectroscopy of 07qd, we find the

following.

1. 07qd was spectroscopically similar to both 08ha and 05hk. Strong lines of Fe II and Co II are present in spectra of all three objects, while Fe III and IME features are most visible at early epochs, though their optical depths decline quickly.
2. The explicit presence of a variety of IMEs in the early-time spectra implies the thermonuclear deflagration of carbon and oxygen, and shows 07qd to be inconsistent with a core-collapse event.
3. Correlations exist between 02cx-like peak luminosity, photospheric velocity, and light-curve stretch, and the events span a sequence from 08ha to 02cx.

Findings (1) and (2) point toward thermonuclear burning during the explosion of 07qd, while point (3) emphasizes that 07qd completes a sequence of 02cx-like SN Ia both energetically and spectroscopically. The composition and velocity of the ejecta support the picture of a deflagration. The low intrinsic brightness points to a small amount of synthesized radioactive nickel, which argues against the unbinding of a Chandrasekhar-mass progenitor. But if the fusion is dominated by IMEs at the expense of nickel, the explosions of massive white dwarfs are still possible.

The low velocities and energies present in 08ha and 07qd enable the analysis of many aspects of 02cx-like SN, otherwise hidden by the Fe II blending present in 05hk and 02cx. Though the velocities and energies span a wide range, together they constitute a well-defined group of peculiar SN Ia.



## CHAPTER 7

---

### Supernova properties as a function of the distance to the host galaxy center

---

TYPE IA supernovae (SNe Ia) are used as reliable and accurate distance indicators on cosmological scales, through several techniques that rest on the empirical correlation between their peak brightness and the width of their light-curve (Phillips, 1993). As both the quantity and the quality of supernova observations have increased, limitations of the homogeneity of SNe Ia after light-curve width and color corrections, have become apparent (Riess et al., 1996, Sullivan et al., 2006b). If these inhomogeneities are not accounted for by the light-curve width and color corrections or by other means, this may introduce systematic errors in the determination of cosmological parameters from supernova surveys. One plausible source of inhomogeneity is a dependence of supernova properties on host galaxy features. Since the average properties of host galaxies evolve with redshift, any dependence will impact the cosmological parameter determination.

There have been many recent studies illustrating the dependence of SN properties on global characteristics of their hosts (Gallagher et al., 2008, Hicken et al., 2009, Howell et al., 2009, Kelly et al., 2010, Sullivan et al., 2006b, 2010), also by the SDSS-II/SNe collaboration (D'Andrea, 2011, Gupta et al., 2011, Konishi et al., 2011, Lampeitl et al., 2010a, Nordin et al., 2011b, Smith et al., 2011). A lot has been learned from these studies. For instance, it has been by now established (Gallagher et al., 2005, Hamuy et al., 1996a, Lampeitl et al., 2010a, Sullivan et al., 2006b) that SNe in passive galaxies are, on average, dimmer than those in star-forming galaxies. They also have narrower light-curves, which corrects for some, but not all, of this effect when applying the

light-curve standardization procedure.

Following earlier work by [Jha et al. 2006a](#) and [Hicken et al. 2009](#), we present here a study of the dependency of SN Ia properties with local characteristics of their host galaxies, using the location of the supernova inside the galaxy as a proxy for physically relevant parameters. We use the full three-year SDSS-II SN sample, as well as the Fall 2004 test campaign sample, and make a restriction to redshifts  $z < 0.25$  in order to minimize observational biases. In particular, we examine the supernova light-curve parameters related to color and decline rate, as well as the Hubble-diagram residuals, as a function of the projected distance between the supernova and the center of its host galaxy. We use data from two light-curve fitters, MLCS2k2 ([Jha et al., 2007](#)) and SALT2 ([Guy et al., 2007](#)). For MLCS2k2 we obtain  $A_V$  as a measure of the color and  $\Delta$  for the light-curve width / decline rate. The corresponding parameters for SALT2 are  $c$  and  $x_1$ . How these parameters are obtained is described in Section 7.2.1. In addition, we also try to correlate these light-curve parameters to an indirect measurement of the local metallicity at the position of the SNe.

This analysis was presented at the *Supernovae and their Host Galaxies* conference which was held at Sydney in June 2011, and it will be published in [Galbany et al. \(2011\)](#).

The outline of this chapter is like follows. In §7.1 we describe the supernova sample and the host galaxy information used in the analysis. Section 7.2 covers the selection of SNe Ia, the procedure used for separating the host galaxies according to their morphology, and the description of the light-curve parameters studied. In §7.3 we introduce the method used in order to extract correlations between light-curve parameters and distance to the host galaxy, and present the results of the analysis. Finally, in §7.4 we discuss these results, and offer some conclusions.

## 7.1 Data Sample

### 7.1.1 SDSS-II Supernova Sample

After three years the Sloan Digital Sky Survey-II Supernova Survey<sup>1</sup> (SDSS-II/SNe, [Frieman et al. 2008b](#)) has discovered and confirmed spectroscopically 559 SNe Ia of which 514 were confirmed by the SDSS-II/SNe collaboration, 36 are likely SNe Ia and 9 were confirmed by other groups. We will refer to these SNe as the “Spec-Ia” sample. Besides the spectroscopically confirmed SNe, SDSS-II/SNe has 759 SNe photometrically classified as Type Ia from their light-curves, with spectroscopic redshifts of the host galaxy either measured previously by SDSS or recently by the SDSS-III Baryon Oscillation Spectroscopic Survey (BOSS, [Eisenstein et al. 2011](#)). We designate this sample as the “Photo-Ia” sample. The number of SNe in the Photo-Ia sample has been largely increased with the BOSS contribution. The whole SDSS-II/SNe sample combining the Spec-Ia and Photo-Ia samples consists of 1318 SNe Ia.

In this analysis we restrict the sample to redshifts  $z < 0.25$ , where the detection efficiency of the SDSS-II SN survey remains reasonably high ( $\gtrsim 0.5$ , [Smith et al. \(2011\)](#))

---

<sup>1</sup>Detailed description in §4.

for the sake of completeness. This provides a sample of 608 SNe Ia, of which 376 have been confirmed spectroscopically and 232 are photometrically probably.

### 7.1.2 Host Galaxy Identification

We have matched every SN Ia in our sample to the closest galaxy within an angular separation of 20 arcsec using the SDSS Data Release 7 (DR7) data set (Abazajian et al., 2009), which contains imaging of more than 8 000 deg<sup>2</sup> of the sky in the five optical bandpasses *ugriz* (Fukugita et al., 1996). The matching was done through the SDSS Image Query Form<sup>2</sup>.

There are several ways the association can fail:

- (i) the nearest object is not the host. This happens mostly at low-z where the galaxies are large on the sky, and star-forming regions and other structure in the galaxy can be tagged as a galaxy.
- (ii) the galaxy is too faint to be detected by the SDSS pipeline.

Based on visual inspection, it is estimated that this procedure picks the correct host  $\sim 90\%$  of the time. Out of the 608 SNe in the redshift range of this analysis, 17 SNe did not have a visible galaxy within 20 arcsec and were consequently excluded from the following analysis, leaving 591 SNe Ia (363 Spec-Ia and 228 Photo-Ia).

For each of the matched galaxies we obtained the photometric parameters needed for determining the morphology and for measuring the (normalized) separation of the supernova from the center of the galaxy: the coordinates, the *ugriz* model magnitudes, and the parameters corresponding to the Sérsic, isophotal, and Petrosian luminosity profiles in the *r* band, to be described in the next section.

#### 7.1.2.1 DR7 parameters

All the galaxies in DR7 have many magnitudes measured: the Sérsic magnitudes (associated with de Vaucouleurs and exponential profile fits), the model magnitudes, which use the better of the two fits (de Vaucouleurs and exponential) in the *r*-band as a matched aperture to calculate the flux in all bands, the isophotal magnitudes, and the Petrosian magnitudes, described below.

The Sérsic brightness profile is described by

$$I(r) = I_0 \exp \left[ -a_n \left[ \left( \frac{r}{r_e} \right)^{1/n} - 1 \right] \right] = I_0 \exp \left[ -a_n \left( \frac{r}{r_e} \right)^{1/n} \right], \quad (7.1)$$

where  $r$  is the distance from the galaxy center,  $I_0$  is the intensity at the center ( $r = 0$ ),  $r_e$  is the radius which contains half of the luminosity, and  $I_e$  is the intensity at the center  $r_e$ . For the measurement of the Sérsic magnitudes, two different models are fitted to the two-dimensional image of each object in each band:

---

<sup>2</sup><http://cas.sdss.org/astrodr7/en/tools/search/IQS.asp>

1. A pure de Vaucouleurs profile ([de Vaucouleurs, 1948](#)), with  $n = 4$ , and  $a_4 = 7.67$ . This profile is truncated beyond  $7r_e$  to smoothly go to zero at  $8r_e$ , and with some softening within  $r < r_e/50$ .
2. A pure exponential profile, with  $n = 1$ , and  $a_1 = 1.68$ , truncated beyond  $3r_e$  to smoothly go to zero at  $4r_e$ .

These fitting procedures yield the effective radius of the model ( $r_X$ ), the axis ratio of the best fit model ( $ab_X$ ), the position angle of the ellipse in degrees East of North ( $\phi_{IX}$ ), the likelihood associated with that model from the  $\chi^2$  fit ( $L_X$ ), and the total magnitudes associated with that fit ( $Mag_X$ ), where  $X$  accounts for de Vaucouleurs ( $dev$ ), or exponential ( $exp$ ) profiles.

Similar parameters are obtained for the isophotal normalization. Although, in this case, the parameters define the ellipse of the 25 mag/arcsec<sup>2</sup> isophote (in all bands). The radius of a particular isophote as a function of angle is measured, and the major and minor axes ( $a_{ISO}$ ,  $b_{ISO}$ ), the position angle ( $\phi_{ISO}$ ), and the average radius of the isophote in question ( $r_{ISO}$ ) are given.

The Petrosian magnitudes use a different approximation. They are a modified form of the [Petrosian \(1976\)](#) magnitude system, which are a measurement of the galaxy flux within a circular aperture whose radius is defined by the shape of the azimuthally averaged light profile. In the SDSS five-band photometry, the aperture in all bands is set by the profile of the galaxy in the  $r$  band alone. This procedure yields the Petrosian radius in each band ( $r_{PET}$ ), and the Petrosian magnitude in each band ( $M_{PET}$ , calculated using only  $r_{PET}$  for the  $r$  band), for circles containing the 50% and the 90% of the Petrosian flux.

Finally, the model magnitudes are taken from the model (exponential or de Vaucouleurs) of higher likelihood in the  $r$  band, and applied in the other bands. Systematic differences from Petrosian colors are in fact often seen due to color gradients, in which case the concept of a global galaxy color is somewhat ambiguous. For faint galaxies, the model colors have appreciably higher signal-to-noise ratio than do the Petrosian colors.

All these parameters are described in the SDSS Early Data Release paper (EDR, [Stoughton et al. 2002](#)).

## 7.2 Measurements

### 7.2.1 Light-curve Parameters

We fit the supernova light-curves with the publicly available Supernova Analyzer package (SNANA<sup>3</sup>, [Kessler et al. 2009b](#)), with both the MLCS2k2 and the SALT2 light-curve fitters<sup>4</sup>.

For the MLCS2k2 fitter we used  $R_V = 2.2$  for the reddening law and an  $A_V$  prior of  $P(A_V) = \exp(-A_V/\tau)$  with  $\tau = 0.33$ , as described in [Kessler et al. 2009b](#). The fitter

---

<sup>3</sup>We used version 9.41 of SNANA, available at <http://sdssdp62.fnal.gov/sdssn/SNANA-PUBLIC/>

<sup>4</sup>For a description of both fitters see §3.4.1.

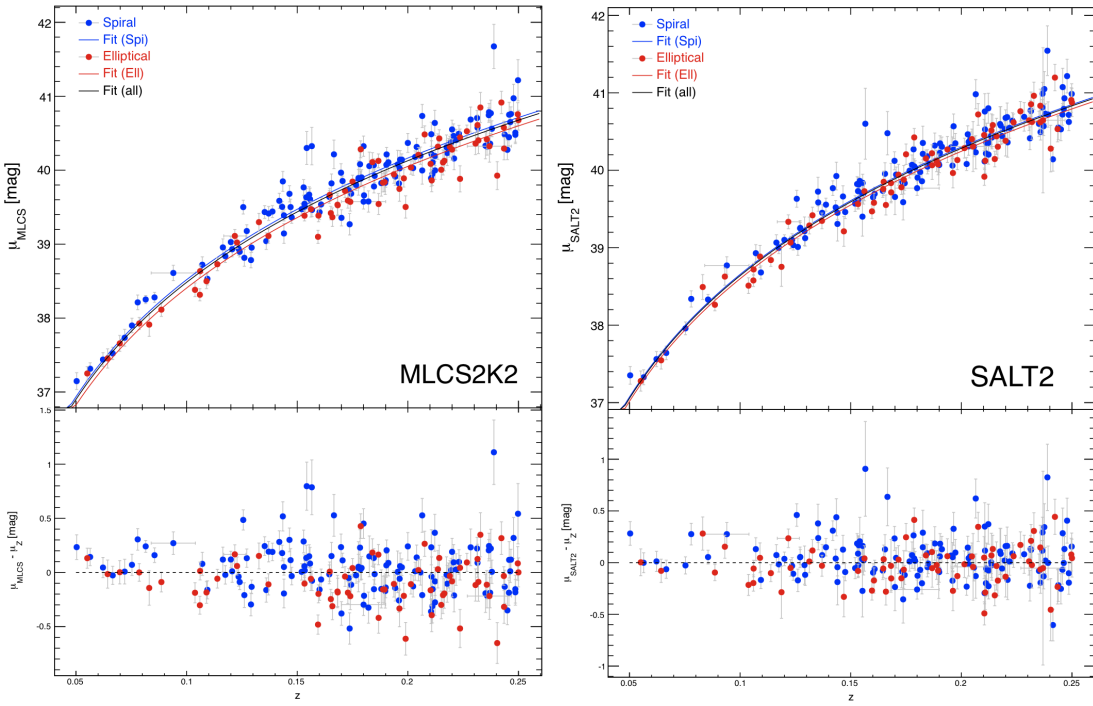


**Figure 7.1:** Hubble diagram and residuals for MLCS2k2 and SALT2 samples. Supernovae exploding in elliptical (red) or spiral (blue) galaxies are fitted separately, leaving the Hubble constant as a free parameter. Another fit is performed to the whole sample (black), which is used for calculate the residuals.

returns four parameters for each SN: epoch of maximum brightness ( $t_0$ ), host galaxy extinction ( $A_V$ ), decline rate of the light-curve ( $\Delta$ ), and distance modulus ( $\mu_{MLCS}$ ), while the SALT2 light-curve fitter returns a value for the color of the supernova ( $c$ ), for the stretch of the light-curve ( $x_1$ ), and for the apparent magnitude at maximum brightness in the  $B$  band ( $m_B$ ). The distance modulus can be calculated by

$$\mu_{SALT2} = m_B - M + \alpha x_1 - \beta c, \quad (7.2)$$

where  $M$ ,  $\alpha$  and  $\beta$  are obtained when minimizing the Hubble diagram residuals. For the average absolute magnitude at peak brightness ( $M$ ) we use  $-19.41 \pm 0.04$  (Guy et al., 2005). For  $\alpha$  and  $\beta$  we use the values obtained from the three-year SDSS-II SN sample, independent of cosmology ( $\alpha = 0.131 \pm 0.052$  and  $\beta = 3.26 \pm 0.49$ , Marriner et al. 2011).

Both  $\Delta$  and  $x_1$  are related to the width of the supernova light-curve. However, they are not linearly correlated, and while  $\Delta$  increases for narrower light-curves,  $x_1$  decreases. The  $A_V$  and  $c$  parameters are both measurements of color variability. MLCS2k2 assumes that the color variations not included in  $\Delta$  can be described by a Milky Way-like dust extinction law with an unknown total-to-selective extinction ratio (usually denoted  $R_V$ ) unique for the full sample and an  $A_V$  that varies between individual supernovae. The  $c$  parameter in SALT2 instead describes the color variation of

a SN Ia relative to a fiducial SN Ia model, and it includes both the extinction by dust in the host galaxy and any intrinsic color variation.

The Hubble residual is defined as  $\delta\mu_{fit} \equiv \mu_{fit} - \mu_z$  where  $_{fit}$  is either MLCS2k2 or SALT2, depending on the light-curve fitter, and

$$\mu_z = 25 + 5 \log_{10} \left[ \frac{c}{H_0} (1 + z_{SN}) \int_0^{z_{SN}} \frac{dz'}{\sqrt{\Omega_M(1+z')^3 + \Omega_\Lambda}} \right] \quad (7.3)$$

is the distance modulus calculated using the supernova redshift and a fiducial cosmology. We assume a flat cosmology with  $\Omega_M = 0.274 = 1 - \Omega_\Lambda$ , and the values for  $H_0$  which minimize the scatter of these samples:  $64.85 \pm 0.24 \text{ km s}^{-1} \text{ Mpc}^{-1}$  for MLCS2k2, and  $60.47 \pm 0.23 \text{ km s}^{-1} \text{ Mpc}^{-1}$  for SALT2<sup>5</sup>. The uncertainties in the Hubble residuals were taken as the uncertainties in the distance moduli extracted from the light-curve fit,  $\mu_{SALT2}$  and  $\mu_{MLCS2k2}$  respectively, without adding any contributions from possible intrinsic dispersion. In Fig. 7.1 the Hubble diagram and the Hubble residuals are shown for the two samples.

#### 7.2.1.1 Light-curve selection cuts

To assure robust light-curve parameters, we applied similar selection cuts as in the SDSS-II/SNe first year cosmology paper (Kessler et al., 2009a). For MLCS2k2 (SALT2), we used the following requirements:

- At least 5 photometric observations at different epochs between -20 and +70 days (+60 days for SALT2) in the supernova rest frame relative to peak brightness in *B* band.
- At least one measurement earlier than 2 days (0 days) in the rest frame before the date of *B*-band maximum.
- At least one measurement later than 10 days (9.5 days) in the rest frame after the date of *B*-band maximum.
- At least one measurement with a signal-to-noise ratio greater than 5 for each of the *g*, *r* and *i* bands not necessarily from the same night.
- A light-curve fit probability of being a SN Ia, based on the  $\chi^2$  per degree of freedom, greater than 0.001.

These cuts were designed to remove objects for which we are not sure of the classification, with uncertain determinations of the time of maximum brightness, or peculiar or badly constrained light-curves.

Out of the 591 objects, there were 248 that failed the selection cuts for MLCS2k2, leaving 343 SNe (228 Spec-Ia and 115 Photo-Ia). For SALT2, there were 249 objects that failed, leaving 342 SNe (217 Spec-Ia and 125 Photo-Ia). Note that the MLCS2k2 and

---

<sup>5</sup>These values are only related to the MLCS2k2 and SALT2 training. They do not have any physical relevance.

SALT2 samples were studied separately, i.e., some SNe are present in both samples while some are in one but not the other. The majority of the SNe in the final sample (171 SNe, out of 192 for the MLCS2k2 sample and 197 for the SALT2 sample) are present in both samples, but some are retained in one but not the other. In Table D.1 we mark the SNe which are only present in either the MLCS2k2 sample or the SALT2 sample.

Furthermore, we removed all SNe with extreme values of the light-curve parameters, in order to have a sample unaffected by peculiar values. We follow the empirically determined cuts in Lampeitl et al. (2010a) which define the location in the light-curve parameter space for the majority of SNe Ia in the SDSS sample. For MLCS2k2 we restricted the sample to  $\Delta > -0.4$ , removing 30 SNe, while for SALT2 the ranges allowed were set to  $-0.3 < c < 0.6$  and  $-4.5 < x_1 < 2.0$ , removing 22 SNe. After the cuts on light-curve parameters we were left with 313 SNe (203 Spec-Ia and 110 Photo-Ia) in the MLCS2k2 sample, and 320 (209 Spec-Ia and 111 Photo-Ia) in the SALT2 sample.

### 7.2.2 Host Galaxy Typing

We split the supernova sample into two groups depending on the morphology of the host galaxy, determined using two photometric parameters: the inverse concentration index, and the comparison of the likelihoods for two different Sérsic brightness profiles (Sérsic, 1963).

Other parameters could be used in order to type galaxies into ellipticals or spirals. One of the methods used within the SDSS collaboration, which is similar to the simply comparison of the likelihoods for two different Sérsic brightness profiles, is the introduction of another term which is the likelihood for the fit to a typical star profile. Then a  $q_X$  parameter is calculated, for the three types (*dev*, *exp*, and *star*):

$$q_X = L_X / (L_{\text{star}} + L_{\text{spiral}} + L_{\text{elliptical}}) \quad (7.4)$$

and if  $q_X > 0.5$ , the galaxy is assigned type X. This works well in the range  $18 < r < 21.5$ ; at the bright end, the likelihoods have a tendency to underflow to zero, which makes them less useful. In particular,  $L_{\text{star}}$  is often zero for bright stars. Using this method, the assignation of the type of galaxy is based only on shape, and does not use color at all. The problem of this procedure is that it can be that no type gets a  $q$  value greater than 0.5.

Another method is the measurement of the  $u - r$  color (Strateva et al., 2001), which seems to be a good color indicator for typing. The problem of this procedure is that it works best at very low redshift, and we are analyzing data up to  $z \sim 0.25$ .

The inverse concentration index (e.g. Shimasaku et al., 2001, Strateva et al., 2001, Yamauchi et al., 2005) is defined as the ratio between the radii of two circles, centered on the core of the galaxy, containing respectively 50% and 90% of the Petrosian flux (see Blanton et al. 2001). These radii were obtained for the  $r$  band for all our host galaxies from SDSS DR7 (Abazajian et al., 2009). Elliptical galaxies have an inverse concentration index of around 0.3, while spirals favor an inverse concentration index of around 0.43.

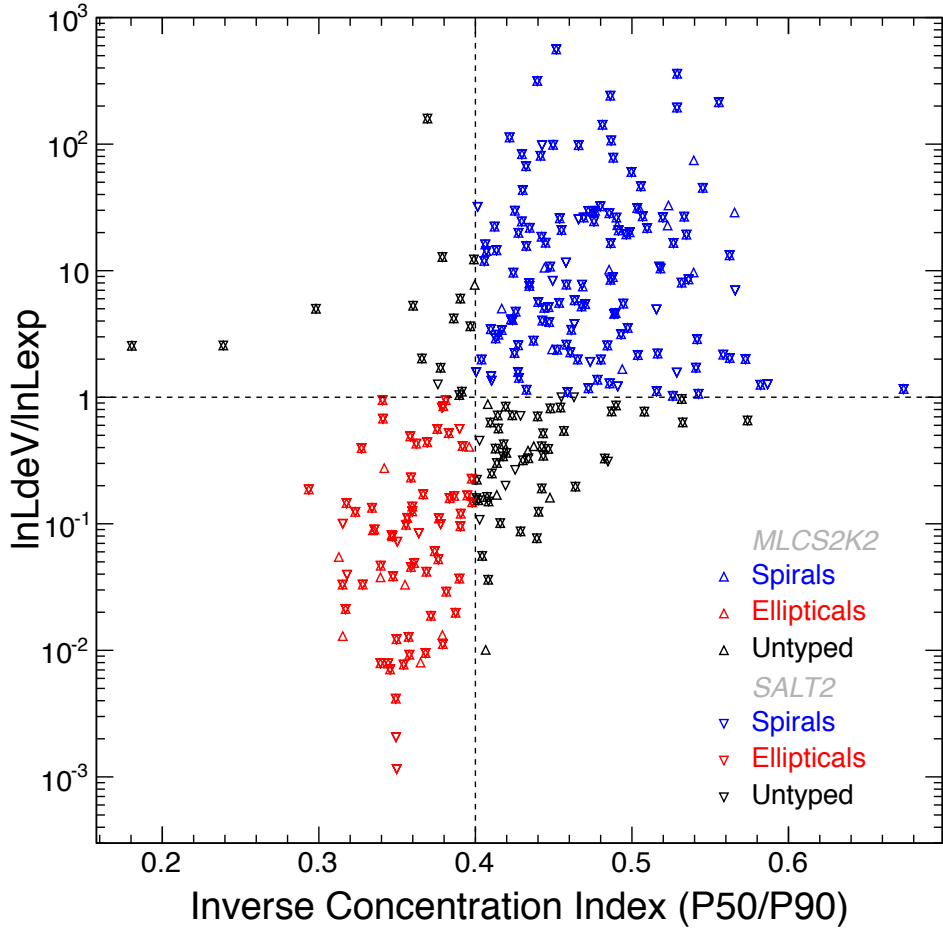


**Figure 7.2:** Determination of the morphology of the host galaxies using the inverse concentration index and the comparison of the likelihoods for the fits to a de Vaucouleur and an exponential Sérsic brightness profile. The y-axis shows the ratio of the logarithmic likelihoods. The dashed lines show the division into elliptical and spiral galaxies. The two methods have to agree in order for a galaxy to be classified as either elliptical (red symbols) or spiral (blue symbols). Galaxies with unknown morphology are marked in black. SNe only present in either the MLCS2k2 sample or the SALT2 sample are marked with special symbols.

As explained in §7.1.2.1, we obtained from SDSS DR7 the  $r$ -band profiles of all host galaxies for two specific patterns: a pure exponential profile ( $n = 1$ ,  $a_1 = 1.68$ ) and a de Vaucouleur profile ( $n = 4$ ,  $a_4 = 7.67$ ) (see Ciotti, 1991, Graham et al., 2005, and references therein). We also obtained the likelihoods for the two fits. The exponential profile is better at describing the decrease in brightness for spiral galaxies, while the de Vaucouleurs profile is better at describing elliptical galaxies.

We consider that a galaxy has elliptical morphology when it has both an inverse concentration index lower than 0.4, and the likelihood for the de Vaucouleurs profile fit is larger than for the exponential fit. A galaxy is classified as spiral if the inverse concentration index is above 0.4, and the likelihood for the exponential profile fit is larger than for the de Vaucouleurs fit. Figure 7.2 illustrates this separation

**Table 7.1:** Number of SNe in the sample used for this analysis after applying selection cuts.

	Spec-Ia		Photo-Ia		Total	
	MLCS	SALT2	MLCS	SALT2	MLCS	SALT2
SN Ia sample ( $z < 0.45$ )	559		759		1318	
Redshift $< 0.25$	376		232		608	
Identified host galaxy	363		228		591	
LC quality cuts	228	217	115	125	343	342
LC parameter cuts	203	209	110	111	313	320
Consistent host type	160	164	79	82	239	246
Distance cuts	128	132	64	65	192	197

	Spiral hosts		Elliptical hosts		Total	
	MLCS	SALT2	MLCS	SALT2	MLCS	SALT2
With host type	159	166	80	80	239	246
Distance cuts	127	131	65	66	192	197

in morphology. Supernovae for which the two morphological indicators disagree are removed from the analysis. There were 74 host galaxies which could not be typed as spiral or elliptical galaxies, leaving 239 SNe Ia in the MLCS2k2 sample and 246 in the SALT2 sample. The host type for each individual SN is presented in Table ??.

### 7.2.3 Galactocentric Distances (GCD)

From the position of the supernova and the center of the host galaxy ( $r = 0$ ), we can easily measure the angular separation between the supernova and its host, and calculate the physical distance using the redshift. We use the same flat cosmology assumed in the calculation of the Hubble Residuals, and a value for the Hubble Constant of  $70.4 \pm 1.4 \text{ km s}^{-1} \text{ Mpc}^{-1}$  taken from the Wilkinson Microwave Anisotropy Probe (WMAP) 7-Years results assuming a  $\Lambda\text{CDM+SZ+LENS}$  cosmological model and considering WMAP+BAO+H0 data (Jarosik et al., 2011).

Galaxies vary in morphology and size. For this reason it makes sense to normalize the SN-galaxy separation in order to be able to compare the light-curve parameters for SNe in different host galaxies at different distances. We use several different methods to normalize the distance from the SN to the galaxy center:

1. The Petrosian 50 radius (P50), defined as the radius of a circle containing 50% of the flux in a filter ( $r$  in our case), is used as one normalization.
2. The shape of the galaxy described by an elliptical Sérsic profile taking into account the orientation of the galaxy is used as another normalization. We distinguish between elliptical galaxies, which are fitted with a de Vaucouleurs (DEV)

## Supernova properties as a function of the distance to the host galaxy center

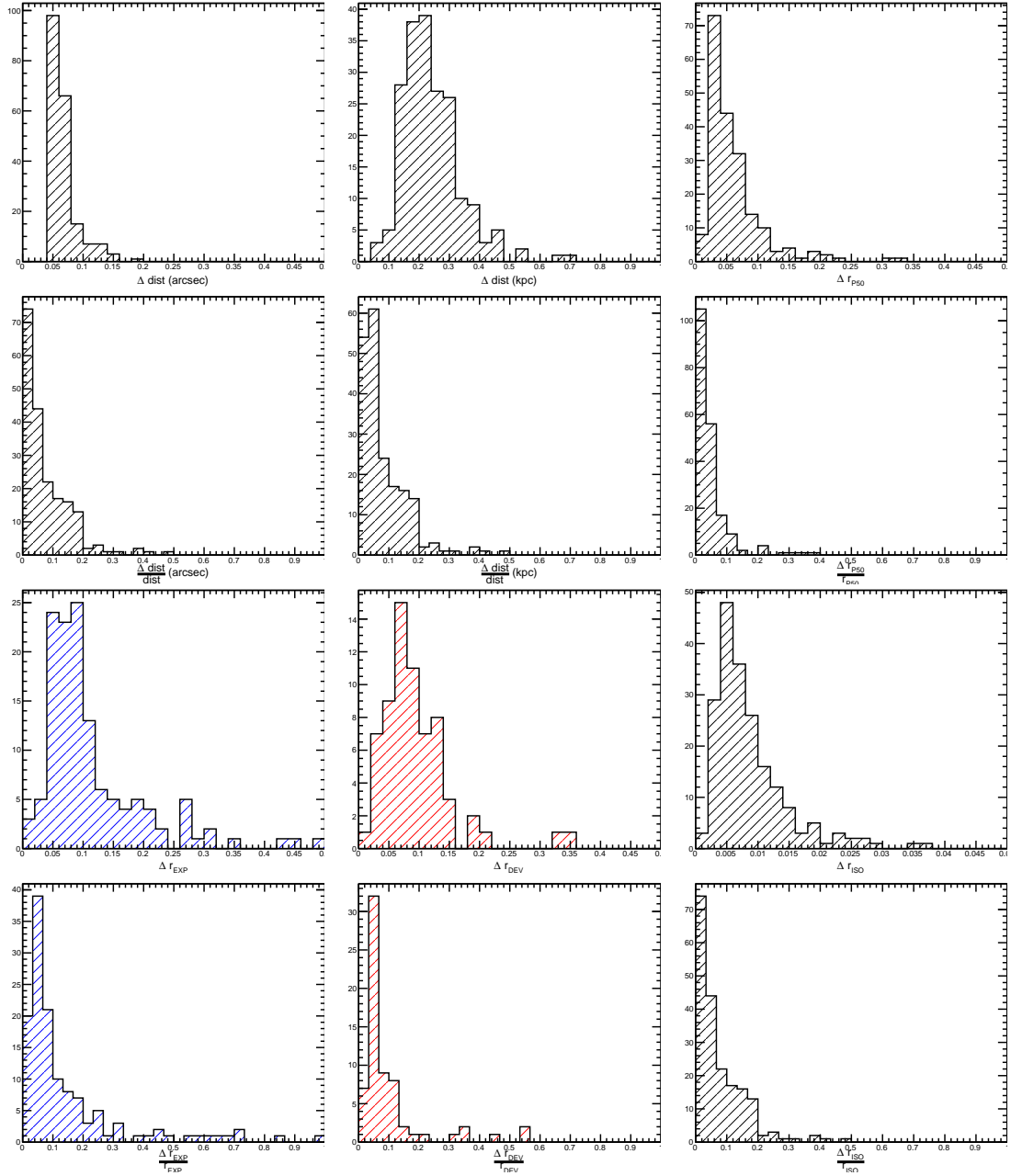


**Figure 7.3:** Absolute and relative error distribution for distances of SN in the SALT2 sample. Plots for the MLCS2k2 sample are very similar.

profile and spiral galaxies which are fitted with a pure exponential (EXP) profile (see Section 7.2.2 for the definitions).

3. We also normalize the distance using the ellipse estimated from the 25 mag/arcsec<sup>2</sup> isophote in the  $r$  band (ISO).

The necessary quantities (Petrosian radius, isophotal minor/major radii and position

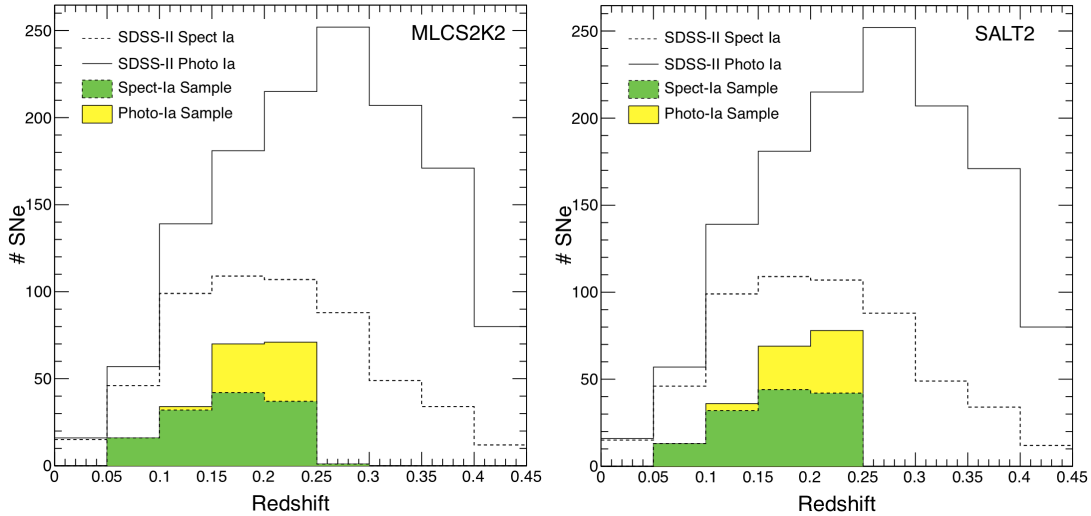


**Figure 7.4:** Redshift distribution for the SDSS SN Ia ( $z < 0.45$ ) sample and for the sample used in this analysis, divided into spectroscopically confirmed SNe Ia and photometrically identified SNe Ia. The left panel shows the sample used with the MLCS2k2 fitter, while the right panel shows the SALT2 sample.

angle, and for the two Sérsic profiles, the major and minor axis and orientation) are obtained from the SDSS DR7 catalogue (Abazajian et al., 2009). The  $r$  band data is used for all these quantities. We exclude the supernovae for which any of these quantities are missing. A detailed description of the measurement of the distance between the SN and the center of the host galaxy, is described in Appendix C. The different projected galactocentric distances for each supernova is presented in Table D.1.

Note that all measurements of the distance here are lower limits to the real separation from the center of the host galaxy due to the unknown inclination of the galactic plane with respect to the observer. We therefore refer to these distances as projected galactocentric distances (GCD).

We exclude all SNe where the normalized GCD is greater than 10 (for any of the normalizations), since these SNe are too far from the center of the closest galaxy for the galaxy to be considered as its host with certainty. We also remove all SNe where the normalizing distance (the radius of the galaxy in the direction of the SN) has a large uncertainty (if any of the radius estimates —P50, DEV/EXP, ISO— has a fractional error larger than 100 % or an absolute error larger than 0.5 arcsec). We also apply a cut in the SN-galaxy distance if the uncertainty in the distance is larger than the actual distance, or if the uncertainty in the distance is larger than either 0.5 arcsec or 1 kpc. The cuts were motivated by the distribution of errors for the full sample, which are shown in Fig. 7.3 for all distance measurements.

There were 47 SNe in the MLCS2k2 sample and 49 in the SALT2 sample which were excluded from the analysis because the matched host galaxy lacked one or more of the parameters needed for the distance calculation, because the supernova was too far from the center of the matched host or because the uncertainty in the sizes or distances was too large.

## Supernova properties as a function of the distance to the host galaxy center

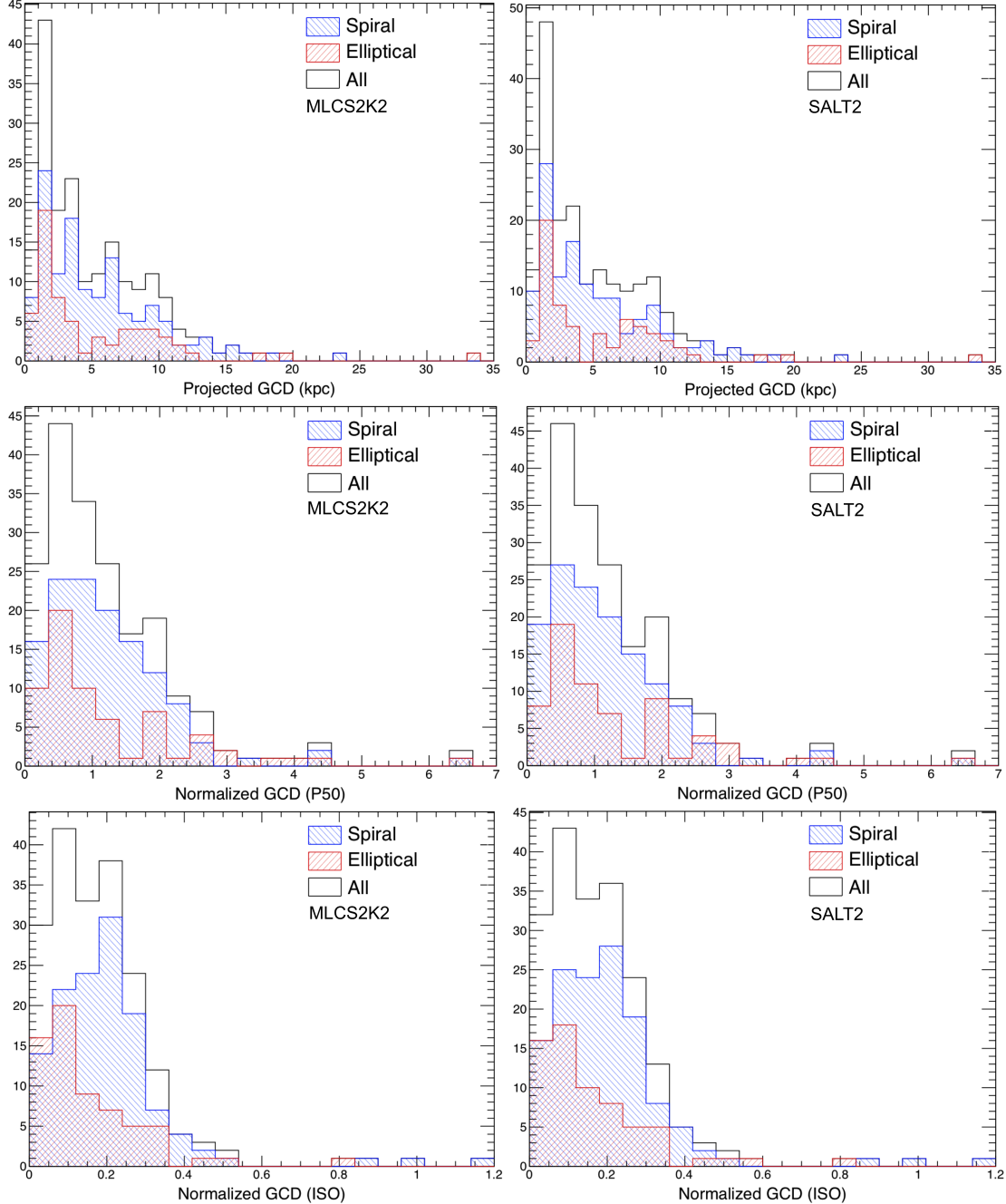


**Figure 7.5:** Distribution of distance between supernova and galaxy core in kpc (top), normalized with the P50 radius (middle), and normalized with the isophotal radius (bottom) for the SNe present in the final MLCS2k2 and SALT2 samples (after all cuts).

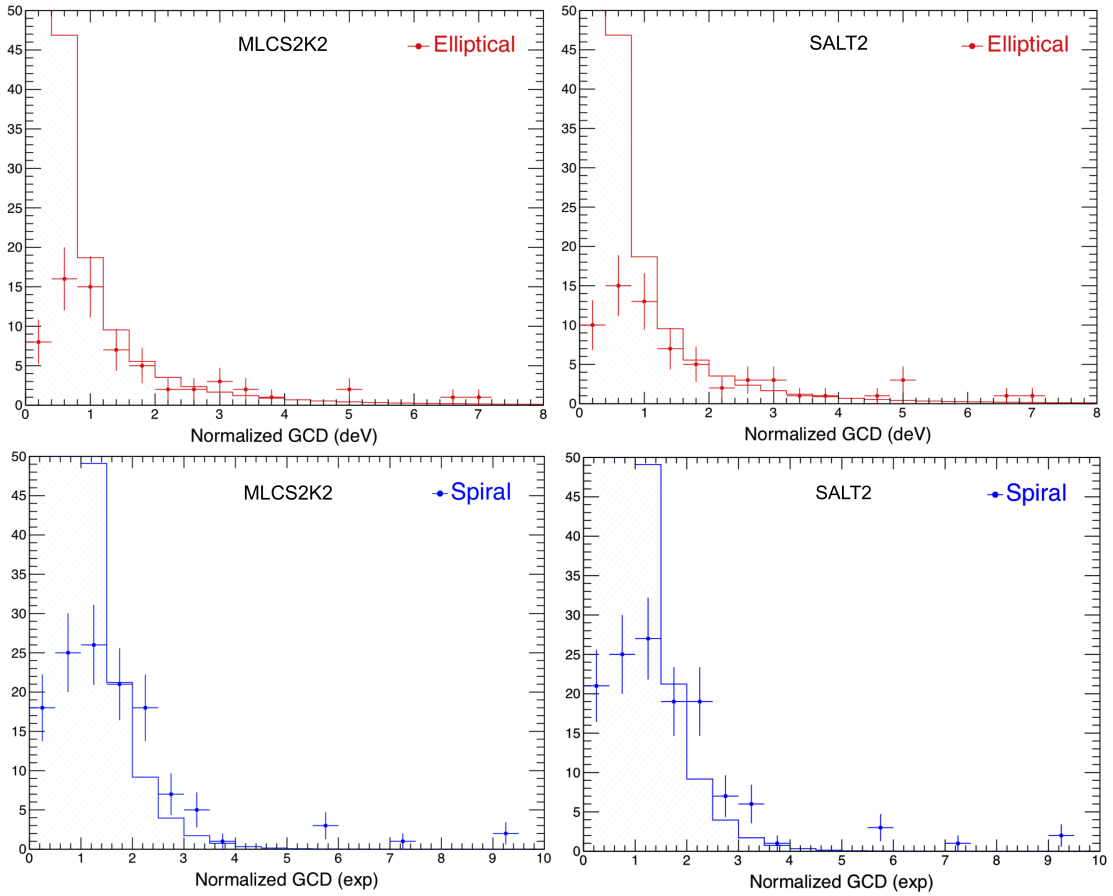


**Figure 7.6:** Comparison between the distribution of distance between supernova and galaxy core in Sérsic normalized radius, and the brightness profiles used for the normalizations.

Finally, after all cuts are considered, the analysis of the light-curve parameters as a function of the separation to the center of the supernova hosts is performed with 192 SNe for MLCS2k2 and 197 for SALT2. In Table 7.1, we present the number of SNe before and after each selection cut. All SNe in the analysis are listed in Table D.1 in Appendix D, together with the redshift, the estimated galactocentric distances and host type. In Fig. 7.4 the redshift distribution of the SNe is shown.

#### 7.2.3.1 Distance and parameter distributions

We show in Fig. 7.5 the distribution of the physical distance and the distributions of distance using the P50 and ISO normalizations for all SNe in our sample. In Fig. 7.6, we show a comparison between the distributions of the galactocentric distance Sérsic normalized and the corresponding galaxy brightness profiles. We find that the distribution of the distance in Sérsic units using both profiles agrees with the brightness of the galaxy at moderate and large distances. The detection of SNe is less efficient at shorter distances, due to the comparable brightness between the galaxy core and the

## Supernova properties as a function of the distance to the host galaxy center

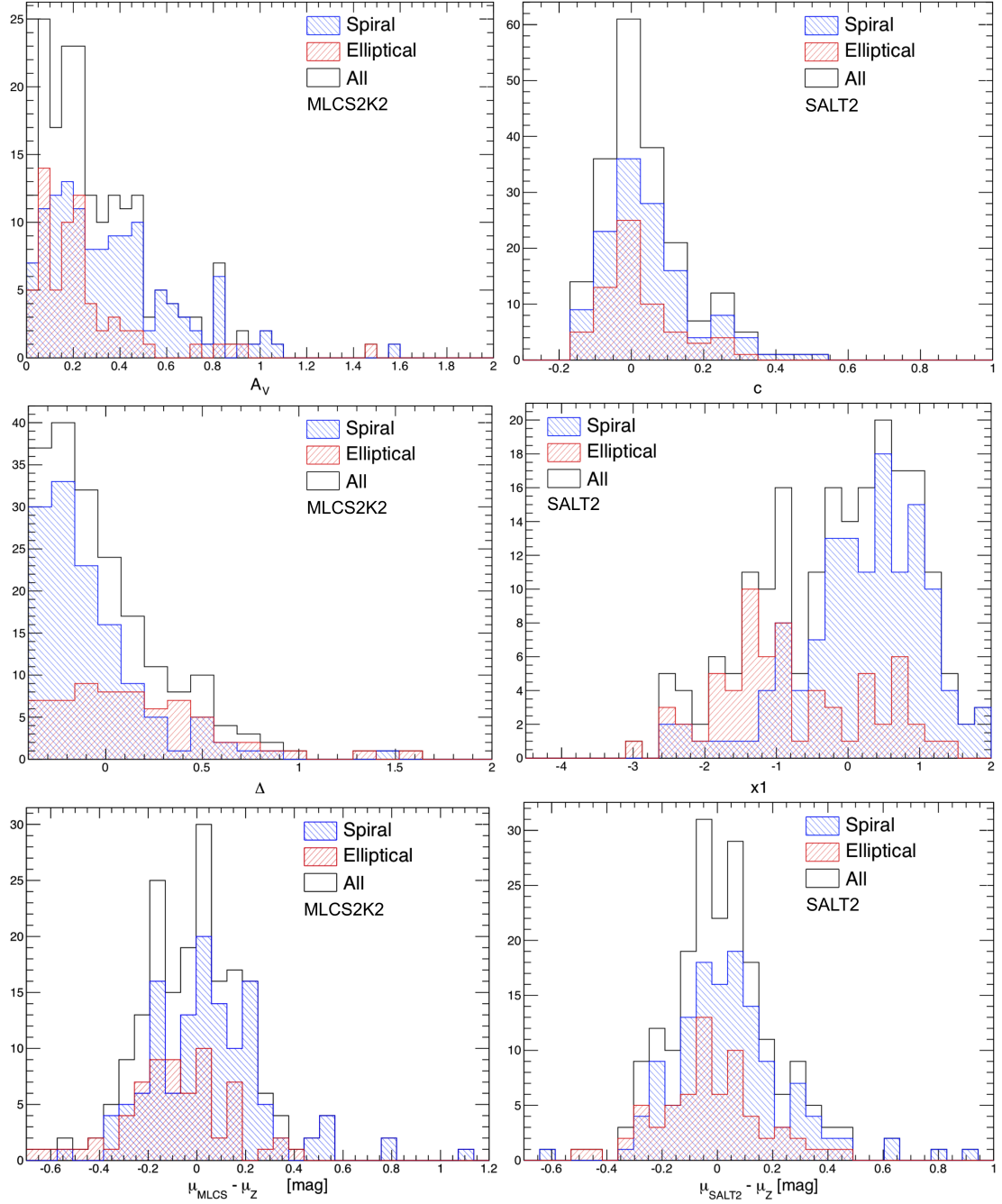


**Figure 7.7:** Distributions of the light-curve parameters and Hubble diagram residuals for both samples.

explosion. This suggests that the number of SNe is related with the local brightness of the galaxy at a certain location.

In Fig. 7.7, the distributions of the light-curve parameters of both samples are shown. In the  $c$  distributions we do not see any relevant difference in the color between SNe exploding in spiral and elliptical galaxies, both mean value and scatter

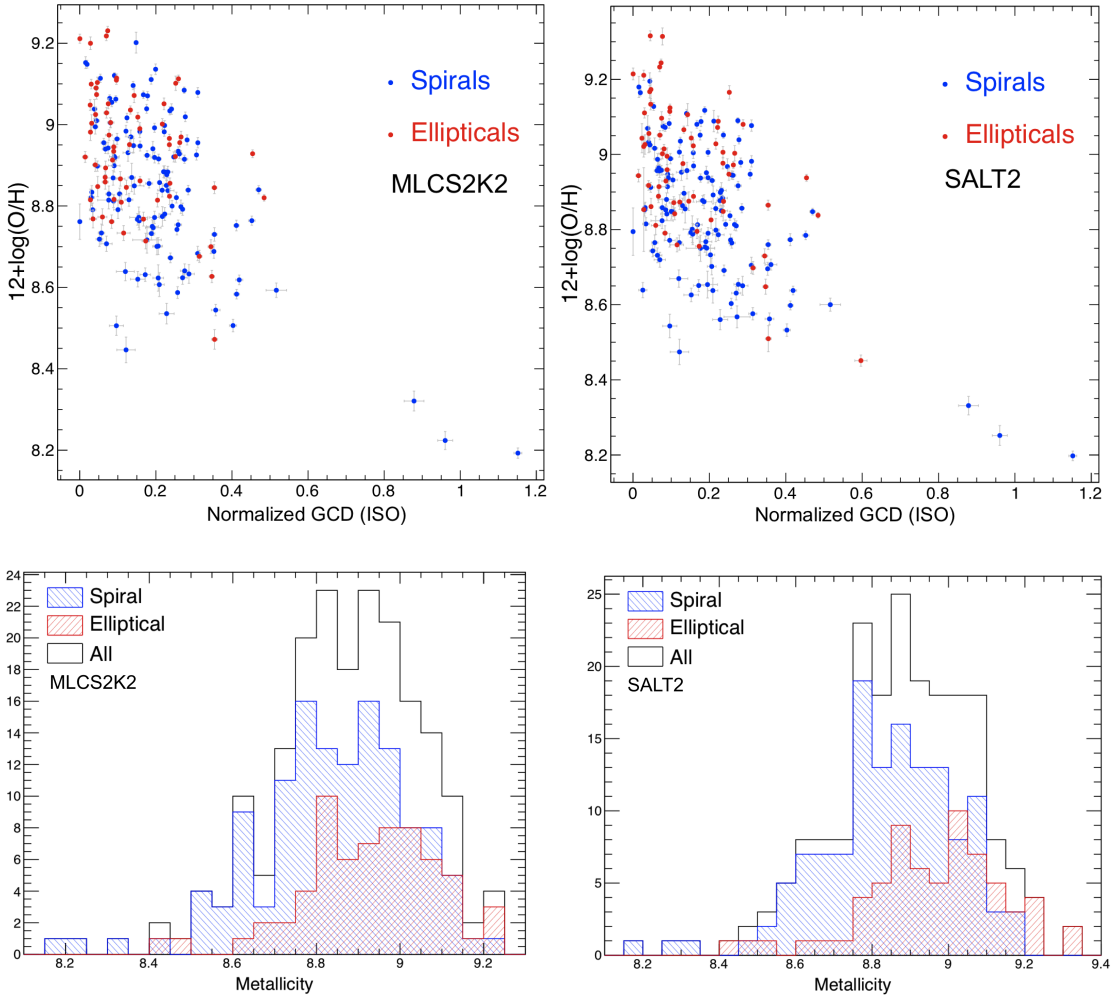


**Figure 7.8:** On top, the relations between the indirect measurement of the local metallicity and the galactocentric distance normalized to isophotal units. On the bottom, distributions of the indirect measurement of the local metallicity.

of the three distributions (also considering the whole sample) are very similar, while for  $A_V$  the mean value for SNe in ellipticals is lower ( $0.252 \pm 0.031$ ) than for SNe in spirals ( $0.363 \pm 0.024$ ), pointing to the known assumption that SNe exploding in spiral galaxies are more extinguished than those in ellipticals.

In the  $\Delta$  distributions, we see that SNe exploding in spiral galaxies tend to have wider light-curves and be brighter ( $\langle \Delta^{\text{spiral}} \rangle = -0.078 \pm 0.026$ ) than those in ellipticals ( $\langle \Delta^{\text{elliptical}} \rangle = 0.162 \pm 0.049$ ). This behavior is recovered in  $x_1$ : SNe in spiral galaxies tend to have higher values of  $x_1$  ( $\langle x_1^{\text{spiral}} \rangle = 0.189 \pm 0.080$ ) than SNe in elliptical galaxies ( $\langle x_1^{\text{elliptical}} \rangle = -0.780 \pm 0.129$ ), which points to brighter, and slow declining SNe. This recovers the result found in Hamuy et al. (2000).

Using the MLCS2k2 fitter, we find a difference between the mean value of the Hub-

ble residuals of SNe in elliptical galaxies ( $\langle \mu_{MLCS}^{elliptical} - \mu_Z \rangle = -0.093 \pm 0.026$ ) and those of SNe in spirals ( $\langle \mu_{MLCS}^{spiral} - \mu_Z \rangle = 0.051 \pm 0.022$ ) of  $0.144 \pm 0.034$ , while in SALT2, the difference is lower ( $0.073 \pm 0.030$ ). In both cases, the mean Hubble residuals are lower in ellipticals, which means brighter SNe after light-curve standarization.

#### 7.2.4 Metallicity

In addition to the distance measurements, we also use the indirect measurement of local metallicity used in [Boissier et al. \(2009\)](#), to look for dependences of light-curve parameters. They found the radial oxygen abundance from the  $B$  band absolute magnitude of the host ( $M_{B,gal}$ ), and the normalized distance of the supernova to the center of the host galaxy, in terms of the isophote of 25 mag/arcsec<sup>2</sup> ( $R_{25}$ ), the same we used for the ISO normalization. Explicitly:

$$[12 + \log(O/H)](R) = 6.837 - 0.104 M_B + \left( \frac{R}{R_{25}} - 0.4 \right) (0.204 + 0.04 M_B), \quad (7.5)$$

where  $R/R_{25}$  is the normalized distance from the center of the host to the position of the SN in ISO units. In SDSS-DR7 the apparent magnitudes of all galaxies are in the SDSS magnitude system. In order to transform these measurements to the Johnson system  $B$  band, we used the relations in [Blanton et al. \(2007\)](#):

$$B = g + 0.2354 + 0.3915 [(g - r) - 0.6102] \quad (7.6)$$

$$R = r - 0.0576 - 0.3718 [(r - i) - 0.2589] \quad (7.7)$$

Once we have the apparent  $B$  magnitude of the host galaxy, we can calculate the absolute magnitude using the distance modulus expression. The last step is to measure the K-correction needed to transform the  $B$  magnitude at the redshift of the host to redshift zero ( $M_B(z=0) = M_B(z) - K_{corr}$ ). For this we use the analytical approximation found in [Chilingarian et al. \(2010\)](#):

$$\begin{aligned} K_{corr} = & (-1.99412 z + 15.9592 z^2 - 101.876 z^3 + 299.29 z^4 - 304.526 z^5) \\ & + (B - R)^1 (3.45377 z - 3.99873 z^2 - 44.4243 z^3 + 86.789 z^4) \\ & + (B - R)^2 (0.818214 z + 6.44175 z^2 - 12.6224 z^3) \\ & + (B - R)^3 (-0.630543 z + 0.828667 z^2). \end{aligned} \quad (7.8)$$

In Fig. 7.8 the relation between the measurement of the local metallicity with the isophotal normalized distance is plotted. In the same figure it is also shown the distribution of the measured local metallicity for both samples, where it can be seen that, in general, elliptical galaxies have higher metallicity than spiral galaxies, as expected.

### 7.3 Results

We have looked for trends in SN Ia light-curve parameters with projected galactocentric distances (GCD). The photometric and the spectroscopic sub-samples were

analysed together since no significant differences were detected between them. The results obtained hold for both sub samples. We look for correlations for the complete sample, as well as when dividing the sample according to host galaxy morphology (spiral and elliptical).

We correlate four light-curve parameters (MLCS2k2:  $A_V, \Delta$  and SALT2:  $x_1, c$ ) and the Hubble residuals with different measurements of the distance to the center of the host galaxy (physical GCD, and normalized GCD expressed in P50, Sérsic (DEV/EXP), and ISO radii), and local metallicity. For every combination of light-curve parameter and distance measurement, we bin the SNe in distance and calculate the mean, both for the light-curve parameter and the distance. In each bin, the uncertainty in the mean light-curve parameter is calculated as the RMS in the bin divided by the square root of the number of SNe in the bin. The uncertainty in the distance is taken as the width of the bin. We also measure the median and the weighted mean in each bin, in order to compare with the results obtained with the mean. The expressions used for these calculations are described in Appendix B.2. For the physical GCD, we use a bin width of 0.5 kpc, while for the normalized GCD we use bins of width 0.25 for P50 and Sérsic (DEV/EXP) and of 0.05 for ISO. When a bin contains less than 5 SNe, this bin is joined with the next one until there are at least 5 SNe. We then perform a linear fit to the binned measurements taking into account their uncertainties. The reduced  $\chi^2$  is calculated, as well as the significance of the slope (the slope divided by the uncertainty of the slope as obtained from the linear fit). Figures 7.9 and 7.10 show the MLCS2k2 parameters for each supernova as a function of the projected separation in various units, together with the binned mean values and the best fitted lines. Figures 7.11 and 7.12 show the corresponding figures for SALT2. The results from these correlation studies are presented in the upper panels of Tables 7.2 to 7.7. For these linear fits to multiple bins, we focus on the results where a dependence with distance is preferred with more than  $2\sigma$  significance and the reduced  $\chi^2$  is lower than 2. A cut in  $\chi^2$  is necessary since some of the light-curve parameters might be correlated with distance, but with a correlation which cannot be modeled with a simple linear fit. For these scenarios we solely study the two-bin analysis (described below), which is model independent.

We also look for the same correlations but using only two bins, “Near” and “Far”, with equal number of objects in each. Note that this means that the distance where the near/far split is made is different depending on whether we study all galaxies, spiral galaxies only or elliptical galaxies only. We then calculate the mean values for the two bins, as well as their uncertainties (the RMS of the distribution in the bin divided by the square root of the number of objects per bin). We study the significance of the difference in the two means by taking the difference divided by the uncertainty. Finally we calculate the difference in the scatter for the two bins and compare it with its uncertainty to obtain the significance. The results from the correlation studies with two bins are presented in the lower panels of Tables 7.2 to 7.7. For the two-bin analysis, we focus on results where the difference between the two means is greater than  $2\sigma$ .

As a consistency check we also fit the measurement points, without binning, with a straight line. The errors on the individual points are increased to include the intrinsic

## Supernova properties as a function of the distance to the host galaxy center

**Table 7.2:** Results when correlating MLCS2k2- $A_V$  with distance binned in multiple bins of equal size (upper table) and binned in a near and a far sample, with equal number of events in each bin (lower table).

Distance unit	Host type	Slope	Sig. <sup>a</sup>	$\chi^2/\text{dof}$	dof
kpc	All	-0.0082 ± 0.0017	-4.9	0.6	17
	Elliptical	0.0009 ± 0.0031	0.3	0.9	7
	Spiral	-0.0031 ± 0.0044	-0.7	1.4	13
P50	All	-0.039 ± 0.016	-2.5	0.6	9
	Elliptical	-0.012 ± 0.016	-0.8	1.0	5
	Spiral	-0.046 ± 0.023	-2.0	1.1	8
ISO	All	-0.21 ± 0.10	-2.1	3.4	7
	Elliptical	-0.31 ± 0.18	-1.8	1.1	3
	Spiral	-0.33 ± 0.13	-2.5	3.5	6
deV	Elliptical	-0.018 ± 0.012	-1.4	0.9	5
exp	Spiral	-0.071 ± 0.013	-5.4	4.5	10

Distance unit	Host type	Cut <sup>b</sup>	Mean $A_V$				Scatter of $A_V$			
			Near $\bar{n}$	Far $\bar{f}$	Difference $\bar{f} - \bar{n}$	Sig. <sup>a</sup>	Near $\sigma_n$	Far $\sigma_f$	Difference $\sigma_f - \sigma_n$	Sig. <sup>a</sup>
kpc	All	3.83	0.346 ± 0.031	0.305 ± 0.023	-0.042 ± 0.039	-1.1	0.305 ± 0.036	0.223 ± 0.019	-0.082 ± 0.040	-2.0
	Elliptical	2.94	0.265 ± 0.049	0.238 ± 0.036	-0.027 ± 0.061	-0.4	0.282 ± 0.081	0.206 ± 0.039	-0.077 ± 0.090	-0.9
	Spiral	4.35	0.403 ± 0.038	0.322 ± 0.028	-0.082 ± 0.047	-1.7	0.305 ± 0.038	0.222 ± 0.022	-0.083 ± 0.044	-1.9
P50	All	0.97	0.343 ± 0.030	0.308 ± 0.024	-0.035 ± 0.039	-0.9	0.295 ± 0.037	0.237 ± 0.020	-0.058 ± 0.042	-1.4
	Elliptical	0.75	0.265 ± 0.050	0.238 ± 0.036	-0.027 ± 0.061	-0.4	0.285 ± 0.081	0.201 ± 0.040	-0.084 ± 0.090	-0.9
	Spiral	1.04	0.420 ± 0.038	0.305 ± 0.027	-0.115 ± 0.047	-2.5	0.302 ± 0.037	0.218 ± 0.023	-0.084 ± 0.043	-1.9
ISO	All	0.16	0.355 ± 0.031	0.296 ± 0.022	-0.059 ± 0.038	-1.5	0.307 ± 0.035	0.217 ± 0.019	-0.090 ± 0.040	-2.3
	Elliptical	0.10	0.263 ± 0.050	0.240 ± 0.035	-0.023 ± 0.061	-0.4	0.287 ± 0.080	0.200 ± 0.040	-0.087 ± 0.090	-1.0
	Spiral	0.19	0.406 ± 0.038	0.319 ± 0.028	-0.087 ± 0.047	-1.8	0.301 ± 0.038	0.225 ± 0.022	-0.076 ± 0.044	-1.7
deV	Elliptical	1.00	0.231 ± 0.033	0.274 ± 0.052	0.044 ± 0.062	0.7	0.189 ± 0.044	0.295 ± 0.078	0.106 ± 0.090	1.2
exp	Spiral	1.35	0.410 ± 0.037	0.315 ± 0.029	-0.095 ± 0.047	-2.0	0.297 ± 0.038	0.230 ± 0.024	-0.066 ± 0.045	-1.5

<sup>a</sup> Significance of non-zero result, value divided by uncertainty.

<sup>b</sup> The distance where the ‘near’ and ‘far’ bins were separated.

spread in the values, by adding in quadrature a term giving a reduced  $\chi^2$  of 1.

We find two (related) trends with very high significance and good fit quality: both  $A_V$  and  $c$  decrease with physical GCD, with the slopes of the linear fits being respectively  $4.9$  and  $4.4\sigma$  away from zero. These and other correlations with lower significance are presented in detail in the following.

### 7.3.1 Correlations between projected distance and supernova color ( $A_V$ , $c$ )

#### 7.3.1.1 MLCS2k2

When studying all SNe Ia, regardless of host galaxy type, we find that the fitted  $A_V$  from MLCS2k2 decreases with SN-galaxy distance (see Table 7.2). In the multi-bin analysis we find deviations from a non-evolving  $A_V$  of  $4.9$  and  $2.5\sigma$  for physical distances and distances normalized to P50, respectively. The reduced  $\chi^2$  of the fit is  $0.6$  in both cases. The fit to  $A_V$  as a function of normalized ISO distance is bad. Using a two-bin analysis, we confirm the sign of the slope, but with lower significances ( $1.1$ ,  $0.9$  and  $1.5\sigma$  for the three different distances) due to the loss of precision in using

only two bins. Using the linear fit to the unbinned data we find trends of similar significance.

When splitting the sample into SNe in elliptical and spiral galaxies we find indications that the trend of decreasing  $A_V$  with distance is driven by the SNe in spiral galaxies, where the deviation from a non-evolving  $A_V$  is 0.7 and 2.0  $\sigma$  for the multi-bin analysis for physical distances and P50 normalized distances. For the two-bin analysis the deviations varies between 1.7 and 2.5  $\sigma$  for the four different types of distances (now also including EXP normalized distances). This is also confirmed with the linear fit to the unbinned data. The sample of SNe in elliptical galaxies is consistent with a non-evolving  $A_V$  with very low significances in the two-bin analysis, and slopes of varying signs.

A potentially confusing result from the multi-bin analysis of  $A_V$  is that the fit to the full sample, for distances measured in kpc, has a steeper slope than for the samples of SNe in elliptical and spiral galaxies separately. Naively one would expect a slope for the full sample between that of the elliptical and spiral samples. The reason for this, seemingly, contradictory result is the different binning. E.g., the sample of all SNe has the center of the last bin at a significantly larger distance than the two other samples, thus increasing the lever arm. As a consistency check, we redid the binned analysis, using the same binning for spiral galaxies and the full sample as for the elliptical sample (which is the smallest of the three). Using equal binning, we obtained a fitted line for the full sample which was in between the lines for elliptical and spiral galaxies. We still see a slope, but with decreased significance because of the lower sensitivity of the fit with lesser bins.

Studying Figs. 7.9 and 7.10, we can see that the most extinguished explosions are close to the center of their host galaxies. A natural consequence is that the scatter diminishes with distance. This is particularly visible when studying the full set of galaxies, comparing the near and far sub samples divided in physical distance (2.0  $\sigma$ ) and normalized with ISO (2.3  $\sigma$ ). We also find that SNe Ia with high values of  $A_V$  preferentially explode in spiral galaxies. Out of the 65 elliptical host galaxies only 6 (9%) have SNe with an  $A_V > 0.5$ , while there are 29 (23%) in the 127 spiral hosts. The mean value of  $A_V$  for the SNe in elliptical galaxies was found to be  $\langle A_V^{\text{elliptical}} \rangle = 0.25 \pm 0.03$ , while it for SNe in spiral galaxies was  $\langle A_V^{\text{spiral}} \rangle = 0.36 \pm 0.02$ .

### 7.3.1.2 SALT2

We now turn to the color term  $c$  from the SALT2 analysis to see if we reproduce similar trends (see Table 7.3). For the linear fit to multiple bins, we also find that  $c$  decreases, with 4.4 and 1.5  $\sigma$  significance, for the full sample with increasing physical distances and distances normalized with the P50 radius. As for  $A_V$ , the fit to distances normalized with ISO was bad. The corresponding numbers when only studying spiral galaxies are 1.5 and 1.8  $\sigma$ . For SNe in elliptical galaxies, the fits are consistent with a non-evolving  $c$ .

Using the two-bin analysis we confirm the results, but with lower significances, the highest being 1.5  $\sigma$  when correlating  $c$  for spiral galaxies with the ISO and EXP

## Supernova properties as a function of the distance to the host galaxy center

**Table 7.3:** Results when correlating SALT2- $c$  with distance binned in multiple bins of equal size (upper table) and binned in a near and a far sample, with equal number of events in each bin (lower table).

Distance unit	Host type	Slope	Sig. <sup>a</sup>	$\chi^2/\text{dof}$	dof
kpc	All	-0.0032 ± 0.0007	-4.4	0.9	18
	Elliptical	-0.0007 ± 0.0021	-0.3	1.0	6
	Spiral	-0.0031 ± 0.0021	-1.5	0.7	11
P50	All	-0.011 ± 0.008	-1.5	0.9	9
	Elliptical	-0.004 ± 0.010	-0.4	0.7	6
	Spiral	-0.019 ± 0.011	-1.8	1.1	8
ISO	All	-0.09 ± 0.04	-2.0	3.0	8
	Elliptical	-0.02 ± 0.08	-0.3	0.9	4
	Spiral	-0.13 ± 0.06	-2.1	4.2	6
deV	Elliptical	-0.006 ± 0.007	-0.9	0.6	6
exp	Spiral	-0.009 ± 0.008	-1.2	3.5	10

Distance unit	Host type	Cut <sup>b</sup>	Mean $c$				Scatter of $c$			
			Near $\bar{n}$	Far $\bar{f}$	Difference $\bar{f} - \bar{n}$	Sig. <sup>a</sup>	Near $\sigma_n$	Far $\sigma_f$	Difference $\sigma_f - \sigma_n$	Sig. <sup>a</sup>
kpc	All	3.74	0.038 ± 0.012	0.030 ± 0.011	-0.007 ± 0.017	-0.4	0.121 ± 0.012	0.114 ± 0.010	-0.008 ± 0.016	-0.5
	Elliptical	3.26	0.005 ± 0.016	0.026 ± 0.020	0.020 ± 0.026	0.8	0.092 ± 0.016	0.118 ± 0.016	0.025 ± 0.022	1.1
	Spiral	3.90	0.054 ± 0.016	0.032 ± 0.014	-0.022 ± 0.021	-1.0	0.131 ± 0.015	0.111 ± 0.013	-0.019 ± 0.020	-1.0
P50	All	0.97	0.038 ± 0.012	0.030 ± 0.012	-0.007 ± 0.017	-0.4	0.117 ± 0.012	0.118 ± 0.010	0.000 ± 0.016	0.0
	Elliptical	0.81	0.010 ± 0.016	0.021 ± 0.020	0.012 ± 0.026	0.4	0.095 ± 0.015	0.116 ± 0.016	0.022 ± 0.022	1.0
	Spiral	0.98	0.056 ± 0.015	0.031 ± 0.015	-0.025 ± 0.021	-1.2	0.123 ± 0.015	0.120 ± 0.013	-0.003 ± 0.020	-0.2
ISO	All	0.16	0.045 ± 0.012	0.023 ± 0.011	-0.021 ± 0.017	-1.3	0.124 ± 0.012	0.110 ± 0.010	-0.013 ± 0.015	-0.9
	Elliptical	0.11	0.011 ± 0.017	0.020 ± 0.020	0.008 ± 0.026	0.3	0.096 ± 0.015	0.116 ± 0.017	0.020 ± 0.022	0.9
	Spiral	0.18	0.059 ± 0.016	0.027 ± 0.014	-0.032 ± 0.021	-1.5	0.128 ± 0.015	0.114 ± 0.013	-0.014 ± 0.020	-0.7
deV	Elliptical	1.08	0.012 ± 0.016	0.019 ± 0.020	0.007 ± 0.026	0.3	0.094 ± 0.015	0.117 ± 0.016	0.023 ± 0.022	1.0
exp	Spiral	1.31	0.059 ± 0.015	0.028 ± 0.014	-0.031 ± 0.021	-1.5	0.126 ± 0.012	0.116 ± 0.017	-0.009 ± 0.021	-0.5

<sup>a</sup> Significance of non-zero result, value divided by uncertainty.

<sup>b</sup> The distance where the ‘near’ and ‘far’ bins were separated.

normalized distances. The same result is found when using a linear fit to unbinned data, with significances of similar strengths.

Just as for the MLCS2κ2  $A_V$  we find a trend between  $c$  and host galaxy type. The mean  $c$  for SNe in spiral galaxies is  $\langle c^{\text{spiral}} \rangle = 0.043 \pm 0.11$ , while it is  $\langle c^{\text{elliptical}} \rangle = 0.015 \pm 0.013$  for elliptical galaxies.

We find no significant differences in scatter between near samples and far samples when it comes to  $c$ .

### 7.3.2 Correlations between projected distance and light-curve shape ( $\Delta$ , $x_1$ )

When looking for correlations between the projected GCD and the MLCS2κ2  $\Delta$  parameter (Table 7.4) we find a weak correlation for elliptical galaxies, using the multi-binning method, where larger  $\Delta$  are found at larger galactocentric distances. The significance of an evolving  $\Delta$  is 2.2, 1.9, 1.8 and 2.4  $\sigma$  for the four different distance measurements (physical, P50, ISO, deV). Note that the fit to  $\Delta$  as a function of physical distance is of limited quality, with a reduced  $\chi^2$  of 2.1. The trend is also visible in the two-bin data, but with lower significance: 1.9, 1.8, 1.7 and 1.3  $\sigma$ . In the fit to unbinned data the correlation is only seen for distances normalized using p50 and deV (1.5 and

**Table 7.4:** Results when correlating MLCS2k2- $\Delta$  with distance binned in multiple bins of equal size (upper table) and binned in a near and a far sample, with equal number of events in each bin (lower table).

Distance unit	Host type	Slope	Sig. <sup>a</sup>	$\chi^2/\text{dof}$	dof
kpc	All	-0.0068 ± 0.0030	-2.2	1.9	17
	Elliptical	0.0220 ± 0.0092	2.4	2.1	7
	Spiral	-0.0077 ± 0.0047	-1.6	0.5	13
P50	All	0.008 ± 0.028	0.3	1.1	9
	Elliptical	0.092 ± 0.050	1.9	0.7	5
	Spiral	-0.028 ± 0.023	-1.2	3.1	8
ISO	All	-0.17 ± 0.11	-1.6	1.2	7
	Elliptical	0.81 ± 0.45	1.8	1.1	3
	Spiral	-0.06 ± 0.14	-0.4	1.4	6
deV	Elliptical	0.103 ± 0.043	2.4	1.4	5
exp	Spiral	-0.008 ± 0.019	-0.5	2.1	10

Distance unit	Host type	Cut <sup>b</sup>	Mean $\Delta$				Scatter of $\Delta$			
			Near $\bar{n}$	Far $\bar{f}$	Difference $\bar{f} - \bar{n}$	Sig. <sup>a</sup>	Near $\sigma_n$	Far $\sigma_f$	Difference $\sigma_f - \sigma_n$	Sig. <sup>a</sup>
kpc	All	3.83	-0.002 ± 0.032	0.008 ± 0.039	0.009 ± 0.050	0.2	0.314 ± 0.032	0.378 ± 0.048	0.063 ± 0.057	1.1
	Elliptical	2.94	0.073 ± 0.058	0.253 ± 0.076	0.180 ± 0.095	1.9	0.333 ± 0.066	0.428 ± 0.069	0.094 ± 0.096	1.0
	Spiral	4.35	-0.068 ± 0.034	-0.088 ± 0.039	-0.020 ± 0.051	-0.4	0.270 ± 0.027	0.308 ± 0.064	0.039 ± 0.069	0.6
P50	All	0.97	0.008 ± 0.035	-0.002 ± 0.036	-0.010 ± 0.050	-0.2	0.339 ± 0.040	0.355 ± 0.044	0.016 ± 0.060	0.3
	Elliptical	0.75	0.078 ± 0.062	0.247 ± 0.072	0.169 ± 0.095	1.8	0.358 ± 0.063	0.409 ± 0.073	0.051 ± 0.096	0.5
	Spiral	1.04	-0.042 ± 0.041	-0.115 ± 0.031	-0.073 ± 0.051	-1.4	0.325 ± 0.054	0.243 ± 0.040	-0.081 ± 0.067	-1.2
ISO	All	0.16	0.030 ± 0.035	-0.024 ± 0.035	-0.054 ± 0.050	-1.1	0.348 ± 0.039	0.345 ± 0.046	-0.003 ± 0.060	-0.0
	Elliptical	0.10	0.082 ± 0.062	0.244 ± 0.073	0.161 ± 0.096	1.7	0.358 ± 0.062	0.410 ± 0.073	0.052 ± 0.096	0.5
	Spiral	0.19	-0.045 ± 0.040	-0.112 ± 0.032	-0.068 ± 0.051	-1.3	0.320 ± 0.055	0.250 ± 0.038	-0.070 ± 0.067	-1.0
deV	Elliptical	1.00	0.099 ± 0.061	0.226 ± 0.075	0.128 ± 0.097	1.3	0.348 ± 0.063	0.425 ± 0.073	0.077 ± 0.096	0.8
exp	Spiral	1.35	-0.057 ± 0.038	-0.099 ± 0.035	-0.042 ± 0.051	-0.8	0.300 ± 0.059	0.277 ± 0.037	-0.024 ± 0.069	-0.3

<sup>a</sup> Significance of non-zero result, value divided by uncertainty.

<sup>b</sup> The distance where the ‘near’ and ‘far’ bins were separated.

$1.3\sigma$ ).

When studying the sample of spiral galaxies, we find only very weak correlations, of the opposite trend as for the SNe in elliptical galaxies. The two most significant correlations are for distances in kpc and normalised to P50 (1.6 and 1.2  $\sigma$ ). However, using a two bin analysis and the fit to unbinned data these correlations are even more insignificant.

The SALT2  $x_1$  parameter provides another measurement of the light-curve width. Since  $x_1$  is inversely proportional to the decline rate of the light-curve we would expect a correlation with the opposite sign compared to the correlation with MLCS2k2- $\Delta$ . We find no correlations with  $2\sigma$  or larger significance in either the multi-binning or the two-bin analyses (see Table 7.5). The highest significance of a deviation from a constant  $x_1$  which we find is for  $x_1$  which diminishes with the P50 normalized distance (1.9  $\sigma$ ). We also find correlations, of similar strength, where  $x_1$  increases with the ISO normalized distance for all galaxies. However, since these two correlations are only visible for one sample (ellipticals, and full sample), for one distance measurement and at low significance, they are most likely spurious.

## Supernova properties as a function of the distance to the host galaxy center

**Table 7.5:** Results when correlating SALT2- $x_1$  with distance binned in multiple bins of equal size (upper table) and binned in a near and a far sample, with equal number of events in each bin (lower table).

Distance unit	Host type	Slope	Sig. <sup>a</sup>	$\chi^2/\text{dof}$	dof
kpc	All	$0.0138 \pm 0.0140$	1.0	1.7	18
	Elliptical	$0.0042 \pm 0.0202$	0.2	0.7	6
	Spiral	$0.0206 \pm 0.0176$	1.2	0.8	11
P50	All	$-0.037 \pm 0.080$	-0.5	2.0	9
	Elliptical	$-0.195 \pm 0.100$	-1.9	1.3	6
	Spiral	$0.032 \pm 0.073$	0.4	3.5	8
ISO	All	$0.73 \pm 0.39$	1.9	1.6	8
	Elliptical	$-0.64 \pm 0.87$	-0.7	1.7	4
	Spiral	$0.07 \pm 0.50$	0.1	1.4	6
deV	Elliptical	$-0.007 \pm 0.097$	-0.1	0.5	6
exp	Spiral	$-0.000 \pm 0.065$	-0.0	1.1	10

Distance unit	Host type	Cut <sup>b</sup>	Mean $x_1$				Scatter of $x_1$			
			Near	Far	Difference	Sig. <sup>a</sup>	Near	Far	Difference	Sig. <sup>a</sup>
kpc	All	3.74	$-0.198 \pm 0.106$	$-0.072 \pm 0.108$	$0.126 \pm 0.151$	0.8	$1.059 \pm 0.063$	$1.065 \pm 0.070$	$0.006 \pm 0.094$	0.1
	Elliptical	3.26	$-0.765 \pm 0.181$	$-0.795 \pm 0.183$	$-0.030 \pm 0.258$	-0.1	$1.040 \pm 0.090$	$1.052 \pm 0.123$	$0.012 \pm 0.152$	0.1
	Spiral	3.90	$0.101 \pm 0.117$	$0.280 \pm 0.107$	$0.179 \pm 0.159$	1.1	$0.952 \pm 0.090$	$0.866 \pm 0.095$	$-0.086 \pm 0.131$	-0.7
P50	All	0.97	$-0.206 \pm 0.105$	$-0.064 \pm 0.108$	$0.141 \pm 0.151$	0.9	$1.050 \pm 0.063$	$1.074 \pm 0.069$	$0.024 \pm 0.094$	0.3
	Elliptical	0.81	$-0.695 \pm 0.183$	$-0.865 \pm 0.180$	$-0.170 \pm 0.257$	-0.7	$1.054 \pm 0.089$	$1.032 \pm 0.126$	$-0.022 \pm 0.154$	-0.1
	Spiral	0.98	$0.124 \pm 0.118$	$0.256 \pm 0.106$	$0.131 \pm 0.159$	0.8	$0.963 \pm 0.093$	$0.858 \pm 0.093$	$-0.105 \pm 0.131$	-0.8
ISO	All	0.16	$-0.270 \pm 0.110$	$0.001 \pm 0.103$	$0.272 \pm 0.150$	1.8	$1.090 \pm 0.061$	$1.019 \pm 0.071$	$-0.070 \pm 0.094$	-0.7
	Elliptical	0.11	$-0.676 \pm 0.188$	$-0.883 \pm 0.174$	$-0.207 \pm 0.256$	-0.8	$1.080 \pm 0.085$	$1.000 \pm 0.132$	$-0.080 \pm 0.157$	-0.5
	Spiral	0.18	$0.116 \pm 0.116$	$0.264 \pm 0.109$	$0.149 \pm 0.159$	0.9	$0.940 \pm 0.094$	$0.881 \pm 0.092$	$-0.059 \pm 0.131$	-0.4
deV	Elliptical	1.08	$-0.782 \pm 0.179$	$-0.778 \pm 0.185$	$0.004 \pm 0.258$	0.0	$1.028 \pm 0.088$	$1.064 \pm 0.123$	$0.037 \pm 0.151$	0.2
exp	Spiral	1.31	$0.201 \pm 0.112$	$0.178 \pm 0.114$	$-0.024 \pm 0.160$	-0.1	$0.908 \pm 0.091$	$0.920 \pm 0.095$	$0.012 \pm 0.132$	0.1

<sup>a</sup> Significance of non-zero result, value divided by uncertainty.

<sup>b</sup> The distance where the ‘near’ and ‘far’ bins were separated.

Leaving aside the dependence with distance, we confirm the results that faint SNe Ia with narrow light-curves favor passive host galaxies (Gallagher et al., 2005, Hamuy et al., 1996a, Lampeitl et al., 2010a, Sullivan et al., 2006b). We find that SNe Ia with low  $\Delta$  / high  $x_1$  (bright SNe) explode preferably in spiral galaxies. We obtain  $\langle x_1^{\text{elliptical}} \rangle = -0.78 \pm 0.13$  for elliptical galaxies compared to  $\langle x_1^{\text{spiral}} \rangle = 0.19 \pm 0.08$  for spiral galaxies. The corresponding numbers for MLCS2k2 are:  $\langle \Delta^{\text{elliptical}} \rangle = 0.16 \pm 0.05$  and  $\langle \Delta^{\text{spiral}} \rangle = -0.08 \pm 0.03$ .

### 7.3.3 Correlations between projected distance and Hubble residuals

When correlating the projected distance with the Hubble residuals from MLCS2k2 and SALT2 (see Table 7.6 and 7.7), the only correlation with a significance larger than  $2\sigma$  is obtained for SALT2 with the multi-bin analysis. We find a correlation where the SALT2 Hubble residual increases with the distance, normalized with the exponential Sérsic profile, for spiral galaxies. This correlation is recovered in the fit to unbinned data, but has a significantly lower significance using the two bin technique ( $0.7 \sigma$ ). Since the correlation is only seen using one distance measurement, the correlation

**Table 7.6:** Results when correlating MLCS2k2 Hubble residuals with distance binned in multiple bins of equal size (upper table) and binned in a near and a far sample, with equal number of events in each bin (lower table).

Distance unit	Host type	Slope	Sig. <sup>a</sup>	$\chi^2/\text{dof}$	dof
kpc	All	$0.0001 \pm 0.0027$	0.0	1.3	17
	Elliptical	$-0.0001 \pm 0.0055$	-0.0	0.6	7
	Spiral	$-0.0008 \pm 0.0037$	-0.2	1.5	13
P50	All	$-0.025 \pm 0.017$	-1.5	2.5	9
	Elliptical	$-0.008 \pm 0.023$	-0.3	0.2	5
	Spiral	$-0.028 \pm 0.023$	-1.2	1.6	8
ISO	All	$0.11 \pm 0.09$	1.3	1.4	7
	Elliptical	$0.15 \pm 0.23$	0.7	0.1	3
	Spiral	$0.02 \pm 0.13$	0.2	1.7	6
deV	Elliptical	$0.002 \pm 0.020$	0.1	0.6	5
exp	Spiral	$0.026 \pm 0.015$	1.7	1.0	10

Distance unit	Host type	Cut <sup>b</sup>	Mean $\delta_{\text{MLCS}}$				Scatter of $\delta_{\text{MLCS}}$			
			Near $\bar{n}$	Far $\bar{f}$	Difference $\bar{f} - \bar{n}$	Sig. <sup>a</sup>	Near $\sigma_n$	Far $\sigma_f$	Difference $\sigma_f - \sigma_n$	Sig. <sup>a</sup>
kpc	All	3.83	$0.000 \pm 0.027$	$0.003 \pm 0.022$	$0.003 \pm 0.035$	0.1	$0.265 \pm 0.030$	$0.217 \pm 0.021$	$-0.048 \pm 0.036$	-1.3
	Elliptical	2.94	$-0.083 \pm 0.041$	$-0.105 \pm 0.033$	$-0.022 \pm 0.052$	-0.4	$0.233 \pm 0.029$	$0.187 \pm 0.030$	$-0.046 \pm 0.042$	-1.1
	Spiral	4.35	$0.064 \pm 0.035$	$0.037 \pm 0.025$	$-0.026 \pm 0.043$	-0.6	$0.277 \pm 0.036$	$0.201 \pm 0.025$	$-0.076 \pm 0.044$	-1.7
P50	All	0.97	$0.010 \pm 0.029$	$-0.007 \pm 0.020$	$-0.017 \pm 0.035$	-0.5	$0.284 \pm 0.029$	$0.193 \pm 0.016$	$-0.091 \pm 0.033$	-2.7
	Elliptical	0.75	$-0.098 \pm 0.041$	$-0.090 \pm 0.033$	$0.007 \pm 0.052$	0.1	$0.234 \pm 0.029$	$0.187 \pm 0.030$	$-0.047 \pm 0.042$	-1.1
	Spiral	1.04	$0.073 \pm 0.037$	$0.028 \pm 0.022$	$-0.045 \pm 0.043$	-1.0	$0.293 \pm 0.035$	$0.174 \pm 0.014$	$-0.119 \pm 0.038$	-3.1
ISO	All	0.16	$-0.012 \pm 0.029$	$0.016 \pm 0.019$	$0.028 \pm 0.035$	0.8	$0.286 \pm 0.030$	$0.188 \pm 0.016$	$-0.098 \pm 0.034$	-2.9
	Elliptical	0.10	$-0.104 \pm 0.040$	$-0.084 \pm 0.034$	$0.020 \pm 0.052$	0.4	$0.228 \pm 0.030$	$0.193 \pm 0.030$	$-0.035 \pm 0.042$	-0.8
	Spiral	0.19	$0.053 \pm 0.036$	$0.048 \pm 0.023$	$-0.005 \pm 0.043$	-0.1	$0.291 \pm 0.037$	$0.181 \pm 0.016$	$-0.110 \pm 0.040$	-2.7
deV	Elliptical	1.00	$-0.085 \pm 0.038$	$-0.103 \pm 0.036$	$-0.018 \pm 0.053$	-0.4	$0.218 \pm 0.027$	$0.205 \pm 0.033$	$-0.013 \pm 0.042$	-0.3
exp	Spiral	1.35	$0.048 \pm 0.034$	$0.053 \pm 0.026$	$0.005 \pm 0.043$	0.1	$0.274 \pm 0.037$	$0.206 \pm 0.024$	$-0.069 \pm 0.044$	-1.5

<sup>a</sup> Significance of non-zero result, value divided by uncertainty.

<sup>b</sup> The distance where the ‘near’ and ‘far’ bins were separated.

might very well be spurious. Using the limit obtained from the Hubble residuals as a function of physical distance for the full sample of SNe, we obtain that the residual will change by less than 0.06 ( $2\sigma$ ) between a SN at the center of the galaxy and one which is 10 kpc away.

The difference in Hubble residual scatter between SNe in spiral galaxies close to the galaxy center and farther away is significant. Depending on light-curve fitter and the distance used, the significance varies between 1.2 and 3.6  $\sigma$ . The scatter is larger close to the center of the galaxy. This scatter differences translates also to the complete sample, while it is not visible in the elliptical sample only.

Note that we find a difference in Hubble residuals between SNe in spiral galaxies and elliptical galaxies, most notably in the MLCS2k2 residuals,  $0.05 \pm 0.02$  compared to  $-0.09 \pm 0.03$ .

### 7.3.4 Correlations between projected distance and local metallicity

When looking for correlations of SN light-curve parameters with the indirect measurement of the local metallicity (see Table 7.8), we found a correlation with a significance

**Table 7.7:** Results when correlating SALT2 Hubble residuals with distance binned in multiple bins of equal size (upper table) and binned in a near and a far sample, with equal number of events in each bin (lower table).

Distance unit	Host type	Slope	Sig. <sup>a</sup>	$\chi^2/\text{dof}$	dof
kpc	All	-0.0020 ± 0.0022	-0.9	1.0	18
	Elliptical	-0.0008 ± 0.0025	-0.3	1.0	6
	Spiral	-0.0024 ± 0.0032	-0.8	0.8	11
P50	All	-0.029 ± 0.015	-1.9	2.3	9
	Elliptical	-0.026 ± 0.020	-1.3	0.2	6
	Spiral	-0.018 ± 0.019	-1.0	2.1	8
ISO	All	-0.04 ± 0.10	-0.4	1.9	8
	Elliptical	-0.10 ± 0.17	-0.6	1.9	4
	Spiral	0.02 ± 0.11	0.2	1.9	6
deV	Elliptical	-0.010 ± 0.016	-0.6	0.8	6
exp	Spiral	0.030 ± 0.014	2.2	1.1	10

Distance unit	Host type	Cut <sup>b</sup>	Mean $\delta_{\text{SALT2}}$				Scatter of $\delta_{\text{SALT2}}$			
			Near $\bar{n}$	Far $\bar{f}$	Difference $\bar{f} - \bar{n}$	Sig. <sup>a</sup>	Near $\sigma_n$	Far $\sigma_f$	Difference $\sigma_f - \sigma_n$	Sig. <sup>a</sup>
kpc	All	3.74	0.035 ± 0.023	0.012 ± 0.019	-0.023 ± 0.030	-0.8	0.231 ± 0.025	0.184 ± 0.014	-0.046 ± 0.029	-1.6
	Elliptical	3.26	-0.010 ± 0.028	-0.041 ± 0.036	-0.031 ± 0.046	-0.7	0.162 ± 0.022	0.209 ± 0.027	0.047 ± 0.035	1.4
	Spiral	3.90	0.058 ± 0.032	0.038 ± 0.020	-0.020 ± 0.037	-0.5	0.256 ± 0.032	0.163 ± 0.014	-0.093 ± 0.035	-2.7
P50	All	0.97	0.030 ± 0.024	0.017 ± 0.017	-0.014 ± 0.030	-0.5	0.240 ± 0.025	0.173 ± 0.014	-0.067 ± 0.028	-2.4
	Elliptical	0.81	-0.029 ± 0.031	-0.021 ± 0.035	0.008 ± 0.046	0.2	0.175 ± 0.022	0.200 ± 0.028	0.024 ± 0.035	0.7
	Spiral	0.98	0.062 ± 0.032	0.034 ± 0.019	-0.028 ± 0.037	-0.7	0.261 ± 0.031	0.154 ± 0.013	-0.108 ± 0.034	-3.2
ISO	All	0.16	0.019 ± 0.024	0.028 ± 0.017	0.009 ± 0.030	0.3	0.241 ± 0.025	0.172 ± 0.014	-0.068 ± 0.029	-2.4
	Elliptical	0.11	-0.029 ± 0.029	-0.022 ± 0.036	0.007 ± 0.046	0.2	0.166 ± 0.023	0.208 ± 0.027	0.042 ± 0.035	1.2
	Spiral	0.18	0.049 ± 0.033	0.047 ± 0.018	-0.002 ± 0.037	-0.1	0.266 ± 0.031	0.147 ± 0.012	-0.119 ± 0.034	-3.6
deV	Elliptical	1.08	-0.032 ± 0.029	-0.018 ± 0.036	0.014 ± 0.046	0.3	0.165 ± 0.023	0.208 ± 0.027	0.043 ± 0.035	1.2
exp	Spiral	1.31	0.036 ± 0.029	0.061 ± 0.023	0.025 ± 0.037	0.7	0.238 ± 0.028	0.188 ± 0.030	-0.050 ± 0.041	-1.2

<sup>a</sup> Significance of non-zero result, value divided by uncertainty.

<sup>b</sup> The distance where the ‘near’ and ‘far’ bins were separated.

greater than  $2\sigma$  when measuring the color  $c$  and the SALT2 Hubble residuals of the SNe exploding in elliptical galaxies. We find that  $c$  increases with metallicity with a slope of  $0.164 \pm 0.067$  ( $2.45\sigma$  significance), while the Hubble residuals decrease with a slope of  $-0.271 \pm 0.122$  ( $2.21\sigma$ , see Fig. 7.13). In the two bin analysis, there is no result with significance greater than  $2\sigma$ .

We do recover the significant trend found by D’Andrea (2011) between the metallicity and the Hubble residuals, but at low significance. Although our results point in the same direction, we are using an indirect measurement of the metallicity at the position of the supernovae instead of a direct measurement (using lines from the spectra) of the global metallicity of the host.

## 7.4 Discussion

Correlating the SN Ia light-curve parameters with the distance of the supernova from the center of the host galaxies, we find strong indications of a decrease in  $A_V$  with distance, in particular for spiral galaxies. If part of the color variations of SNe Ia is explained by dust, and dust is mainly present in spiral galaxies and decreasing with

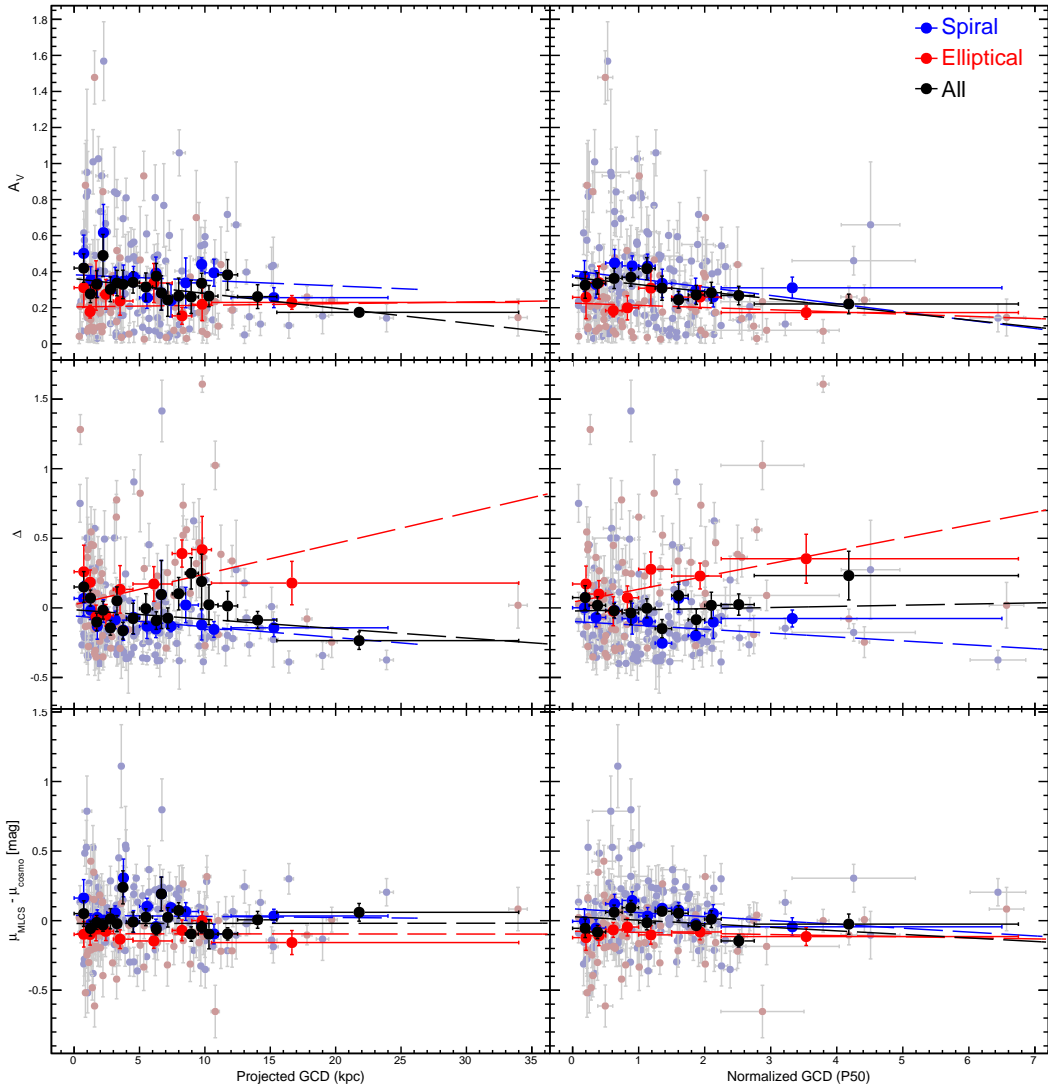


**Figure 7.9:** MLCS2k2 parameters and Hubble residuals as a function of projected distance in kiloparsec and P50 normalization. SNe in elliptical galaxies are marked in red and SNe in spiral galaxies in blue. Each individual supernova is shown as a faint point, and the bold points are used for the mean values in each bin. The lines show the best fit to the mean values.

distance from the center, this would be expected. The trend is also reproduced when correlating the SALT2 color parameter  $c$  with distance. Note that due to the difficulty to observe faint SNe close to the galaxy center, we would expect fewer dust extinguished SNe (with high  $A_V$ ) at small distances. However, this is opposite of what we find, so if we corrected for the brightness bias, the trend would most likely be stronger.

We find some indications that SNe in elliptical galaxies tend to have narrower light-curves (larger  $\Delta$ ) if they explode farther from the galaxy core. Since the width of the light-curve is related to the supernova brightness, this result would mean that

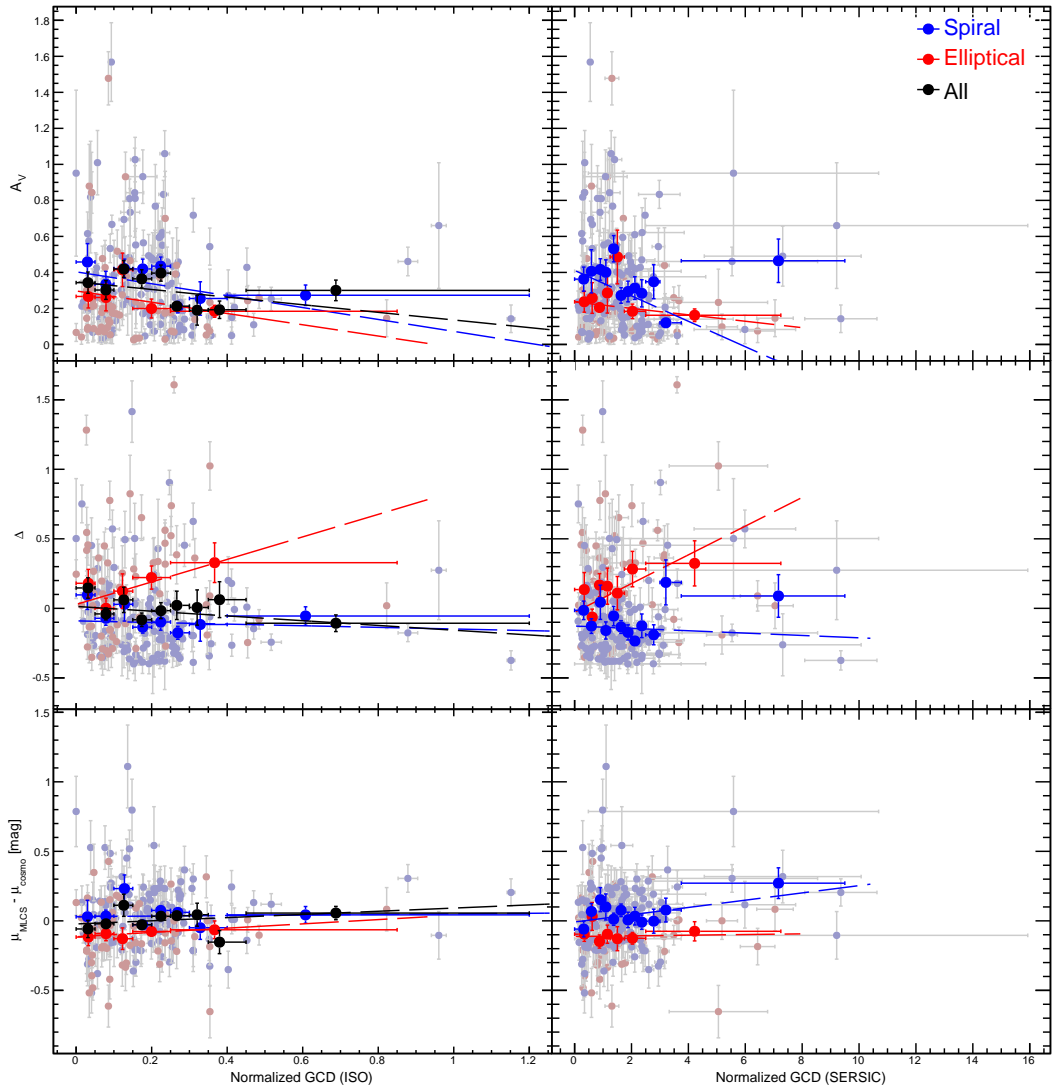


**Figure 7.10:** MLCS2k2 parameters and Hubble residuals as a function of projected distance in the ISO and Sérsic normalizations. Note that the values in the plots for the Sérsic profile cannot be compared between spiral galaxies and elliptical galaxies. SNe in elliptical galaxies are marked in red and SNe in spiral galaxies in blue. Each individual supernova is shown as a faint point, and the bold points are used for the mean values in each bin. The lines show the best fit to the mean values.

SNe exploding at larger galactocentric distances seem to be fainter. Therefore, this result could, at least partly, be explained by the difficulty to detect faint SNe close to the galaxy center, where the galaxy light is stronger. Furthermore, the significances found for an evolving  $\Delta$  are not very strong ( $< 2.4\sigma$ ) and the trend is mainly visible when using the  $\Delta$  parameter from MLCS2k2 as a measure of the light-curve width, compared to the homologous  $x_1$  parameter in SALT2.

We find no strong correlations between the galactocentric distance and the Hubble

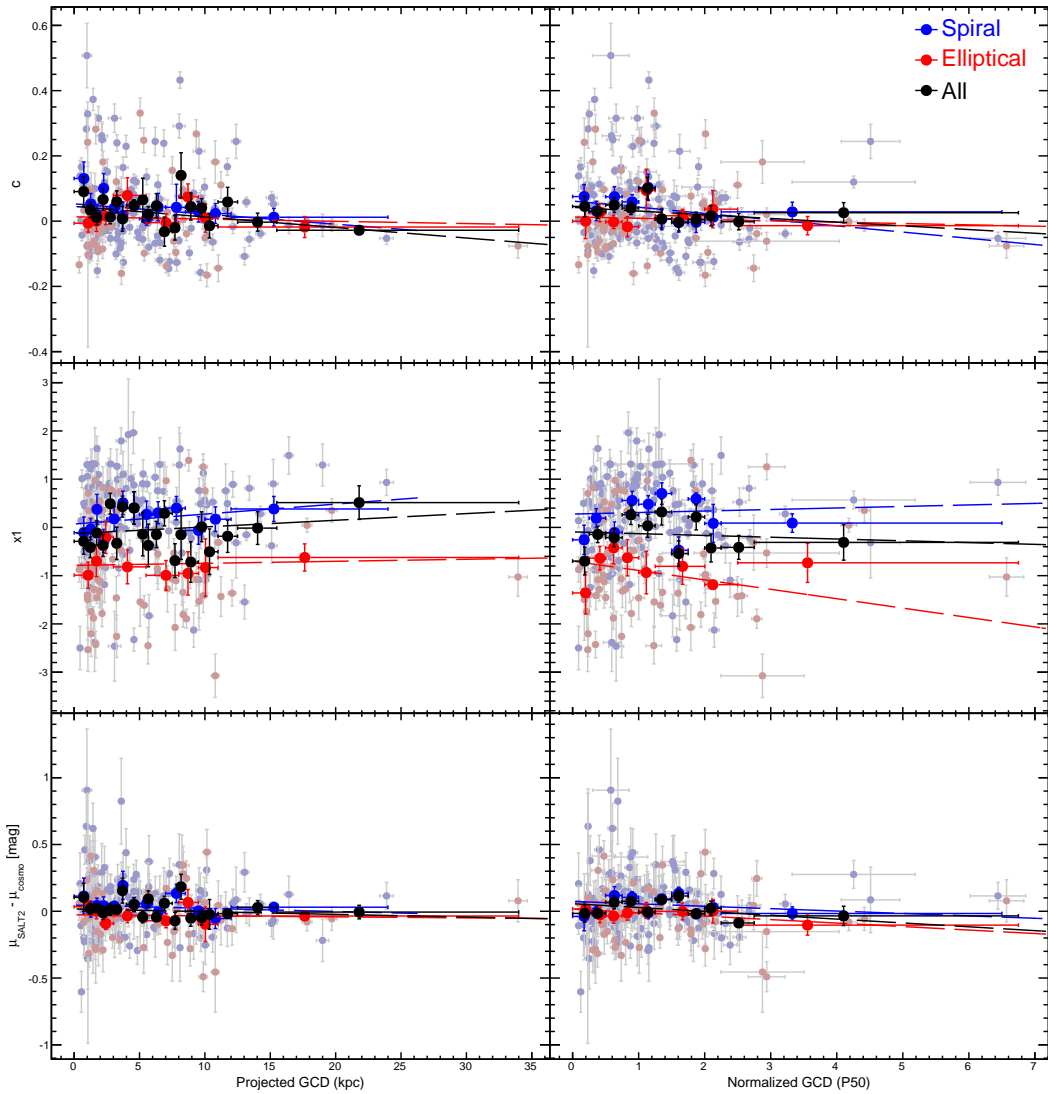


**Figure 7.11:** SALT2 parameters and Hubble residuals as a function of projected distance in kiloparsec and P50 normalization. SNe in elliptical galaxies are marked in red and SNe in spiral galaxies in blue. Each individual supernova is shown as a faint point, and the bold points are used for the mean values in each bin. The lines show the best fit to the mean values.

residuals. Since the distance of the SN from the core of the galaxy can be used as a proxy for the local metallicity (see e.g. Boissier et al., 2009), this can be seen as an indication of a limited correlation between Hubble residuals and local metallicity. Since there is also a correlation between the metallicity and the luminosity of the host galaxy, there could be a bias in our sample where there are fewer SNe detected in bright galaxies (with high metallicity) at small galactocentric distances. However, even if we would exclude the data with the smallest SN-galaxy distances, we still see no significant correlations between the galactocentric distance and the Hubble residuals.

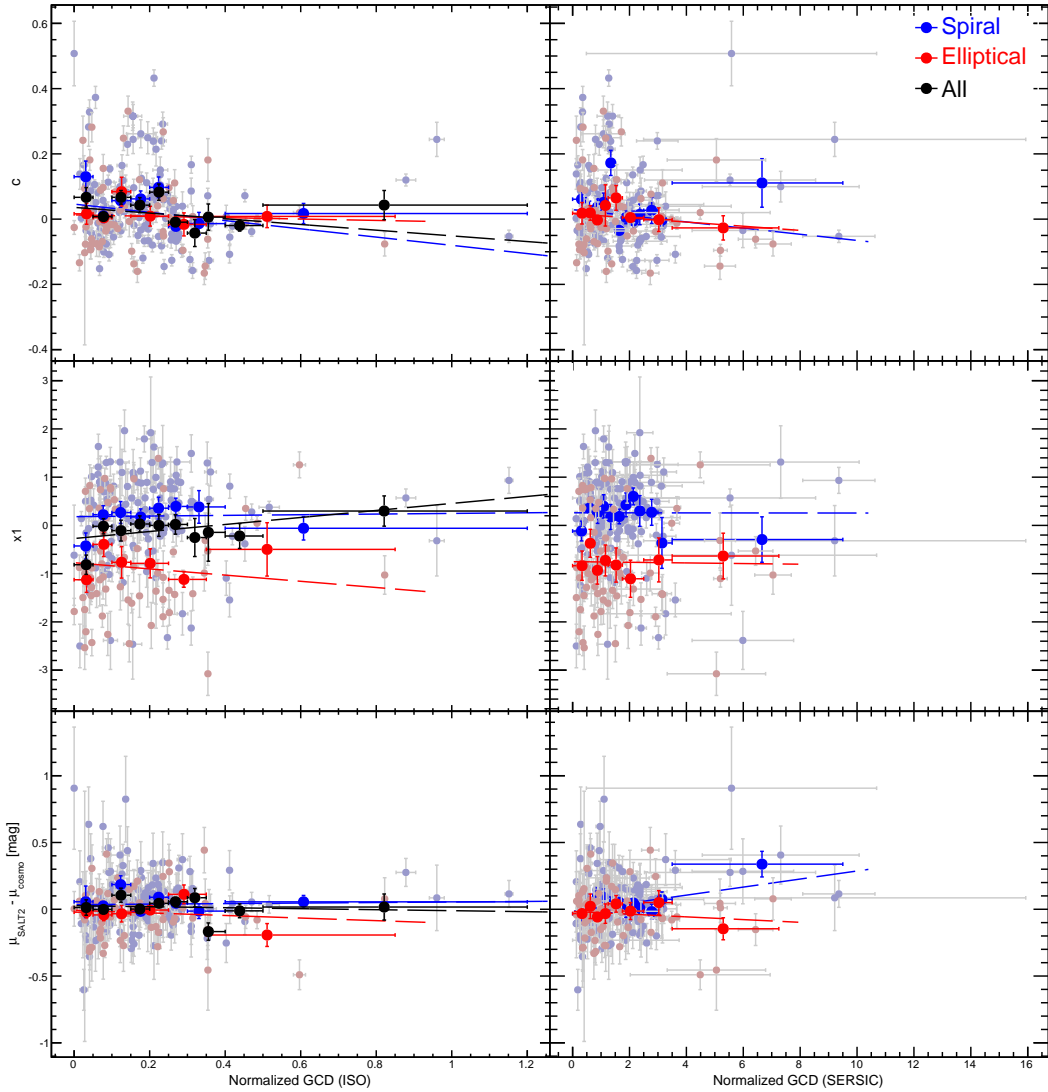


**Figure 7.12:** SALT2 parameters and Hubble residuals as a function of projected distance in the ISO and Sérsic normalizations. Note that the values in the plots for the Sérsic profile cannot be compared between spiral galaxies and elliptical galaxies. SNe in elliptical galaxies are marked in red and SNe in spiral galaxies in blue. Each individual supernova is shown as a faint point, and the bold points are used for the mean values in each bin. The lines show the best fit to the mean values.

Gallagher et al. (2005) suggest that progenitor age should be a more important factor than metallicity when it comes to the variability of the supernova peak brightness. Gupta et al. (2011) found a correlation between the Hubble residuals and the mass-weighted average age of the host galaxy in SDSS data. However, a correlation between the Hubble residuals and the *global* metallicity has also been detected (D’Andrea, 2011). We also find that the scatter of the Hubble residuals for SNe in spiral galaxies diminishes with the distance from the galaxy center.

**Table 7.8:** Same results than in the previous tables, but using the indirect measurement of the local metallicity, instead of the distance, to look for correlations with light-curve parameters.

SN Parameter	Host type	Slope	Sig. <sup>a</sup>	$\chi^2/\text{dof}$	dof
$A_V$	All	-0.0569 $\pm$ 0.0663	-0.9	2.0	11
	Elliptical	0.1114 $\pm$ 0.0725	1.5	1.8	6
	Spiral	0.0398 $\pm$ 0.0816	0.49	2.3	9
$\Delta$	All	0.0251 $\pm$ 0.1469	0.2	3.2	11
	Elliptical	0.3336 $\pm$ 0.3122	1.1	3.7	6
	Spiral	-0.3955 $\pm$ 0.1032	-3.8	2.9	9
$\delta\mu_{MLCS}$	All	-0.0325 $\pm$ 0.0822	-0.4	1.1	11
	Elliptical	0.0678 $\pm$ 0.1328	0.5	3.2	6
	Spiral	0.0921 $\pm$ 0.1031	0.9	1.094	9
$c$	All	0.0409 $\pm$ 0.0395	1.0	0.9	13
	Elliptical	0.1639 $\pm$ 0.0668	2.5	1.5	6
	Spiral	0.0522 $\pm$ 0.0449	1.2	1.2	10
$x_1$	All	-0.9063 $\pm$ 0.3363	-2.7	2.3	13
	Elliptical	0.0432 $\pm$ 0.6932	0.1	0.7	6
	Spiral	0.3560 $\pm$ 0.3978	0.9	2.2	10
$\delta\mu_{SALT2}$	All	-0.0772 $\pm$ 0.0691	-1.1	1.0	13
	Elliptical	-0.2711 $\pm$ 0.1228	-2.2	1.5	6
	Spiral	0.0588 $\pm$ 0.0985	0.6	1.4	10

SN Par.	Host type	Cut <sup>b</sup>	Mean Metallicity				Scatter Metallicity	
			Near	Far	Difference	Sig. <sup>a</sup>	Scatter Dif.	Sig. <sup>a</sup>
$A_V$	All	8.88	0.3369 $\pm$ 0.0277	0.3139 $\pm$ 0.0270	-0.0230 $\pm$ 0.0386	-0.6	-0.007 $\pm$ 0.045	-0.2
	Elliptical	8.93	0.2391 $\pm$ 0.0491	0.2654 $\pm$ 0.0365	0.0263 $\pm$ 0.0612	0.4	-0.075 $\pm$ 0.094	-0.8
	Spiral	8.85	0.3530 $\pm$ 0.0292	0.3729 $\pm$ 0.0380	0.0199 $\pm$ 0.0480	0.4	0.068 $\pm$ 0.047	1.4
$\Delta$	All	8.88	-0.0302 $\pm$ 0.0295	0.0363 $\pm$ 0.0402	0.0665 $\pm$ 0.0499	1.3	0.105 $\pm$ 0.053	2.0
	Elliptical	8.93	0.0937 $\pm$ 0.0577	0.2316 $\pm$ 0.0773	0.1380 $\pm$ 0.0964	1.4	0.106 $\pm$ 0.089	1.2
	Spiral	8.85	-0.0550 $\pm$ 0.0336	-0.1015 $\pm$ 0.0388	-0.0466 $\pm$ 0.0513	-0.9	0.039 $\pm$ 0.070	0.6
$\delta\mu_{MLCS}$	All	8.88	0.0076 $\pm$ 0.0260	-0.0025 $\pm$ 0.0234	-0.0101 $\pm$ 0.0350	-0.3	-0.025 $\pm$ 0.036	-0.7
	Elliptical	8.93	-0.0654 $\pm$ 0.0440	-0.1216 $\pm$ 0.0273	-0.0562 $\pm$ 0.0518	-1.1	-0.098 $\pm$ 0.037	-2.6
	Spiral	8.85	0.0210 $\pm$ 0.0281	0.0824 $\pm$ 0.0323	0.0614 $\pm$ 0.0428	1.4	0.032 $\pm$ 0.045	0.7
$c$	All	8.88	0.0281 $\pm$ 0.0118	0.0401 $\pm$ 0.0119	0.0120 $\pm$ 0.0167	0.7	0.001 $\pm$ 0.016	0.1
	Elliptical	8.98	-0.0060 $\pm$ 0.0179	0.0369 $\pm$ 0.0183	0.0429 $\pm$ 0.0256	1.7	0.002 $\pm$ 0.022	0.1
	Spiral	8.85	0.0390 $\pm$ 0.0147	0.0478 $\pm$ 0.0154	0.0087 $\pm$ 0.0213	0.4	0.004 $\pm$ 0.020	0.2
$x_1$	All	8.88	-0.1045 $\pm$ 0.1050	-0.1665 $\pm$ 0.1093	-0.0620 $\pm$ 0.1516	-0.4	0.038 $\pm$ 0.094	0.4
	Elliptical	8.98	-0.6573 $\pm$ 0.1792	-0.9023 $\pm$ 0.1825	-0.2449 $\pm$ 0.2558	-1.0	0.019 $\pm$ 0.163	0.1
	Spiral	8.85	0.1080 $\pm$ 0.1134	0.2720 $\pm$ 0.1117	0.1639 $\pm$ 0.1591	1.0	-0.021 $\pm$ 0.132	-0.2
$\delta\mu_{SALT2}$	All	8.88	0.0357 $\pm$ 0.0230	0.0130 $\pm$ 0.0189	-0.0227 $\pm$ 0.0298	-0.8	-0.041 $\pm$ 0.030	-1.4
	Elliptical	8.98	0.0103 $\pm$ 0.0379	-0.0591 $\pm$ 0.0252	-0.0694 $\pm$ 0.0455	-1.5	-0.073 $\pm$ 0.033	-2.2
	Spiral	8.85	0.0224 $\pm$ 0.0257	0.0759 $\pm$ 0.0271	0.0535 $\pm$ 0.0373	1.4	0.010 $\pm$ 0.041	0.2

<sup>a</sup> Significance of non-zero result, value divided by uncertainty.

<sup>b</sup> The distance where the ‘near’ and ‘far’ bins were separated.

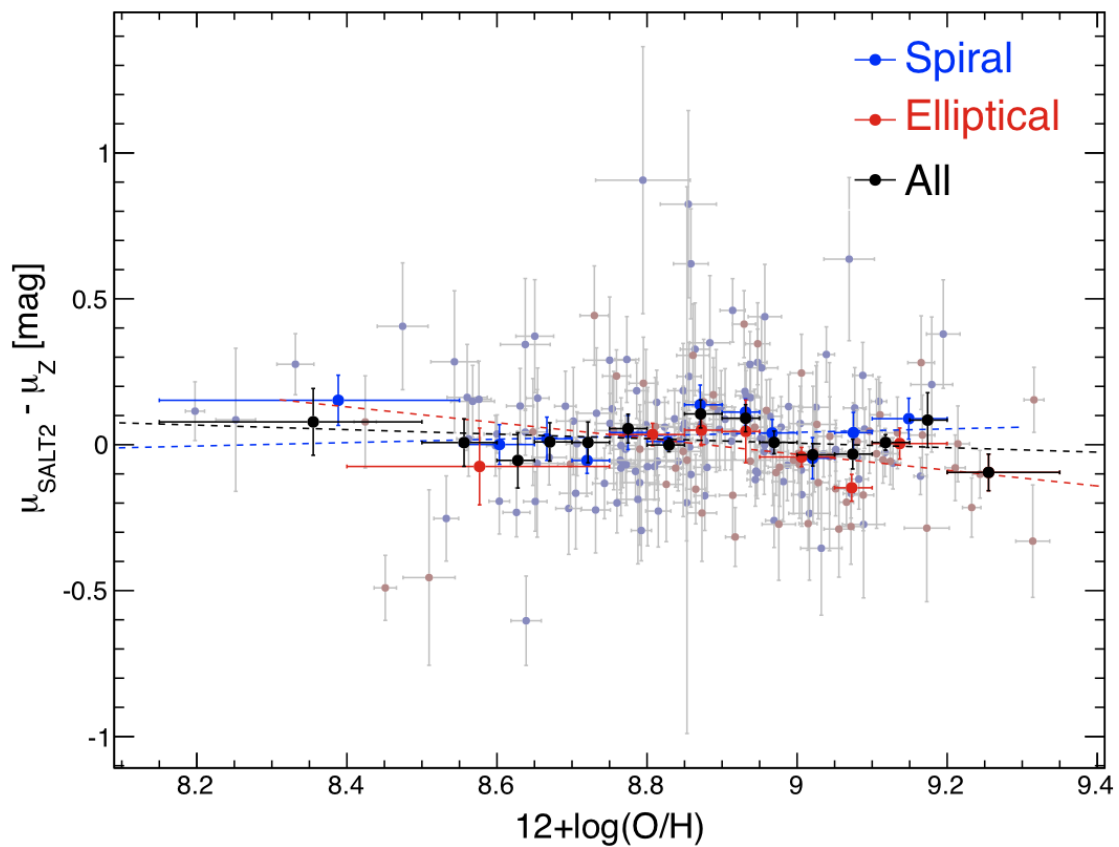


**Figure 7.13:** SALT2 Hubble residuals as a function of the local metallicity.

## CHAPTER 8

---

### Summary and Conclusions

---

In this thesis two analyses about Type Ia supernovae (SNe) properties using the SNe discovered by SDSS-II/SNe Survey are presented: a spectroscopic analysis of the peculiar SN 2007qd, and a study of correlations of photometric parameters of Type Ia SNe as a function of the distance to the host galaxy center.

As a part of the spectroscopic follow-up of the objects discovered by SDSS-II/SNe collaboration, we contributed observing and taking spectra during four nights in October and November (5-6 Oct. and 4-5 Nov.) of 2007 using the Telescopio Nazionale Galileo (TNG) located at the Observatorio del Roque de Los Muchachos (ORM) in La Palma. The raw data obtained resulted in 23 SNe spectra calibrated in flux and wavelength, which have been added to the SDSS-II/SNe spectra database. The reduction procedure consists in several steps described in §5.

One of these spectra, was the first spectrum taken of a peculiar subluminous event, labeled as SN 2007qd. Thanks to the configuration of the spectroscopic follow-up of SDSS-II/SNe events, our early notice allowed other telescopes to obtain three other high-resolution spectra of this object, in different wavelength ranges and epochs.

We compared their light-curves to those of the peculiar SNe 2005hk and 2008ha, two SNe included in a subclass of subluminous (02cx-like) events. We saw that 07qd rose and declined faster in *ugr* bands than 05hk, and had similar light-curves than 08ha. Comparing the color evolution of 07qd and 05hk, we found that 07qd is bluer near maximum brightness. discarding dust extinction as a major cause of the low luminosity of 07qd compared with 05hk.

We then correlated the *B*-band peak magnitude to the *B*-band light-curve stretch of 07qd and other normal Ia SNe with  $z < 0.12$  from the SDSS-II/SNe sample. Although the low redshift set were clustered near stretch $\sim 1$  and at  $M_B \sim -19$ , there appears to

## Summary and Conclusions

---

be a sequence connecting the 02cx-like events, from the bright events 05hk and 02cx, to the extreme 08ha with the intermediate 07qd.

Analyzing the 07qd spectra, we found that it was spectroscopically similar to both 08ha and 05hk, showing strong lines of Fe II and Co II. Other intermediate mass element (IME) features and Fe III absorptions were visible at early epochs, though their optical depths declined quickly with time. The explicit presence of IMEs in the early-time spectra implies the thermonuclear deflagration of carbon and oxygen, showing that 07qd is inconsistent with a core-collapse event. This result contrasts with the conclusion reached by a previous analysis of 08ha ([Valenti et al., 2009](#)).

After a detailed analysis of the photometry and spectroscopy of 07qd, we find that it completes a sequence of 02cx-like SN Ia both energetically and spectroscopically, linking the extreme 08ha to the well-studied 05hk and 02cx events. This work is compiled in §6 and published in [McClelland et al. \(2010\)](#).

On the other hand, in §7, the three-year sample of Type Ia SNe discovered by the SDSS-II/SNe Survey is used to look for dependencies between SN Ia properties and the projected distance (in both absolute and using several normalizations) to the galactocentric distance (GCD), using the distance as a proxy for local galaxy properties (local star-formation rate, local metallicity, etc.).

We find that the excess color of the SN, parametrized by  $A_V$  in MLCS2k2 and by  $c$  in SALT2 shows strong indications of a decrease with the projected distance, in particular for spiral galaxies. If part of the color variations of SNe is explained by dust, and dust is mainly present in spiral galaxies and decreasing with distance from the center, this would be expected.

We find some indication that SNe in elliptical galaxies tend to have narrower light-curves (larger  $\Delta$ ) if they explode farther from the galaxy core. Since the width of the light-curve is related to the SN brightness, this means that SNe exploding at larger GCDs seem to be fainter. This result could in part be explained by the difficulty to detect faint SNe close to the galaxy center, where the galaxy light is stronger. Furthermore, the significances found for an evolving  $\Delta$  are not very strong ( $< 2.4\sigma$ ) and the trend is mainly visible when using the  $\Delta$  parameter from MLCS2k2 as a measure of the light-curve width, compared to the homologous  $x_1$  parameter in SALT2.

We find no strong correlations between the GCD and the Hubble residuals (HR). Since the distance of the SN from the core of the galaxy can be used as a proxy for the local metallicity (see e.g. [Boissier et al., 2009](#)), this can be seen as an indication of a limited correlation between HR and local metallicity. [Gallagher et al. \(2005\)](#) suggest that progenitor age should be a more important factor than metallicity when it comes to the variability of the SN peak brightness. [Gupta et al. \(2011\)](#) found a correlation between HR and the mass-weighted average age of the host galaxy in SDSS data. However, a correlation between HR and the *global* metallicity has also been detected ([D'Andrea, 2011](#)). We also find that the scatter of HR for SNe in spiral galaxies diminishes with the GCD. This analysis was presented in the *Supernovae and their Host Galaxies* conference which was held at Sydney in June 2011, and it will be published in [Galbany et al. \(2011\)](#).

## APPENDIX A

---

### TNG images

---

Here we present a table with all the images taken and saved at the Telescopio Nazionale Galileo (TNG) as part of the SDSS-II/SNe observations. Each image type is painted in different colors, making easier their identification. The spectra are in dark green. The reduction of these images is discussed in §5.

**Table A.1:** Images taken and saved at TNG

Date <sup>a</sup>	Filename	Image	Seconds	Slit	Grism	Lamp
Oct 5 (1)	JKVA0003	FLAT	60	1.0arcsec	LR-B	Halogen2
Oct 5 (1)	JKVA0004	FLAT	60	1.0arcsec	LR-B	Halogen2
Oct 5 (1)	JKVA0005	FLAT	60	1.0arcsec	LR-B	Halogen2
Oct 5 (1)	JKVA0006	FLAT	60	1.0arcsec	LR-B	Halogen2
Oct 5 (1)	JKVA0007	FLAT	60	1.0arcsec	LR-B	Halogen2
Oct 5 (1)	JKVA0008	FLAT	100	1.0arcsec	LR-B	Halogen2
Oct 5 (1)	JKVA0009	FLAT	100	1.0arcsec	LR-B	Halogen2
Oct 5 (1)	JKVA0010	FLAT	100	1.0arcsec	LR-B	Halogen2
Oct 5 (1)	JKVA0011	FLAT	100	1.0arcsec	LR-B	Halogen2
Oct 5 (1)	JKVA0012	FLAT	100	1.0arcsec	LR-B	Halogen2
Oct 5 (1)	JKVA0015	ARC	30	1.0arcsec	LR-B	Neon
Oct 5 (1)	JKVA0016	ARC	60	1.0arcsec	LR-B	Helium
Oct 5 (1)	JKVA0018	ARC	20	1.0arcsec	LR-B	Argon
Oct 5 (1)	JKVA0019	BIAS	0	1.0arcsec	LR-B	Helium
Oct 5 (1)	JKVA0020	BIAS	0	1.0arcsec	LR-B	Helium
Oct 5 (1)	JKVA0021	BIAS	0	1.0arcsec	LR-B	Helium
Oct 5 (1)	JKVA0022	BIAS	0	1.0arcsec	LR-B	Helium
Oct 5 (1)	JKVA0023	BIAS	0	1.0arcsec	LR-B	Helium
Oct 5 (1)	JKVA0024	BIAS	0	1.0arcsec	LR-B	Helium
Oct 5 (1)	JKVA0025	BIAS	0	1.0arcsec	LR-B	Helium

## TNG images

---

Table A.1 – Continued

Date <sup>a</sup>	Filename	Image	Seconds	Slit	Grism	Lamp
Oct 5 (1)	JKVA0026	BIAS	0	1.0arcsec	LR-B	Helium
Oct 5 (1)	JKVA0027	BIAS	0	1.0arcsec	LR-B	Helium
Oct 5 (1)	JKVA0028	BIAS	0	1.0arcsec	LR-B	Helium
Oct 5 (1)	JKVA0029	FLAT	60	0.7arcsec	LR-B	Halogen2
Oct 5 (1)	JKVA0030	FLAT	60	0.7arcsec	LR-B	Halogen2
Oct 5 (1)	JKVA0031	FLAT	60	0.7arcsec	LR-B	Halogen2
Oct 5 (1)	JKVA0032	FLAT	60	0.7arcsec	LR-B	Halogen2
Oct 5 (1)	JKVA0033	FLAT	60	0.7arcsec	LR-B	Halogen2
Oct 5 (1)	JKVA0034	FLAT	60	0.7arcsec	LR-B	Halogen2
Oct 5 (1)	JKVA0035	FLAT	60	0.7arcsec	LR-B	Halogen2
Oct 5 (1)	JKVA0036	FLAT	60	0.7arcsec	LR-B	Halogen2
Oct 5 (1)	JKVA0037	FLAT	60	0.7arcsec	LR-B	Halogen2
Oct 5 (1)	JKVA0038	FLAT	60	0.7arcsec	LR-B	Halogen2
Oct 5 (1)	JKVA0039	ARC	60	0.7arcsec	LR-B	Neon
Oct 5 (1)	JKVA0040	ARC	60	0.7arcsec	LR-B	Helium
Oct 5 (1)	JKVA0041	ARC	20	0.7arcsec	LR-B	Argon
Oct 5 (1)	JKVA0042	SLIT POS	3	0.7arcsec	Open	Halogen2
Oct 5 (1)	JKVA0043	SLIT POS	1	1.0arcsec	Open	Halogen2
Oct 5 (1)	JKVA0044	SLIT POS	1	1.5arcsec	Open	Halogen2
Oct 5 (1)	JKVA0045	SLIT POS	1	5.0arcsec	Open	Neon
Oct 5 (1)	JKVA0046	SLIT POS	1	5.0arcsec	Open	Halogen2
Oct 5 (1)	JKVA0047	FLAT	15	5.0arcsec	LR-B	Halogen2
Oct 5 (1)	JKVA0048	FLAT	15	5.0arcsec	LR-B	Halogen2
Oct 5 (1)	JKVA0049	FLAT	15	5.0arcsec	LR-B	Halogen2
Oct 5 (1)	JKVA0050	FLAT	15	5.0arcsec	LR-B	Halogen2
Oct 5 (1)	JKVA0051	FLAT	15	5.0arcsec	LR-B	Halogen2
Oct 5 (1)	JKVA0052	FLAT	15	5.0arcsec	LR-B	Halogen2
Oct 5 (1)	JKVA0053	FLAT	15	5.0arcsec	LR-B	Halogen2
Oct 5 (1)	JKVA0054	FLAT	15	5.0arcsec	LR-B	Halogen2
Oct 5 (1)	JKVA0055	FLAT	15	5.0arcsec	LR-B	Halogen2
Oct 5 (1)	JKVA0056	FLAT	15	5.0arcsec	LR-B	Halogen2
Oct 5 (1)	JKVA0057	ARC	10	5.0arcsec	LR-B	Neon
Oct 5 (1)	JKVA0058	ARC	10	5.0arcsec	LR-B	Helium
Oct 5 (1)	JKVA0059	ARC	3	5.0arcsec	LR-B	Argon
Oct 5 (1)	JKVA0132	SN18408	15	Open	Open	Parking
Oct 5 (1)	JKVA0133	SN18408	15	Open	Pyramid	Parking
Oct 5 (1)	JKVA0134	SN18408	15	1.0arcsec	Open	Parking
Oct 5 (1)	JKVA0135	SN18408	15	Open	Open	Parking
Oct 5 (1)	JKVA0136	SN18408	15	Open	Open	Parking
Oct 5 (1)	JKVA0137	SN18408	15	1.0arcsec	Open	Parking
Oct 5 (1)	JKVA0138	SN18408	600	1.0arcsec	LR-B	Parking
Oct 5 (1)	JKVA0139	SN18408	1200	1.0arcsec	LR-B	Parking
Oct 6 (1)	JKVA0164	SN18321	30	Open	Open	Parking
Oct 6 (1)	JKVA0165	SN18321	45	Open	Open	Parking
Oct 6 (1)	JKVA0166	SN18321	60	1.0arcsec	Open	Parking
Oct 6 (1)	JKVA0167	SN18321	1800	1.0arcsec	LR-B	Parking
Oct 6 (1)	JKVA0168	SN18321	1800	1.0arcsec	LR-B	Parking
Oct 6 (1)	JKVA0169	SN18321	1800	1.0arcsec	LR-B	Parking
Oct 6 (1)	JKVA0171	SN18441	20	Open	Open	Parking
Oct 6 (1)	JKVA0172	SN18441	20	Open	Open	Parking
Oct 6 (1)	JKVA0173	SN18441	20	1.0arcsec	Open	Parking

Table A.1 – Continued

Date <sup>a</sup>	Filename	Image	Seconds	Slit	Grism	Lamp
Oct 6 (1)	JKVA0174	SN18441	1500	1.0arcsec	LR-B	Parking
Oct 6 (1)	JKVA0175	SN18441	1500	1.0arcsec	LR-B	Parking
Oct 6 (1)	JKVA0177	SN17886	20	Open	Open	Parking
Oct 6 (1)	JKVA0178	SN17886	20	Open	Open	Parking
Oct 6 (1)	JKVA0179	SN17886	20	Open	Open	Parking
Oct 6 (1)	JKVA0180	SN17886	20	1.0arcsec	Open	Parking
Oct 6 (1)	JKVA0181	SN17886	20	Open	Open	Parking
Oct 6 (1)	JKVA0182	SN17886	20	Open	Open	Parking
Oct 6 (1)	JKVA0183	SN17886	20	Open	Open	Parking
Oct 6 (1)	JKVA0184	SN17886	20	1.0arcsec	Open	Parking
Oct 6 (1)	JKVA0185	SN17886	600	1.0arcsec	LR-B	Parking
Oct 6 (1)	JKVA0186	SN17886	600	1.0arcsec	LR-B	Parking
Oct 6 (1)	JKVA0190	G191-B2B	1	Open	Open	Parking
Oct 6 (1)	JKVA0191	G191-B2B	1	Open	Open	Parking
Oct 6 (1)	JKVA0192	G191-B2B	1	5.0arcsec	Open	Parking
Oct 6 (1)	JKVA0196	G191-B2B	15	5.0arcsec	LR-B	Parking
Oct 6 (1)	JKVA0199	HILT600	5	5.0arcsec	LR-B	Parking
Oct 6 (2)	JKWA0002	BIAS	0	Open	Open	Parking
Oct 6 (2)	JKWA0003	BIAS	0	Open	Open	Parking
Oct 6 (2)	JKWA0004	BIAS	0	Open	Open	Parking
Oct 6 (2)	JKWA0005	BIAS	0	Open	Open	Parking
Oct 6 (2)	JKWA0006	BIAS	0	Open	Open	Parking
Oct 6 (2)	JKWA0007	BIAS	0	Open	Open	Parking
Oct 6 (2)	JKWA0008	BIAS	0	Open	Open	Parking
Oct 6 (2)	JKWA0009	BIAS	0	Open	Open	Parking
Oct 6 (2)	JKWA0010	BIAS	0	Open	Open	Parking
Oct 6 (2)	JKWA0011	BIAS	0	Open	Open	Parking
Oct 6 (2)	JKWA0012	FLAT	120	1.0arcsec	LR-B	Halogen 2
Oct 6 (2)	JKWA0013	FLAT	120	1.0arcsec	LR-B	Halogen 2
Oct 6 (2)	JKWA0014	FLAT	120	1.0arcsec	LR-B	Halogen 2
Oct 6 (2)	JKWA0015	FLAT	120	1.0arcsec	LR-B	Halogen 2
Oct 6 (2)	JKWA0016	FLAT	120	1.0arcsec	LR-B	Halogen 2
Oct 6 (2)	JKWA0017	FLAT	120	1.0arcsec	LR-B	Halogen 2
Oct 6 (2)	JKWA0018	FLAT	120	1.0arcsec	LR-B	Halogen 2
Oct 6 (2)	JKWA0019	ARC	60	1.0arcsec	LR-B	Neon
Oct 6 (2)	JKWA0020	ARC	60	1.0arcsec	LR-B	Helium
Oct 6 (2)	JKWA0021	ARC	20	1.0arcsec	LR-B	Argon
Oct 6 (2)	JKWA0023	FLAT	80	1.5arcsec	LR-B	Halogen 2
Oct 6 (2)	JKWA0024	FLAT	80	1.5arcsec	LR-B	Halogen 2
Oct 6 (2)	JKWA0025	FLAT	80	1.5arcsec	LR-B	Halogen 2
Oct 6 (2)	JKWA0026	FLAT	80	1.5arcsec	LR-B	Halogen 2
Oct 6 (2)	JKWA0027	FLAT	80	1.5arcsec	LR-B	Halogen 2
Oct 6 (2)	JKWA0032	ARC	40	1.5arcsec	LR-B	Neon
Oct 6 (2)	JKWA0033	ARC	40	1.5arcsec	LR-B	Helium
Oct 6 (2)	JKWA0034	ARC	15	1.5arcsec	LR-B	Argon
Oct 6 (2)	JKWA0036	FLAT	25	5.0arcsec	LR-B	Halogen 2
Oct 6 (2)	JKWA0037	FLAT	25	5.0arcsec	LR-B	Halogen 2
Oct 6 (2)	JKWA0038	FLAT	25	5.0arcsec	LR-B	Halogen 2
Oct 6 (2)	JKWA0039	FLAT	25	5.0arcsec	LR-B	Halogen 2
Oct 6 (2)	JKWA0040	FLAT	25	5.0arcsec	LR-B	Halogen 2
Oct 6 (2)	JKWA0041	ARC	15	5.0arcsec	LR-B	Neon

Table A.1 – Continued

Date <sup>a</sup>	Filename	Image	Seconds	Slit	Grism	Lamp
Oct 6 (2)	JKWA0042	ARC	15	5.0arcsec	LR-B	Helium
Oct 6 (2)	JKWA0043	ARC	5	5.0arcsec	LR-B	Argon
Oct 6 (2)	JKWA0052	BD+28d4211	1	Open	Open	Parking
Oct 6 (2)	JKWA0060	BD+28d4211	10	5.0arcsec	LR-B	Parking
Oct 6 (2)	JKWA0066	G93-48	20	5.0arcsec	LR-B	Parking
Oct 6 (2)	JKWA0068	SN15822	30	Open	Open	Parking
Oct 6 (2)	JKWA0069	SN15822	30	Open	Open	Parking
Oct 6 (2)	JKWA0072	SN15822	30	1.0arcsec	Open	Parking
Oct 6 (2)	JKWA0073	SN15822	30	1.0arcsec	Open	Parking
Oct 6 (2)	JKWA0074	SN15822	1800	1.0arcsec	LR-B	Parking
Oct 6 (2)	JKWA0078	SN15892	30	1.0arcsec	Open	Parking
Oct 6 (2)	JKWA0079	SN15892	1800	1.0arcsec	LR-B	Parking
Oct 6 (2)	JKWA0080	SN15892	1800	1.0arcsec	LR-B	Parking
Oct 6 (2)	JKWA0083	SN14445	30	Open	Open	Parking
Oct 6 (2)	JKWA0084	SN14445	30	1.0arcsec	Open	Parking
Oct 6 (2)	JKWA0085	SN14445	1200	1.0arcsec	LR-B	Parking
Oct 6 (2)	JKWA0086	SN14445	1200	1.0arcsec	LR-B	Parking
Oct 6 (2)	JKWA0089	SN18297	30	Open	Open	Parking
Oct 6 (2)	JKWA0090	SN18297	30	Open	Open	Parking
Oct 6 (2)	JKWA0091	SN18297	30	1.0arcsec	Open	Parking
Oct 6 (2)	JKWA0092	SN18297	1800	1.0arcsec	LR-B	Parking
Oct 7 (2)	JKWA0093	SN18297	1800	1.0arcsec	LR-B	Parking
Oct 7 (2)	JKWA0095	SN17884	30	Open	Open	Parking
Oct 7 (2)	JKWA0096	SN17884	30	Open	Open	Parking
Oct 7 (2)	JKWA0097	SN17884	30	Open	Open	Parking
Oct 7 (2)	JKWA0100	SN17884	90	1.0arcsec	Open	Parking
Oct 7 (2)	JKWA0101	SN17884	1800	1.0arcsec	LR-B	Parking
Oct 7 (2)	JKWA0102	SN17884	1800	1.0arcsec	LR-B	Parking
Oct 7 (2)	JKWA0104	SN18457	30	Open	Open	Parking
Oct 7 (2)	JKWA0105	SN18457	30	Open	Open	Parking
Oct 7 (2)	JKWA0106	SN18457	30	1.0arcsec	Open	Parking
Oct 7 (2)	JKWA0107	SN18457	1800	1.0arcsec	LR-B	Parking
Oct 7 (2)	JKWA0108	SN18457	1800	1.0arcsec	LR-B	Parking
Oct 7 (2)	JKWA0110	SN18109	30	Open	Open	Parking
Oct 7 (2)	JKWA0111	SN18109	30	Open	Open	Parking
Oct 7 (2)	JKWA0112	SN18109	30	1.0arcsec	Open	Parking
Oct 7 (2)	JKWA0113	SN18109	1800	1.0arcsec	LR-B	Parking
Oct 7 (2)	JKWA0115	SN18299	30	Open	Open	Parking
Oct 7 (2)	JKWA0116	SN18299	30	Open	Open	Parking
Oct 7 (2)	JKWA0117	SN18299	60	1.0arcsec	Open	Parking
Oct 7 (2)	JKWA0118	SN18299	1800	1.0arcsec	LR-B	Parking
Oct 7 (2)	JKWA0119	SN18299	1800	1.0arcsec	LR-B	Parking
Oct 7 (2)	JKWA0121	SN17880	30	Open	Open	Parking
Oct 7 (2)	JKWA0122	SN17880	30	Open	Open	Parking
Oct 7 (2)	JKWA0123	SN17880	30	1.0arcsec	Open	Parking
Oct 7 (2)	JKWA0124	SN17880	1200	1.0arcsec	LR-B	Parking
Oct 7 (2)	JKWA0126	SN17784	30	Open	Open	Parking
Oct 7 (2)	JKWA0127	SN17784	30	Open	Open	Parking
Oct 7 (2)	JKWA0128	SN17784	30	1.0arcsec	Open	Parking
Oct 7 (2)	JKWA0129	SN17784	600	1.0arcsec	LR-B	Parking
Oct 7 (2)	JKWA0135	G191-B2B	15	5.0arcsec	LR-B	Parking

Table A.1 – Continued

Date <sup>a</sup>	Filename	Image	Seconds	Slit	Grism	Lamp
Oct 7 (2)	JKWA0140	HILT600	5	5.0arcsec	LR-B	Parking
Nov 3 (3)	JMNA0002	FLAT	120	1.0arcsec	LR-B	Halogen2
Nov 3 (3)	JMNA0003	FLAT	120	1.0arcsec	LR-B	Halogen2
Nov 3 (3)	JMNA0004	FLAT	120	1.0arcsec	LR-B	Halogen2
Nov 3 (3)	JMNA0005	FLAT	120	1.0arcsec	LR-B	Halogen2
Nov 3 (3)	JMNA0006	FLAT	120	1.0arcsec	LR-B	Halogen2
Nov 3 (3)	JMNA0007	FLAT	80	1.5arcsec	LR-B	Halogen2
Nov 3 (3)	JMNA0008	FLAT	80	1.5arcsec	LR-B	Halogen2
Nov 3 (3)	JMNA0009	FLAT	80	1.5arcsec	LR-B	Halogen2
Nov 3 (3)	JMNA0010	FLAT	80	1.5arcsec	LR-B	Halogen2
Nov 3 (3)	JMNA0011	FLAT	80	1.5arcsec	LR-B	Halogen2
Nov 3 (3)	JMNA0012	FLAT	25	5.0arcsec	LR-B	Halogen2
Nov 3 (3)	JMNA0013	FLAT	25	5.0arcsec	LR-B	Halogen2
Nov 3 (3)	JMNA0014	FLAT	25	5.0arcsec	LR-B	Halogen2
Nov 3 (3)	JMNA0015	FLAT	25	5.0arcsec	LR-B	Halogen2
Nov 3 (3)	JMNA0016	FLAT	25	5.0arcsec	LR-B	Halogen2
Nov 3 (3)	JMNA0017	ARC	60	1.0arcsec	LR-B	Helium
Nov 3 (3)	JMNA0018	ARC	60	1.0arcsec	LR-B	Helium
Nov 3 (3)	JMNA0019	ARC	60	1.0arcsec	LR-B	Helium
Nov 3 (3)	JMNA0020	ARC	20	1.0arcsec	LR-B	Argon
Nov 3 (3)	JMNA0021	ARC	60	1.0arcsec	LR-B	Neon
Nov 3 (3)	JMNA0022	ARC	40	1.5arcsec	LR-B	Helium
Nov 3 (3)	JMNA0023	ARC	40	1.5arcsec	LR-B	Helium
Nov 3 (3)	JMNA0024	ARC	40	1.5arcsec	LR-B	Helium
Nov 3 (3)	JMNA0025	ARC	15	1.5arcsec	LR-B	Argon
Nov 3 (3)	JMNA0026	ARC	40	1.5arcsec	LR-B	Neon
Nov 3 (3)	JMNA0028	ARC	15	5.0arcsec	LR-B	Helium
Nov 3 (3)	JMNA0029	ARC	15	5.0arcsec	LR-B	Helium
Nov 3 (3)	JMNA0030	ARC	15	5.0arcsec	LR-B	Helium
Nov 3 (3)	JMNA0031	ARC	5	5.0arcsec	LR-B	Argon
Nov 3 (3)	JMNA0032	ARC	15	5.0arcsec	LR-B	Neon
Nov 3 (3)	JMNA0033	BIAS	0	Open	Open	Parking
Nov 3 (3)	JMNA0034	BIAS	0	Open	Open	Parking
Nov 3 (3)	JMNA0035	BIAS	0	Open	Open	Parking
Nov 3 (3)	JMNA0036	BIAS	0	Open	Open	Parking
Nov 3 (3)	JMNA0037	BIAS	0	Open	Open	Parking
Nov 3 (3)	JMNA0038	BIAS	0	Open	Open	Parking
Nov 3 (3)	JMNA0039	BIAS	0	Open	Open	Parking
Nov 3 (3)	JMNA0040	BIAS	0	Open	Open	Parking
Nov 3 (3)	JMNA0041	BIAS	0	Open	Open	Parking
Nov 3 (3)	JMNA0042	BIAS	0	Open	Open	Parking
Nov 3 (3)	JMNA0043	SLIT POS	1	1.0arcsec	Open	Halogen2
Nov 3 (3)	JMNA0044	SLIT POS	1	1.5arcsec	Open	Halogen2
Nov 3 (3)	JMNA0046	SLIT POS	1	5.0arcsec	Open	Halogen2
Nov 3 (3)	JMNA0047	SLIT POS	0.1	5.0arcsec	Open	Halogen2
Nov 3 (3)	JMNA0056	BD+28d4211	10	5.0arcsec	LR-B	Parking
Nov 3 (3)	JMNA0060	G93-48	30	5.0arcsec	LR-B	Parking
Nov 3 (3)	JMNA0065	SN19940	1200	1.0arcsec	LR-B	Parking
Nov 3 (3)	JMNA0066	SN19940	1200	1.0arcsec	LR-B	Parking
Nov 3 (3)	JMNA0069	SN19775	40	Open	Open	Parking
Nov 3 (3)	JNMA0071	SN19775	1800	1.0arcsec	LR-B	Parking

## TNG images

---

Table A.1 – Continued

Date <sup>a</sup>	Filename	Image	Seconds	Slit	Grism	Lamp
Nov 3 (3)	JNMA0072	SN19775	1800	1.0arcsec	LR-B	Parking
Nov 3 (3)	JMNA0077	SN19953	1800	1.0arcsec	LR-B	Parking
Nov 3 (3)	JMNA0078	SN19953	1800	1.0arcsec	LR-B	Parking
Nov 4 (3)	JMNA0083	SN20084	1800	1.0arcsec	LR-B	Parking
Nov 4 (3)	JMNA0098	SN19969	1800	1.5arcsec	LR-B	Parking
Nov 4 (4)	JMOA0003	FLAT	120	1.0arcsec	LR-B	Halogen2
Nov 4 (4)	JMOA0004	FLAT	120	1.0arcsec	LR-B	Halogen2
Nov 4 (4)	JMOA0005	FLAT	120	1.0arcsec	LR-B	Halogen2
Nov 4 (4)	JMOA0006	FLAT	120	1.0arcsec	LR-B	Halogen2
Nov 4 (4)	JMOA0007	FLAT	120	1.0arcsec	LR-B	Halogen2
Nov 4 (4)	JMOA0008	FLAT	80	1.5arcsec	LR-B	Halogen2
Nov 4 (4)	JMOA0009	FLAT	80	1.5arcsec	LR-B	Halogen2
Nov 4 (4)	JMOA0010	FLAT	80	1.5arcsec	LR-B	Halogen2
Nov 4 (4)	JMOA0011	FLAT	80	1.5arcsec	LR-B	Halogen2
Nov 4 (4)	JMOA0012	FLAT	80	1.5arcsec	LR-B	Halogen2
Nov 4 (4)	JMOA0013	FLAT	60	2.0arcsec	LR-B	Halogen2
Nov 4 (4)	JMOA0014	FLAT	60	2.0arcsec	LR-B	Halogen2
Nov 4 (4)	JMOA0015	FLAT	60	2.0arcsec	LR-B	Halogen2
Nov 4 (4)	JMOA0016	FLAT	60	2.0arcsec	LR-B	Halogen2
Nov 4 (4)	JMOA0017	FLAT	60	2.0arcsec	LR-B	Halogen2
Nov 4 (4)	JMOA0018	FLAT	25	5.0arcsec	LR-B	Halogen2
Nov 4 (4)	JMOA0019	FLAT	25	5.0arcsec	LR-B	Halogen2
Nov 4 (4)	JMOA0020	FLAT	25	5.0arcsec	LR-B	Halogen2
Nov 4 (4)	JMOA0021	FLAT	25	5.0arcsec	LR-B	Halogen2
Nov 4 (4)	JMOA0022	FLAT	25	5.0arcsec	LR-B	Halogen2
Nov 4 (4)	JMOA0023	ARC	60	1.0arcsec	LR-B	Helium
Nov 4 (4)	JMOA0024	ARC	60	1.0arcsec	LR-B	Helium
Nov 4 (4)	JMOA0025	ARC	60	1.0arcsec	LR-B	Helium
Nov 4 (4)	JMOA0026	ARC	20	1.0arcsec	LR-B	Argon
Nov 4 (4)	JMOA0027	ARC	60	1.0arcsec	LR-B	Neon
Nov 4 (4)	JMOA0028	ARC	40	1.5arcsec	LR-B	Helium
Nov 4 (4)	JMOA0029	ARC	40	1.5arcsec	LR-B	Helium
Nov 4 (4)	JMOA0030	ARC	40	1.5arcsec	LR-B	Helium
Nov 4 (4)	JMOA0031	ARC	15	1.5arcsec	LR-B	Argon
Nov 4 (4)	JMOA0032	ARC	40	1.5arcsec	LR-B	Neon
Nov 4 (4)	JMNA0033	ARC	25	2.0arcsec	LR-B	Helium
Nov 4 (4)	JMOA0034	ARC	25	2.0arcsec	LR-B	Helium
Nov 4 (4)	JMOA0035	ARC	25	2.0arcsec	LR-B	Helium
Nov 4 (4)	JMOA0036	ARC	10	2.0arcsec	LR-B	Argon
Nov 4 (4)	JMOA0037	ARC	25	2.0arcsec	LR-B	Neon
Nov 4 (4)	JMOA0038	ARC	15	5.0arcsec	LR-B	Helium
Nov 4 (4)	JMOA0039	ARC	15	5.0arcsec	LR-B	Helium
Nov 4 (4)	JMOA0040	ARC	15	5.0arcsec	LR-B	Helium
Nov 4 (4)	JMOA0041	ARC	5	5.0arcsec	LR-B	Argon
Nov 4 (4)	JMOA0042	ARC	15	5.0arcsec	LR-B	Neon
Nov 4 (4)	JMOA0043	ARC	5	5.0arcsec	LR-B	Argon
Nov 4 (4)	JMOA0044	ARC	15	5.0arcsec	LR-B	Neon
Nov 4 (4)	JMOA0045	ARC	15	1.5arcsec	LR-B	Argon
Nov 4 (4)	JMOA0046	ARC	40	1.5arcsec	LR-B	Neon
Nov 4 (4)	JMOA0047	BIAS	0	Open	Open	Parking
Nov 4 (4)	JMOA0048	BIAS	0	Open	Open	Parking

Table A.1 – Continued

Date <sup>a</sup>	Filename	Image	Seconds	Slit	Grism	Lamp
Nov 4 (4)	JMOA0049	BIAS	0	Open	Open	Parking
Nov 4 (4)	JMOA0050	BIAS	0	Open	Open	Parking
Nov 4 (4)	JMOA0051	BIAS	0	Open	Open	Parking
Nov 4 (4)	JMOA0052	BIAS	0	Open	Open	Parking
Nov 4 (4)	JMOA0053	BIAS	0	Open	Open	Parking
Nov 4 (4)	JMOA0054	BIAS	0	Open	Open	Parking
Nov 4 (4)	JMOA0055	BIAS	0	Open	Open	Parking
Nov 4 (4)	JMOA0056	BIAS	0	Open	Open	Parking
Nov 4 (4)	JMOA0057	SLIT POS	1	1.0arcsec	Open	Halogen2
Nov 4 (4)	JMOA0058	SLIT POS	0.5	1.5arcsec	Open	Halogen2
Nov 4 (4)	JMOA0059	SLIT POS	0.2	2.0arcsec	Open	Halogen2
Nov 4 (4)	JMOA0060	SLIT POS	0.1	5.0arcsec	Open	Halogen2
Nov 4 (4)	JMOA0067	G93-48	30	5.0arcsec	LR-B	Parking
Nov 4 (4)	JMOA0071	BD+28d4211	10	5.0arcsec	LR-B	Parking
Nov 4 (4)	JMOA0076	SN20350	1800	1.0arcsec	LR-B	Parking
Nov 4 (4)	JMOA0077	SN20350	1800	1.0arcsec	LR-B	Parking
Nov 4 (4)	JMOA0085	SN19992	1800	1.0arcsec	LR-B	Parking
Nov 4 (4)	JMOA0086	SN19992	1800	1.0arcsec	LR-B	Parking
Nov 4 (4)	JMOA0087	SN19992	1800	1.0arcsec	LR-B	Parking
Nov 5 (4)	JMOA0092	SN19658	1800	1.0arcsec	LR-B	Parking
Nov 5 (4)	JMOA0093	SN19658	1800	1.0arcsec	LR-B	Parking
Nov 5 (4)	JMOA0096	SN20208	90	Open	Open	Parking
Nov 5 (4)	JMOA0098	SN20208	1800	1.0arcsec	LR-B	Parking
Nov 5 (4)	JMOA0099	SN20208	1800	1.0arcsec	LR-B	Parking
Nov 5 (4)	JMOA0100	SN20208	1800	1.0arcsec	LR-B	Parking
Nov 5 (4)	JMOA0106	SN19849	1800	1.0arcsec	LR-B	Parking
Nov 5 (4)	JMOA0107	SN19849	1800	1.0arcsec	LR-B	Parking
Nov 5 (4)	JMOA0112	HILT600	5	5.0arcsec	LR-B	Parking
Nov 5 (4)	JMOA0116	BD+28d4211	2	5.0arcsec	LR-B	Parking
Nov 5 (4)	JMOA0117	BD+28d4211	5	5.0arcsec	LR-B	Parking

<sup>a</sup> Date of observation. In brackets, the number of observation nights from 1 to 4.



## APPENDIX B

# Maths

### B.1 Chebyshev polynomials

The SN spectra obtained at TNG, whose reduction is discussed in §5, have to be calibrated in wavelengths, since, after the primary reduction, they are given in column number. The correspondence between pixels and wavelengths is performed in two steps. First, we used the images with the lamp spectra to match the known emission lines to the pixel column where they appear. Then an interpolation of the rest of the pixels is done through a sum of Chebyshev polynomials up to order 5. The expressions of the Chebyshev polynomials are

$$T_0(x) = 1 \quad (\text{B.1})$$

$$T_1(x) = x \quad (\text{B.2})$$

$$T_2(x) = 2x^2 - 1 \quad (\text{B.3})$$

$$T_3(x) = 4x^3 - 3x \quad (\text{B.4})$$

$$T_4(x) = 8x^4 - 8x^2 + 1 \quad (\text{B.5})$$

$$T_5(x) = 16x^5 - 20x^3 + 5x \quad (\text{B.6})$$

$$T_n(x) = 2x(T_{n-1}) - T_{n-2}, \quad (\text{B.7})$$

and the function used for the interpolation, a sum of the polynomials up to order  $n$ , is

$$F(x) = \sum_{i=0}^n c_i T_i(x), \quad (\text{B.8})$$

where the coefficients  $c_i$  are left free and calculated by IRAF routines.

## B.2 Binning error calculation

In order to look for trends in SN Ia light-curve parameters with increasing distance, we first bin the SNe in distance and calculate the mean, the weighted mean, the median and their uncertainties for each of the bins. We then perform a linear fit to these measurements, and calculate the reduced  $\chi^2$  of the fit. We present here the expressions used for all these measurements.

The expressions used for the measurement of the mean and its error ( $\mu \pm \Delta\mu$ ) are

$$\mu = \frac{\sum_i^n x_i}{n} \quad \Delta\mu = \frac{\sigma_\mu}{\sqrt{n}}, \quad (\text{B.9})$$

where  $x_i$  is the light-curve parameter for SN  $i$ ,  $n$  is the number of SNe in the bin, and  $\sigma_\mu$  is the standard deviation expressed as

$$\sigma_\mu = \sqrt{\frac{\sum_i^n (x_i - \mu)^2}{n}} = \sqrt{\langle x^2 \rangle - \langle x \rangle^2}. \quad (\text{B.10})$$

For the measurement of the weighted mean ( $w\mu$ ) we used the expression

$$w\mu = \frac{\sum_i^n \frac{x_i}{\sigma_i^2}}{\sum_i^n \frac{1}{\sigma_i^2}}, \quad (\text{B.11})$$

where  $\sigma_i$  is the error of the light-curve parameter for SN  $i$ . For the measurement of the weighted mean error, instead of using the commonly used expression,

$$\Delta w\mu = \frac{1}{\sqrt{\sum_i^n \frac{1}{\sigma_i^2}}}, \quad (\text{B.12})$$

we used the same error definition and standard deviation as for the mean,

$$\sigma_{w\mu} = \sqrt{\frac{\sum_i^n (x_i - w\mu)^2}{n}} \quad (\text{B.13})$$

$$\Delta w\mu = \frac{\sigma_{w\mu}}{\sqrt{n}}. \quad (\text{B.14})$$

This was motivated by the fact that when a SN has a very small value, the error of the weighted mean becomes very small, and we prefer to give a measure of the dispersion around the weighted mean.

We used the common definition of the median ( $m$ ) to calculate it. The value such that half of measurements are above, and half are below. When the sample median lies between two observed values, the median is set to be the mean value of these two. The median is generally more robust than the mean, as it is insensitive to the exact shape of the tails of a distribution. For the measurement of its error, we used a procedure from [Olive \(2005\)](#) which uses the following expressions,

$$\begin{aligned} L &= \left\lfloor \frac{n}{2} \right\rfloor - \left\lceil \sqrt{\frac{n}{4}} \right\rceil \\ U &= n - L \\ \Delta m &= \frac{x_U - x_{L+1}}{2}, \end{aligned} \quad (\text{B.15})$$

where  $n$  is the total number of events,  $L$  and  $U$  denote positions once the events are ordered from low to high values,  $\Delta m$  is the measured error of the median, and  $\lceil x \rceil$  denote the smallest integer greater than or equal to  $x$ , while  $\lfloor x \rfloor$  denote the greatest integer smaller than or equal to  $x$  (e.g.,  $\lceil 6.8 \rceil = 7$ ,  $\lfloor 6.8 \rfloor = 6$ ).

Finally, once we have measured the values of the three statistics ( $\mu$ ,  $w\mu$  and  $m$ ) in each of the bins, we perform three linear fits to these points, obtaining the slope and its error ( $\beta \pm \Delta\beta$ ) as a measure of correlation. For this, we minimize the chisquared function

$$\chi^2(\alpha, \beta) = \sum_{i=0}^N \left( \frac{y_i - F(x_i; \alpha, \beta)}{\rho_i} \right)^2 = \sum_{i=0}^N \left( \frac{y_i - (\alpha + \beta x_i)}{\rho_i} \right)^2 \quad (\text{B.16})$$

where  $x_i$  and  $y_i$  are the distance measurement and the light-curve parameter of the SN  $i$ , and  $\mu_x$  and  $\mu_y$  are the mean values of the distance and the light-curve parameter, respectively,  $N$  is the number of points to be fitted (number of bins),  $\alpha = \mu_y - \beta\mu_x$  is the y-axis intersection of the linear fit, and  $\rho_i$  is the error of the SN  $i$ , since the error along  $x$ , is projected along the  $y$ -direction by calculating the function at the points  $x - \sigma_{xl}$  and  $x + \sigma_{xh}$ , and

$$\rho_i = \sigma_{y,i}^2 + \left( \left( \frac{\sigma_{xl,i} + \sigma_{xh,i}}{2} \right) \beta \right)^2. \quad (\text{B.17})$$

As described in §7, we also look for the same correlations but using only two bins with equal number of SNe in each. We measure the mean, the weighted mean and the median values for the two bins using the expressions explained before, with the only difference that we estimate the error of the median through bootstrapping ([Efron, 1979](#)). This technique allows the measurement of estimators through the construction of several samples from the original data. We select a thousand samples, of equal size as the number of SNe in the bin, each of which obtained by random sampling with replacement from the original sample. Then, we measure the median of all these thousand samples. The RMS of the distribution of these thousand median measurements, is taken as the error of the median in the bin.

In this 2-bin analysis, the difference in the scatter with respect to each of mean,

weighted mean, and median, is also measured using,

$$\sigma_\mu = \sqrt{\frac{\sum_i^n (x_i - \mu)^2}{n}} \quad \sigma_{w\mu} = \sqrt{\frac{\sum_i^n (x_i - w\mu)^2}{n}} \quad \sigma_m = \sqrt{\frac{\sum_i^n (x_i - m)^2}{n}}, \quad (\text{B.18})$$

and the errors are obtained through

$$\Delta\sigma_\mu = \frac{1}{2\sigma_\mu\sqrt{n}} \sqrt{\frac{(x_i - \mu)^4 - (n - 3)\sigma_\mu^4}{n - 1}} \quad (\text{B.19})$$

$$\Delta\sigma_{w\mu} = \frac{1}{2\sigma_{w\mu}\sqrt{n}} \sqrt{\frac{(x_i - w\mu)^4 - (n - 3)\sigma_{w\mu}^4}{n - 1}}. \quad (\text{B.20})$$

The error of the scatter with respect to the median is taken from bootstrapping. It is the RMS of the distribution of the thousand RMSs of the constructed distributions.

## APPENDIX C

---

# Computation of distances

---

In this appendix, all the distance measurements that are used for the analysis in §7 are presented.

### C.1 Spherical trigonometry

We have to make use of the laws of spherical trigonometry and the astronomical coordinates in order to measure angular distances between objects in the sky. There are three relations between the sides and angles of a spherical triangle composed of three segments of great circles:

*Law of sines*

$$\frac{\sin a}{\sin A} = \frac{\sin b}{\sin B} = \frac{\sin c}{\sin C} \quad (\text{C.1})$$

*Law of cosines for sides*

$$\cos a = \cos b \cos c + \sin b \sin c \cos A \quad (\text{C.2})$$

*Law for cosines for angles*

$$\cos A = -\cos B \cos C + \sin B \sin C \cos a. \quad (\text{C.3})$$

where the angles are defined in Fig. C.1.

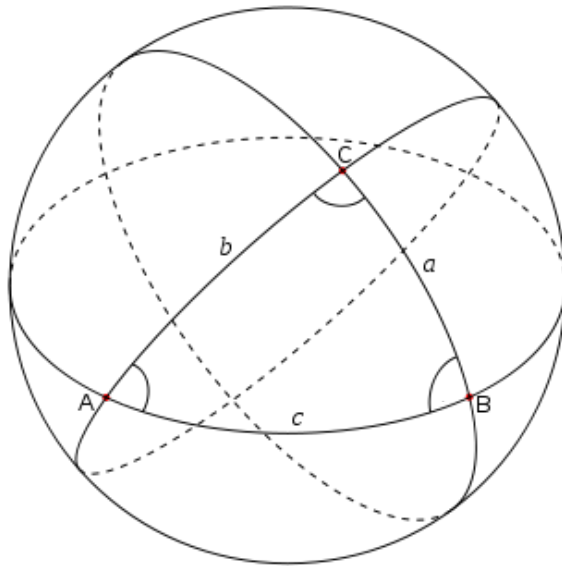


**Figure C.1:** Spherical trigonometry. A spherical triangle defined in the surface of a sphere.  $a, b$  and  $c$  are the angles measured from the center of the sphere, while  $A, B$  and  $C$  are angles between the major arcs from the intersection.

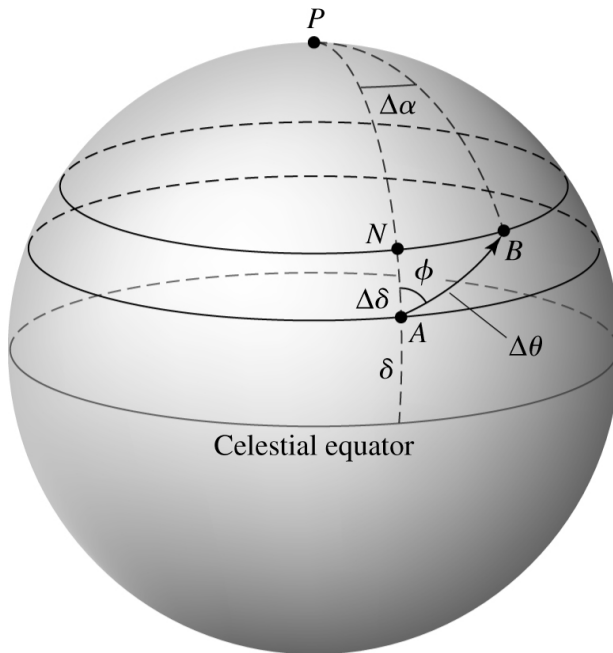


**Figure C.2:** Equatorial coordinates of two objects on the surface of a sphere, and the measurement of the separation  $\Delta\theta$  from  $A$  to  $B$ , a segment of a great circle. Image from [Carroll et al. \(2006\)](#).

## C.2 Projected galactocentric distances (PGCD)

### C.2.1 Angular separation

In Fig. C.2, we can see the equatorial coordinates of two objects,  $A$  and  $B$ , in the celestial sphere. The angular separation between them is  $\Delta\theta = AB$ . This distance, together with the angular separations from the north celestial pole ( $P$ ) to the objects ( $PA = 90 - \delta_A$  and  $PB = 90 - \delta_B$ ), form a spherical triangle composed by segments of great circles, where we can use the law of cosines for sides to obtain an expression for the angular separation  $dist \equiv \Delta\theta$ ,

$$\begin{aligned}\cos(dist) &= \cos(90 - \delta_A) \cos(90 - \delta_B) + \sin(90 - \delta_A) \sin(90 - \delta_B) \cos \Delta\alpha \\ &= \sin \delta_A \sin \delta_B + \cos \delta_A \cos \delta_B \cos \Delta\alpha.\end{aligned}\quad (\text{C.4})$$

Once we have an expression for the angular distance between the two objects (in our case a SN and the center of its host galaxy), we can substitute the generic coordinates with the right ascension and declination of the supernova  $(\alpha, \delta)$  measured by SDSS-II/SNe Survey, and the host galaxy matched  $(\alpha_G, \delta_G)$  from SDSS-DR7 as

$$\cos(dist) = \sin(\delta_G) \sin(\delta) + \cos(\delta_G) \cos(\delta) \cos(\alpha - \alpha_G). \quad (\text{C.5})$$

Then, the angular separation between the supernova and the center of its host galaxy is

$$dist = \arccos [\sin(\delta_G) \sin(\delta) + \cos(\delta_G) \cos(\delta) \cos(\alpha - \alpha_G)] \quad (\text{C.6})$$

### C.2.2 Projected galactocentric distance

With the measurements of the angular separation and the angular diameter distance<sup>1</sup> ( $d_A$ ) from the observer to the host galaxy, we will able to calculate the projected galactocentric distance in physical units of kiloparsec<sup>2</sup> ( $dist_{kpc}$ ). For this measurement, we are going to need the redshift of the objects. As the SN is supposed to be in the host, we can obtain the redshift of both through three different ways. If we have spectroscopy of the host galaxy, we can easily measure the redshift from the absorptions in the spectrum. When this is not possible, but we have spectroscopy of the SN, we can measure the redshift from the host galaxy lines in the SN spectrum. If these lines are weak or if the SN is far enough from the galaxy that when the spectrum was measured the slit was positioned with no host in it, we can measure the redshift from the SN spectrum lines. When no spectroscopy of the host galaxy or the SN are available, the redshift is measured photometrically from host galaxy colors.

By definition, the angular distance ( $d_A$ ) is the transverse comoving distance divided by a factor  $(1 + z)$ ,

$$d_A = \frac{c}{H_0} \frac{1}{(1 + z)} \int_0^{z'} \frac{dz'}{\sqrt{\Omega_M (1 + z)^3 + \Omega_\Lambda}} \quad (\text{C.7})$$

---

<sup>1</sup>Defined in §2.1.7.

<sup>2</sup>1 pc =  $3.0857 \cdot 10^{16}$  m.

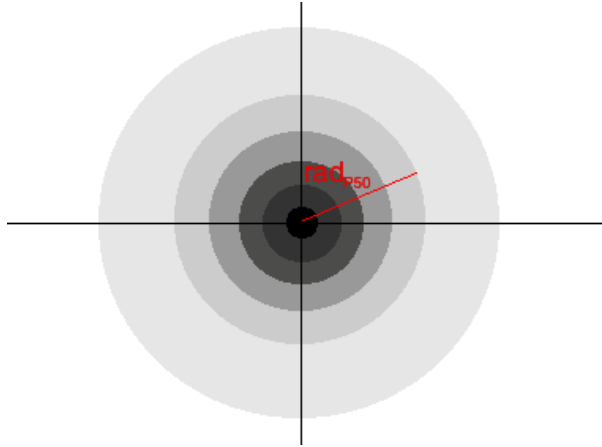


**Figure C.3:** Petrosian radius 50. Radius of a circle that contains the 50% of the flux within it.

where  $H_0 = 65 \text{ km s}^{-1} \text{ Mpc}^{-1}$  because it is the value at which MLCS2k2 is trained, and we have assumed a flat  $\Lambda\text{CDM}$  cosmology with  $\Omega_M = 1 - \Omega_\Lambda = 0.274$ . Then,

$$dist_{kpc} = d_A \times dist, \quad (\text{C.8})$$

with  $dist$  in rad.

### C.3 Normalized Galactocentric Distances (NGCD)

#### C.3.1 Petrosian normalization

The Petrosian 50 radius ( $rad_{P50}$ ) is defined as the radius of a circle that contains the 50% of the total flux of the galaxy (see Fig. C.3). We do not have to define any orientation angle due to the symmetry in all directions. Simply dividing the distance from the SN to the center of the host by the Petrosian 50 radius, we can obtain the distance in units of Petrosian 50 radius ( $dist_{P50}$ ),

$$dist_{P50} = \frac{dist_{kpc}}{rad_{P50}} = \frac{dist}{rad_{P50}(angle)}. \quad (\text{C.9})$$

#### C.3.2 Sérsic normalization

In [de Vaucouleurs \(1948, 1953\)](#), the fractional flux emitted at a distance up to  $r$  from to the galactic center is defined as

$$K(r) = \frac{L_r}{L_T} = \frac{\int_0^r I(r) r dr}{\int_0^\infty I(r) r dr}, \quad (\text{C.10})$$

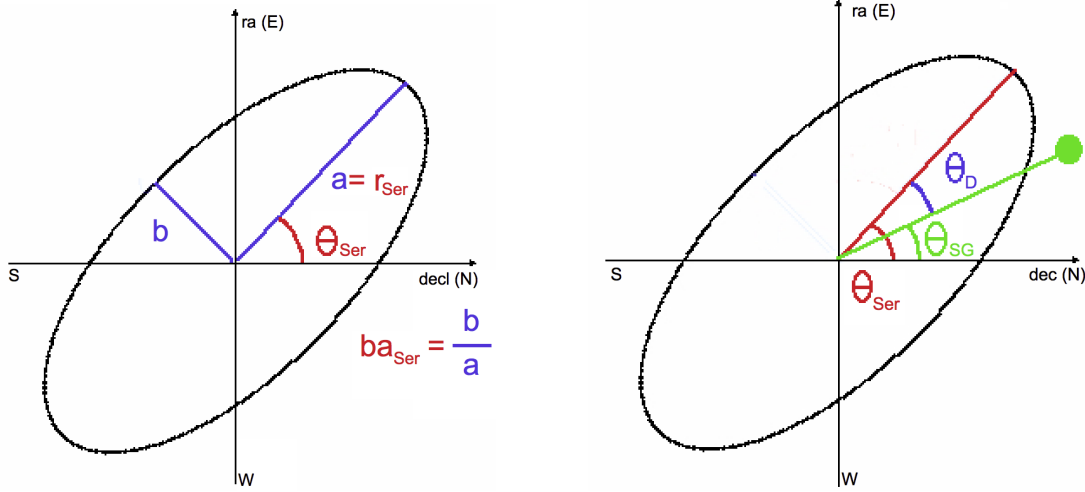


**Figure C.4:** Definition of Sérsic parameters. On the left, the two radii and the orientation angle from north to east. On the right, the definition of  $\theta_D$ , the angle from the long axis of the ellipse to the radius of the location of the supernova.

and the profile used for this parametrization is

$$I(r) = I_e \exp \left[ -a_n \left[ \left( \frac{r}{r_e} \right)^{\frac{1}{n}} - 1 \right] \right], \quad (\text{C.11})$$

where  $r_e$  is the value for what  $K(r_e) = 0.5$ , and  $I_e$  the intensity at this radius. At the center ( $r = 0$ ) we have

$$I(0) = I_e \exp(a_n) \equiv I_0. \quad (\text{C.12})$$

Then,

$$I(r) = I_0 \exp \left[ -a_n \left( \frac{r}{r_e} \right)^{\frac{1}{n}} \right]. \quad (\text{C.13})$$

Two profiles are applied to hosts with different morphologies. A pure exponential profile ( $n = 1, a_n = 1.61$ ) is used for spiral galaxies, while the de Vaucouleurs profile ( $n = 4, a_n = 7.67$ ) is used to elliptical hosts. Sérsic parameters needed for the normalization are defined in Fig. C.4. In order to perform this normalization we will need the angle from the declination (north) axis to the line from the center of the host galaxy to the SN ( $\theta_{SG}$ ), which can be defined as

$$\begin{aligned} \sin \theta_{SG} &= \frac{\alpha - \alpha_G}{dist} \\ \cos \theta_{SG} &= \frac{\delta - \delta_G}{dist} \\ \theta_{SG} &= \arctan \frac{\alpha - \alpha_G}{\delta - \delta_G}. \end{aligned} \quad (\text{C.14})$$

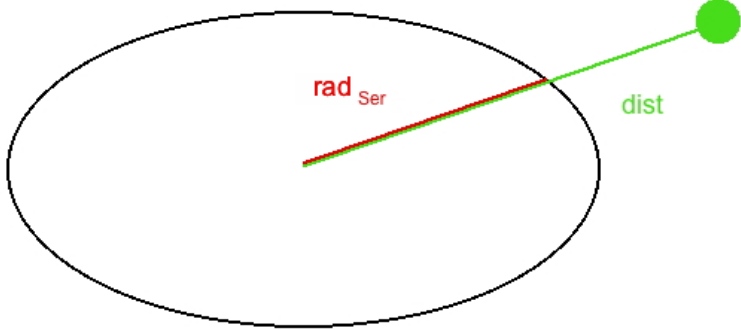


**Figure C.5:** Sérsic normalization. The red line is the radius of the ellipse in the direction where the supernova is located. It will be the unit of normalization. The green line is the angular distance between the center of the host and the supernova.

From there, we can define de angle between the major axis of the ellipse and the radius of the SN in the host galaxy ( $\theta_D$ , shown in Fig. C.4) as

$$\theta_D = \theta_{Ser} - \theta_{SG}. \quad (\text{C.15})$$

There are several ways to define  $\theta_D$ , because we do not care about which quadrant the supernova is in. There are horizontal and vertical symmetries and we are only measuring the angle in order to normalize the radius. Once we have this angle, the radius of the ellipse in this direction is

$$rad_{Ser} = \frac{1}{\sqrt{\left(\frac{\cos \theta_D}{r_{Ser}}\right)^2 + \left(\frac{\sin \theta_D}{r_{Ser} ba_{Ser}}\right)^2}} = \frac{r_{Ser} ba_{Ser}}{\sqrt{ba_{Ser}^2 \cos^2 \theta_D + \sin^2 \theta_D}} \quad (\text{C.16})$$

Finally, the distance from the SN to the center of the host in Sérsic profile units (see Fig. C.5) is

$$dist_{Ser} = \frac{dist_{kpc}}{rad_{Ser}} = \frac{dist}{rad_{Ser}(angle)}. \quad (\text{C.17})$$

### C.3.3 Isophotal normalization

The same procedure as for the Sérsic normalization is used here. But in this case the ellipse is defined considering the isophote of 25 mag/arcsec<sup>2</sup> in the *r* band.

## APPENDIX D

---

# SNe distance measurements

---

We present here a table with all the distance measurements from the analysis presented in §7.

**Table D.1:** Final SN sample after all cuts have been applied.

ID <sup>a</sup>	$z$	$D_{\text{kpc}}$	$D_{\text{PSO}}$	$D_{\text{ISO}}$	$D_{\text{Sersic}}^b$	Host type <sup>c</sup>	In sample <sup>d</sup>
2004hz	0.142	$10.14 \pm 0.26$	$1.553 \pm 0.044$	$0.277 \pm 0.004$	$1.631 \pm 0.054$	spiral	both
2004ie	0.050	$7.29 \pm 0.16$	$2.137 \pm 0.032$	$0.307 \pm 0.003$	$1.754 \pm 0.033$	spiral	both
2005eg	0.190	$12.14 \pm 0.30$	$1.831 \pm 0.036$	$0.282 \pm 0.004$	$2.194 \pm 0.081$	spiral	both
2005ez	0.129	$4.57 \pm 0.15$	$1.576 \pm 0.048$	$0.247 \pm 0.006$	$3.019 \pm 0.203$	spiral	both
2005fa	0.161	$8.76 \pm 0.22$	$1.793 \pm 0.046$	$0.223 \pm 0.004$	$2.755 \pm 0.115$	elliptical	SALT2
2005ff	0.089	$6.40 \pm 0.15$	$1.983 \pm 0.056$	$0.263 \pm 0.004$	$1.582 \pm 0.081$	elliptical	both
2005fm	0.152	$3.77 \pm 0.15$	$1.926 \pm 0.109$	$0.259 \pm 0.009$	$2.964 \pm 0.425$	spiral	both
2005fp	0.212	$5.72 \pm 0.30$	$1.514 \pm 0.178$	$0.287 \pm 0.014$	$3.271 \pm 2.305$	spiral	both
2005fu	0.190	$5.71 \pm 0.22$	$1.373 \pm 0.056$	$0.207 \pm 0.007$	$2.291 \pm 0.168$	spiral	both
2005fv	0.117	$13.18 \pm 0.29$	$2.200 \pm 0.053$	$0.237 \pm 0.002$	$1.575 \pm 0.037$	spiral	both
2005fw	0.143	$5.24 \pm 0.19$	$1.271 \pm 0.056$	$0.275 \pm 0.009$	$1.741 \pm 0.153$	spiral	both
2005fy	0.194	$10.01 \pm 0.27$	$1.587 \pm 0.051$	$0.220 \pm 0.004$	$1.690 \pm 0.072$	spiral	MLCS2k2
2005ga	0.173	$6.57 \pm 0.21$	$1.763 \pm 0.052$	$0.196 \pm 0.005$	$1.692 \pm 0.059$	spiral	both
2005gb	0.086	$8.02 \pm 0.18$	$1.748 \pm 0.024$	$0.274 \pm 0.003$	$2.417 \pm 0.048$	spiral	both
2005gc	0.165	$1.17 \pm 0.31$	$0.241 \pm 0.068$	$0.088 \pm 0.023$	$0.713 \pm 0.289$	spiral	both
2005gd	0.160	$1.88 \pm 0.27$	$0.499 \pm 0.072$	$0.091 \pm 0.013$	$0.520 \pm 0.082$	spiral	both
2005ge	0.212	$10.76 \pm 0.29$	$2.028 \pm 0.070$	$0.270 \pm 0.005$	$1.965 \pm 0.108$	spiral	both
2005gf	0.249	$10.60 \pm 0.31$	$2.527 \pm 0.098$	$0.257 \pm 0.005$	$2.361 \pm 0.177$	spiral	both
2005gp	0.126	$3.42 \pm 0.16$	$0.708 \pm 0.038$	$0.121 \pm 0.005$	$0.723 \pm 0.047$	spiral	both
2005gx	0.161	$2.67 \pm 0.23$	$0.898 \pm 0.120$	$0.191 \pm 0.016$	$1.304 \pm 0.383$	spiral	both
2005hj	0.056	$1.01 \pm 0.12$	$0.524 \pm 0.063$	$0.063 \pm 0.008$	$0.422 \pm 0.053$	spiral	both
2005hn	0.107	$1.48 \pm 0.11$	$0.771 \pm 0.060$	$0.098 \pm 0.007$	$1.005 \pm 0.087$	spiral	both
2005hv	0.179	$1.27 \pm 0.16$	$0.473 \pm 0.177$	$0.086 \pm 0.011$	$0.637 \pm 0.126$	elliptical	both
2005hx	0.120	$5.74 \pm 0.32$	$2.040 \pm 0.252$	$0.517 \pm 0.027$	$2.614 \pm 1.186$	spiral	both
2005hy	0.155	$3.60 \pm 0.39$	$0.972 \pm 0.113$	$0.186 \pm 0.020$	$1.091 \pm 0.164$	spiral	SALT2
2005hz	0.129	$2.40 \pm 0.15$	$0.637 \pm 0.039$	$0.095 \pm 0.006$	$0.623 \pm 0.040$	spiral	both
2005if	0.067	$1.20 \pm 0.07$	$0.290 \pm 0.016$	$0.054 \pm 0.003$	$0.328 \pm 0.020$	spiral	both
2005ij	0.124	$0.53 \pm 0.14$	$0.090 \pm 0.024$	$0.019 \pm 0.005$	$0.125 \pm 0.034$	spiral	both
2005ir	0.075	$5.25 \pm 0.15$	$1.229 \pm 0.027$	$0.188 \pm 0.004$	$1.082 \pm 0.026$	spiral	both
2005is	0.173	$1.75 \pm 0.18$	$0.524 \pm 0.053$	$0.070 \pm 0.007$	$0.984 \pm 0.130$	elliptical	both
2005je	0.093	$1.74 \pm 0.09$	$0.503 \pm 0.024$	$0.045 \pm 0.002$	$0.399 \pm 0.019$	elliptical	SALT2
2005jh	0.109	$1.48 \pm 0.10$	$0.617 \pm 0.043$	$0.075 \pm 0.005$	$0.753 \pm 0.063$	elliptical	both
2005jk	0.190	$15.10 \pm 0.41$	$2.315 \pm 0.073$	$0.452 \pm 0.008$	$2.307 \pm 0.116$	spiral	both
2005jl	0.179	$2.30 \pm 0.24$	$0.431 \pm 0.049$	$0.074 \pm 0.008$	$0.411 \pm 0.049$	spiral	both
2005js	0.079	$9.80 \pm 0.21$	$3.793 \pm 0.088$	$0.259 \pm 0.002$	$3.600 \pm 0.061$	elliptical	MLCS2k2
2005kp	0.116	$3.53 \pm 0.25$	$1.254 \pm 0.114$	$0.232 \pm 0.016$	$1.634 \pm 0.437$	spiral	both
2005kt	0.064	$0.74 \pm 0.07$	$0.464 \pm 0.045$	$0.028 \pm 0.003$	$0.543 \pm 0.052$	elliptical	both

## SNe distance measurements

Table D.1 – Continued

ID <sup>a</sup>	$z$	$D_{\text{kpc}}$	$D_{\text{P50}}$	$D_{\text{ISO}}$	$D_{\text{Sersic}}^b$	Host type <sup>c</sup>	In sample <sup>d</sup>
2005mi	0.214	2.68 ± 0.19	0.426 ± 0.031	0.070 ± 0.005	0.595 ± 0.049	spiral	SALT2
2006er	0.083	8.34 ± 0.19	1.942 ± 0.026	0.252 ± 0.002	2.015 ± 0.051	elliptical	both
2006ex	0.146	16.42 ± 0.35	2.248 ± 0.025	0.310 ± 0.002	2.188 ± 0.045	spiral	both
2006ey	0.168	7.63 ± 0.21	2.938 ± 0.099	0.354 ± 0.006	6.434 ± 0.607	elliptical	both
2006fa	0.166	8.88 ± 0.23	2.008 ± 0.040	0.221 ± 0.004	1.656 ± 0.053	elliptical	both
2006fb	0.244	19.00 ± 0.47	1.828 ± 0.065	0.352 ± 0.005	1.866 ± 0.071	spiral	both
2006fc	0.121	7.28 ± 0.20	1.453 ± 0.045	0.223 ± 0.004	1.336 ± 0.039	spiral	MLCS2k2
2006fl	0.171	3.21 ± 0.19	0.447 ± 0.028	0.079 ± 0.004	0.528 ± 0.041	spiral	both
2006fu	0.197	1.77 ± 0.22	0.319 ± 0.040	0.067 ± 0.008	0.479 ± 0.075	spiral	both
2006fx	0.223	9.56 ± 0.31	1.522 ± 0.051	0.254 ± 0.006	1.567 ± 0.060	spiral	both
2006fy	0.082	1.83 ± 0.09	0.592 ± 0.026	0.091 ± 0.004	0.624 ± 0.030	spiral	MLCS2k2
2006gg	0.202	1.95 ± 0.25	0.697 ± 0.122	0.152 ± 0.019	1.872 ± 1.873	spiral	both
2006gp	0.211	2.15 ± 0.29	0.610 ± 0.093	0.195 ± 0.026	1.262 ± 0.416	spiral	SALT2
2006gx	0.180	3.42 ± 0.21	0.701 ± 0.043	0.134 ± 0.008	0.934 ± 0.102	spiral	MLCS2k2
2006he	0.213	5.27 ± 0.25	1.149 ± 0.064	0.361 ± 0.016	3.204 ± 0.449	spiral	SALT2
2006hh	0.237	13.03 ± 0.34	1.715 ± 0.044	0.412 ± 0.007	3.611 ± 0.181	spiral	both
2006hl	0.147	6.39 ± 0.24	1.231 ± 0.050	0.259 ± 0.008	1.698 ± 0.168	spiral	both
2006hp	0.246	13.40 ± 0.36	2.672 ± 0.091	0.412 ± 0.007	3.119 ± 0.141	spiral	both
2006hr	0.157	6.36 ± 0.20	1.337 ± 0.326	0.222 ± 0.005	1.580 ± 0.070	spiral	MLCS2k2
2006hw	0.139	4.56 ± 0.17	0.792 ± 0.031	0.140 ± 0.005	1.315 ± 0.078	spiral	both
2006iy	0.203	8.95 ± 0.27	2.683 ± 0.168	0.419 ± 0.009	3.181 ± 0.451	spiral	both
2006ja	0.106	2.94 ± 0.12	1.322 ± 0.050	0.133 ± 0.005	1.781 ± 0.089	elliptical	both
2006jn	0.224	10.01 ± 0.27	1.864 ± 0.059	0.237 ± 0.004	1.919 ± 0.115	elliptical	both
2006jp	0.159	1.39 ± 0.13	0.281 ± 0.027	0.044 ± 0.004	0.298 ± 0.033	elliptical	MLCS2k2
2006jq	0.127	0.98 ± 0.13	0.573 ± 0.084	0.085 ± 0.012	0.796 ± 0.139	spiral	SALT2
2006jr	0.177	6.56 ± 0.35	1.464 ± 0.120	0.182 ± 0.009	1.231 ± 0.094	spiral	both
2006jw	0.249	2.11 ± 0.29	0.172 ± 0.024	0.032 ± 0.004	0.159 ± 0.022	spiral	both
2006jy	0.203	1.36 ± 0.20	0.563 ± 0.087	0.096 ± 0.014	1.849 ± 0.957	spiral	SALT2
2006jz	0.198	12.08 ± 0.31	1.597 ± 0.046	0.217 ± 0.003	1.072 ± 0.042	elliptical	both
2006ka	0.247	7.24 ± 0.25	1.573 ± 0.064	0.238 ± 0.007	2.120 ± 0.133	spiral	both
2006kd	0.135	4.57 ± 0.17	0.972 ± 0.035	0.178 ± 0.006	1.181 ± 0.073	spiral	both
2006kl	0.220	7.80 ± 0.36	1.769 ± 0.149	0.276 ± 0.011	1.828 ± 0.359	spiral	both
2006kq	0.196	3.21 ± 0.18	0.530 ± 0.029	0.080 ± 0.004	0.501 ± 0.030	spiral	MLCS2k2
2006ks	0.208	8.33 ± 0.26	1.361 ± 0.050	0.251 ± 0.006	1.404 ± 0.119	elliptical	both
2006kt	0.237	23.89 ± 0.52	6.441 ± 0.421	1.152 ± 0.010	9.360 ± 1.269	spiral	both
2006ku	0.187	1.09 ± 0.15	0.231 ± 0.032	0.030 ± 0.004	0.221 ± 0.034	elliptical	both
2006kw	0.185	4.86 ± 0.23	0.968 ± 0.051	0.177 ± 0.008	1.045 ± 0.065	spiral	both
2006kx	0.160	1.61 ± 0.17	0.643 ± 0.070	0.081 ± 0.009	1.126 ± 0.138	elliptical	both
2006ky	0.183	2.79 ± 0.36	1.347 ± 0.423	0.272 ± 0.034	1.913 ± 1.151	spiral	SALT2
2006kz	0.185	8.81 ± 0.27	1.478 ± 0.061	0.285 ± 0.006	1.650 ± 0.090	spiral	both
2006la	0.126	0.82 ± 0.14	0.405 ± 0.073	0.090 ± 0.015	0.620 ± 0.143	spiral	both
2006lb	0.181	1.75 ± 0.24	0.382 ± 0.054	0.064 ± 0.009	0.384 ± 0.055	spiral	SALT2
2006lj	0.242	10.15 ± 0.30	2.008 ± 0.082	0.345 ± 0.008	2.730 ± 0.304	elliptical	both
2006lo	0.179	3.22 ± 0.22	0.981 ± 0.084	0.196 ± 0.013	1.561 ± 0.389	spiral	both
2006lp	0.221	9.14 ± 0.27	2.144 ± 0.077	0.310 ± 0.007	2.406 ± 0.189	spiral	both
2006md	0.246	1.56 ± 0.30	0.593 ± 0.127	0.096 ± 0.019	5.986 ± 1.785	spiral	both
2006mt	0.220	3.29 ± 0.21	0.721 ± 0.051	0.105 ± 0.007	0.925 ± 0.074	spiral	both
2006mv	0.185	1.43 ± 0.28	0.589 ± 0.136	0.120 ± 0.024	0.912 ± 0.425	spiral	both
2006mz	0.245	10.03 ± 0.30	2.385 ± 0.100	0.403 ± 0.009	2.605 ± 0.178	spiral	both
2006nb	0.206	1.07 ± 0.23	0.362 ± 0.082	0.070 ± 0.015	0.543 ± 0.155	spiral	both
2006nc	0.123	3.39 ± 0.17	0.666 ± 0.038	0.124 ± 0.006	0.758 ± 0.044	spiral	both
2006ni	0.174	11.23 ± 0.27	2.498 ± 0.061	0.266 ± 0.003	3.160 ± 0.163	elliptical	both
2006nn	0.196	4.53 ± 0.29	0.844 ± 0.066	0.133 ± 0.008	0.803 ± 0.067	spiral	SALT2
2006no	0.250	11.02 ± 0.31	2.742 ± 0.084	0.347 ± 0.007	5.181 ± 0.544	elliptical	both
2006od	0.204	1.74 ± 0.67	0.347 ± 0.134	0.076 ± 0.029	0.393 ± 0.165	spiral	both
2006of	0.154	1.53 ± 0.18	0.451 ± 0.058	0.105 ± 0.012	1.003 ± 0.233	spiral	SALT2
2006oy	0.200	6.79 ± 0.23	1.194 ± 0.053	0.223 ± 0.006	1.476 ± 0.098	spiral	MLCS2k2
2006pa	0.250	9.66 ± 0.38	1.610 ± 0.086	0.314 ± 0.011	2.246 ± 0.329	spiral	SALT2
2007hx	0.078	4.75 ± 0.17	4.256 ± 0.933	0.879 ± 0.026	5.535 ± 3.008	spiral	both
2007ih	0.170	3.33 ± 0.20	0.941 ± 0.071	0.217 ± 0.012	2.134 ± 0.557	spiral	both
2007ik	0.184	1.97 ± 0.22	0.479 ± 0.070	0.107 ± 0.012	0.614 ± 0.212	elliptical	both
2007jd	0.072	7.00 ± 0.17	1.799 ± 0.030	0.241 ± 0.003	1.514 ± 0.033	spiral	MLCS2k2
2007jk	0.182	9.69 ± 0.27	2.254 ± 0.094	0.354 ± 0.007	2.945 ± 0.221	spiral	both
2007jt	0.144	5.57 ± 0.19	0.933 ± 0.030	0.167 ± 0.005	0.836 ± 0.036	spiral	both
2007ju	0.062	0.60 ± 0.12	0.273 ± 0.053	0.046 ± 0.009	0.252 ± 0.052	spiral	both
2007jw	0.136	6.13 ± 0.19	1.117 ± 0.028	0.199 ± 0.005	1.455 ± 0.043	spiral	MLCS2k2
2007jz	0.231	6.20 ± 0.30	1.362 ± 0.110	0.270 ± 0.012	2.373 ± 0.945	spiral	both
2007kb	0.143	3.97 ± 0.27	0.912 ± 0.072	0.141 ± 0.009	0.938 ± 0.161	spiral	both
2007kj	0.155	3.74 ± 0.19	1.090 ± 0.062	0.197 ± 0.009	1.662 ± 0.286	spiral	both
2007ks	0.094	1.15 ± 0.17	0.550 ± 0.067	0.092 ± 0.010	0.563 ± 0.072	spiral	both
2007kt	0.238	7.84 ± 0.30	1.945 ± 0.121	0.357 ± 0.011	2.254 ± 0.286	spiral	both
2007kx	0.153	2.78 ± 0.20	1.147 ± 0.120	0.223 ± 0.015	2.589 ± 1.191	spiral	both
2007lc	0.114	2.25 ± 0.13	0.447 ± 0.026	0.073 ± 0.004	0.431 ± 0.029	elliptical	both
2007lg	0.109	1.58 ± 0.12	0.685 ± 0.049	0.084 ± 0.006	0.960 ± 0.071	spiral	both
2007li	0.119	1.65 ± 0.12	0.346 ± 0.026	0.047 ± 0.003	0.365 ± 0.031	elliptical	SALT2
2007lk	0.219	1.68 ± 0.20	0.523 ± 0.063	0.067 ± 0.008	0.877 ± 0.123	elliptical	MLCS2k2
2007lo	0.137	1.92 ± 0.21	0.810 ± 0.151	0.193 ± 0.020	2.769 ± 1.840	spiral	both
2007lp	0.175	8.59 ± 0.24	2.789 ± 0.077	0.235 ± 0.005	2.917 ± 0.151	elliptical	both
2007lq	0.227	7.04 ± 0.25	1.131 ± 0.055	0.158 ± 0.005	1.374 ± 0.091	elliptical	both
2007lr	0.155	8.10 ± 0.23	1.155 ± 0.028	0.211 ± 0.004	1.270 ± 0.034	spiral	SALT2
2007ly	0.070	0.48 ± 0.07	0.267 ± 0.042	0.027 ± 0.004	0.284 ± 0.046	elliptical	MLCS2k2
2007ma	0.106	2.90 ± 0.12	0.785 ± 0.034	0.097 ± 0.004	0.499 ± 0.029	elliptical	both

Table D.1 – Continued

ID <sup>a</sup>	<i>z</i>	<i>D</i> <sub>kpc</sub>	<i>D</i> <sub>P50</sub>	<i>D</i> <sub>ISO</sub>	<i>D</i> <sub>Sersic</sub> <sup>b</sup>	Host type <sup>c</sup>	In sample <sup>d</sup>
2007mb	0.190	9.55 ± 0.23	2.166 ± 0.051	0.235 ± 0.003	2.402 ± 0.123	elliptical	both
2007mc	0.153	17.81 ± 0.38	4.184 ± 0.122	0.484 ± 0.004	3.486 ± 0.275	elliptical	both
2007mh	0.127	14.25 ± 0.36	3.220 ± 0.087	0.470 ± 0.007	3.051 ± 0.155	spiral	both
2007mi	0.131	7.78 ± 0.20	2.048 ± 0.047	0.288 ± 0.005	5.197 ± 0.239	elliptical	SALT2
2007mj	0.123	2.80 ± 0.13	0.725 ± 0.034	0.096 ± 0.004	0.646 ± 0.036	elliptical	both
2007mz	0.231	1.29 ± 0.24	0.318 ± 0.059	0.064 ± 0.012	0.526 ± 0.130	spiral	SALT2
2007ne	0.205	0.39 ± 0.19	0.091 ± 0.045	0.014 ± 0.007	0.142 ± 0.074	elliptical	both
2007nf	0.236	9.87 ± 0.29	2.562 ± 0.083	0.314 ± 0.007	3.136 ± 0.341	elliptical	both
2007ni	0.210	9.87 ± 0.33	2.939 ± 0.278	0.597 ± 0.016	4.486 ± 2.459	elliptical	SALT2
2007nj	0.153	9.88 ± 0.28	1.472 ± 0.051	0.176 ± 0.004	1.063 ± 0.037	spiral	both
2007nt	0.212	0.79 ± 0.20	0.216 ± 0.054	0.034 ± 0.008	0.284 ± 0.073	spiral	both
2007oj	0.122	0.98 ± 0.15	0.610 ± 0.125	0.115 ± 0.017	1.192 ± 0.671	elliptical	both
2007ok	0.165	19.70 ± 0.42	4.418 ± 0.079	0.454 ± 0.004	3.667 ± 0.129	elliptical	both
2007ol	0.055	2.13 ± 0.07	0.889 ± 0.025	0.000 ± 0.000	0.997 ± 0.033	elliptical	both
2007om	0.104	3.51 ± 0.13	0.639 ± 0.034	0.070 ± 0.002	0.430 ± 0.019	elliptical	both
2007or	0.165	0.99 ± 0.15	0.293 ± 0.045	0.043 ± 0.007	0.905 ± 0.151	elliptical	MLCS2k2
2007ow	0.210	3.23 ± 0.19	1.001 ± 0.087	0.173 ± 0.009	1.551 ± 0.340	elliptical	both
2007ox	0.210	4.84 ± 0.21	1.144 ± 0.057	0.151 ± 0.006	1.030 ± 0.082	spiral	both
2007oy	0.218	12.39 ± 0.35	4.512 ± 0.444	0.960 ± 0.020	9.214 ± 6.718	spiral	both
2007pc	0.137	1.20 ± 0.14	0.471 ± 0.062	0.077 ± 0.009	0.759 ± 0.126	elliptical	both
2007pt	0.174	6.09 ± 0.21	1.616 ± 0.050	0.262 ± 0.007	1.953 ± 0.080	spiral	both
2007qf	0.203	4.94 ± 0.37	0.847 ± 0.082	0.169 ± 0.012	0.811 ± 0.103	spiral	SALT2
2007qb	0.246	15.23 ± 0.37	1.965 ± 0.042	0.255 ± 0.004	2.006 ± 0.063	spiral	both
2007qo	0.217	4.15 ± 0.24	1.310 ± 0.092	0.203 ± 0.011	2.362 ± 0.462	spiral	both
2007qq	0.237	8.24 ± 0.54	1.534 ± 0.176	0.209 ± 0.013	0.864 ± 0.175	spiral	both
2007rk	0.195	9.55 ± 0.44	1.620 ± 0.157	0.217 ± 0.009	1.321 ± 0.172	spiral	both
2007ro	0.165	1.83 ± 0.13	0.382 ± 0.028	0.044 ± 0.003	0.245 ± 0.019	elliptical	SALT2
2007sb	0.211	2.39 ± 0.44	0.367 ± 0.070	0.089 ± 0.016	0.433 ± 0.097	spiral	both
779	0.237	1.34 ± 0.23	0.307 ± 0.053	0.052 ± 0.009	0.358 ± 0.065	spiral	both
911	0.206	6.20 ± 0.28	1.041 ± 0.098	0.156 ± 0.006	0.805 ± 0.068	spiral	both
1415	0.211	2.20 ± 0.21	0.307 ± 0.030	0.042 ± 0.004	0.351 ± 0.037	elliptical	both
2057	0.211	0.74 ± 0.20	0.167 ± 0.045	0.030 ± 0.008	0.250 ± 0.071	spiral	both
2162	0.172	5.36 ± 0.20	1.331 ± 0.053	0.152 ± 0.005	1.245 ± 0.074	elliptical	both
2639	0.215	1.12 ± 0.21	0.377 ± 0.069	0.041 ± 0.007	0.812 ± 0.165	elliptical	both
3049	0.166	1.34 ± 0.23	0.233 ± 0.040	0.044 ± 0.007	0.271 ± 0.050	spiral	both
3426	0.232	3.62 ± 0.23	0.922 ± 0.065	0.167 ± 0.010	1.186 ± 0.157	elliptical	both
3959	0.183	2.11 ± 0.45	0.587 ± 0.138	0.177 ± 0.038	1.086 ± 0.761	spiral	both
4019	0.180	11.72 ± 0.28	1.907 ± 0.034	0.310 ± 0.004	2.479 ± 0.087	spiral	both
4690	0.199	1.56 ± 0.16	0.494 ± 0.114	0.086 ± 0.009	1.311 ± 0.243	elliptical	MLCS2k2
5199	0.221	2.54 ± 0.23	1.125 ± 0.143	0.228 ± 0.020	2.373 ± 1.480	spiral	both
5486	0.228	6.55 ± 0.39	1.301 ± 0.099	0.206 ± 0.011	1.172 ± 0.127	spiral	both
5689	0.170	1.45 ± 0.20	0.334 ± 0.047	0.057 ± 0.008	0.355 ± 0.050	spiral	both
5785	0.147	7.50 ± 0.19	0.736 ± 0.016	0.077 ± 0.001	0.748 ± 0.019	elliptical	SALT2
5859	0.239	3.61 ± 0.25	0.685 ± 0.049	0.136 ± 0.009	1.106 ± 0.130	spiral	both
5963	0.236	3.90 ± 0.32	0.705 ± 0.074	0.172 ± 0.014	1.018 ± 0.195	spiral	both
6274	0.206	1.44 ± 0.15	0.603 ± 0.067	0.076 ± 0.008	0.967 ± 0.146	spiral	both
6326	0.222	11.59 ± 0.29	2.111 ± 0.064	0.266 ± 0.004	2.013 ± 0.086	spiral	both
6530	0.194	1.02 ± 0.20	0.352 ± 0.080	0.059 ± 0.012	0.879 ± 0.360	elliptical	both
6614	0.168	5.05 ± 0.18	1.235 ± 0.041	0.143 ± 0.004	1.082 ± 0.055	elliptical	both
6831	0.211	8.04 ± 0.47	1.261 ± 0.072	0.235 ± 0.013	1.285 ± 0.097	spiral	both
6861	0.190	3.09 ± 0.48	0.659 ± 0.113	0.155 ± 0.024	1.229 ± 0.369	spiral	both
7350	0.154	6.71 ± 0.22	0.883 ± 0.027	0.148 ± 0.004	0.987 ± 0.035	spiral	MLCS2k2
7600	0.187	3.25 ± 0.19	0.741 ± 0.046	0.089 ± 0.005	0.889 ± 0.095	elliptical	both
8254	0.188	1.83 ± 0.21	0.696 ± 0.084	0.100 ± 0.011	0.993 ± 0.142	spiral	both
8555	0.197	2.32 ± 0.19	0.863 ± 0.075	0.129 ± 0.010	1.479 ± 0.226	spiral	both
9740	0.237	1.05 ± 0.20	0.229 ± 0.044	0.028 ± 0.005	0.406 ± 0.080	elliptical	both
9817	0.224	0.87 ± 0.23	0.219 ± 0.058	0.035 ± 0.009	0.593 ± 0.193	elliptical	MLCS2k2
10106	0.147	2.02 ± 0.36	0.635 ± 0.120	0.143 ± 0.025	0.894 ± 0.296	spiral	MLCS2k2
11172	0.135	1.19 ± 0.16	0.266 ± 0.035	0.044 ± 0.006	0.277 ± 0.037	spiral	SALT2
12804	0.133	1.52 ± 0.14	0.592 ± 0.062	0.089 ± 0.008	0.917 ± 0.163	elliptical	both
13323	0.232	5.79 ± 0.29	1.164 ± 0.064	0.188 ± 0.009	1.311 ± 0.109	spiral	both
13545	0.214	1.31 ± 0.22	0.234 ± 0.039	0.031 ± 0.005	0.227 ± 0.038	elliptical	both
13897	0.231	3.27 ± 0.19	0.823 ± 0.048	0.109 ± 0.006	1.438 ± 0.136	elliptical	both
13907	0.196	5.54 ± 0.23	1.151 ± 0.050	0.228 ± 0.008	2.114 ± 0.175	spiral	both
14113	0.241	0.56 ± 0.23	0.123 ± 0.052	0.026 ± 0.011	0.182 ± 0.085	spiral	SALT2
14317	0.180	4.25 ± 0.27	0.875 ± 0.039	0.158 ± 0.006	1.351 ± 0.085	spiral	both
14389	0.232	9.34 ± 0.25	2.012 ± 0.049	0.236 ± 0.004	1.714 ± 0.080	elliptical	both
14445	0.236	5.65 ± 0.21	1.229 ± 0.119	0.146 ± 0.005	1.505 ± 0.105	elliptical	SALT2
14525	0.153	3.27 ± 0.19	1.030 ± 0.070	0.231 ± 0.013	2.978 ± 0.730	spiral	both
14554	0.250	3.93 ± 0.28	1.005 ± 0.081	0.206 ± 0.014	1.659 ± 0.384	spiral	MLCS2k2
14784	0.191	9.97 ± 0.25	1.893 ± 0.239	0.229 ± 0.004	1.475 ± 0.060	spiral	both
15033	0.216	1.29 ± 0.20	0.214 ± 0.034	0.028 ± 0.004	0.274 ± 0.045	elliptical	both
15343	0.174	1.04 ± 0.17	0.252 ± 0.042	0.041 ± 0.007	0.347 ± 0.060	spiral	both
15587	0.218	9.86 ± 0.29	1.701 ± 0.065	0.243 ± 0.005	2.178 ± 0.121	spiral	both
15748	0.156	1.54 ± 0.14	0.404 ± 0.037	0.046 ± 0.004	0.488 ± 0.050	elliptical	both
15823	0.214	2.18 ± 0.18	0.502 ± 0.050	0.067 ± 0.005	0.355 ± 0.046	elliptical	both
15829	0.248	1.59 ± 0.32	0.882 ± 0.257	0.122 ± 0.024	7.316 ± 2.757	spiral	both
15850	0.250	33.95 ± 0.71	6.571 ± 0.261	0.822 ± 0.005	7.045 ± 0.642	elliptical	both
15866	0.189	6.37 ± 0.18	1.090 ± 0.037	0.158 ± 0.003	0.944 ± 0.047	elliptical	both
16052	0.144	1.86 ± 0.15	0.980 ± 0.090	0.156 ± 0.012	1.405 ± 0.252	spiral	both
16103	0.201	1.94 ± 0.16	0.754 ± 0.076	0.084 ± 0.007	2.137 ± 0.994	elliptical	both
16163	0.154	0.45 ± 0.14	0.090 ± 0.028	0.015 ± 0.005	0.132 ± 0.042	spiral	both

## SNe distance measurements

---

Table D.1 – Continued

ID <sup>a</sup>	$z$	$D_{\text{kpc}}$	$D_{\text{P50}}$	$D_{\text{ISO}}$	$D_{\text{Sersic}}^b$	Host type <sup>c</sup>	In sample <sup>d</sup>
16452	0.205	1.04 ± 0.19	0.178 ± 0.032	0.023 ± 0.004	0.133 ± 0.025	elliptical	SALT2
16462	0.243	7.14 ± 0.26	0.803 ± 0.038	0.122 ± 0.004	0.786 ± 0.050	elliptical	both
16467	0.220	7.72 ± 0.24	1.791 ± 0.060	0.204 ± 0.005	1.954 ± 0.131	elliptical	both
17206	0.156	6.40 ± 0.24	1.307 ± 0.073	0.192 ± 0.006	1.902 ± 0.200	spiral	both
17408	0.239	3.17 ± 0.21	0.571 ± 0.040	0.121 ± 0.008	0.911 ± 0.093	spiral	SALT2
17434	0.178	4.35 ± 0.20	0.978 ± 0.043	0.158 ± 0.006	1.026 ± 0.051	spiral	both
17748	0.178	3.74 ± 0.39	0.732 ± 0.080	0.127 ± 0.013	0.566 ± 0.070	spiral	both
17908	0.233	1.50 ± 0.21	0.386 ± 0.098	0.047 ± 0.006	0.507 ± 0.086	elliptical	both
17928	0.196	5.32 ± 0.18	1.009 ± 0.046	0.131 ± 0.004	1.163 ± 0.063	elliptical	both
18362	0.235	1.36 ± 0.20	0.328 ± 0.049	0.057 ± 0.008	0.472 ± 0.078	spiral	both
18839	0.157	0.98 ± 0.36	0.578 ± 0.277	0.000 ± 0.000	5.586 ± 5.102	spiral	both
19317	0.178	2.26 ± 0.15	0.530 ± 0.035	0.093 ± 0.006	0.549 ± 0.042	spiral	MLCS2k2
19987	0.240	10.79 ± 0.31	2.875 ± 0.629	0.354 ± 0.008	5.056 ± 1.729	elliptical	both
20088	0.243	4.20 ± 0.21	0.651 ± 0.039	0.090 ± 0.004	0.745 ± 0.057	elliptical	MLCS2k2
20232	0.216	2.01 ± 0.18	0.478 ± 0.043	0.068 ± 0.006	0.656 ± 0.092	elliptical	both
20480	0.167	0.94 ± 0.17	0.235 ± 0.043	0.038 ± 0.007	0.284 ± 0.054	spiral	both
20721	0.211	6.86 ± 0.24	1.233 ± 0.042	0.210 ± 0.006	1.337 ± 0.061	spiral	both

<sup>a</sup> IAU name when exists, otherwise internal SDSS name.

<sup>b</sup> Distance normalized using exponential profile for SNe in spiral hosts and in de Vaucouleur profile for SNe in elliptical hosts.

<sup>c</sup> Host galaxy type as defined from concentration index and likelihoods from Sérsic brightness profile fits.

<sup>d</sup> Indicates if SN is present only in the MLCS2k2 or SALT2 samples, or in both.

---

## List of Figures

---

2.1	Original figure from Hubble's paper relating the recession velocity with distance from the Earth. . . . .	6
2.2	Measurements of the density parameters of Dark Energy ( $\Omega_\Lambda$ ) and matter ( $\Omega_m$ ), and in the $(\Omega_m, w)$ plane. . . . .	12
2.3	Redshift dependence of the different definitions of distance. . . . .	16
2.4	Zero points for AB and Vega magnitude system definitions. . . . .	18
2.5	Density parameter ( $\Omega_X$ ) as a function of the scale factor ( $a(t)$ ) for the components of the universe. . . . .	20
2.6	Observational constraints on the relative abundances of the lightest nuclei. . . . .	21
2.7	Historic Cosmic Microwave Background (CMB) signal measurements. . . . .	23
2.8	The CMB temperature power spectrum. . . . .	24
2.9	The large-scale correlation function of the SDSS LRG sample. . . . .	25
2.10	Composition of the universe according to the $\Lambda$ CDM model. . . . .	26
3.1	Remnants of the historical supernovae. . . . .	28
3.2	Binding energy per nucleon as a function of mass number. . . . .	30
3.3	Scheme of supernovae spectral classification. . . . .	33
3.4	Spectra of four different SNe types (Ia, II, Ic and Ib). . . . .	34
3.5	Spectra of several type Ia SNe at different epochs. . . . .	35
3.6	Schematic representation of light-curves of five different SNe types. . . . .	36
3.7	Standardized <i>B</i> -band light-curves of low- <i>z</i> Type Ia SNe. . . . .	37
3.8	Johnson and SDSS photometric systems. . . . .	38
3.9	Spectrum and bandwidth shifting. . . . .	39
3.10	Phillips relation. . . . .	41
3.11	SN Ia rate as a function of redshift. . . . .	45
3.12	Hubble diagram and residuals for MLCS2k2 and SALT2 fitters. . . . .	47

## LIST OF FIGURES

---

4.1	SDSS telescope and camera.	51
4.2	SDSS observing strategy.	52
4.3	Example of a reduced spectrum of SN2006fz measured at Hiltner.	56
4.4	SDSS photometry epochs.	57
4.5	SN2006fz spectrum flux calibrated with the galaxy contribution removed.	58
4.6	<i>ugriz</i> light-curves for SN2006fz.	59
4.7	SDSS-II/SNe spectroscopically confirmed Type Ia SNe.	60
5.1	Schematic drawing of the TNG parts.	62
5.2	Telescopio Nazionale Galileo (TNG).	63
5.3	DOLORES instrument mounted on the Nasmyth B focus of the TNG.	64
5.4	Quantum efficiency of the E2V CCD.	66
5.5	Header Unit of a FITS file.	68
5.6	FITS file of the SN2007jh spectrum before and after <i>debias</i> .	70
5.7	Averaged flat fields using slits of 1.0 and 5.0 arcsec.	71
5.8	Procedure for the obtention the flat field factor.	71
5.9	Spectra of the <i>Ne</i> , <i>He</i> and <i>Ar</i> lamps used for wavelength calibration.	72
5.10	Region used for the SN spectrum extraction.	73
5.11	SN spectrum extraction, step by step.	74
5.12	Reduced spectrum of the standard star G93-48.	76
5.13	Obtention of the flux calibration layer.	77
5.14	Spectra of four SNe observed at TNG. (1)	82
5.15	Spectra of four SNe observed at TNG. (2)	83
5.16	Spectra of four SNe observed at TNG. (3)	84
5.17	Spectra of four SNe observed at TNG. (4)	85
5.18	Spectra of four SNe observed at TNG. (5)	86
5.19	Spectra of three SNe observed at TNG. (6)	87
5.20	SNID output of the SN spectra of the SN2007ot obtained on November 4th.	88
6.1	Image of 07qd (denoted by arrow) relative to its host galaxy.	91
6.2	SDSS apparent light-curves of 07qd given in flux-density units.	92
6.3	<i>g – r</i> color of 05hk and 07qd for the first 3 weeks past-max brightness.	94
6.4	Temporal evolution of the spectrum of 07qd.	95
6.5	SNANA fits for the 02cx and 05hk using MLCS2k2 fitter.	96
6.6	SNANA fits for the 07qd and 08ha using MLCS2k2 fitter.	97
6.7	Light-curve stretch factors are compared to the <i>M</i> of peculiar SN Ia.	98
6.8	Spectrum of 07qd at 3 days past maximum and the best SYNOW fit.	100
6.9	Normalized 07qd spectrum 8 days past-max, with SYNOW fit.	102
6.10	Normalized 07qd spectrum 10 days past-max, with SYNOW fit.	104
6.11	Normalized 07qd spectrum 15 days past-max, with SYNOW fit.	106
6.12	Comparison of the spectrum of 07qd at 10 days past maximum brightness with that of 08ha, 05hk, and 02cx at similar epochs.	107
6.13	Normalized 02cx spectrum 12 days past-max, with SYNOW fit.	108

---

6.14 Normalized spectra of peculiar 02cx-like SN Ia, observed near maximum brightness. . . . .	109
6.15 Estimated photospheric velocities at $\sim 10$ days past maximum brightness plotted against maximum absolute magnitudes. . . . .	110
7.1 Hubble diagram and residuals for MLCS2K2 and SALT2 samples. . . . .	117
7.2 Determination of the morphology of the host galaxies. . . . .	120
7.3 Absolute and relative error distribution for distances of SN. . . . .	122
7.4 Redshift distribution for the SDSS SN Ia sample and for the sample used in this analysis. . . . .	123
7.5 Distribution of distance between supernova and galaxy core. . . . .	124
7.6 Comparison between the distribution of Sérsic normalized distances and the brightness profiles. . . . .	125
7.7 Distributions of the light-curve parameters and Hubble diagram residuals. . . . .	126
7.8 Local metallicity measurement. . . . .	127
7.9 MLCS2K2 parameters and Hubble residuals as a function of projected distance in kiloparsec and P50 normalization. . . . .	137
7.10 MLCS2K2 parameters and Hubble residuals as a function of projected distance in the ISO and Sérsic normalizations. . . . .	138
7.11 SALT2 parameters and Hubble residuals as a function of projected distance in kiloparsec and P50 normalization. . . . .	139
7.12 SALT2 parameters and Hubble residuals as a function of projected distance in the ISO and Sérsic normalizations. . . . .	140
7.13 SALT2 Hubble residuals as a function of the local metallicity. . . . .	142
C.1 Spherical trigonometry. . . . .	158
C.2 Equatorial coordinates of two objects on the surface of a sphere. . . . .	158
C.3 Petrosian radius 50. . . . .	160
C.4 Definition of Sérsic parameters. . . . .	161
C.5 Sérsic normalization. . . . .	162



---

## List of Tables

---

4.1	All SDSS-II/SNe candidates classified in groups. . . . .	59
5.1	Spectral lines of the Hydrogen Balmer series, the sky lines (Fraunhofer and atmospheric), and the three lamps available in LRS, used to calibrate in wavelength the SNe and standard stars spectra. All the wavelengths are in angstroms (Å). . . . .	78
5.2	Preliminary classification of the spectra given by the SNID software. The epoch is in days respect to the <i>B</i> maximum brightness. . . . .	80
5.3	SN spectra from the TNG in the SDSS-II/SNe database. . . . .	81
6.1	Observed SDSS photometry for 07qd (SN 20208), converted into fluxes. All measurements are given in $\mu\text{Jy}$ , and have not been corrected for reddening. Data associated with poor seeing have been omitted from this list. . . . .	92
6.2	Spectra observation schedule . . . . .	93
6.3	SYNOW Parameters for Fig. 6.8 (3 days after <i>B</i> -max), using a photospheric velocity ( $v_{\text{phot}}$ ) of 2800 km/s and a black-body temperature ( $T_{\text{bb}}$ ) of 10000 K. Velocities ( $v_{\text{min}}$ , $v_{\text{max}}$ , and $v_e$ , described in §6.2.2) are given in units of 1000 km/s and $T_{\text{exc}}$ values are given in units of 1000 K. . . . .	99
6.4	SYNOW Parameters for Fig. 6.9 (8 days after <i>B</i> -max), using a photospheric velocity ( $v_{\text{phot}}$ ) of 2800 km/s and a black-body temperature ( $T_{\text{bb}}$ ) of 9000 K. Velocities are given in units of 1000 km/s and $T_{\text{exc}}$ values are given in units of 1000 K. . . . .	101

## LIST OF TABLES

---

6.5	SYNOW Parameters for Fig. 6.10 (10 days after $B$ -max), using a photospheric velocity ( $v_{\text{phot}}$ ) of 2800 km/s and a black-body temperature ( $T_{\text{bb}}$ ) of 8000 K. Velocities are given in units of 1000 km/s and $T_{\text{exc}}$ values are given in units of 1000 K. . . . .	103
7.1	Number of SNe in the sample used for this analysis after applying selection cuts. . . . .	121
7.2	Results when correlating MLCS2κ2- $A_V$ with distance binned in multiple bins of equal size (upper table) and binned in a near and a far sample, with equal number of events in each bin (lower table). . . . .	130
7.3	Results when correlating SALT2-c with distance binned in multiple bins of equal size (upper table) and binned in a near and a far sample, with equal number of events in each bin (lower table). . . . .	132
7.4	Results when correlating MLCS2κ2- $\Delta$ with distance binned in multiple bins of equal size (upper table) and binned in a near and a far sample, with equal number of events in each bin (lower table). . . . .	133
7.5	Results when correlating SALT2- $x_1$ with distance binned in multiple bins of equal size (upper table) and binned in a near and a far sample, with equal number of events in each bin (lower table). . . . .	134
7.6	Results when correlating MLCS2κ2 Hubble residuals with distance binned in multiple bins of equal size (upper table) and binned in a near and a far sample, with equal number of events in each bin (lower table). . . . .	135
7.7	Results when correlating SALT2 Hubble residuals with distance binned in multiple bins of equal size (upper table) and binned in a near and a far sample, with equal number of events in each bin (lower table). . . . .	136
7.8	Same results than in the previous tables, but using the indirect measurement of the local metallicity, instead of the distance, to look for correlations with light-curve parameters. . . . .	141
A.1	Images taken and saved at TNG . . . . .	145
D.1	Final SN sample after all cuts have been applied. . . . .	163

---

## Bibliography

---

- Abazajian, K., et al., *The first data release of the sloan digital sky survey*, *Astrophys.J.*, 126, 2081 (2003)
- Abazajian, K. N., et al., *The seventh data release of the sloan digital sky survey*, *Astrophys.J.S Suppl.*, 182, 543 (2009)
- Abbott, T., et al., *The dark energy survey*, eprint arXiv, 10346 (2005)
- Ade, P. A. R., et al., *Planck early results: The planck mission*, eprint arXiv, 1101, 2022 (2011)
- Adelman-McCarthy, J. K., et al., *The fifth data release of the sloan digital sky survey*, *Astrophys.J.S Suppl.*, 172, 634 (2007)
- Adelman-McCarthy, J. K., et al., *The sixth data release of the sloan digital sky survey*, *Astrophys.J.S Suppl.*, 175, 297 (2008)
- Aldering, G., et al., *Overview of the nearby supernova factory*, Survey and Other Telescope Technologies and Discoveries. Edited by Tyson, 4836, 61 (2002)
- Aldering, G., et al., *Nearby supernova factory observations of sn 2005gj: Another type ia supernova in a massive circumstellar envelope*, *The Astrophysical Journal*, 650, 510 (2006)
- Allen, C. W., *Astrophysical quantities*, London: University of London (1973)
- Alpher, R. A., Herman, R., & Gamow, G. A., *Erratum: Thermonuclear reactions in the expanding universe*, *Physical Review*, 75, 701 (1949)
- Amanullah, R., et al., *Spectra and hubble space telescope light curves of six type ia supernovae at  $0.511 < z < 1.12$  and the union2 compilation*, *Astrophys.J.*, 716, 712 (2010)

## BIBLIOGRAPHY

---

- Annis, J. T., et al., *The sdss southern survey coadd data*, 2007 AAS/AAPT Joint Meeting, 209, 1197 (2006)
- Baade, W. & Zwicky, F., *On super-novae*, Proceedings of the National Academy of Sciences of the United States of America, 20, 254 (1934)
- Bailey, S., et al., *Using spectral flux ratios to standardize sn ia luminosities*, Astron.Astrophys., 500, L17 (2009)
- Barbon, R., Ciatti, F., & Rosino, L., *On the light curve and properties of type i supernovae.*, Astron. Astrophys., 25, 241 (1973), a&AA ID. AAA009.125.024
- Barbon, R., Ciatti, F., & Rosino, L., *Photometric properties of type ii supernovae*, Astron.Astrophys., 72, 287 (1979), a&AA ID. AAA025.125.014
- Baron, E., Lentz, E. J., & Hauschildt, P. H., *Detectability of mixed unburnt c+o in type ia supernova spectra*, The Astrophysical Journal, 588, L29 (2003)
- Bassett, B., et al., *Supernova 2007qd*, Central Bureau Electronic Telegrams, 1137, 1 (2007a)
- Bassett, B., et al., *Supernovae 2007ju and 2007kl-2007ld*, Central Bureau Electronic Telegrams, 1098, 1 (2007b)
- Bassett, B., et al., *Supernovae 2007oq-2007pj*, Central Bureau Electronic Telegrams, 1128, 1 (2007c)
- Bazin, G., et al., *The core-collapse rate from the supernova legacy survey*, Astron.Astrophys., 499, 653 (2009)
- Benetti, S., Cappellaro, E., Turatto, M., Taubenberger, S., Harutyunyan, A., & Valenti, S., *Supernova 2002ic: The collapse of a stripped-envelope, massive star in a dense medium?*, The Astrophysical Journal, 653, L129 (2006)
- Benetti, S., et al., *The diversity of type ia supernovae: Evidence for systematics?*, The Astrophysical Journal, 623, 1011 (2005)
- Bessell, M. S., *Ubvri passbands*, Astronomical Society of the Pacific, 102, 1181 (1990)
- Bethe, H. A., *Energy production in stars*, Physical Review, 55, 434 (1939)
- Blanton, M. R. & Roweis, S., *K-corrections and filter transformations in the ultraviolet, optical, and near-infrared*, Astrophys.J., 133, 734 (2007)
- Blanton, M. R., et al., *The luminosity function of galaxies in sdss commissioning data*, The Astronomical Journal, 121, 2358 (2001)
- Blondin, S. & Tonry, J. L., *Determining the type, redshift, and phase of a supernova spectrum, THE MULTICOLORED LANDSCAPE OF COMPACT OBJECTS AND THEIR EXPLOSIVE ORIGINS*. AIP Conference Proceedings, 924, 312 (2007)

---

## BIBLIOGRAPHY

- Boissier, S. & Prantzos, N., *Relative frequencies of supernovae types: dependence on host galaxy magnitude, galactocentric radius, and local metallicity*, Astron.Astrophys., 503, 137 (2009)
- Bombaci, I., *The maximum mass of a neutron star.*, Astron.Astrophys., 305, 871 (1996)
- Branch, D., *Type i supernovae and the value of the hubble constant*, Royal Astronomical Society, 179, 401 (1977), a&AA ID. AAA019.125.036
- Branch, D., *Some statistical properties of type i supernovae*, Astrophysical Journal, 248, 1076 (1981), a&AA ID. AAA030.125.016
- Branch, D., Baron, E., Thomas, R. C., Kasen, D., Li, W., & Filippenko, A. V., *Reading the spectra of the most peculiar type ia supernova 2002cx*, Publ.Astron.Soc.Pac., 116, 903 (2004)
- Branch, D., Doggett, J. B., Nomoto, K., & Thielemann, F.-K., *Accreting white dwarf models for the type i supernovae. iv the optical spectrum of a carbon-deflagration supernova*, Astrophys.J., 294, 619 (1985)
- Branch, D., Drucker, W., & Jeffery, D. J., *Differences among expansion velocities of type ia supernovae*, Astrophysical Journal, 330, L117 (1988)
- Branch, D., Fisher, A., & Nugent, P., *On the relative frequencies of spectroscopically normal and peculiar type ia supernovae*, The Astronomical Journal (ISSN 0004-6256), 106, 2383 (1993)
- Branch, D., Lacy, C. H., McCall, M. L., Sutherland, P. G., Uomoto, A., Wheeler, J. C., & Wills, B. J., *The type i supernova 1981b in ngc 4536 - the first 100 days*, Astrophys.J., 270, 123 (1983)
- Branch, D., Livio, M., Yungelson, L. R., Boffi, F. R., & Baron, E., *In search of the progenitors of type ia supernovae*, Publ.Astron.Soc.Pac., 107, 1019 (1995)
- Branch, D., et al., *Comparative direct analysis of type ia supernova spectra. ii. maximum light*, Publ.Astron.Soc.Pac., 118, 560 (2006)
- Bravo, E. & García-Senz, D., *A three-dimensional picture of the delayed-detonation model of type ia supernovae*, Astron.Astrophys., 478, 843 (2008)
- Brown, G. E., Lee, C.-H., & Méndez, E. M., *Gamma-ray bursts and hypernova explosions of some galactic sources*, The Astrophysical Journal, 671, L41 (2007)
- Brown, M. L., et al., *Improved measurements of the temperature and polarization of the cosmic microwave background from quad*, The Astrophysical Journal, 705, 978 (2009)
- Cardelli, J. A., Clayton, G. C., & Mathis, J. S., *The relationship between infrared, optical, and ultraviolet extinction*, Astrophys.J., 345, 245 (1989)

## BIBLIOGRAPHY

---

- Carroll, B. W. & Ostlie, D. A., *An introduction to modern astrophysics*, An introduction to modern astrophysics and cosmology / B. W. Carroll and D. A. Ostlie. 2nd edition. San Francisco: Pearson (2006)
- Chandrasekhar, S., *The highly collapsed configurations of a stellar mass*, Monthly Notices, 91, 456 (1931)
- Chevallier, M. & Polarski, D., *Accelerating universes with scaling dark matter*, International Journal of Modern Physics D, 10, 213 (2001)
- Chilingarian, I. V., Melchior, A.-L., & Zolotukhin, I. Y., *Analytical approximations of k-corrections in optical and near-infrared bands*, Monthly Notices, 405, 1409 (2010)
- Chornock, R., Filippenko, A. V., Branch, D., Foley, R. J., Jha, S., & Li, W., *Spectropolarimetry of the peculiar type ia supernova 2005hk*, Publ.Astron.Soc.Pac., 118, 722 (2006)
- Ciotti, L., *Stellar systems following the r exp 1/m luminosity law*, Astronomy and Astrophysics (ISSN 0004-6361), 249, 99 (1991)
- Colgate, S. A. & McKee, C., *Early supernova luminosity*, Astrophysical Journal, 157, 623 (1969), a&AA ID. AAA002.125.006
- Conley, A., et al., *Sifto: An empirical method for fitting sn ia light curves*, The Astrophysical Journal, 681, 482 (2008)
- Contardo, G., Leibundgut, B., & Vacca, W. D., *Epochs of maximum light and bolometric light curves of type ia supernovae*, Astron.Astrophys., 359, 876 (2000)
- Cooper, M. C., Newman, J. A., & Yan, R., *The large-scale environments of type ia supernovae: Evidence for a metallicity bias in the rate or luminosity of prompt ia events*, The Astrophysical Journal, 704, 687 (2009)
- Cousins, A. W. J., *Standard stars for vri photometry with s25 response photocathodes [errata: 1974mnssa..33....1c]*, Monthly Notes of the Astron. Soc. Southern Africa, 33, 149 (1974), a&AA ID. AAA012.113.052
- D'Andrea, C. B., *Spectroscopic host-galaxy properties and type ia supernova hubble residuals in a complete sample*, in prep., 1–31 (2011)
- de Vaucouleurs, G., *Recherches sur les nébuleuses extragalactiques*, Annales d'Astrophysique, 11, 247 (1948)
- de Vaucouleurs, G., *On the distribution of mass and luminosity in elliptical galaxies*, Monthly Notices, 113, 134 (1953)
- Deng, J., et al., *Subaru spectroscopy of the interacting type ia supernova sn 2002ic: Evidence of a hydrogen-rich, asymmetric circumstellar medium*, The Astrophysical Journal, 605, L37 (2004)

- Dilday, B., et al., *A measurement of the rate of type ia supernovae at redshift  $z \sim 0.1$  from the first season of the sdss-ii supernova survey*, *Astrophys.J.*, 682, 262 (2008)
- Dilday, B., et al., *A measurement of the rate of type ia supernovae in galaxy clusters from the sdss-ii supernova survey*, *Astrophys.J.*, 715, 1021 (2010a)
- Dilday, B., et al., *Measurements of the rate of type ia supernovae at redshift  $\sim 0.3$  from the sloan digital sky survey ii supernova survey*, *Astrophys.J.*, 713, 1026 (2010b)
- Dodelson, S., *Modern cosmology*, Modern cosmology / Scott Dodelson. Amsterdam (Netherlands): Academic Press. ISBN 0-12-219141-2 (2003), iISBN: 0-12-219141-2 Academic Press
- Duenas, F. J. C., Tejada, C., Hill, G. J., & G., F. P., *Hobby-eberly telescope low-resolution spectrograph: optical design*, Proc. SPIE Vol. 3355, 3355, 424 (1998)
- Efron, B., *Bootstrap methods: another look at the jackknife*, *The annals of Statistics* (1979)
- Einstein, A., *Die grundlage der allgemeinen relativitätstheorie*, *Annalen der Physik*, 354, 769 (1916)
- Eisenstein, D. J., et al., *Detection of the baryon acoustic peak in the large-scale correlation function of sdss luminous red galaxies*, *Astrophys.J.*, 633, 560 (2005)
- Eisenstein, D. J., et al., *Sdss-iii: Massive spectroscopic surveys of the distant universe, the milky way galaxy, and extra-solar planetary systems*, eprint arXiv, 1101, 1529 (2011), submitted to the Astronomical Journal
- Ellis, R. S., et al., *Verifying the cosmological utility of type ia supernovae: Implications of a dispersion in the ultraviolet spectra*, *The Astrophysical Journal*, 674, 51 (2008)
- Filippenko, A. V., *Optical spectra of supernovae*, *Annu. Rev. Astron. Astrophys.*, 35, 309 (1997)
- Filippenko, A. V., *Optical spectra and light curves of supernovae*, From Twilight to Highlight: The Physics of Supernovae: Proceedings of the ESO/MPA/MPE Workshop Held at Garching, 171 (2003)
- Filippenko, A. V., et al., *The peculiar type ia sn 1991t - detonation of a white dwarf?*, *Astrophysical Journal*, 384, L15 (1992a)
- Filippenko, A. V., et al., *The subluminous, spectroscopically peculiar type ia supernova 1991bg in the elliptical galaxy ngc 4374*, *Astronomical Journal (ISSN 0004-6256)*, 104, 1543 (1992b)
- Fisher, A., Branch, D., Hoflich, P., & Khokhlov, A., *The minimum ejection velocity of calcium in type ia supernovae and the value of the hubble constant*, *Astrophys.J. Letters*, 447, L73 (1995)

## BIBLIOGRAPHY

---

- Fisher, A., Branch, D., Nugent, P., & Baron, E., *Evidence for a high-velocity carbon-rich layer in the type ia sn 1990n*, *Astrophys.J. Letters*, 481, L89 (1997)
- Fisher, A. K., *Direct analysis of type ia supernovae spectra*, Thesis (PhD). THE UNIVERSITY OF OKLAHOMA, 6 (2000)
- Foley, R. J., Brown, P. J., Rest, A., Challis, P. J., Kirshner, R. P., & Wood-Vasey, W. M., *Early- and late-time observations of sn 2008ha: Additional constraints for the progenitor and explosion*, *Astrophys.J. Letters*, 708, L61 (2010)
- Foley, R. J., et al., *Sn 2008ha: An extremely low luminosity and exceptionally low energy supernova*, *Astrophys.J.*, 138, 376 (2009)
- Frebel, A., Christlieb, N., Norris, J. E., Thom, C., Beers, T. C., & Rhee, J., *Discovery of he 1523-0901, a strongly r-process-enhanced metal-poor star with detected uranium*, *The Astrophysical Journal*, 660, L117 (2007)
- Freedman, W. L., et al., *The carnegie supernova project: First near-infrared hubble diagram to  $z = 0.7$* , *Astrophys.J.*, 704, 1036 (2009)
- Friedmann, A., *Über die möglichkeit einer welt mit konstanter negativer krümmung des raumes*, *Zeitschrift für Physik*, 21, 326 (1924)
- Frieman, J. A., Turner, M. S., & Huterer, D., *Dark energy and the accelerating universe*, *Annu. Rev. Astron. Astrophys.*, 46, 385 (2008a)
- Frieman, J. A., et al., *The sloan digital sky survey-ii supernova survey: Technical summary*, *Astrophys.J.*, 135, 338 (2008b)
- Fukugita, M., Ichikawa, T., Gunn, J. E., Doi, M., Shimasaku, K., & Schneider, D. P., *The sloan digital sky survey photometric system*, *Astron.J.*, 111, 1748 (1996)
- Galbany, L., Miquel, R., & Östman, L., *Type-ia supernova properties as a function of the distance to the host galaxy in the sdss-ii/sne survey*, in prep. (2011)
- Gallagher, J. S., Garnavich, P. M., Berlind, P., Challis, P., Jha, S., & Kirshner, R. P., *Chemistry and star formation in the host galaxies of type ia supernovae*, *Astrophys.J.*, 634, 210 (2005)
- Gallagher, J. S., Garnavich, P. M., Caldwell, N., Kirshner, R. P., Jha, S. W., Li, W., Ganeshalingam, M., & Filippenko, A. V., *Supernovae in early-type galaxies: Directly connecting age and metallicity with type ia luminosity*, *Astrophys.J.*, 685, 752 (2008)
- Gamezo, V. N., Khokhlov, A. M., & Oran, E. S., *Numerical simulations of type ia supernovae: deflagrations and detonations*, *Cosmic explosions in three dimensions : asymmetries in supernovae and gamma-ray bursts*. Edited by P. Hoflich, 121 (2004)
- Gamow, G., *The evolution of the universe*, *Nature*, 162, 680 (1948a)

---

## BIBLIOGRAPHY

- Gamow, G., *The origin of elements and the separation of galaxies*, Physical Review, 74, 505 (1948b)
- Garnavich, P. M., et al., *The luminosity of sn 1999by in ngc 2841 and the nature of “peculiar” type ia supernovae*, The Astrophysical Journal, 613, 1120 (2004)
- Goldhaber, G., et al., *Timescale stretch parameterization of type ia supernova b-band light curves*, Astrophys.J., 558, 359 (2001)
- Graham, A. W. & Driver, S. P., *A concise reference to (projected) sérsic r1/n quantities, including concentration, profile slopes, petrosian indices, and kron magnitudes*, Publications of the Astronomical Society of Australia, 22, 118 (2005)
- Greggio, L. & Cappellaro, E., *The rate of type ia supernovae and the star formation history*, PROBING STELLAR POPULATIONS OUT TO THE DISTANT UNIVERSE: CEFALU 2008, 1111, 477 (2009)
- Gunn, J. E., et al., *The sloan digital sky survey photometric camera*, Astrophys.J., 116, 3040 (1998)
- Gunn, J. E., et al., *The 2.5 m telescope of the sloan digital sky survey*, Astrophys.J., 131, 2332 (2006)
- Gupta, R. R., et al., *Improved constraints on type ia supernova host galaxy properties using multi-wavelength photometry and their correlations with supernova properties*, eprint arXiv, 1107, 6003 (2011), the Astrophysical Journal (in press)
- Guy, J., Astier, P., Nobili, S., Regnault, N., & Pain, R., *Salt: a spectral adaptive light curve template for type ia supernovae*, Astron.Astrophys., 443, 781 (2005)
- Guy, J., et al., *Salt2: using distant supernovae to improve the use of type ia supernovae as distance indicators*, Astron.Astrophys., 466, 11 (2007)
- Guy, J., et al., *The supernova legacy survey 3-year sample: Type ia supernovae photometric distances and cosmological constraints*, Astron.Astrophys., 523, 7 (2010)
- Hadjietska, E. I., Rabinowitz, D., Baltay, C., Zinn, R., Coppi, P., Ellman, N., & Miller, L. R., *La silla-quest variability survey*, American Astronomical Society, 217, 43318 (2011), (c) 2011: American Astronomical Society
- Hamuy, M., Phillips, M. M., Maza, J., Suntzeff, N. B., Schommer, R. A., & Aviles, R., *A hubble diagram of distant type ia supernovae*, The Astronomical Journal (ISSN 0004-6256), 109, 1 (1995)
- Hamuy, M., Phillips, M. M., Suntzeff, N. B., Schommer, R. A., Maza, J., & Aviles, R., *The absolute luminosities of the calan/tololo type ia supernovae*, Astron.J., 112, 2391 (1996a)

## BIBLIOGRAPHY

---

- Hamuy, M., Trager, S. C., Pinto, P. A., Phillips, M. M., Schommer, R. A., Ivanov, V., & Suntzeff, N. B., *A search for environmental effects on type ia supernovae*, The Astronomical Journal, 120, 1479 (2000)
- Hamuy, M., et al., *The 1990 calan/tololo supernova search*, The Astronomical Journal (ISSN 0004-6256), 106, 2392 (1993)
- Hamuy, M., et al., *Bvri light curves for 29 type ia supernovae*, Astron.J., 112, 2408 (1996b)
- Hamuy, M., et al., *An asymptotic-giant-branch star in the progenitor system of a type ia supernova*, Nature, 424, 651 (2003)
- Hamuy, M., et al., *The carnegie supernova project: The low-redshift survey*, Publ.Astron.Soc.Pac., 118, 2 (2006)
- Harkness, R., *Type ia supernovae*, Supernova 1987A and other supernovae, 37, 447 (1991)
- Harkness, R. P. & Wheeler, J. C., *Classification of supernovae.*, Supernovae, 1 (1990)
- Hatano, K., Branch, D., Fisher, A., Millard, J., & Baron, E., *Ion signatures in supernova spectra*, Astrophys.J.Suppl., 121, 233 (1999)
- Hayden, B. T., et al., *The rise and fall of type ia supernova light curves in the sdss-ii supernova survey*, Astrophys.J., 712, 350 (2010)
- Hicken, M., et al., *Cfa3: 185 type ia supernova light curves from the cfa*, Astrophys.J., 700, 331 (2009)
- Hillebrandt, W. & Niemeyer, J. C., *Type ia supernova explosion models*, Annu. Rev. Astron. Astrophys., 38, 191 (2000)
- Holtzman, J. A., et al., *The Sloan digital sky survey-ii: Photometry and supernova ia light curves from the 2005 data*, Astrophys.J., 136, 2306 (2008)
- Howell, D. A., et al., *The type ia supernova snls-03d3bb from a super-chandrasekhar-mass white dwarf star*, Nature, 443, 308 (2006)
- Howell, D. A., et al., *The effect of progenitor age and metallicity on luminosity and 56ni yield in type ia supernovae*, Astrophys.J., 691, 661 (2009)
- Hoyle, F. & Tayler, R. J., *The mystery of the cosmic helium abundance*, Nature, 203, 1108 (1964)
- Hubble, E., *A relation between distance and radial velocity among extra-galactic nebulae*, Proceedings of the National Academy of Sciences of the United States of America, 15, 168 (1929)
- Ivezić, Ž., et al., *Sloan digital sky survey standard star catalog for stripe 82: The dawn of industrial 1% optical photometry*, The Astronomical Journal, 134, 973 (2007)

---

## BIBLIOGRAPHY

- Jarosik, N., et al., *Seven-year wilkinson microwave anisotropy probe (wmap) observations: Sky maps, systematic errors, and basic results*, *Astrophys.J.Suppl.*, 192, 14 (2011)
- Jeffery, D. J., *The sobolev-p method. iii - the sobolev-p method generalized for three-dimensional systems*, *Astrophysical Journal*, 352, 267 (1990)
- Jha, S., Branch, D., Chornock, R., Foley, R. J., Li, W., Swift, B. J., Casebeer, D., & Filippenko, A. V., *Late-time spectroscopy of sn 2002cx: The prototype of a new subclass of type ia supernovae*, *Astrophys.J.*, 132, 189 (2006a)
- Jha, S., Riess, A. G., & Kirshner, R. P., *Improved distances to type ia supernovae with multicolor light-curve shapes: Mlcs2k2*, *Astrophys.J.*, 659, 122 (2007)
- Jha, S., et al., *Ubvri light curves of 44 type ia supernovae*, *The Astronomical Journal*, 131, 527 (2006b)
- Johnson, H. L. & Morgan, W. W., *Fundamental stellar photometry for standards of spectral type on the revised system of the yerkes spectral atlas*, *Astrophys. J.* 117, 117, 313 (1953)
- Kaiser, N. & Team, P.-S., *The pan-starrs optical survey telescope project*, *American Astronomical Society*, 201, 1304 (2002)
- Karttunen, H., Krüger, P., Oja, H., Poutanen, M., & Donner, K. J., *Fundamental astronomy*, *Fundamental Astronomy* (2007)
- Keller, S. C., et al., *The skymapper telescope and the southern sky survey*, *Publications of the Astronomical Society of Australia*, 24, 1 (2007)
- Kelly, P. L., Hicken, M., Burke, D. L., Mandel, K. S., & Kirshner, R. P., *Hubble residuals of nearby type ia supernovae are correlated with host galaxy masses*, *Astrophys.J.*, 715, 743 (2010)
- Kessler, R., et al., *First-year Sloan digital sky survey-ii supernova results: Hubble diagram and cosmological parameters*, *Astrophys.J.Suppl.*, 185, 32 (2009a)
- Kessler, R., et al., *Snana: A public software package for supernova analysis*, *Publ.Astron.Soc.Pac.*, 121, 1028 (2009b)
- Kim, A. G., Linder, E. V., Miquel, R., & Mostek, N., *Effects of systematic uncertainties on the supernova determination of cosmological parameters*, *Monthly Notices*, 347, 909 (2004)
- Knop, R. A., et al., *New constraints on  $\Omega_m$ ,  $\Lambda$ , and  $w$  from an independent set of 11 high-redshift supernovae observed with the hubble space telescope*, *Astrophys.J.*, 598, 102 (2003)
- Komatsu, E., et al., *Seven-year wilkinson microwave anisotropy probe (wmap) observations: Cosmological interpretation*, *The Astrophysical Journal Supplement*, 192, 18 (2011)

## BIBLIOGRAPHY

---

- Konishi, K., et al., *Dependences of type ia supernovae lightcurve parameters on the host galaxy star formation rate and metallicity*, eprint arXiv, 1101, 4269 (2011)
- Kurucz, R. & Bell, B., *Atomic line data*, Atomic Line Data (R.L. Kurucz and B. Bell) Kurucz CD-ROM No. 23. Cambridge, 23 (1995)
- Lampeitl, H., et al., *The effect of host galaxies on type ia supernovae in the sdss-ii supernova survey*, *Astrophys.J.*, 722, 566 (2010a)
- Lampeitl, H., et al., *First-year Sloan Digital Sky Survey-II supernova results: consistency and constraints with other intermediate-redshift data sets*, *Monthly Notices*, 401, 2331 (2010b)
- Larson, D., et al., *Seven-year Wilkinson microwave anisotropy probe (wmap) observations: Power spectra and wmap-derived parameters*, *The Astrophysical Journal Supplement*, 192, 16 (2011)
- Leibundgut, B., Tammann, G. A., Cadonau, R., & Cerrito, D., *Supernova studies. vii - an atlas of light curves of supernovae type I*, *Astronomy and Astrophysics Supplement Series* (ISSN 0365-0138), 89, 537 (1991)
- Leibundgut, B., et al., *Sn 1991bg - a type Ia supernova with a difference*, *Astronomical Journal* (ISSN 0004-6256), 105, 301 (1993)
- Li, W., et al., *The unique type Ia supernova 2000cx in NGC 524*, *Publ. Astron. Soc. Pac.*, 113, 1178 (2001)
- Li, W., et al., *Sn 2002cx: The most peculiar known type Ia supernova*, *Publ. Astron. Soc. Pac.*, 115, 453 (2003)
- Li, W., et al., *Nearby supernova rates from the Lick Observatory Supernova Search - ii. the observed luminosity functions and fractions of supernovae in a complete sample*, *Monthly Notices*, 412, 1441 (2011)
- Liddle, A. R., *An introduction to modern cosmology*, Book (2003)
- Linder, E. V., *Exploring the expansion history of the universe*, *Physical Review Letters*, 90, 91301 (2003)
- Lupton, R., Gunn, J. E., Ivezić, Z., Knapp, G. R., & Kent, S., *The SDSS imaging pipelines*, *Astronomical Data Analysis Software and Systems X*, 238, 269 (2001)
- Lupton, R. H., Ivezić, Z., Gunn, J. E., Knapp, G., Strauss, M. A., & Yasuda, N., *SDSS imaging pipelines*, *Survey and Other Telescope Technologies and Discoveries*. Edited by Tyson, 4836, 350 (2002)
- Maeda, K., Röpke, F. K., Fink, M., Hillebrandt, W., Travaglio, C., & Thielemann, F.-K., *Nucleosynthesis in two-dimensional delayed detonation models of type Ia supernova explosions*, *The Astrophysical Journal*, 712, 624 (2010)

---

## BIBLIOGRAPHY

- Marriner, J., et al., *A more general model for the intrinsic scatter in type ia supernova distance moduli*, eprint arXiv, 1107, 4631 (2011)
- Mather, J. C., et al., *Measurement of the cosmic microwave background spectrum by the cobe firas instrument*, The Astrophysical Journal, 420, 439 (1994)
- Matheson, T., et al., *Optical spectroscopy of type ia supernovae*, Astrophys.J., 135, 1598 (2008)
- McClelland, C. M., et al., *The subluminous supernova 2007qd: A missing link in a family of low-luminosity type ia supernovae*, Astrophys.J., 720, 704 (2010)
- Miknaitis, G., et al., *The essence supernova survey: Survey optimization, observations, and supernova photometry*, The Astrophysical Journal, 666, 674 (2007)
- Minkowski, R., *Spectra of supernovae*, Publications of the Astronomical Society of the Pacific, 53, 224 (1941)
- Mochkovitch, R., *An introduction to the physics of type ii supernova explosions*, Matter Under Extreme Conditions, 440, 49 (1994)
- Nakamura, K. & Group, P. D., *Review of particle physics*, Journal of Physics G: Nuclear and Particle Physics, 37, 5021 (2010)
- Neill, J. D., et al., *The type ia supernova rate at z 0.5 from the supernova legacy survey*, The Astronomical Journal, 132, 1126 (2006)
- Neill, J. D., et al., *The local hosts of type ia supernovae*, Astrophys.J., 707, 1449 (2009)
- Nomoto, K., Iwamoto, K., & Kishimoto, N., *Type ia supernovae: their origin and possible applications in cosmology*, Science, 276, 1378 (1997)
- Nomoto, K., Umeda, H., Kobayashi, C., Hachisu, I., Kato, M., & Tsujimoto, T., *Type ia supernovae: Progenitors and evolution with redshift*, COSMIC EXPLOSIONS: Tenth Astrophysics Conference. AIP Conference Proceedings, 522, 35 (2000)
- Nomoto, K., Yamaoka, H., Pols, O. R., van den Heuvel, E. P. J., Iwamoto, K., Kumagai, S., & Shigeyama, T., *A carbon-oxygen star as progenitor of the type ic supernova 1994i*, Nature, 371, 227 (1994), (c) 1994: Nature
- Nordin, J., et al., *Evidence for a correlation between the si ii  $\lambda\lambda$ 4000 width and type ia supernova color*, The Astrophysical Journal, 734, 42 (2011a)
- Nordin, J., et al., *Spectral properties of type ia supernovae up to z = 0.3*, Astron.Astrophys., 526, 119 (2011b)
- Nugent, P., Kim, A. G., & Perlmutter, S., *K-corrections and extinction corrections for type ia supernovae*, Publ.Astron.Soc.Pac., 114, 803 (2002)

## BIBLIOGRAPHY

---

- Nugent, P., Phillips, M., Baron, E., Branch, D., & Hauschildt, P., *Evidence for a spectroscopic sequence among type 1a supernovae*, *Astrophysical Journal Letters* v.455, 455, L147 (1995)
- Oemler, A. & Tinsley, B. M., *Type i supernovae come from short-lived stars*, *Astronomical Journal*, 84, 985 (1979), a&AA ID. AAA026.125.019
- Oke, J. B. & Gunn, J. E., *Secondary standard stars for absolute spectrophotometry*, *Astrophys.J.*, 266, 713 (1983)
- Oke, J. B. & Sandage, A., *Energy distributions, k corrections, and the stebbins-whitford effect for giant elliptical galaxies*, *Astrophys.J.*, 154, 21 (1968)
- Oke, J. B., et al., *The keck low-resolution imaging spectrometer*, *Publications of the Astronomical Society of the Pacific*, 107, 375 (1995)
- Olive, D., *A simple confidence interval for the median*, *Manuscript* (2005)
- Oppenheimer, J. R. & Volkoff, G. M., *On massive neutron cores*, *Physical Review*, 55, 374 (1939)
- Oyaizu, H., Lima, M., Cunha, C. E., Lin, H., Frieman, J., & Sheldon, E. S., *A galaxy photometric redshift catalog for the sloan digital sky survey data release 6*, *Astrophys.J.*, 674, 768 (2008)
- Paczynski, B., *Evolutionary processes in close binary systems*, *Annu. Rev. Astron. Astrophys.*, 9, 183 (1971), a&AA ID. AAA006.117.004
- Penzias, A. A. & Wilson, R. W., *A measurement of excess antenna temperature at 4080 mc/s.*, *Astrophysical Journal*, 142, 419 (1965)
- Perlmutter, S., et al., *Measurements of the cosmological parameters omega and lambda from the first seven supernovae at  $z \geq 0.35$* , *Astrophys.J.*, 483, 565 (1997a)
- Perlmutter, S., et al., *Measurements of omega and lambda from 42 high-redshift supernovae*, *Astrophys.J.*, 517, 565 (1999)
- Perlmutter, S. A. & et al., *Scheduled discovery of 7+ high-redshift sne: first cosmology results and bounds on q0*, *Thermonuclear Supernovae*, 749 (1997b)
- Petrosian, V., *Surface brightness and evolution of galaxies*, *Astrophysical Journal*, 209, L1 (1976), a&AA ID. AAA018.158.044
- Phillips, M. M., *The absolute magnitudes of type ia supernovae*, *Astrophys.J.*, 413, L105 (1993)
- Phillips, M. M., Lira, P., Suntzeff, N. B., Schommer, R. A., Hamuy, M., & Maza, J., *The reddening-free decline rate versus luminosity relationship for type ia supernovae*, *Astrophys.J.*, 118, 1766 (1999)

---

## BIBLIOGRAPHY

- Phillips, M. M., Wells, L. A., Suntzeff, N. B., Hamuy, M., Leibundgut, B., Kirshner, R. P., & Foltz, C. B., *Sn 1991t - further evidence of the heterogeneous nature of type ia supernovae*, Astronomical Journal (ISSN 0004-6256), 103, 1632 (1992)
- Phillips, M. M., et al., *The peculiar sn 2005hk: Do some type ia supernovae explode as deflagrations?1*, Publ.Astron.Soc.Pac., 119, 360 (2007)
- Pier, J. R., Munn, J. A., Hindsley, R. B., Hennessy, G. S., Kent, S. M., Lupton, R. H., & Ivezić, Ž., *Astrometric calibration of the Sloan digital sky survey*, The Astronomical Journal, 125, 1559 (2003)
- Popper, D. M., *The spectrum of the super-nova in IC 4182*, Publications of the Astronomical Society of the Pacific, 49, 283 (1937)
- Poznanski, D., Gal-Yam, A., Maoz, D., Filippenko, A. V., Leonard, D. C., & Matheson, T., *Not color-blind: Using multiband photometry to classify supernovae*, Publ.Astron.Soc.Pac., 114, 833 (2002)
- Prieto, J., Garnavich, P., Depoy, D., Marshall, J., Eastman, J., & Frank, S., *Supernova 2005gj*, Central Bureau Electronic Telegrams, 302, 1 (2005)
- Prieto, J. L., Rest, A., & Suntzeff, N. B., *A new method to calibrate the magnitudes of type ia supernovae at maximum light*, Astrophys.J., 647, 501 (2006)
- Pskovskii, I. P., *Light curves, color curves, and expansion velocity of type I supernovae as functions of the rate of brightness decline*, (Astronomicheskii Zhurnal, 21, 675 (1977))
- Rau, A., et al., *Exploring the optical transient sky with the Palomar Transient Factory*, Publications of the Astronomical Society of the Pacific, 121, 1334 (2009)
- Reichardt, C. L., et al., *High-resolution CMB power spectrum from the complete ACBAR data set*, The Astrophysical Journal, 694, 1200 (2009)
- Richardson, D., Branch, D., Casebeer, D., Millard, J., Thomas, R. C., & Baron, E., *A comparative study of the absolute magnitude distributions of supernovae*, Astrophys.J., 123, 745 (2002)
- Richardson, D., Thomas, R. C., Casebeer, D., Blankenship, Z., Ratowt, S., Baron, E., & Branch, D., *Suspect - the online supernova spectrum database*, American Astronomical Society, 199, 1428 (2001)
- Riess, A. G., Press, W. H., & Kirshner, R. P., *A precise distance indicator: Type Ia supernova multicolor light-curve shapes*, Astrophys.J., 473, 88 (1996)
- Riess, A. G., et al., *Observational evidence from supernovae for an accelerating universe and a cosmological constant*, Astrophys.J., 116, 1009 (1998)
- Riess, A. G., et al., *BVRI light curves for 22 type Ia supernovae*, The Astronomical Journal, 117, 707 (1999)

## BIBLIOGRAPHY

---

- Roos, M., *Introduction to cosmology*, Book (2003)
- Röpke, F. K., Hillebrandt, W., Kasen, D., & Woosley, S. E., *Modeling the diversity of type ia supernova explosions*, Numerical Modeling of Space Plasma Flows, 429, 142 (2010)
- Rubin, V. C., Ford, W. K. J., & Thonnard, N. ., *Rotational properties of 21 sc galaxies with a large range of luminosities and radii, from ngc 4605 /r = 4kpc/ to ugc 2885 /r = 122 kpc/*, Astrophysical Journal, 238, 471 (1980), a&AA ID. AAA027.158.318
- Ruiz-Lapuente, P., *Dark energy, gravitation and supernovae*, eprint arXiv, 0704, 1058 (2007)
- Ryden, B., *Introduction to cosmology*, Book (2003), ISBN: 0-8053-8912-1 Addison Wesley
- Sachs, R. K. & Wolfe, A. M., *Perturbations of a cosmological model and angular variations of the microwave background*, Astrophys.J., 147, 73 (1967)
- Sako, M., et al., *The fall 2004 sdss supernova survey*, Proceedings of the 22nd Texas Symposium on Relativistic Astrophysics at Stanford, 415 (2005)
- Sako, M., et al., *The Sloan Digital Sky Survey-II supernova survey: Search algorithm and follow-up observations*, Astrophys.J., 135, 348 (2008)
- Sako, M., et al., *Photometric sn ia candidates from the three-year sdss-ii sn survey data*, eprint arXiv, 1107, 5106 (2011)
- Schechter, P. L., Mateo, M., & Saha, A., *Dophot, a ccd photometry program: Description and tests*, Astronomical Society of the Pacific, 105, 1342 (1993)
- Schlegel, D. J., Finkbeiner, D. P., & Davis, M., *Maps of dust infrared emission for use in estimation of reddening and cosmic microwave background radiation foregrounds*, Astrophysical Journal v.500, 500, 525 (1998)
- Schmidt, B. P., et al., *The high-z supernova search: Measuring cosmic deceleration and global curvature of the universe using type ia supernovae*, Astrophys.J., 507, 46 (1998)
- Sérsic, J. L., *Influence of the atmospheric and instrumental dispersion on the brightness distribution in a galaxy*, Boletin de la Asociacion Argentina de Astronomia, 6, 41 (1963)
- Shimasaku, K., et al., *Statistical properties of bright galaxies in the Sloan Digital Sky Survey photometric system*, Astrophys.J., 122, 1238 (2001)
- Smith, J. A., et al., *The u'g'r'i'z' standard-star system*, The Astronomical Journal, 123, 2121 (2002)
- Smith, M., et al., *The sdss-ii supernova survey: Parameterizing the type ia supernova rate as a function of host galaxy properties*, eprint arXiv, 1108, 4923 (2011), 46 pages, submitted to ApJ

- Smoot, G. F., et al., *Preliminary results from the cobe differential microwave radiometers - large angular scale isotropy of the cosmic microwave background*, *Astrophysical Journal*, 371, L1 (1991)
- Smoot, G. F., et al., *Structure in the cobe differential microwave radiometer first-year maps*, *Astrophysical Journal*, 396, L1 (1992)
- Sollerman, J., et al., *First-year Sloan digital sky survey-ii (sdss-ii) supernova results: Constraints on nonstandard cosmological models*, *Astrophys.J.*, 703, 1374 (2009)
- Stoughton, C., et al., *Sloan digital sky survey: Early data release*, *Astrophys.J.*, 123, 485 (2002)
- Strateva, I., et al., *Color separation of galaxy types in the Sloan digital sky survey imaging data*, *Astrophys.J.*, 122, 1861 (2001)
- Strömgren, L.-G., Riess, A. G., & Dahlen, T., *Probing acceleration now with supernovae: The pans high er-z supernova survey, 1604-2004: Supernovae as Cosmological Lighthouses*, 342, 471 (2005)
- Sullivan, M., et al., *Photometric selection of high-redshift type ia supernova candidates*, *Astrophys.J.*, 131, 960 (2006a)
- Sullivan, M., et al., *Rates and properties of type ia supernovae as a function of mass and star formation in their host galaxies*, *Astrophys.J.*, 648, 868 (2006b)
- Sullivan, M., et al., *The dependence of type ia supernovae luminosities on their host galaxies*, *Monthly Notices*, 406, 782 (2010)
- Sunyaev, R. A. & Zeldovich, I. B., *Microwave background radiation as a probe of the contemporary structure and history of the universe*, In: Annual review of astronomy and astrophysics. Volume 18. (A81-20334 07-90) Palo Alto, 18, 537 (1980), a&AA ID. AAA028.162.060
- Swartz, D. A., Filippenko, A. V., Nomoto, K., & Wheeler, J. C., *Spectra of low-mass helium star models and the type ic supernova sn 1987m*, *Astrophysical Journal*, 411, 313 (1993)
- Tonry, J. & Davis, M., *A survey of galaxy redshifts. i - data reduction techniques*, *Astronomical Journal*, 84, 1511 (1979), a&AA ID. AAA026.158.108
- Tripp, R., *A two-parameter luminosity correction for type ia supernovae*, *Astron.Astrophys.*, 331, 815 (1998)
- Trumpler, R. J., *Preliminary results on the distances, dimensions and space distribution of open star clusters*, Lick Observatory bulletin ; no. 420; Lick Observatory bulletins ; no. 420., 14, 154 (1930)

## BIBLIOGRAPHY

---

- Turatto, M., Benetti, S., Cappellaro, E., Danziger, I. J., della Valle, M., Gouiffes, C., Mazzali, P. A., & Patat, F., *The properties of the peculiar type ia supernova 1991bg. i. analysis and discussion of two years of observations.*, Mon. Not. R. Astron. Soc., 283, 1 (1996)
- Tyson, J. A., Wittman, D. M., Hennawi, J. F., & Spergel, D. N., *Lsst: a complementary probe of dark energy*, Nuclear Physics B Proceedings Supplements, 124, 21 (2003)
- Uomoto, A., et al., *The sloan digital sky survey spectrographs*, American Astronomical Society, 195, 1501 (1999)
- Valenti, S., et al., *The carbon-rich type ic sn 2007gr: The photospheric phase*, The Astrophysical Journal, 673, L155 (2008)
- Valenti, S., et al., *A low-energy core-collapse supernova without a hydrogen envelope*, Nature, 459, 674 (2009)
- Wang, L., Goldhaber, G., Aldering, G., & Perlmutter, S., *Color-magnitude intercept calibrations (cmagic) for type ia supernovae*, American Astronomical Society, 201, 1305 (2002)
- Wang, L., Strovink, M., Conley, A., Goldhaber, G., Kowalski, M., Perlmutter, S., & Siegrist, J., *Nonlinear decline-rate dependence and intrinsic variation of type ia supernova luminosities*, The Astrophysical Journal, 641, 50 (2006)
- Wang, X., Wang, L., Zhou, X., Lou, Y.-Q., & Li, Z., *A novel color parameter as a luminosity calibrator for type ia supernovae*, The Astrophysical Journal, 620, L87 (2005)
- Weinberg, S., *Cosmology*, Cosmology (2008), ISBN: 978-0-19-852682-7
- Wheeler, J. C. & Harkness, R. P., *Type i supernovae*, Reports on Progress in Physics, 53, 1467 (1990)
- Wilson, R. W. & Penzias, A. A., *Isotropy of cosmic background radiation at 4080 megahertz*, Science, 156, 1100 (1967)
- Woosley, S. & Janka, T., *The physics of core-collapse supernovae*, Nature Physics, 1, 147 (2005)
- Woosley, S. E., Langer, N., & Weaver, T. A., *The evolution of massive stars including mass loss - presupernova models and explosion*, Astrophysical Journal - Part 1 (ISSN 0004-637X), 411, 823 (1993)
- Woosley, S. E., Langer, N., & Weaver, T. A., *The presupernova evolution and explosion of helium stars that experience mass loss*, Astrophysical Journal v.448, 448, 315 (1995)
- Woosley, S. E., et al., *Type ia supernovae*, Journal of Physics: Conference Series, 78, 2081 (2007)

## BIBLIOGRAPHY

---

- Yamauchi, C., et al., *Morphological classification of galaxies using photometric parameters: The concentration index versus the coarseness parameter*, *Astrophys.J.*, 130, 1545 (2005)
- York, D. G., et al., *The sloan digital sky survey: Technical summary*, *Astrophys.J.*, 120, 1579 (2000)
- Zheng, C., et al., *First-year spectroscopy for the sloan digital sky survey-ii supernova survey*, *Astrophys.J.*, 135, 1766 (2008)
- Zwicky, F., *Die rotverschiebung von extragalaktischen nebeln*, *Helvetica Physica Acta*, 6, 110 (1933)

